INVEST. BUILD. GROW.

MANITOBA

GEOSCIENTIFIC REPORT GR2020-1

GEOLOGY OF THE CAT CREEK–EUCLID LAKE AREA, BIRD RIVER GREENSTONE BELT, SOUTHEASTERN MANITOBA (PARTS OF NTS 52L11, 12)

Manitoba Geological Survey

Manitoba

Geoscientific Report GR2020-1

Geology of the Cat Creek–Euclid Lake area, Bird River greenstone belt, southeastern Manitoba (parts of NTS 52L11, 12)

by X.M. Yang and M.G. Houlé
Manitoba Geological Survey
Winnipeg, 2020

Yang, X.M. and Houlé, M.G. 2020: Geology of the Cat Creek–Euclid Lake area, Bird River greenstone belt, southeastern Manitoba (parts of NTS 52L11, 12); Manitoba Agriculture and Resource Development, Manitoba Geological Survey, Geoscientific Report GR2020-1, 105 p. plus 1 colour map at 1:20 000 scale.

NTS grid: 52L11, 52L12

External author address:

M.G. Houlé
Geological Survey of Canada
Natural Resources Canada
Québec, QC G1K 9A9

Published by:
Manitoba Agriculture and Resource Development
Manitoba Geological Survey
360-1395 Ellice Avenue
Winnipeg, Manitoba
R3G 3P2 Canada
Telephone: 1-800-223-5215 (General Enquiry)
204-945-6569 (Publication Sales)
Fax: 204-945-8427
E-mail: minesinfo@gov.mb.ca
Website: manitoba.ca/minerals

ISBN: 978-0-7711-1610-0

This publication is available to download free of charge at manitoba.ca/minerals

Front cover photo:
Rusty exposure of the M2 deposit by a trench at Mayville.

Abstract

The Cat Creek–Euclid Lake map area is located about 145 km northeast of Winnipeg, Manitoba, and covers an area of ~130 km^2 in the northern arm of the Neoarchean Bird River greenstone belt (BRGB). This greenstone belt, which is tectonically situated at the western edge of the Superior province, consists of a set of east-trending terranes (and basins) and is flanked to the north by the English River basin and to the south by the Winnipeg River terrane.

Bedrock mapping in the Cat Creek–Euclid Lake area indicates the presence of 14 lithostratigraphic units that record a diverse history of geodynamic evolution; more importantly, various types of mineralization formed at different stages of the evolution. Unit 1 is represented by the older phases of the Maskwa Lake batholith I (Mesoarchean), which forms the basement to the BRGB. Deposited atop unit 1 are tholeiitic to transitional basalts and related synvolcanic gabbroic rocks of unit 2, interpreted to have formed in an island-arc to back-arc environment at or near a continental margin. Units 3–7 represent mappable lithological units of the Mayville and Euclid Lake mafic–ultramafic intrusions that are comparable to the Bird River sill in the southern arm of the BRGB. These intrusions were formed at ca. 2743 Ma by the Bird River magmatic event (BRME). Unit 8 consists of discrete gabbroic intrusions and is interpreted as the product of the waning stage of the BRME that formed in an extensional regime over a large area. Unit 9 consists of sedimentary and minor volcanic sedimentary rocks with local occurrences of mafic intrusive rocks as sills or dikes; this unit underwent amphibolite-facies metamorphism. Unit 10 comprises dominantly tonalite-trondhjemite-granodiorite suite (TTG) rocks that constitute younger phases of the Maskwa Lake batholith II (Neoarchean), which formed in a magmatic-arc setting related to plate subduction. Unit 11 is dominated by sedimentary and minor volcaniclastic rocks and associated mafic intrusive rocks, interpreted as part of the BRGB that was deposited in a back-arc setting. Unit 12 is composed of the Inconnu pluton, consisting mainly of granodiorite and granite, as well as gneissic granodiorite to granite that contain muscovite or garnet but lack late mafic dikes, which could be part of the plutonic rocks emplaced into the English River basin. Unit 13 is composed mainly of muscovite±garnet–bearing granites that occur along the southern margin of the English River basin; these are mostly S-type granites formed by partial melting of sedimentary rocks in a thickened crust due to collision between the Winnipeg River terrane to the south and the North Caribou terrane to the north. Unit 14 consists of pegmatite and minor aplite dikes, some of which contain rare-metal (e.g., Li, Cs, Nb, Ta) mineralization.

Distinctively different types of mineralization formed at specific stages during the geodynamic evolution, requiring suitable tectonic environments and favourable geological conditions. Magmatic Ni–Cu–platinum-group element (PGE)–Cr mineralization is genetically associated with the ca. 2743 Ma mafic–ultramafic intrusions that formed in an extensional geodynamic setting likely related to back-arc extension and (or) arc rifting. Porphyry Cu (Au) and skarn Cu-Au-Ag-(W) mineralization is related to arc magmatism typified by some of the I-type phases of the TTG suite in an environment akin to a modern subduction setting. Rare-metals (Li, Cs, Nb, Ta) mineralization is hosted in pegmatites that are genetically related to younger, peraluminous, S-type granitoid rocks (between ca. 2660 and 2640 Ma) that were emplaced in a continental-collision setting.

Résumé

La région géographique du ruisseau Cat et du lac Euclid se trouve à environ 145 km au nord-est de Winnipeg, au Manitoba, et couvre une superficie de quelque 130 km^2 dans le bras nord de la ceinture de roches vertes de la rivière Bird (la « ceinture »), formée pendant le Néoarchéen. Tectoniquement située à la limite ouest de la province du lac Supérieur, cette ceinture est constituée d'un ensemble de terranes et de bassins d'orientation est-ouest. Elle est bordée au nord par le bassin de la rivière English et au sud par le terrane de la rivière Winnipeg.

La cartographie du substrat rocheux de la région du ruisseau Cat et du lac Euclid révèle la présence de 14 unités lithostratigraphiques témoignant d'une évolution géodynamique diversifiée et, plus précisément, de diverses minéralisations qui se sont produites à différents stades de son évolution. L'unité 1 comprend les phases les plus anciennes du batholite du lac Maskwa (Mésoarchéen), qui constitue le socle de la ceinture. On trouve sur l'unité 1 des dépôts de basalte tholéiitique à intermédiaire et de roches gabbroïques synvolcaniques de l'unité 2, qui se seraient formés dans une zone d'arc insulaire et d'arrière-arc sur une marge continentale ou à proximité. Les unités 3 à 7 correspondent aux unités lithostratigraphiques cartographiables des intrusions mafiques-ultramafiques de la région de Mayville et du lac Euclid, qui sont semblables au Filon-couche de la rivière Bird dans le bras sud de la ceinture. Ces intrusions se sont formées il y a environ 2 743 millions d'années à la suite de l'événement magmatique de la rivière Bird. L'unité 8 est constituée d'intrusions gabbroïques séparées qui se seraient mises en place pendant la phase de déclin de l'événement magmatique de la rivière Bird, dans un régime extensif de grande étendue. L'unité 9 est constituée de roches sédimentaires et de roches volcano-sédimentaires mineures, avec des venues localisées de roches intrusives mafiques formant des filons-couches ou des dykes. Cette unité a subi un métamorphisme au faciès des amphibolites. L'unité 10 se compose principalement de roches de la suite tonalite-trondhjémite-granodiorite. Elles constituent les phases plus récentes du batholite II du lac Maskwa (Néoarchéen), lequel batholite s'est formé dans l'arc magmatique d'une zone de subduction. L'unité 11 est constituée principalement de roches sédimentaires, de roches volcano-sédimentaires mineures et de roches intrusives mafiques connexes. Cette partie de la ceinture se serait formée par dépôt en zone d'arrière-arc. L'unité 12 est constituée du pluton Inconnu, majoritairement formé de granodiorite et de granite ainsi que de granodiorite et de granite gneissiques contenant de la muscovite ou du grenat, mais sans dykes mafiques tardifs, qui pourraient faire partie des roches plutoniques mises en place dans le bassin de la rivière English. L'unité 13 est constituée principalement de granite à muscovite ± grenat qui se trouve le long de la limite sud du bassin de la rivière English; il s'agit surtout de granite de type S formé par la fonte partielle de roches sédimentaires qui produit une couche épaissie à la suite de la collision du terrane de la rivière Winnipeg au sud et du terrane de North Caribou au nord. L'unité 14 est constituée de pegmatite et de dykes d'aplite mineurs, dont certains contiennent des minéralisations de métaux rares (p. ex. Li, Cs, Nb, Ta).

Différents types de minéralisations se sont formés à des stades précis de l'évolution géodynamique, lorsque les conditions tectoniques et géologiques y étaient propices. Les minéralisations magmatiques de nickel-cuivre-éléments du groupe du platine sont associées génétiquement aux intrusions mafiques-ultramafiques datant d'environ 2 743 millions d'années qui se sont formées dans une zone géodynamique d'extension probablement liée à une extension d'arrière-arc ou à un rifting d'arc. Les minéralisations du porphyre à Cu (Au) et du skarn à Cu-Au-Ag-(W) sont liées au magmatisme d'arc caractérisé par certaines phases de type I de la suite tonalite-trondhjémite-granodiorite dans un environnement qui s'apparente à une zone de subduction moderne. Des minéralisations de métaux rares (Li, Cs, Nb, Ta) se trouvent dans des pegmatites associées génétiquement à des granitoïdes de type S hyperalumineux plus récents (datant de 2 660 à 2 640 millions d'années) mis en place lors d'une collision continentale.

TABLE OF CONTENTS

Page

TABLES

FIGURES

MAP

DIGITAL DATA

Introduction

The Manitoba Geological Survey (MGS) initiated a multi-year bedrock geological mapping project in 2011 that focused on the Cat Creek–Euclid Lake area in the northern arm of the Bird River greenstone belt (BRGB) within the western Superior province (Percival et al., 2012). This project was conducted in collaboration with the Geological Survey of Canada (GSC) through the Targeted Geoscience Initiative Phase IV and Phase V (TGI-4 and -5) programs, and with the University of Windsor (since 2017) via P. Sotiriou's Ph.D. thesis work that was supervised by A. Polat and supported by mining companies including Mustang Minerals Corp. (now Grid Metals Corp.) and Gossan Resources Limited. The main objectives of the project are to 1) update the bedrock geology in the Cat Creek–Euclid Lake area; 2) address the geological evolution and geodynamic environments; and 3) assess the economic potential of various mineral deposits and occurrences, including magmatic-sulphide Ni-Cu-PGE-Cr mineralization within the northern arm of the BRGB.

The Cat Creek–Euclid Lake map area is located in the northern limb of the BRGB of the western Superior province, southeastern Manitoba (Figure 1). The BRGB is in fault contact with the English River basin to the north and with the Winnipeg River terrane to the south (Figure 2), and is divided into northern and southern arms separated by the Maskwa Lake batholith (Gilbert et al., 2008). This study focuses on the northern arm of the BRGB, from Cat Creek in the northwest to the southeastern end of Euclid Lake, covering an area of ~130 km^2.

This report presents the results of three consecutive field seasons (2012–2014) of bedrock mapping carried out by the MGS, together with new petrological, lithogeochemical, Sm-Nd isotopic and geochronological data acquired during the course

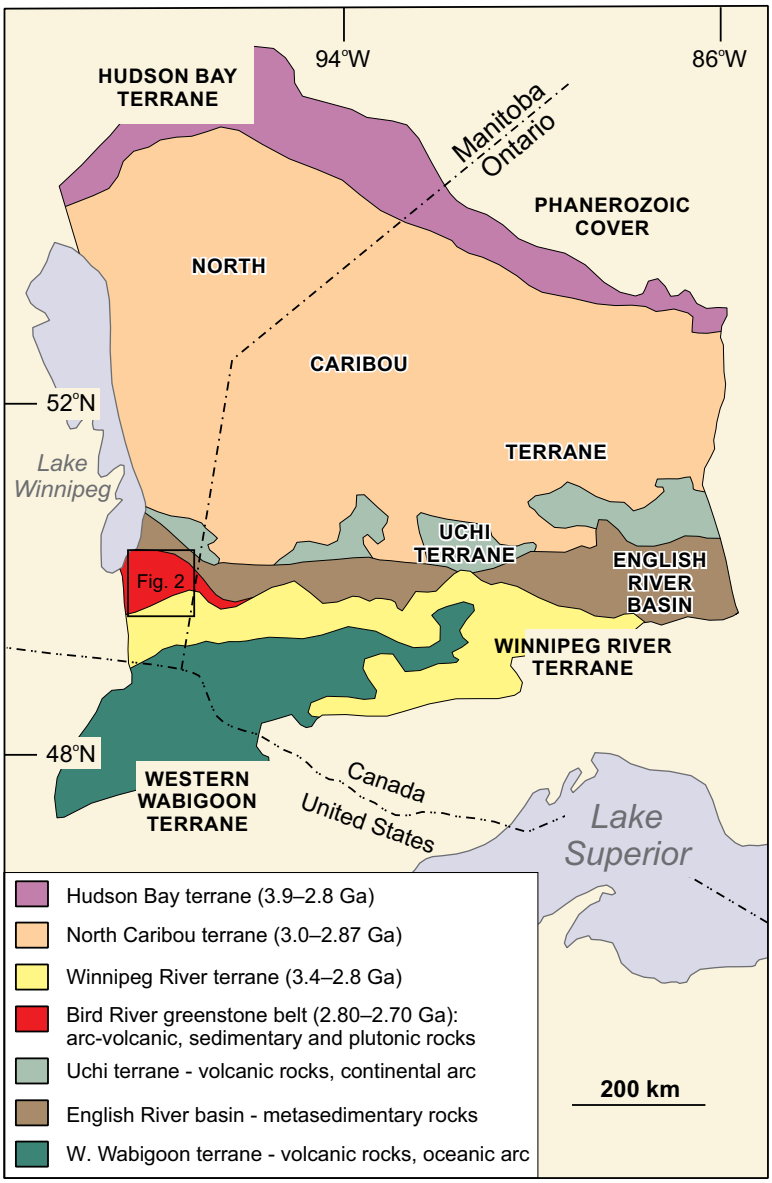

Figure 1: *Tectonic elements of the western Superior province, southeastern Manitoba and western Ontario (modified after Gilbert et al., 2008). Box shows the location of Figure 2.*

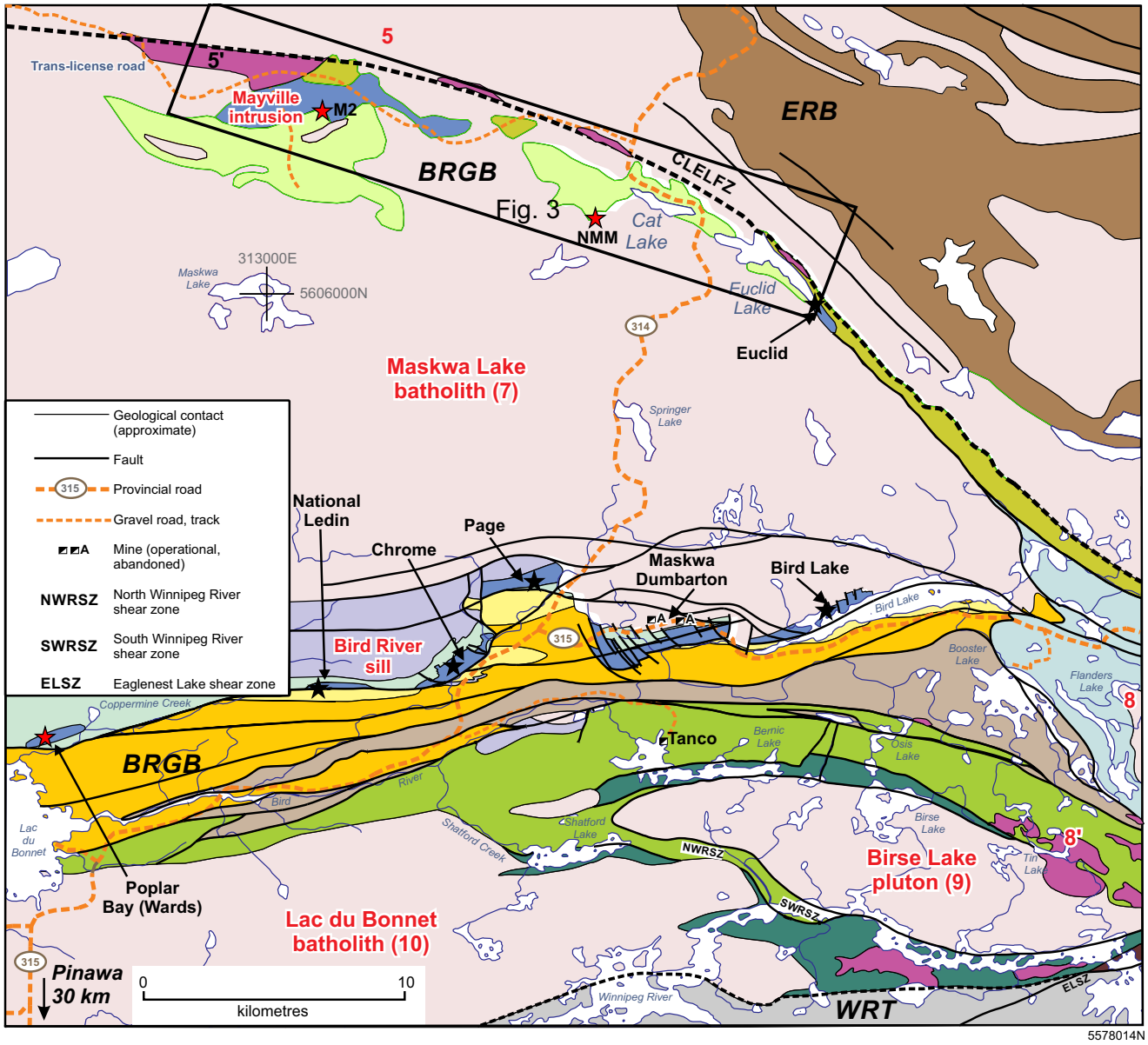

Bird River greenstone belt

INTRUSIVE ROCKS

- S-type granite
- Granite, granodiorite, tonalite
- Gabbro, diorite, quartz diorite
- Pyroxenite, anorthosite, gabbro

LATE SEDIMENTARY ROCKS

Flanders Lake formation

- Arenite, polymictic conglomerate

Booster Lake formation

- Greywacke, siltstone

VOLCANIC AND SEDIMENTARY ROCKS

BIRD RIVER BELT SOUTH PANEL

Bernic Lake formation

- Heterolithic volcanic breccia, rhyolite, basalt, andesite

Eaglenest Lake formation

- Greywacke, siltstone

Southern MORB-type formation

- Basalt, aphyric; gabbro

BIRD RIVER BELT NORTH PANEL

Diverse arc assemblage

- Massive to fragmental, mafic to felsic volcanic and sedimentary rocks

Peterson Creek formation

- Massive to fragmental felsic volcanic rocks

Northern MORB-type formation

- Basalt, aphyric; gabbro

CAT LAKE AREA

- Sedimentary and volcanic rocks, related gneiss
- Tholeiitic basalt

English River basin

- Paragneiss, granitoid intrusive rocks, migmatite, pegmatite

Winnipeg River terrane

- Tonalite, granodiorite, granitoid gneiss

- Ni-Cu-PGE deposit/occurrence
- Cr-PGE deposit/occurrence
- Domain or terrane boundary

Figure 2: *Tectonic assemblages of the Bird River greenstone belt, southeastern Manitoba (modified from Gilbert et al., 2008, 2013; Yang et al., 2013). Box shows the location of the Cat Creek–Euclid Lake area (Figure 3). Granitoid plutons keyed by numbers (Yang, 2014b; Yang et al., 2019): 5, Inconnu pluton; 5′, Cat Creek intrusion; 7, Maskwa Lake batholith; 8, Marijane Lake pluton; 8′, Tin-Osis lakes intrusion; 9, Birse Lake pluton. Abbreviations: BRGB, Bird River greenstone belt; CLELFZ, Cat Lake–Euclid Lake fault zone, indicated by the bold dashed line; ERB, English River basin; M2, Mayville deposit; NMM, New Manitoba mine; WRT, Winnipeg River terrane.*

of mapping and subsequently. It is accompanied by a 1:20 000 scale bedrock geology map (Map GR2020-1-1) covering the Cat Creek–Euclid Lake area, together with a set of tables (Data Repository Item DRI2020024) that present the detailed data used in preparing the report.

Previous work

The BRGB has long been the subject of mineral exploration and geological investigations, primarily because it contains magmatic Ni-Cu-PGE-Cr minerals, a world-class Cs–Ta–Nb–Li–rare-earth element (REE) deposit at the Tanco mine, and numerous other mineral deposits and/or occurrences, such as Au and Cu-Zn (Davies et al., 1962; Trueman and Macek, 1971; Trueman, 1980; Scoates, 1983; Macek, 1985a, b; Watson, 1985; Theyer, 1986, 1991, 2003; Scoates et al., 1989; Peck et al., 1999, 2000, 2002; Hulbert and Scoates, 2000; Gilbert, 2006, 2007, 2008, 2011, 2012; Kremer and Lin, 2006; Gilbert and Kremer, 2008; Gilbert et al., 2008, 2013; Mealin, 2008; Duguet et al., 2009; Good et al., 2009; Kremer, 2010; Percival et al., 2012). Its tectonic location between two continental cratonic blocks, the North Caribou and Winnipeg River terranes (Figure 1), guides the general understanding of the BRGB. This is corroborated by systematic geological and multidisciplinary investigations (e.g., Percival et al., 2006a, 2006b, 2012; Percival, 2007; Anderson, 2008, 2013; Corkery et al., 2010; Rinne, 2017; Sotiriou et al., 2019, 2020), and by larger scale studies on geodynamic processes involving the assembly of different terranes within the Archean craton (e.g., Hoffman, 1988; Böhm et al., 2000; Burke, 2011; Percival et al., 2012).

Regional geological mapping at a scale of 1 inch to 1 mile (1:63 360) was carried out by Springer (1949, 1950) in the area between Maskwa Lake and Cat Lake, as well as in the Bird River area to the south. He suggested that the dominant structure in the region is anticlinal, with the Bird River sill (BRS; Figure 2) in the south limb dipping steeply to the south, and the north limb (including the Mayville intrusion) being partly overturned and also dipping to the south. Therefore, the configuration of the mafic–ultramafic BRS, the Mayville intrusion and analogous rocks at Euclid Lake reflect the closure of an east-plunging anticlinal fold (Springer, 1949, 1950). This interpretation was supported by Trueman and Macek (1971), Trueman (1980), Černý et al. (1981) and Macek (1985a, b). The regional bedrock geology, including the BRGB, was compiled by the MGS at a scale of 1:250 000 (Manitoba Energy and Mines, 1987), as well as by subsequent collaborative mapping projects involving the MGS, GSC and Ontario Geological Survey (Bailes et al., 2003; Lemkow et al., 2006).

Macek (1985b) published a preliminary 1:10 000 scale geological map of the western part of the Mayville intrusion and surrounding rocks, tentatively suggesting that the intrusion was part of the BRGB. Subsequently, detailed geological mapping was carried out mainly by various mineral-exploration companies (e.g., Exploratus Ltd., Falconbridge Ltd., Tantalum Mining Corporation of Canada Ltd.) on their respective properties. Most recently, Mustang Minerals Corp. completed 1:1000 scale geological mapping of the western part of the Mayville intrusion, where diamond-drilling targeted rocks hosting PGE-Cu-Ni-Cr mineralization (Mustang Minerals Corp., 2011; C. Galeschuk, pers. comm., 2012, 2013, 2014).

In 2005, the MGS initiated a five-year mapping project focusing on the main, southern part of the BRGB, in collaboration with the University of Waterloo and mineral-exploration companies (Gilbert, 2008; Gilbert and Kremer, 2008; Gilbert et al., 2008; Mealin, 2008; Duguet et al., 2009; Kremer, 2010). The northern limb of the BRGB (Figure 2) has, however, received less attention. Thus, a bedrock mapping project was initiated in 2011 by the MGS, focusing on the Cat Creek–Euclid Lake area. As a result of this mapping, three preliminary maps were released at scales of 1:12 500 and 1:10 000 (Yang, 2012, 2013, 2014a).

Geochronological investigations of the GSC's TGI-4 and -5 programs have yielded a precise U-Pb zircon age of 2742.8 ±0.8 Ma for the Mayville intrusion (Houlé et al., 2013), virtually identical with the 2743.0 ±0.5 Ma age (Scoates and Scoates, 2013) of the Bird River sill, located in the southern limb of the BRGB. This result strongly suggests that these two intrusions are comagmatic and part of the same Neoarchean magmatic event—the Bird River magmatic event—within the BRGB (Houlé et al., 2013). Preliminary results from Bécu et al. (2013) indicate that the Coppermine Bay intrusion, located close to Coppermine Creek in the westernmost part of the main belt (Figure 2), is texturally and petrographically similar to the Euclid Lake intrusion, located 34 km to the northeast, at the northeastern margin of the BRGB. The Coppermine Bay and Euclid Lake intrusions are also similar texturally and compositionally to the Mayville intrusion, supporting their proposed linkage with the Bird River magmatic event. Preliminary results of the collaborative MGS-GSC investigations support the major conclusions of earlier workers that genetic links exist between the northern and main parts of the BRGB, referred to as the Bird River Intrusive Suite by Houlé et al. (2015, 2020), and that the mineral endowment (e.g., chromitite seams) of the two parts of the belt might, especially in some cases, be directly related.

Methods

The Cat Creek–Euclid Lake mapping project was initiated by the MGS in June 2011, using detailed bedrock mapping, structural analysis, petrology, mineral chemistry, lithogeochemistry, U-Pb geochronology and Sm-Nd isotopic analysis to update the bedrock geology and resolve some fundamental problems related to geodynamic evolution and various types of mineralization. Fieldwork in the map area took place in 2012, 2013 and 2014 after a geological reconnaissance in the

summer of 2011. Laboratory analyses continued until 2018. Preliminary results of fieldwork were published in the MGS *Report of Activities* (Yang et al., 2011, 2012, 2013; Yang and Gilbert, 2014a, b) and as MGS preliminary maps (Yang, 2012, 2013, 2014a). This report and the accompanying 1:20 000 scale map (Map GR2020-1-1) supersede the preliminary publications.

The western part of the map area is accessed by the Trans-license road (an abandoned logging road) off PR 314 that connects Lac du Bonnet and Pinawa to the northeast. All shoreline outcrops on Cat and Euclid lakes in the eastern part of the BRGB were accessed by boat. Numerous off-road trails were accessed by all-terrain vehicle. All inland areas were investigated by traverse, using hand-held GPS, data collector (Trimble) and orthorectified aerial photographs for navigation and plotting. Bedrock exposures are generally abundant in the study area and the quality of the exposures is generally good, although some outcrops were heavily covered by lichen and moss. In the Cat Creek area (Mayville), a number of exploration trenches provided great exposures for examining the Mayville mafic–ultramafic intrusion.

In the field, lithological and structural features of each outcrop were examined, measured, photographed and described. A suite of rock samples was collected to obtain thin sections for petrographic and mineral-chemistry analysis. A representative suite of 194 least-altered rock samples was collected and submitted to Activation Laboratories Ltd. (Ancaster, Ontario) for major- and trace-element compositional analysis by high-precision inductively coupled plasma–emission spectrometry (ICP-ES) and –mass spectrometry (ICP-MS). A subset of 20 samples was submitted to the University of Alberta Radiogenic Isotope Facility for Sm-Nd isotope analysis. In addition, three samples were submitted for U-Pb dating to the same facility: one sample for isotope dilution–thermal ionization mass spectrometry (ID-TIMS) and two samples for laser-ablation, multicollector, inductively coupled plasma–mass spectrometry (LA-MC-ICP-MS). Mineral chemical compositions were analyzed by an electron microprobe at the University of Manitoba. Detailed analytical procedures and methods are contained in DRI2020024. All of these analytical data are presented in this report and provided as a set of Microsoft® Excel® tables in DRI2020024.

General geology

The Neoarchean BRGB is situated between the English River basin and Winnipeg River terrane of the western Superior province (Figure 1; Peck et al., 2002; Gilbert et al., 2008; Percival et al., 2012). It is part of an approximately 150 km long, east-trending supracrustal belt that extends from Lac du Bonnet in the west to Separation Lake (Ontario) in the east, where it is termed the 'Separation Lake greenstone belt' (Percival et al., 2006a, b). Regional aeromagnetic data and Nd-isotope evidence suggest that the BRGB extends westward beneath the Paleozoic sedimentary cover (McGregor, 1986; Stevenson et al., 2000, 2001; Percival et al., 2006b). Investigations of the complex history of deformation, tectonism, metamorphism, magmatism and associated mineralization in the southern part of the BRGB (Percival, 2007; Gilbert et al., 2008; Duguet et al., 2009) have shown it to be in a key position for studies of crustal tectonic processes, crustal growth and the geodynamics of ancient cratons, with reference to modern concepts of plate tectonics (e.g., Hoffman, 1988; Burke, 2011; Percival et al., 2012; Sotiriou et al., 2019, 2020; Yang et al., 2019; Babuŝka and Plomerová, 2020). These studies have also indicated that the greenstone belt is a prospective area for base metals (Ni, Cu, Cr), precious metals (PGEs, Au), rare metals (Li, Cs, Ta, Nb) and REEs.

The Cat Creek–Euclid Lake area is located in the northern limb of the BRGB (Figure 2), which is underlain by a suite of typical greenstone assemblages. These greenstone assemblages formed in a continental-margin setting adjacent to the Mesoarchean Maskwa Lake batholith, which consists of a tonalite-trondhjemite-granodiorite (TTG) suite of rocks. The greenstone assemblages consist mainly of supracrustal rocks that include mafic–felsic volcanic and related intrusive rocks, and epiclastic and minor volcaniclastic rocks; and mafic–ultramafic layered intrusion(s). These were intruded by younger phases of TTG-suite rocks (i.e., Maskwa Lake batholith II), late peraluminous granitoid rocks and related pegmatites. The oldest rocks in the area, referred to as Maskwa Lake batholith I in Gilbert et al. (2008) and corresponding to unit 1 in Yang et al. (2012, 2013) and this report, consist of various granitoid intrusions, dated at 2852.8 ±1.1 Ma to 2832.3 ±0.9 Ma (Gilbert et al., 2008, 2013) and 2844 ±12 Ma (Wang, 1993), that represent the basement to the BRGB. The supracrustal rocks of the BRGB extend along the northern and southern margins of the older Maskwa Lake batholith cratonic block (Figure 2), suggesting that they may have been deposited in a continental-margin setting.

Intruded into the supracrustal rocks are various mafic–ultramafic intrusions, from west to east the Mayville, Cat Lake, New Manitoba Mine and Euclid Lake intrusions, as well as other smaller intrusions. The Mayville intrusion, the largest mafic–ultramafic layered intrusion in the northern arm of the BRGB, consists of an east-trending lopolith approximately 10.5 km in length and up to 1.5 km in width. The intrusion was emplaced in a pillowed to massive basalt flow sequence, geochemically akin to mid-ocean–ridge basalt (MORB), to the south and west and is in structural contact with granitoid rocks to the east. To the north, the Mayville intrusion is in fault contact with metasedimentary and intercalated volcaniclastic rocks, and is locally structurally juxtaposed against granitoid rocks. The setting and composition of the other, smaller mafic–ultramafic intrusions are comparable to those of the Mayville intrusion.

Interestingly, the Bird River sill (BRS; Trueman, 1980), Mayville intrusion (Peck et al., 2002; Yang et al., 2011, 2012) and Euclid Lake mafic–ultramafic intrusion (Yang et al., 2013)

were all emplaced ca. 2743 Ma: the BRS according to Scoates and Scoates (2013) and the Mayville and Euclid Lake intrusions according to Bécu et al. (2013) and Houlé et al. (2013). They all may have been formed by the 'Bird River magmatic event' (BRME; Houlé et al., 2013). These intrusions—all of which host magmatic Ni-Cu-PGE-Cr mineralization—were apparently emplaced at a relatively early stage of volcanic- to continental-arc magmatism at ca. 2.75–2.72 Ga (Percival et al., 2006a, b; Gilbert et al., 2008, 2013).

Relatively younger granitoid rocks (Maskwa Lake batholith II, unit 10 in this report; 2725 ±6 Ma; Wang, 1993) belong to a TTG suite that was emplaced in both the granitoid basement and the supracrustal rocks of the BRGB. The TTG suite was, in turn, intruded by late, gneissic, peraluminous granitoid rocks, strongly foliated to massive granitoid rocks, and related pegmatites.

Local geology: map unit descriptions

Fourteen map units were defined during the course of bedrock mapping in the Cat Creek–Euclid Lake area. These map units are summarized in Table 1. Unit 1 is represented by the older phases of the Maskwa Lake batholith I (Mesoarchean), which occur as the basement to the BRGB. Deposited atop unit 1 are tholeiitic to transitional basalts and related synvolcanic gabbroic rocks, which are assigned to unit 2 and interpreted to have formed in a continental island-arc to back-arc environment at or near a continental margin. Units 3–7 represent mappable lithological units of the Mayville and Euclid Lake mafic–ultramafic intrusions (Yang et al., 2012, 2013) that are comparable to the Bird River sill in the southern arm of the BRGB (Gilbert et al., 2008, 2013; Yang and Gilbert, 2014b). Unit 8 consists of discrete gabbroic intrusions, occurring as dikes, sills or stocks. Unit 9, known as the 'Cat Creek assemblage', consists of sedimentary and minor volcanic sedimentary rocks with local occurrences of mafic intrusive rocks as sills or dikes. Unit 10 comprises mainly a tonalite-trondhjemite-granodiorite suite (TTG) that constitutes younger phases of the Maskwa Lake batholith II (Neoarchean). Unit 11 is dominated by sedimentary rocks and minor volcaniclastic rocks and associated mafic intrusive rocks of the Euclid Lake assemblage. Unit 12 is composed of the Inconnu pluton, consisting mainly of biotite (±amphibole) granodiorite and granite. Unit 13 is composed of muscovite±garnet–bearing granites represented by the Cat Creek intrusion. Unit 14 consists largely of pegmatite and minor aplite dikes, some of which display rare-metal mineralization (e.g., Li, Cs, Nb and Ta).

The map units are described in the following sections, and displayed in Figure 3, which is simplified from the accompanying 1:20 000 scale geology map (Map GR2020-1-1). All supracrustal rocks in the BRGB were metamorphosed at greenschist to amphibolite facies; however, for brevity, the prefix 'meta' is omitted in most parts of this report.

Maskwa Lake batholith I: Mesoarchean granitoid basement (unit 1)

The Maskwa Lake batholith is a multiphase composite pluton that is well exposed in the southern parts of the Cat Creek–Euclid Lake area. Field relationships provide constraints on the relative timing of emplacement of various phases in the batholith. This composite batholith can be grouped into two parts (i.e., the older phases [I] and younger phases [II], in terms of their respective crosscutting relations with the mafic volcanic rocks of unit 2 basalt and related synvolcanic gabbroic rocks in the field). The older granitoid rocks of the Maskwa Lake batholith I were cut or intruded by synvolcanic rocks of unit 2, whereas the younger phases of Maskwa Lake batholith II cut or intruded the unit 2 mafic volcanic rocks (Yang et al., 2012, 2013; Yang, 2014a).

Unit 1 is represented by the older phases of Maskwa Lake batholith I, dated at 2852.8 ±1.1 Ma, 2832.3 ±0.9 Ma and 2782 ±11 Ma, spanning at least 70 m.y. in age on the basis of the published U-Pb zircon age determinations (Wang, 1993; Gilbert et al., 2008, 2013; Duguet et al., 2009). Unit 1 phases consist mainly of granodiorite, tonalite and quartz diorite (Figure 4a, b; Yang et al., 2012, 2013; Yang, 2014a, b), and related granitic gneiss. Coarse-grained, equigranular, locally porphyritic pink granodiorite of the Maskwa Lake batholith I is in contact with massive and pillowed MORB-type basalt (unit 2; Mayville assemblage of Bailes et al., 2003), which is comparable to the Northern MORB-type formation in the southern limb of the BRGB (Gilbert et al., 2008). The granitoid rocks of the Maskwa Lake batholith I were intruded, brecciated and fragmented (Figure 4c–e) at the contact zone by fine-grained gabbro (or diabase) that is thought to be synvolcanic and genetically related to the MORB-type basalt (Yang et al., 2012, 2013). The granitoid rocks were also intruded by occasional gabbro dikes up to 5 m wide. Some of the mafic dikes can be traced back to the pillowed basalt (Figure 4d), and some, together with granitoid xenoliths, exhibit strong deformation (Figure 4f). Based on these intrusive relationships, unit 1 granitoid rocks (>2782 Ma; Gilbert et al., 2008) are thought to be older than the MORB-type basalt and synvolcanic gabbroic rocks (unit 2), and are thus interpreted to form the continental basement to the BRGB (Gilbert et al., 2008; Yang, 2014b).

The basement granitoid rocks of unit 1 are subsolvus because of the coexistence of two feldspars (i.e., plagioclase and K-feldspar; Černý et al., 1981; Yang, 2014b). These rocks contain 20–25% quartz, 30–40% plagioclase, 15–25% K-feldspar, a ferromagnesian mineral assemblage of hornblende±biotite, and accessory minerals comprising magnetite, ilmenite, titanite, zircon and apatite. They display moderate to high magnetic-susceptibility (MS) values of $0.585–2.580 \times 10^{-3}$ SI (Yang, 2014b), typical of magnetite-series granitoids (Ishihara, 1977, 1981, 2004) and consistent with I-type granites (Chappell and White, 1974, 1992, 2001). However, primary hornblende is rarely present and mostly altered

Table 1: Lithostratigraphic units and intrusive suites in the Cat Creek–Euclid Lake area, Neoarchean Bird River greenstone belt, southeastern Manitoba (after Yang, 2012, 2013, 2014a; Gilbert et al., 2013; this study).

Map unit	Rock type	Affiliation
		Neoarchean
14	Pegmatitic granite, pegmatite and minor aplite	Granitoid intrusive rocks
	Intrusive contact	
13	Car Creek intrusion: late granodiorite, granite; fine to coarse grained, locally porphyritic (biotite±muscovite±garnet)	Granitoid intrusive rocks
12	Inconnu pluton I: granodiorite, granite and minor diorite to quartz diorite, and gneissic granitoids	Inconnu pluton
12b	Inconnu pluton II: fine- to coarse-grained gneissic granodiorite and granite; strongly foliated (biotite, ±amphibole, ±muscovite, ±garnet)	
	Inferred faulted contact	
12a	Inconnu pluton I: medium- to very coarse grained granodiorite and granite; locally porphyritic, pinkish granodiorite and granite (amphibole, ±biotite, ±muscovite), and minor diorite to quartz diorite	
	Intrusive contact	
11	Euclid Lake assemblage (2657.1 ±7.4 Ma)[4]: lithic greywacke, siltstone, arkose and minor iron formation, and fine- to medium-grained, dark grey volcaniclastic sandstone, and intercalated mafic rocks	Sedimentary, and volcaniclastic and related intrusive rocks
	Inferred faulted contact	
10	TTG suite, including Maskwa Lake batholith II (2725 ±6 Ma[1]): tonalite, trondhjemite, granodiorite, minor quartz diorite and quartz-feldspar porphyry; medium to coarse grained, locally porphyritic (amphibole, ±biotite); minor fine- to medium-grained gabbroic dikes cutting the TTG suite	TTG suite
	Intrusive contact	
9	Cat Creek assemblage (2735.7 ±3.8 Ma)[4]: lithic greywacke, siltstone, conglomerate with felsic volcanic and granitoid clasts, and garnet-bearing gneiss; minor volcaniclastic sandstone, lapillistone; minor gabbroic dikes	Sedimentary, volcaniclastic and volcanic rocks
	Inferred faulted contact	
8	Gabbroic rocks: fine- to coarse-grained gabbro occurring as dikes or sills, with locally leucocratic to melanocratic varieties	Mafic to ultramafic intrusive rocks
	Intrusive contact	
7	Gabbro: medium grained, locally strongly magnetic; part of Mayville intrusion	Mayville intrusion (units 3 to 7; 2742.8 ±0.8 Ma[2]) and Euclid Lake intrusion (units 3 and 6; 2743 ±1 Ma[2])
6	Leucogabbro to gabbroic anorthosite: coarse to very coarse grained, locally megacrystic	
5	Gabbroic anorthosite to anorthosite: coarse to very coarse grained, and locally megacrystic, glomeroporphyritic	
4	Heterolithic breccia: very coarse grained to megacrystic leucogabbro, anorthosite and basalt fragments (sub-metre to decametre in size) in a mafic to ultramafic matrix; locally with massive to disseminated sulphide minerals and/or disruptive chromitite layering	
3	Melagabbroic and pyroxenitic rocks: medium to coarse grained, locally very coarse grained; fine- to medium-grained melagabbro; locally strongly foliated, magnetite-bearing chlorite schist and/or amphibolite (after pyroxenite and/or olivine pyroxenite), and minor chromitite	
	Intrusive contact	
2	MORB-type basalt: aphanitic, very fine to fine grained, pillowed to massive basalt and plagioclase-phyric basalt; minor quartzite	Mafic volcanic rocks and synvolcanic gabbroic rocks (Mayville assemblage of Bailes et al. [2003]; Northern MORB-type formation of Gilbert et al. [2008])
2a	Synvolcanic gabbro: fine to medium grained	
	Inferred uncomformity	
1	Maskwa Lake batholith I: medium- to coarse-grained, locally porphyritc granite, granodiorite, tonalite and quartz diorite (2782 ±11 Ma[1]; 2832.3 ±0.9 Ma[3], 2844 ±12 Ma[1], 2852.8 ±1.1 Ma[3]), and granitic gneiss	Mesoarchean Granitoid intrusive rocks (granitoid basement)

[1] Wang (1993)
[2] Houlé et al. (2013)
[3] Gilbert et al. (2008)
[4] This study

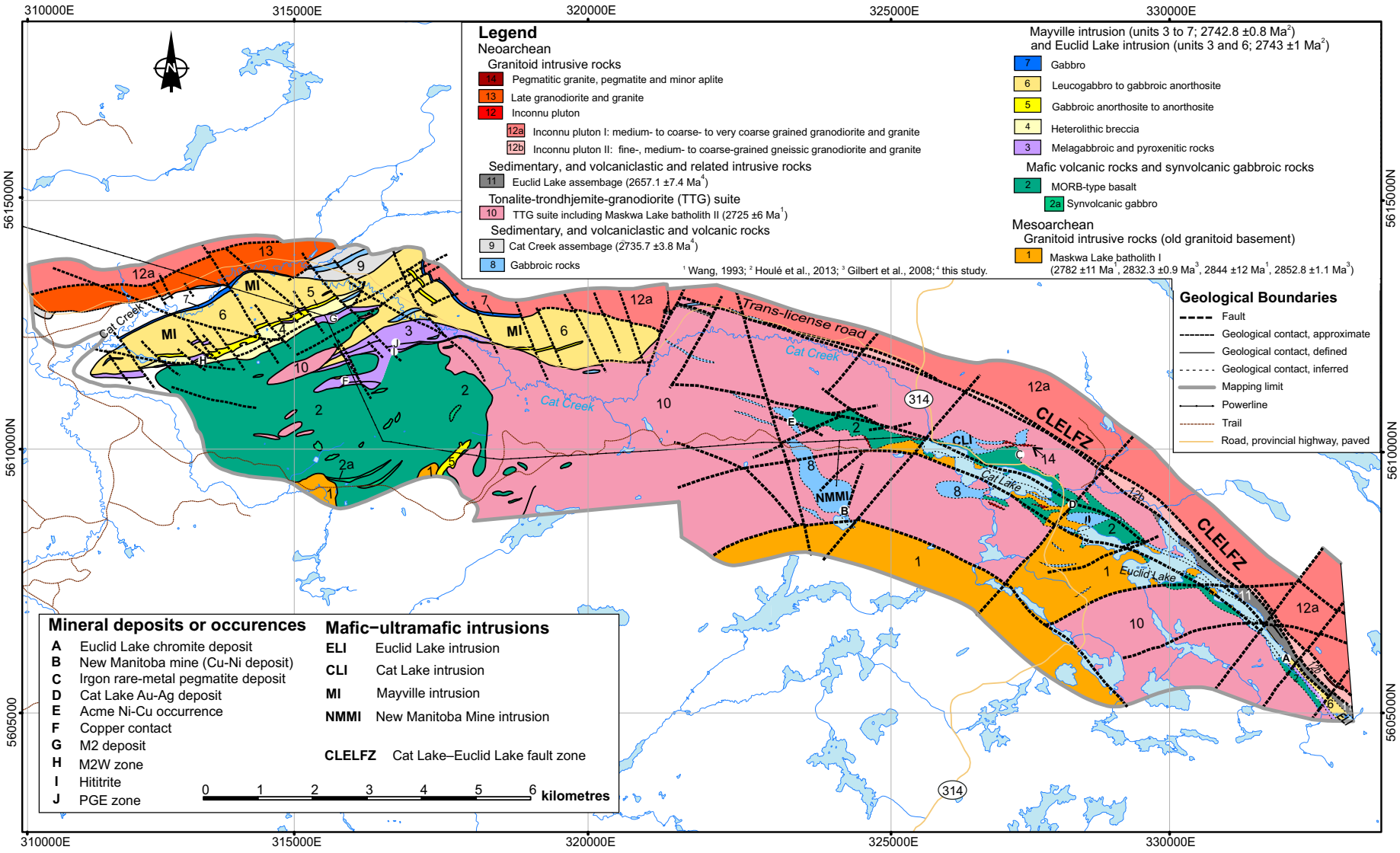

Figure 3: *Simplified geology of the Cat Creek–Euclid Lake area, Bird River greenstone belt, southeastern Manitoba (modified from Map GR2020-1-1).*

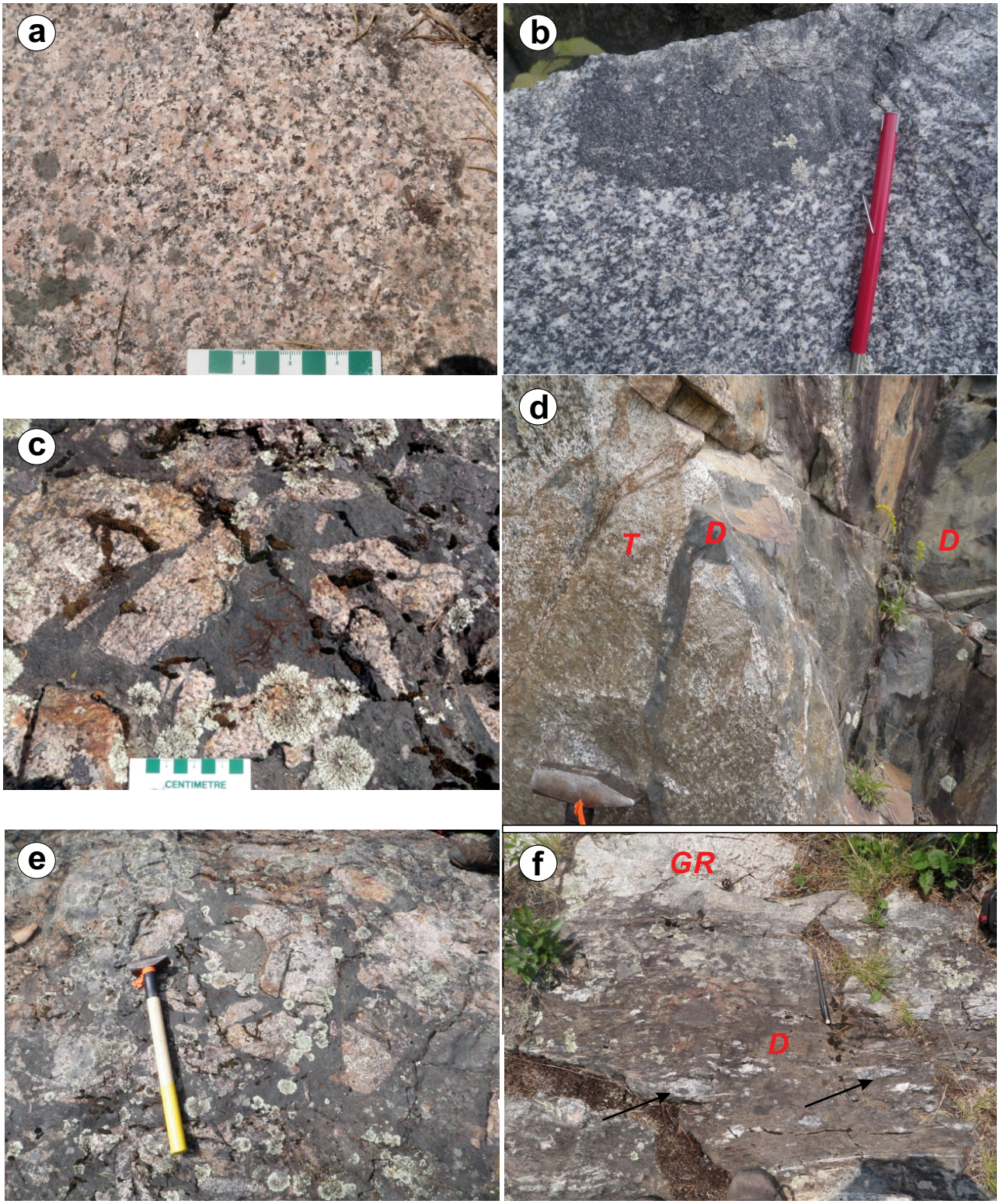

Figure 4: *Field photographs of typical granitoid rocks of the Maskwa Lake batholith I (map unit 1), showing lithological characteristics and/or field relationships, Cat Creek–Euclid Lake area:* ***a)*** *medium- to coarse-grained, massive pink granodiorite with subhedral K-feldspar phenocrysts, Maskwa Lake batholith I (UTM 315347E, 5608476N; all co-ordinates are in UTM Zone 15N, NAD83);* ***b)*** *medium- to coarse-grained tonalite with subrounded and elongated mafic xenoliths (UTM 328799E, 5606450N);* ***c)*** *coarse-grained granodiorite (unit 1) of the Maskwa Lake batholith I is fragmented, brecciated and cemented at the contact zone by unit 2 basalt and associated synvolcanic mafic rock, suggesting that this phase of the batholith I is older than the basalt (UTM 315328E, 5608468N);* ***d)*** *medium-grained tonalite (unit 1) cut by a diabase (or gabbroic) dike at the contact zone with pillowed basalt (UTM 328700E, 5606539N);* ***e)*** *angular and irregular granodiorite breccia of the Maskwa Lake batholith I (unit 1) at the contact zone with very fine grained basalt (UTM 315337E, 5608472N);* ***f)*** *strongly deformed granitoid (unit 1) xenoliths (two examples indicated by black arrows) in a mafic dike that is sheared and cuts the Maskwa Lake batholith I granitoid rocks (UTM 323969E, 5608326N). Abbreviations: D, diabase; GR, granodiorite; T, tonalite.*

to biotite and chlorite. Sericite alteration is common in plagioclase, while argillic alteration occurs in microcline and perthitic feldspars. In addition, epidotic alteration and plagioclase saussuritization (epidote-calcite-sericite) are evident in less abundant quartz diorite (McRitchie, 1971; Černý et al., 1981) in the Maskwa Lake batholith I.

The younger granitoid phases of the Maskwa Lake batholith II include quartz diorite, tonalite and granodiorite to granite; these were dated at 2725 ±6 Ma (Wang, 1993) and are therefore younger than both the Bird River sill (2743.0 ±0.5 Ma; Scoates and Scoates, 2013) and the Northern MORB-type formation in which the sill is emplaced (Gilbert et al., 2008). The Maskwa Lake batholith II is unit 10 in this report (Table 1) and is described later.

MORB-type basalt and synvolcanic gabbro (unit 2 and subunit 2a)

Unit 2 mid-ocean–ridge basalt (MORB)–type basalt and associated synvolcanic gabbro (subunit 2a; Table 1) are exposed mainly to the south of the Mayville mafic–ultramafic intrusion (Yang, 2012, 2014a; Yang et al., 2012). This unit is also exposed intermittently in the northwestern and northern parts of Cat Lake, as well as between Cat and Euclid lakes and in the southeastern part of Euclid Lake (Figure 3; Bécu et al., 2013; Yang, 2013; Yang et al., 2013). The basaltic rocks of unit 2 are comparable to the Northern MORB-type formation in the southern part of the BRGB (Gilbert et al., 2008), based on lithologies, deformation style, metamorphic grade and lithogeochemical attributes (Yang et al., 2011, 2012, 2013). At the regional scale, Bailes et al. (2003) collectively called these basaltic rocks the Mayville assemblage, which is equivalent to the basal basalt sequence in the BRGB to the south (Davies et al., 1962; Trueman, 1980). The unit 2 basalt is intruded by the Mayville intrusion (Peck et al., 1999, 2000, 2002; Yang et al., 2011, 2012), which was dated at 2742.8 ±0.8 Ma (Houlé et al., 2013).

Unit 2 mafic volcanic rocks comprise massive to pillowed basalt flows locally cut by synvolcanic gabbroic dikes and sills (subunit 2a), which were metamorphosed from greenschist to lower-amphibolite facies. In low-strain areas, pillows are well preserved, varying from 15 to 50 cm (Figure 5a) and locally up to 100 cm. Pillow tops face north, consistent with the observations of Macek (1985a, 1985b). However, pillow tops are unknown in high-strain areas, where pillows are strongly stretched parallel to approximately east-trending foliation planes that dip steeply to the south. The basalt is very fine grained to aphanitic and is largely aphyric, but locally includes plagioclase-phyric, glomerocrystic and megaphyric varieties (Figure 5a, 5b). Epidote patches or veins are common in outcrops. Angular to irregularly shaped fragments of the basalt are common in contact zones with the TTG suite (unit 10) that locally occurs as dikes crosscutting the basalt (Yang et al., 2012, 2013) and the Mayville intrusion (Yang et al., 2011, 2012). A megacrystic gabbroic anorthosite to anorthosite sill, exposed west of the Donner Lake road, is comparable to part of the Mayville intrusion (Yang, 2012). This anorthositic sill displays igneous layering defined by grain-size variation, suggesting that it is likely north facing and consistent with north-facing pillowed flows in the same area (Macek, 1985a; Peck et al., 2002; Yang et al., 2012). Similar megacrystic gabbroic anorthosite sills are present in the Bernic Lake area in the southern arm of the BRGB (Gilbert et al., 2008).

At the southern contact with the Mayville intrusion, unit 2 pillow basalt is strongly foliated, although some of the stretched hyaloclastite selvages are still discernible (Figure 5c). The basalt is recrystallized and consists largely of very fine grained, elongate amphibole and plagioclase laths, typically aligned within main foliation planes, together with minor magnetite, chlorite, epidote and albite (Figure 5d). Disseminated magnetite is common; pyrrhotite (±pyrite±chalcopyrite) occurs locally in the basalt (Figure 5e), suggesting that it may have been saturated in sulphide. Chloritic alteration is commonly weak. Unit 2 basalt is geochemically and petrologically equivalent to the Northern MORB-type formation of Gilbert et al. (2008). Locally, thin-bedded, fine-grained quartzite occurs atop the basalt.

Synvolcanic gabbro (subunit 2a), present as sills or dikes up to 130 m in thickness, is fine to medium grained and consists dominantly of plagioclase and amphibole (Figure 5f). Locally, disseminated sulphide minerals (pyrrhotite±chalcopyrite±pyrite) are present in the gabbroic rocks.

Mayville intrusion (units 3–7) and Euclid Lake intrusion (units 3 and 6)

The Mayville mafic–ultramafic intrusion is a Neoarchean, layered, mafic–ultramafic intrusion (Macek, 1985a; Peck et al., 1999, 2002; Theyer, 2003; Yang et al., 2011, 2012; Houlé et al., 2013; Yang and Gilbert, 2014b; Sotiriou et al., 2020) that consists dominantly of anorthositic gabbro, gabbroic anorthosite and anorthosite, with subordinate melagabbro and pyroxenite at the base and gabbro at the top. The intrusion is an east-trending lopolith, approximately 10.5 km in length and up to 1.5 km in width, that hosts significant Cu-Ni-PGE-Cr mineral resources. It was emplaced into unit 2 basalt and associated synvolcanic gabbro; its contact with granitoid rocks to the east is interpreted as faulted or tectonic (Yang et al., 2012). To the north, the intrusion is thought to be in fault contact with a sequence of intercalated metasedimentary and volcaniclastic rocks (unit 9; Table 1) and structurally juxtaposed against granitoid rocks (Figure 6). The Mayville intrusion is similar in compositional range to many other Archean anorthosite complexes elsewhere in the Superior province (e.g., Ashwal, 1993; Sotiriou et al., 2019, 2020), and can generally be subdivided into a lower heterolithic breccia zone (HBX) and an upper anorthosite to leucogabbro zone (ALZ), as suggested by detailed trench mapping (Peck et al., 1999, 2002; Mackie, 2003; Theyer, 2003). The intrusion is cut by late quartz diorite

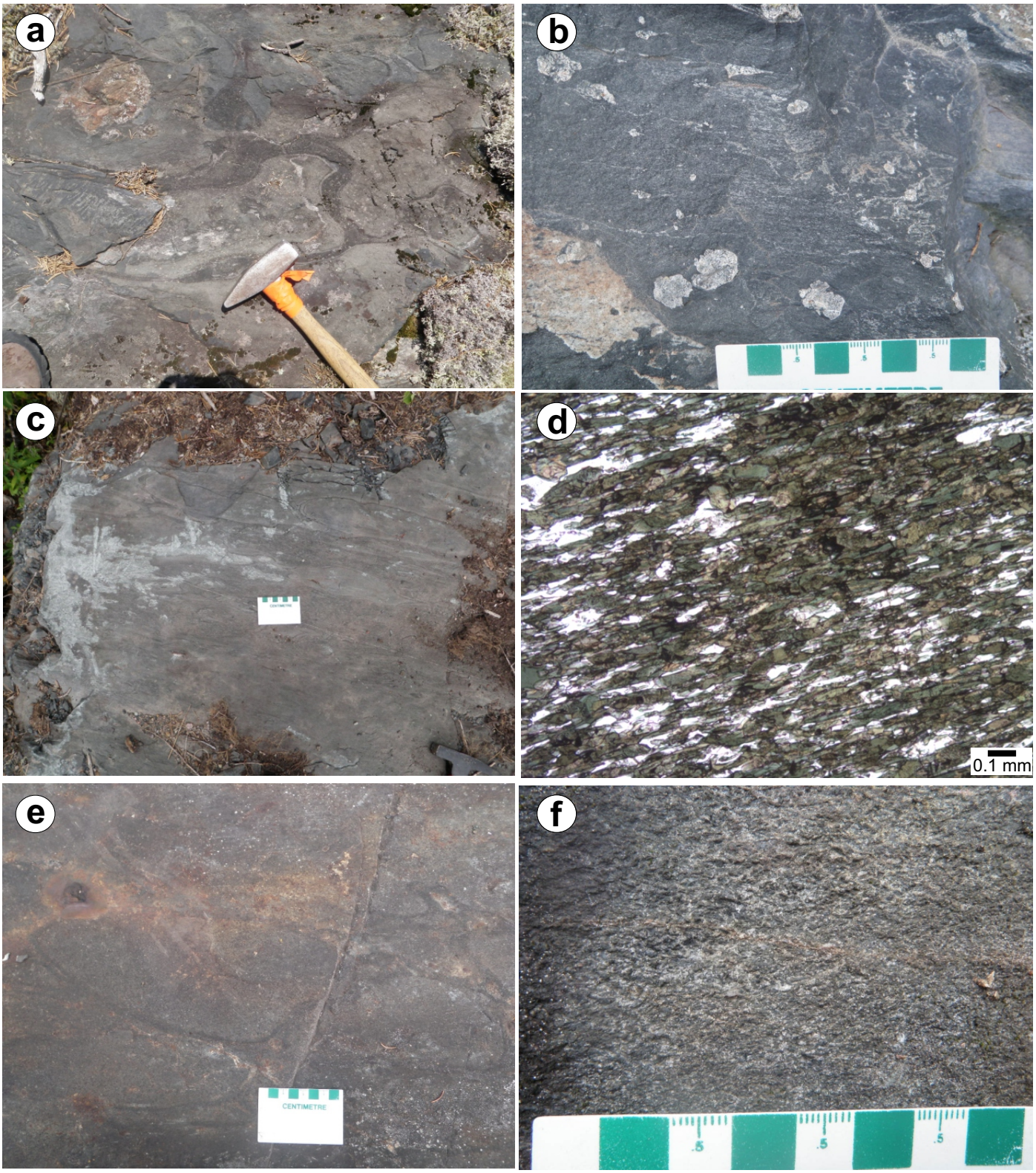

Figure 5: *Field photographs and photomicrograph of mafic volcanic rocks (unit 2) and synvolcanic gabbroic rocks (subunit 2a), showing lithological characteristics and/or field relationships and mineral assemblages, Cat Creek–Euclid Lake area:* ***a)*** *pillowed basalt flow (unit 2) with granitoid xenolith similar to the unit 1 Maskwa Lake granodiorite (UTM 315261E, 5609647N);* ***b)*** *plagioclase-phyric basalt (unit 2) cut by a late, fine-grained granitoid dike (lower left corner; UTM 314038E, 5611851N);* ***c)*** *strongly foliated pillow basalt with discernible stretched hyaloclastite selvages (unit 2; UTM 314091E, 5612056N);* ***d)*** *photomicrograph of strongly foliated pillow basalt in photo c (sample 111-11-03), showing that very fine grained, elongate amphibole and plagioclase laths are aligned along foliation together with disseminated magnetite; weak chloritic alteration; plane polarized light;* ***e)*** *foliated pillow basalt (unit 2) with iron-oxide–stained surface and disseminated pyrrhotite (UTM 313836E, 5611527N);* ***f)*** *fine-grained, massive gabbro (subunit 2a) as a dike in unit 2 MORB-type basalt (UTM 313963E, 5611679N).*

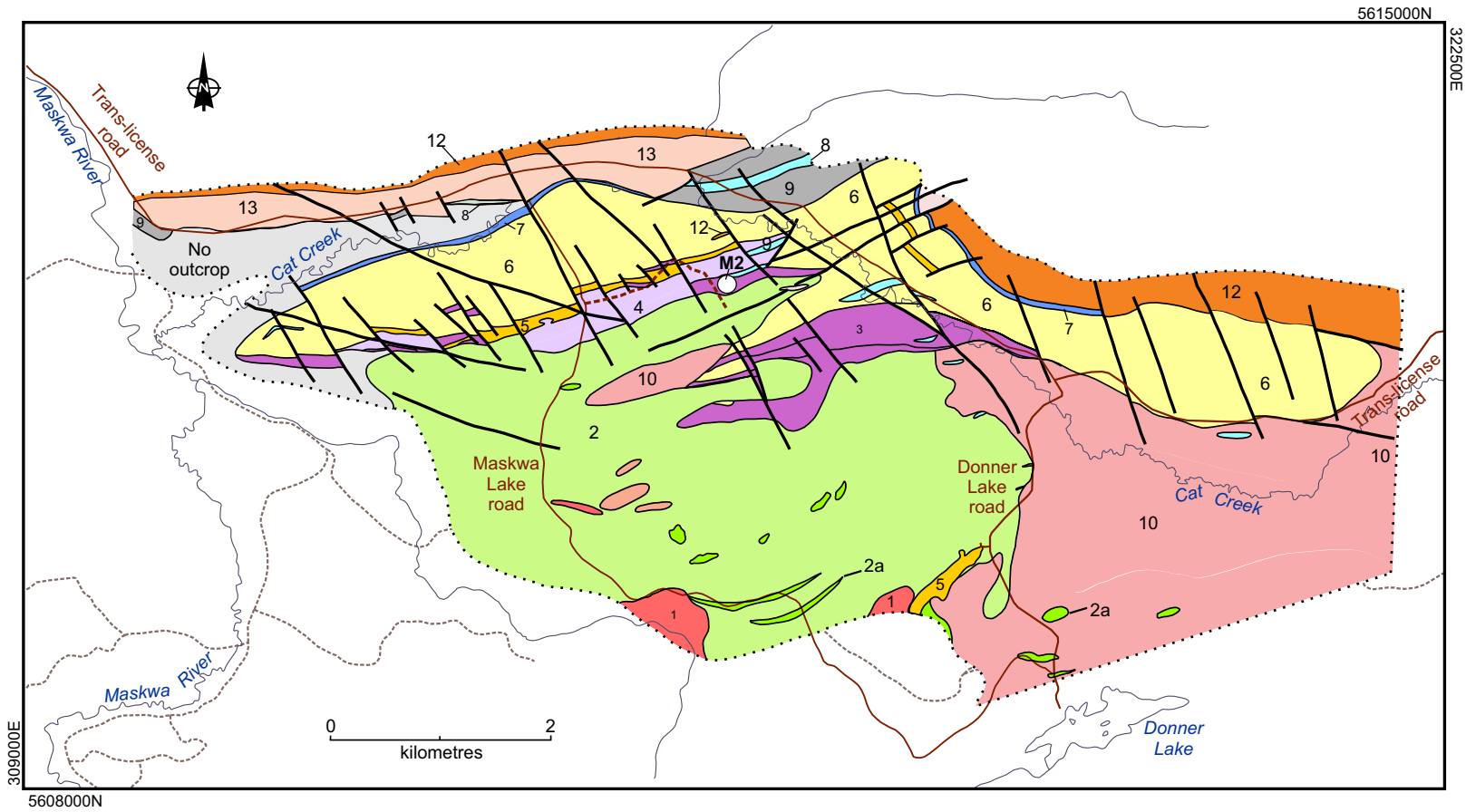

Granitoid intrusive rocks

- 14 Pegmatite
- 13 Muscovite/garnet-bearing granodiorite, granite
- 12 Granite, granodiorite, minor quartz diorite
- 10 Tonalite, trondhjemite, granodiorite

Mayville mafic–ultramafic intrusion

- 7 Gabbro
- 6 Leucogabbro
- 5 Gabbroic anorthosite to anorthosite
- 4 Heterolithic breccia
- 3 Basal mafic–ultramafic rocks

Metasedimentary, metavolcanic and related intrusive rocks

- 9 Lithic greywacke, siltstone, conglomerate
- 8 Diabase/gabbro
- 2 MORB-type basalt
- 2a Gabbro

Old granitoids

- 1 Maskwa Lake batholith granitoids

- Geological contact
- Fault
- Limit of mapping
- Gravel road
- Trail
- Mustang drill trail
- M2 deposit

Figure 6: *Simplified geology of the Neoarchean Mayville mafic–ultramafic intrusion in the northern arm of the Bird River greenstone belt (modified after Yang, 2012; Yang, 2014a). The location of the Ni-Cu-PGE deposit at Mayville is shown as 'M2'. Unit numbers are marked (for details, see Table 1).*

to tonalite dikes (Yang et al., 2011, 2013) that are attributed to a part of the TTG suite (unit 10). It is divided into five mappable units (Table 1; Figure 7), which are described in the subsections below.

Geochronological investigation of a leucogabbro xenolith from the heterolithic breccia zone (unit 4) yielded an ID-TIMS U-Pb zircon age of 2742.8 ±0.8 Ma, interpreted as the crystallization age for the Mayville intrusion (Houlé et al., 2013). This result, within error, is identical with the age of 2743.0 ±0.5 Ma for a leucogabbro sample collected from the Chrome property of the Bird River sill (Scoates and Scoates, 2013) in the southern arm of the BRGB.

The Euclid Lake mafic–ultramafic intrusion is partly exposed at the southeastern end and on the south shore of the northwestern part of Euclid Lake (Figure 3; Yang, 2013; Yang et al., 2013), where it occurs as leucogabbro to gabbroic anorthosite (unit 6) and pyroxenite and amphibolite (unit 3), respectively. Drilling data indicate that the Euclid Lake intrusion consists of a lower ultramafic zone characterized by alternating peridotite and chromitite layers, and an upper mafic zone composed of variable proportions of gabbro, leucogabbro and anorthositic gabbro (Bécu et al., 2013, 2015). Zircon grains retrieved from a leucogabbroic (unit 6; Table 1) whole-rock sample collected from the Euclid Lake intrusion yielded ID-TIMS U-Pb zircon ages of 2744–2743 Ma (Bécu et al., 2015; Houlé et al., 2015).

Although more internal stratigraphic variations are evident in the Euclid Lake intrusion (Bécu et al., 2013, 2015) than in the Mayville intrusion (Yang et al., 2012, 2013), these two intrusions, together with the Bird River sill (Trueman, 1981; Gilbert et al., 2008, 2013; Scoates and Scoates, 2013), are interpreted to have been formed by a single, large, mafic–ultramafic magmatic event—the Bird River magmatic event (Houlé et al., 2013). Houlé et al. (2015) termed these intrusions the Bird River intrusive suite, emplaced between 2744 and 2742 Ma. The tectonic setting of the ca. 2743 Ma mafic–ultramafic intrusions in the BRGB is discussed in a later section.

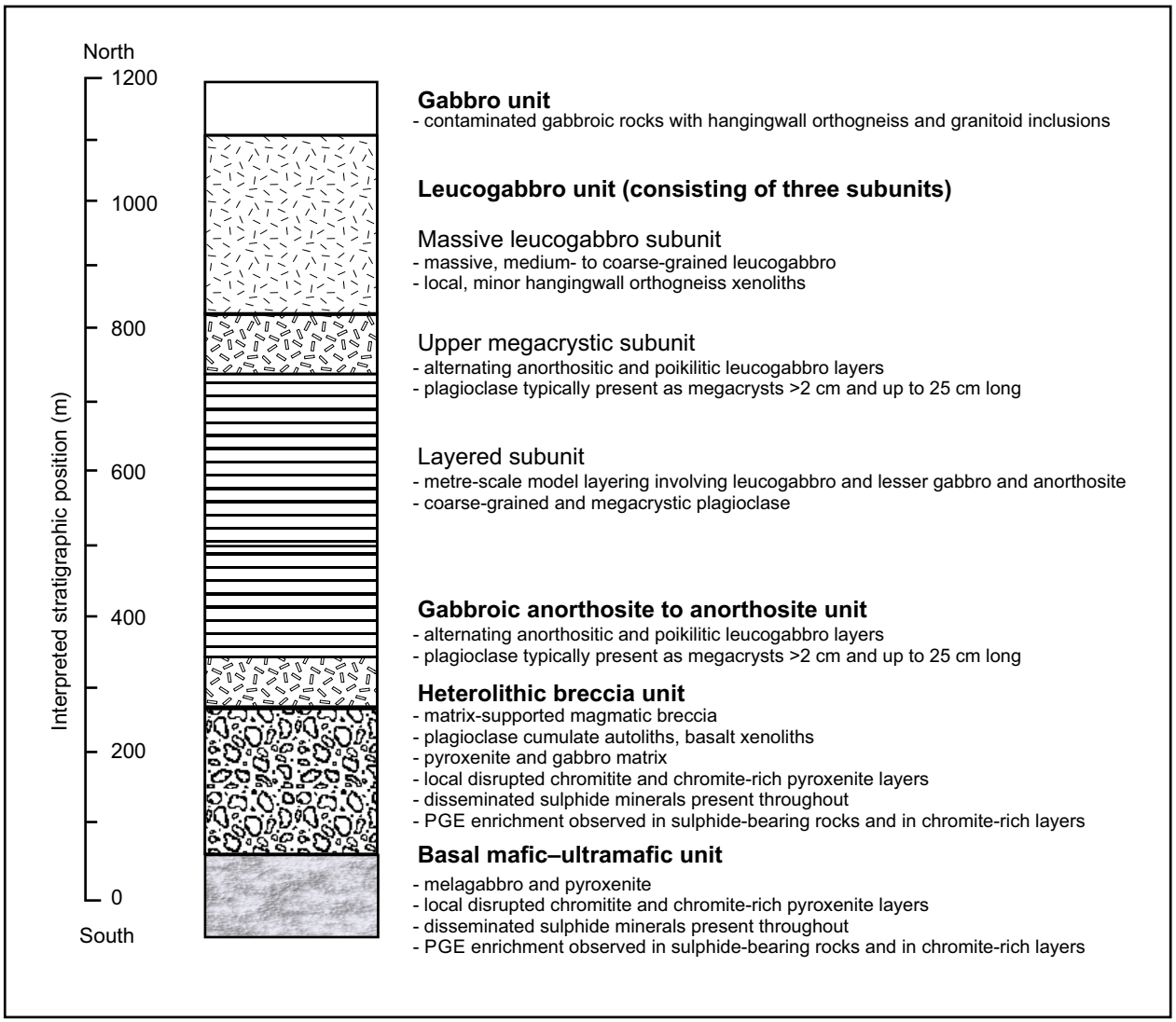

Figure 7: *Lithostratigraphic section through the Mayville mafic–ultramafic intrusion (modified after Peck et al., 2002; Yang et al., 2012), Bird River greenstone belt. Note that neither the top nor the base of the intrusion is exposed. Abbreviation: PGE, platinum-group element.*

Melagabbroic and pyroxenitic rocks: basal mafic–ultramafic rocks of the Mayville and Euclid Lake intrusions (unit 3)

This map unit occurs at the stratigraphic base of the western portion of the Mayville intrusion, but it is absent in the eastern portion where the southern contact of the intrusion is in fault contact with granodiorite to tonalite assigned as unit 10 in this report. The basal mafic–ultramafic unit consists mainly of fine- to medium-grained melagabbro, and medium- to coarse-grained, locally strongly foliated and magnetite-bearing, chlorite-amphibole schist and hornblendite (both after pyroxenite; Figure 8a). This basal unit is estimated to be at least 100 m thick, although its southern extent is largely covered by swamps and/or thick marsh. Disrupted chromitite layers or bands are locally present in the upper part of the unit (Figure 8b) and disseminated chromite is evident in some places. Diamond-drill holes intersected a chromitite zone up to 5.9 m in width (PGE zone; drillhole MAY-11-07 of Mustang Minerals Corp.), the occurrence of which is supported by chromitite banding and disseminated chromite in pyroxenite reported by Hiebert (2003) elsewhere in the Mayville intrusion.

Basal melagabbro (unit 3) is fine to medium grained and consists of 50–60% anhedral to subhedral hornblende, some displaying sutured and diffuse grain boundaries (Figure 8c); some hornblende crystals contain small anhedral to subhedral plagioclase inclusions; simple twinning is evident. This suggests that hornblende may have crystallized later than plagioclase. Plagioclase, making up 30–40% of the rock, displays varied grain shapes, ranging from anhedral to euhedral or equant, with simple and albite twinning, and locally showing sutured grain boundaries; some plagioclase crystals include tiny amphibole inclusions, typical of poikilitic texture. Pyrrhotite-chalcopyrite±pyrite aggregates are disseminated interstitially between hornblende and plagioclase crystals; some pyrrhotite blebs are included in hornblende and plagioclase crystals, indicative of sulphide saturation in the silicate magma. Secondary magnetite is common, and chromite is commonly included in hornblende crystals. Petrographic observation indicates that clinopyroxene was metamorphosed to hornblende, hornblende was partially altered to chlorite and magnetite, and plagioclase was altered to a mixture of epidote, calcite and sericite (±quartz).

Magnetite stringers and thin layers are locally common and exhibit strong magnetic response (Figure 8d). Nonmagnetic chlorite-amphibole schist (after pyroxenite), however, is also evident in unit 3 (Figure 8e), where coarse-grained pyroxenite contains hornblende with chromite inclusions (Figure 8f). Chlorite and carbonate alteration is common.

Disseminated, semimassive to locally massive sulphide minerals, mainly pyrrhotite, chalcopyrite and pentlandite, are commonly present in this unit, particularly at the bottom of the M2 deposit (Figure 8g), the M2W zone, the Copper Contact zone and the Hititrite occurrence (Figure 8h; Yang et al., 2011, 2012; C. Galeschuk, pers. comm., 2012, 2013; Yang, 2014a; for location of mineral deposit or occurrence, see Figure 3 and Map GR2020-1-1).

Unit 3 pyroxenite and amphibolite underlie a small islet (measuring <10 m by 2 m) close to the south shore of the northwestern part of Euclid Lake. They form a lower part of the Euclid intrusion and are comparable to the basal ultramafic rocks (unit 3) of the Mayville intrusion. These rocks are medium to coarse grained, brown-grey to dark green-grey weathering and variously foliated (Figure 9a). Pyroxene is altered to a secondary amphibole-chlorite assemblage; the rock contains disseminated pyrrhotite and is strongly magnetic. Very coarse grained to megacrystic amphibolite occurs within a strongly foliated and folded mafic–ultramafic rock unit at the lakeshore, southeast of the pyroxenite occurrence. The amphibolite is weakly magnetic and consists entirely of clusters of radial tremolite-actinolite prisms up to 5 cm long (Figure 9b), attributed to retrograde metamorphism. A west-northwest-trending, elongated positive magnetic anomaly at this locality (C. Galeschuk, pers. comm., 2013) is coincident with the exposures of pyroxenite and amphibolite.

Olivine-bearing pyroxenite and serpentinized peridotite, reported in diamond-drill logs from the southeastern part of Euclid Lake (Bannatyne and Trueman, 1982), are interpreted as part of unit 3. The drill logs show that the ultramafic rocks contain several chromitite horizons and are overlain by a thick gabbro–leucogabbro sequence (unit 5; Bécu et al., 2013, 2015) that underlies an island at the southeastern end of Euclid Lake. Springer (1950) located an ultramafic rock exposure and observed that “disseminated and dense chromite may be seen in the few feet of peridotite exposed”. However, no peridotite outcrop was encountered during this mapping project.

Heterolithic breccia (unit 4)

Unit 4 heterolithic breccia (HBX) or the ‘heterolithic breccia zone’ (Peck et al., 2002; Mackie, 2003; Yang et al., 2011, 2012) is an intrusive breccia composed of diverse rock types, including medium- to coarse-grained and megacrystic, variably textured melagabbro, gabbro and pyroxenite, as well as associated mafic pegmatite or megacrystic leucogabbro (Figure 10a) and anorthosite (Figure 10b). These lithological phases occur as irregular pods, diffuse patches, veins and layers ranging up to 100 m in thickness. Rusty basalt xenoliths from the country rocks (unit 2; Figure 10c) occur in the lower part of the HBX, whereas irregular leucogabbro to anorthosite fragments (Figure 10d, e) cemented by melagabbroic matrix are widespread higher up in this unit, where the rock consists almost entirely of magmatic phases derived from the Mayville intrusion. Locally, amphibolite (after pyroxenite) dikes cutting the HBX zone are evident (Figure 10f) and contain abundant disseminated chromite grains. The most southerly (inferred basal) HBX appears to have been emplaced later than the upper leucogabbro and

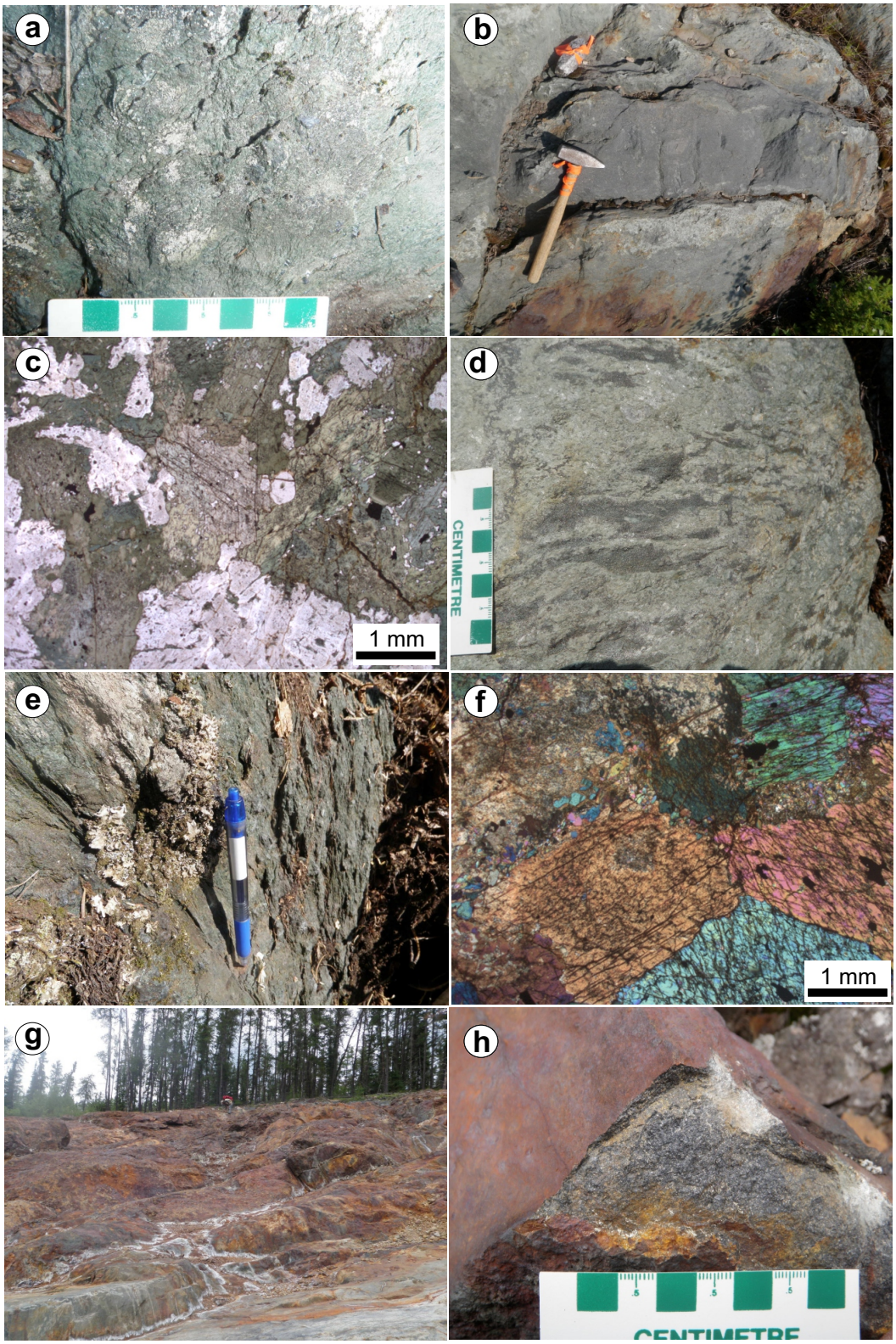

Figure 8: *Field photographs and photomicrographs of unit 3 basal mafic–ultramafic rocks in the Mayville intrusion, showing lithological characteristics and/or field relationships, Cat Creek–Euclid Lake area:* ***a)*** *foliated and strongly magnetic chlorite-magnetite-amphibole schist (after pyroxenite; unit 3; UTM 313763E, 5612308N);* ***b)*** *disrupted, ~40 cm wide chromitite band in pyroxenite (UTM 314616E, 5612596N);* ***c)*** *photomicrograph of melagabbro, sample 111-11-02 (UTM 316601E, 5611951N; PPL);* ***d)*** *magnetite stringers in pyroxenite (UTM 314610E, 5612593N);* ***e)*** *sulphide-bearing and nonmagnetic chlorite-amphibole schist (after pyroxenite; UTM 313108E, 56123391N);* ***f)*** *photomicrograph of coarse-grained pyroxenite (UTM 314287E, 5612272N) containing hornblende, with chlorite and carbonate alteration and chromite inclusions (sample 111-11-12; XPL);* ***g)*** *mineralized heterolithic breccia zone at the M2 deposit (person at top of stripped area for scale; UTM 315410E, 5612608N);* ***h)*** *mineralized melagabbro containing disseminated to net-textured pyrrhotite±chalcopyrite±pentlandite (UTM 316601E, 5611951N). Abbreviations: PPL, plane-polarized light; XPL, cross-polarized light.*

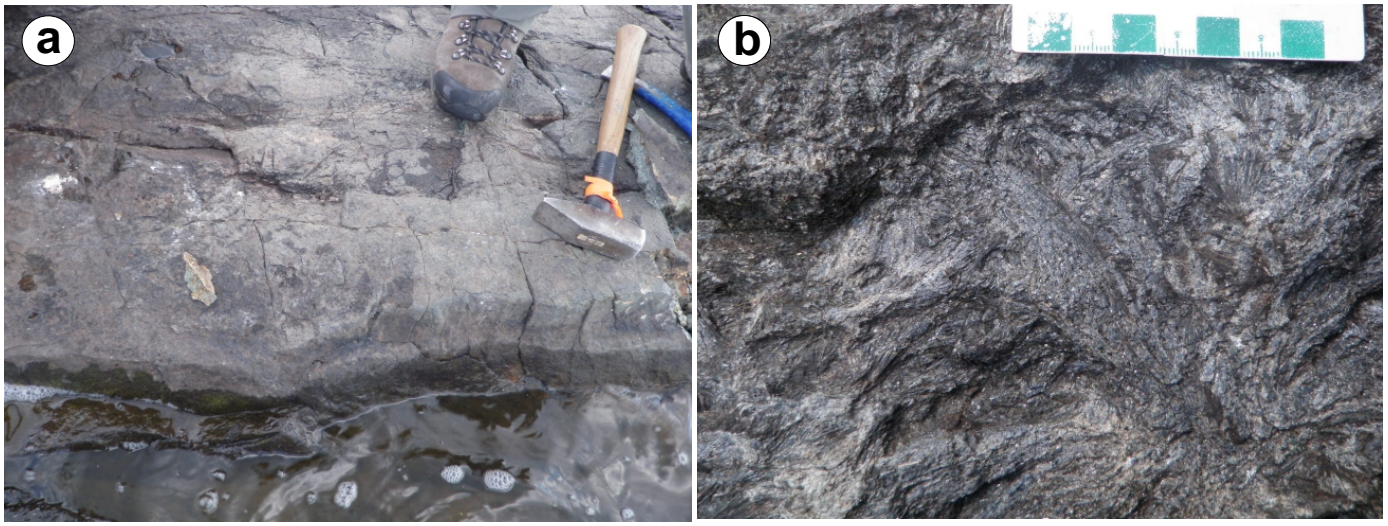

Figure 9: *Field photographs of representative mafic–ultramafic intrusive rocks (map unit 3) in the Euclid Lake intrusion, Cat Creek–Euclid Lake area:* ***a)*** *medium- to coarse-grained pyroxenite, strongly magnetic, with disseminated pyrrhotite (unit 4; UTM 329664E, 5607287N);* ***b)*** *very coarse grained amphibolite, consisting of radiating amphibole crystals up to 5 cm in length (unit 4; 329700E, 5607237N).*

anorthosite units because it contains leucogabbro and anorthosite fragments that appear to have been derived from the ALZ (units 5 and 6; Table 1).

The HBX is locally intruded by fine- to medium-grained (locally very fine grained to aphanitic) quartz diorite to tonalite dikes (Figure 10g) that are attributed to the unit 10 TTG suite, as mentioned previously. These dikes locally contain rare sulphide disseminations. Some of them are very fine grained to aphanitic (Figure 10h), consistent with textures formed by fast cooling (or quenching). Felsic minerals comprise quartz, plagioclase and minor K-feldspar, accounting for 70% of the rock, and mafic minerals are 15% biotite and 5% subhedral hornblende. Tiny acicular apatite crystals are included in quartz and plagioclase; disseminated magnetite and pyrite are also evident. The quartz diorite dikes appear less deformed to undeformed, and are interpreted to have been emplaced in a cold setting (i.e., after the Mayville intrusion had cooled).

Sulphide minerals (mainly pyrrhotite with minor chalcopyrite±pyrite) occur sporadically in the HBX as disseminations, net-textured veins and/or locally massive sulphide bands. Massive chromitite bands and disrupted chromitite-pyroxenite layers are locally present in the middle to upper parts of the HBX (Peck et al., 2002; Hiebert, 2003).

The eastern part of the Mayville intrusion (i.e., northeast of the Donner Lake road), however, lacks both the HBX and the uppermost gabbro of map unit 7 (Figure 6).

Gabbroic anorthosite to anorthosite (unit 5)

Unit 5 comprises coarse-grained and very coarse grained to megacrystic, locally glomeroporphyritic, gabbroic anorthosite to anorthosite. In the gabbroic anorthosite, calcic plagioclase occurs as equant, euhedral to subhedral crystals up to 10 cm in size, accounting for >80% of the rock, with minor interstitial amphibole oikocrysts (after pyroxenes; Figure 11a). Where amphibole (pyroxene) constitutes less than 10% of plagioclase-rich rock, it is termed anorthosite (Ashwal, 1993), which is mineralogically very similar to gabbroic anorthosite. Primary layered textures (or igneous layering) are evident in this unit, manifested by the varied grain size of equant to subhedral plagioclase, ranging from 'golf-ball' (4–5 cm) to 'tennis-ball' (8–10 cm; Figure 11b).

Some of the glomerophyric gabbroic anorthosite has a fine- to medium-grained melagabbro matrix (Figure 11c) instead of the more commonly seen interstitial amphibole (after pyroxene?), as shown in Figure 11a. The boundary between plagioclase crystals and the melagabbro matrix is sharp and is also indicated by the wrapping of fine-grained amphibole crystals (Figure 11d). This suggests that at least two epidote crystallization events were recorded: an earlier plagioclase in much coarser phenocrystic aggregates and a late plagioclase (plus pyroxene) in the matrix assemblage, similar to the scenarios of porphyritic rocks (e.g., Winter, 2010). Alternatively, this study proposes that the 'golf-ball' to 'tennis-ball' plagioclase aggregates are internal xenoliths that were derived from an earlier anorthosite body and experienced a highly dynamic system: they were broken up and trundled, partially melted, sorted in a mafic chamber, and then the crystal and melt mush was emplaced as sills and/or dikes along faults cutting the unit 2 MORB-type basalt.

Generally, unit 5 gabbroic anorthosite to anorthosite displays coarse-grained to megacrystic mosaic or cumulus texture, where finer amphibole inclusions randomly occur in larger equant plagioclase crystals (Figure 11e). However, plagioclase laths occur mostly as a finer variety of this unit, where they are euhedral to subhedral. It is common that some plagioclase grains show diffuse boundaries. Albite and Carlsbad twinning

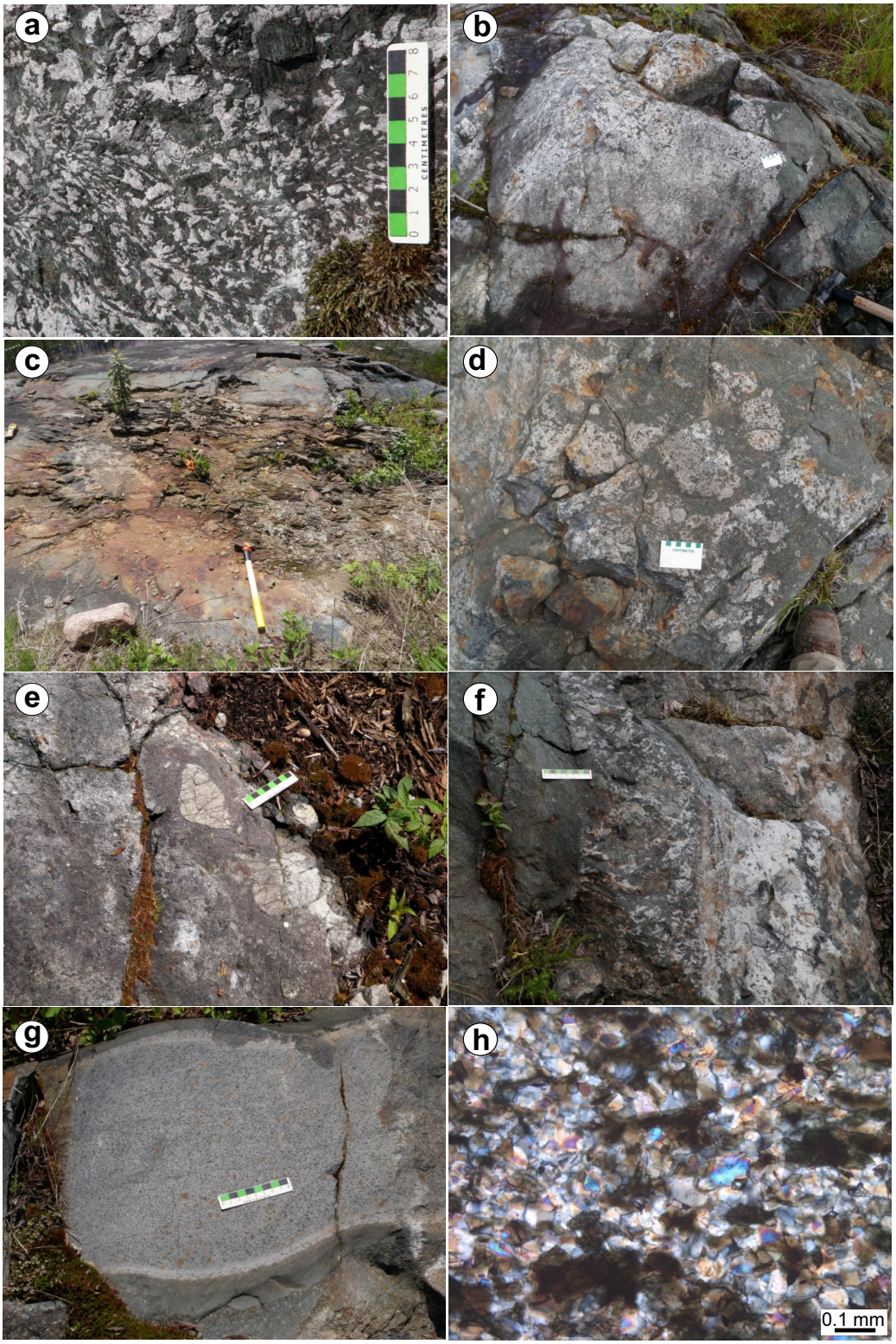

Figure 10: *Field photographs and photomicrograph of unit 4 heterolithic breccia in the Mayville intrusion, showing lithological characteristics and/or field relationships, Cat Creek–Euclid Lake area:* ***a)*** *megacrystic gabbro to leucogabbro (UTM 315037E, 5612797N);* ***b)*** *subrounded anorthosite xenolith, 2 by 3 m in size, in coarse-grained melagabbro (UTM 314297E, 5612264N);* ***c)*** *strongly sheared rusty basalt xenolith (derived from unit 2 basalt), 2 by 3 m in size, in unit 4 heterolithic breccia of the Mayville intrusion (UTM 314213E, 5612544N);* ***d)*** *leucogabbro to anorthosite fragments and/or breccia cemented by melagabbro matrix in the heterolithic breccia zone (UTM 315405E, 5612630N);* ***e)*** *heterolithic breccia zone containing leucogabbro to anorthosite fragments and disseminated sulphide mineralization (UTM 314064E, 5612456N);* ***f)*** *amphibolite (after pyroxenite, left) dike cuts very coarse grained leucogabbro (right) that is gradational to anorthosite (UTM 314666E, 5612593N);* ***g)*** *fine- to medium-grained quartz diorite dike (likely belonging to the unit 10 TTG suite) with chilled margin, cutting pyroxenite and gabbro in the heterolithic breccia zone (UTM 314465E, 5612457N);* ***h)*** *photomicrograph of very fine grained quartz diorite (UTM 316626E, 5611931N), sample 111-11-05 (XPL). Abbreviations: TTG, tonalite-trondhjemite-granodiorite; XPL, cross-polarized light.*

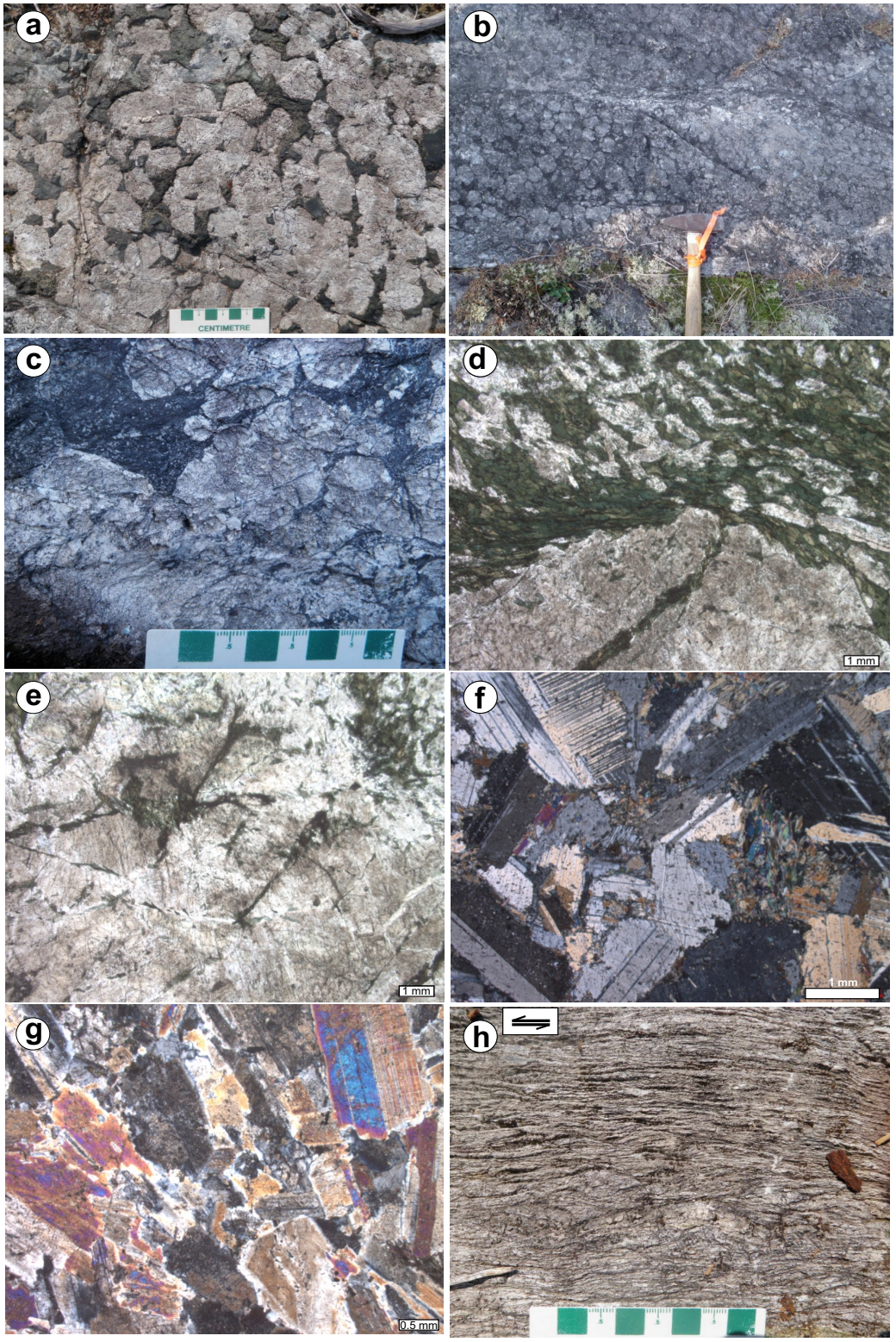

Figure 11: *Field photographs and photomicrographs of unit 5 gabbroic anorthosite to anorthosite in the Mayville intrusion, showing lithological characteristics and/or field relationships, Cat Creek–Euclid Lake area:* ***a)*** *megacrystic anorthosite (UTM 319580E, 5611714N);* ***b)*** *'golf-ball' to 'tennis-ball' gabbroic anorthosite exhibiting primary layered texture, with interstitial amphibole crystals (UTM 317573E, 5610186N; length of hammer head is 12.3 cm);* ***c)*** *glomeroporphyritic plagioclase crystals in a matrix consisting of fine- to medium-grained melagabbro (UTM 317573E, 5610186N), rather than interstitial amphibole as shown in Figure 11a;* ***d)*** *photomicrograph of 'golf-ball' anorthosite showing sharp boundary between large plagioclase crystal and fine-grained melagabbo matrix consisting of amphibole and plagioclase, sample 111-12-677A01 (UTM 317590E, 5612959N; PPL);* ***e)*** *photomicrograph of megacrystic plagioclase crystals containing randomly distributed amphibole grains, sample 111-12-677A01 (PPL);* ***f)*** *photomicrograph of coarse-grained anorthosite containing minor phlogopite; sample 111-11-16 (XPL);* ***g)*** *photomicrograph of coarse-grained anorthosite, sample 111-11-15 (XPL);* ***h)*** *sheared gabbroic anorthosite with mylonitic characteristics (unit 6; UTM 319438E, 5611789N). Abbreviations: PPL, plane-polarized light; XPL, cross-polarized light.*

and pericline lamellae are evident, and minor phlogopite is present (Figure 11f). Sericitic alteration is commonly seen together with quartz, albite and epidote grains (Figure 11g). Where alteration is apparent, tiny hornblende grains are either included in plagioclase or occur as interstitial aggregates. Hornblende is locally concentrated and anhedral to subhedral; it is locally altered to chlorite and magnetite.

Unit 5 is a relatively thin (less than 50 m wide) but persistent member of the Mayville intrusion. Where megacrystic subrounded plagioclase occurs in the rock, it is called 'golf-ball' to 'tennis-ball' leucogabbro or anorthosite (Figure 11b; C. Galeschuk, pers. comm., 2012). Much larger, rounded plagioclase aggregates, up to soccer-ball size, are evident as dikes cutting the MORB-type basalt in anorthositic rocks at Bernic Lake, in the southern arm of the BRGB (e.g., Gilbert et al., 2008).

At one locality, gabbroic anorthosite is strongly sheared and displays only a few sporadic plagioclase megacryst relicts (Figure 11h). Asymmetric plagioclase relicts, 'S-C' fabrics and shear bands indicate a sinistral movement related to the D_2 deformation event. Sulphide minerals are rarely present in this unit.

Leucogabbro to gabbroic anorthosite (unit 6)

Leucogabbro to gabbroic anorthosite (Figure 12a–d) is the most abundant rock type within the Mayville intrusion. Primary igneous layering is present in various parts of this unit, defined by variations in grain size and/or mineralogical composition. Locally, pegmatitic leucogabbro zones/patches consist of euhedral plagioclase laths and elongate poikilitic hornblende crystals. The pegmatitic patches are up to 2 m across and have gradational contacts with the surrounding leucogabbro. Near the top of this unit, embayed xenoliths of gneiss and fine-grained volcanic rocks occur within the leucogabbro.

Leucogabbro is typically coarse- to very coarse grained (Figure 12a) and locally megacrystic (Figure 12b), and contains 65–80% calcic plagioclase, 15–25% hornblende (after pyroxene) and accessory minerals comprising Fe-Ti oxide(s), zircon and apatite. Plagioclase occurs as equant, subhedral to euhedral crystals without notable optical (or compositional) zoning. At the top of this unit, plagioclase laths display decreasing grain size in a zone that is gradational with the overlying gabbro (see unit 7, below). Hornblende is typically anhedral and interstitial (Figure 12e), and locally displays simple twinning. Plagioclase included in hornblende is evident (Figure 12e, f), although most of the hornblende occurs interstitially among plagioclase. Simply twinned plagioclase crystals are included in a single, large hornblende grain that is optically homogeneous (Figure 12f), suggesting that such hornblende could be magmatic in origin (A. Polat, pers. comm., 2018; Sotiriou et al., 2020). Whether at least some hornblende is primary or, alternatively, all is of secondary (metamorphic) origin requires further investigation. Sulphide minerals (disseminated pyrite±chalcopyrite) occur locally in shear zones.

Unit 6 leucogabbro to gabbroic anorthosite (Figure 12g, h) is the dominant rock type in the limited number of exposures of the Euclid Lake intrusion in the southeastern part of Euclid Lake. The mineral composition and texture of this unit are comparable to those of leucogabbro to gabbroic anorthosite in the Mayville intrusion (Bécu et al., 2013; Yang et al., 2013). Igneous layering, defined by variations in grain size and/or mineralogical composition, was observed at several localities. Leucogabbro is typically coarse- to very coarse grained and locally megacrystic, and contains 65–80% calcic plagioclase, 15–25% hornblende (after pyroxene) and accessory Fe-Ti oxide, zircon and apatite. Plagioclase occurs as equant, subhedral to euhedral crystals that lack optical zoning. Subordinate gabbroic anorthosite contains >85% plagioclase (Ashwal, 1993).

Gabbro (unit 7)

Unit 7 gabbro (Figure 13a–c) occurs at the top of the western part of the Mayville intrusion but is apparently absent in the eastern part (east of the Donner Lake road; Figure 6). The gabbro is massive, equigranular, medium to coarse grained and locally strongly magnetic. It is moderately to strongly foliated (Figure 13a, c). The gabbro consists of 50–60% plagioclase, 30–40% hornblende, and accessory magnetite and ilmenite. Plagioclase laths (0.3–0.5 cm long) and subhedral to anhedral hornblende (0.2–0.5 cm; after pyroxene) locally display ophitic texture. Sericite, chlorite, epidote and biotite alteration are common, especially in fault zones, whereas sulphide minerals (e.g., pyrite) are rare.

Large plagioclase relicts are partially preserved and show sericitic alteration in unit 7 gabbro (Figure 13d). These large plagioclase relicts are surrounded by numerous finer plagioclase and hornblende grains that are relatively unaltered. Some large plagioclase crystals are broken into many smaller pieces, but their original equant outlines are still discernible (Figure 13e). The unaltered, finer plagioclase grains display typical triple-junction texture (Figure 13f), which is good evidence for the gabbro having been recrystallized. Consequently, anorthite number (An) of the plagioclase is reduced to ~18 ±2, within the An range of oligoclase and reflecting a disequilibrium state for the unit 7 gabbro.

Gabbroic rocks (unit 8)

Unit 8 gabbro (Figure 14a, b) is the main rock type observed in the New Manitoba Mine intrusion (NMMI) and Cat Lake intrusion, as well as other, smaller gabbroic intrusions in the map area, many of which are unnamed. Marginal phases of the NMMI and some other intrusions are characterized locally by fine-grained ophitic gabbro (Figure 14c). The gabbro is leucocratic to melanocratic and typically massive, equigranular and medium- to coarse-grained (2–5 mm crystals); locally, it

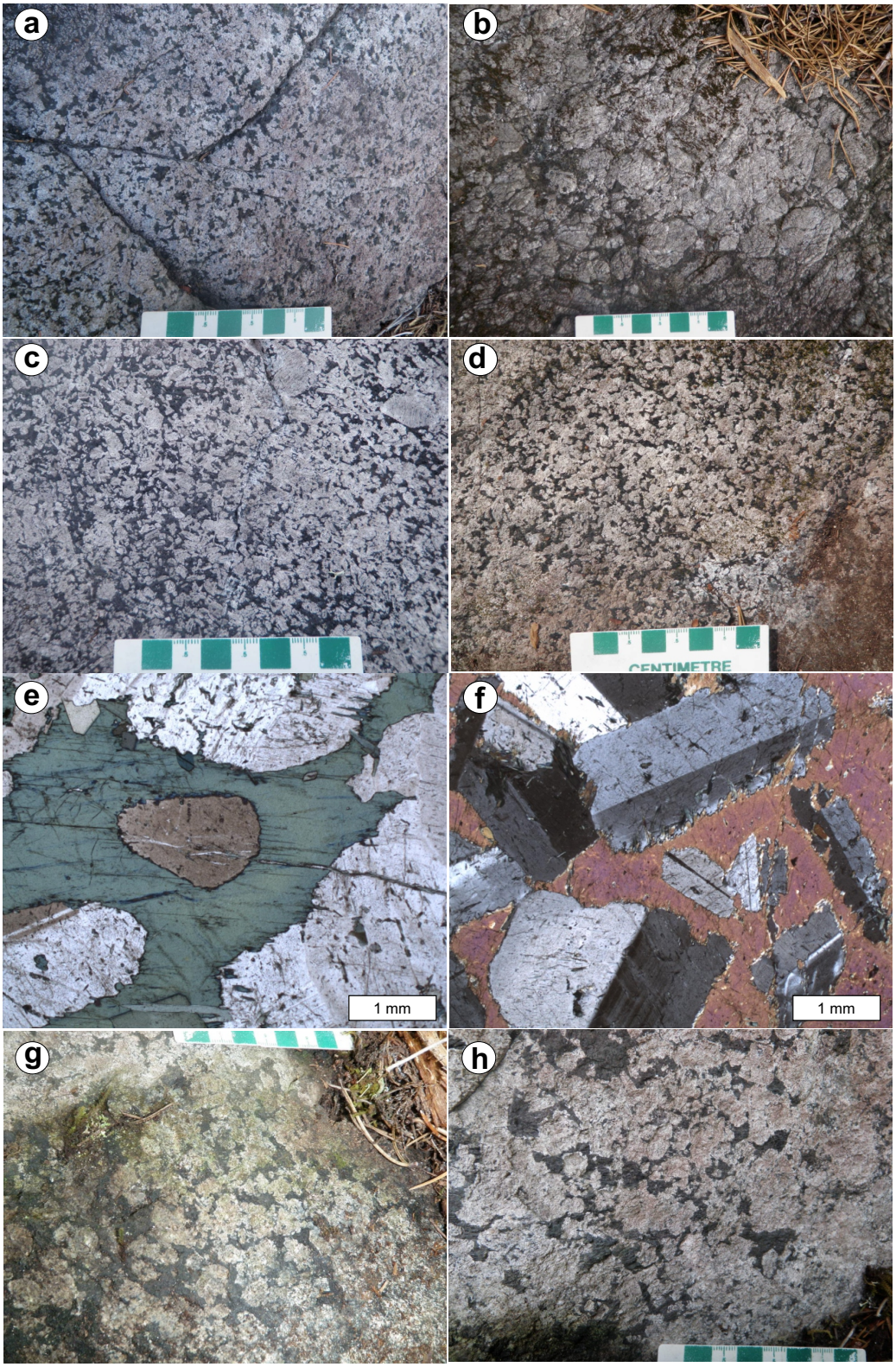

Figure 12: *Field photographs and photomicrographs of unit 6, exhibiting lithological characteristics and/or field relationships, Cat Creek–Euclid Lake area:* ***a)*** *coarse-grained leucogabbro (UTM 313722E, 5612269N);* ***b)*** *megacrystic leucogabbro to gabbroic anorthosite (UTM 313704E, 5612799N);* ***c)*** *medium- to coarse-grained leucogabbro with few larger plagioclase crystals (>2 cm; UTM 313769E, 5612930N);* ***d)*** *massive, medium- to coarse-grained leucogabbro to gabbroic anorthosite (UTM 313769E, 5612930N);* ***e)*** *photomicrograph of leucogabbro, showing interstitial hornblende that includes an equant plagioclase crystal, sample 111-12-538A01 (PPL; courtesy of A. Polat, 2018);* ***f)*** *photomicrograph of leucogabbro showing a single hornblende crystal that includes subhedral, twinned plagioclase laths, sample MV2017-1B-10 (PPL; courtesy of A. Polat, 2018);* ***g)*** *very coarse grained to megacrystic leucogabbro to anorthositic gabbro (unit 6, Euclid Lake intrusion; UTM 332361E, 5605049N), with euhedral to subhedral plagioclase crystals and interstitial amphibole;* ***h)*** *very coarse grained to megacrystic leucogabbro to gabbroic anorthosite (unit 6, Euclid Lake intrusion; UTM 332626E, 5605024N). Abbreviation: PPL, plane-polarized light.*

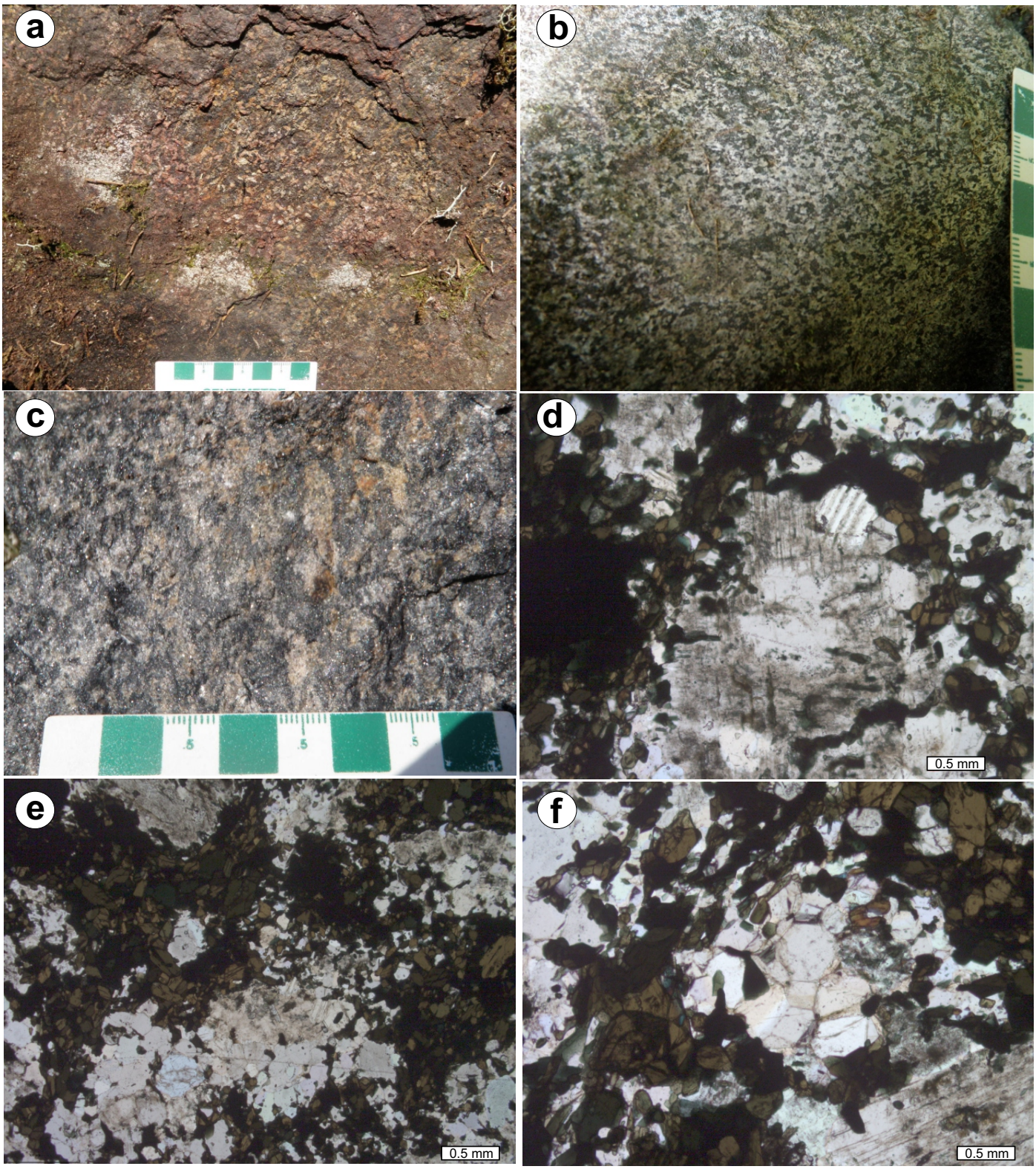

Figure 13: *Field photographs and photomicrographs of unit 7, exhibiting lithological characteristics and/or field relationships, Mayville intrusion, Cat Creek–Euclid Lake area:* ***a)*** *moderately foliated, medium-grained, massive gabbro that is rusty and strongly magnetic (UTM 313544E, 5613280N);* ***b)*** *medium-grained, massive gabbro with notable magnetism (UTM 313138E, 5612992N);* ***c)*** *foliated, strongly altered, medium-grained gabbro that is strongly magnetic (UTM 313610E, 5613265N);* ***d)*** *photomicrograph of gabbro with large relict plagioclase grain (notable sericitic alteration) surrounded by recrystallized, finer grained plagioclase (relatively unaltered) and hornblende, sample 111-12-621A01 (UTM 313610E, 5613265N; PPL);* ***e)*** *photomicrograph of recrystallized gabbro consisting of fine-grained plagioclase and hornblende, sample 111-12-621A01 (PPL);* ***f)*** *photomicrograph of recrystallized texture in gabbro as shown by triple junction of plagioclase crystals, sample 111-12-621A01 (UTM 313610E, 5613265N; PPL). Abbreviation: PPL, plane-polarized light.*

Figure 14: *Field photographs of unit 8 gabbroic rocks, Cat Creek–Euclid Lake area:* ***a)*** *medium- to coarse-grained gabbro with disseminated chalcopyrite and pyrrhotite, New Manitoba Mine intrusion (UTM 324533E, 5608618N);* ***b)*** *coarse-grained massive gabbro containing chalcopyrite and pyrrhotite disseminations and blebs (UTM 324444E, 5608654N)* ***c)*** *fine-grained gabbro displaying ophitic texture, marginal phase of the New Manitoba Mine intrusion (UTM 324035E, 5609005N);* ***d)*** *fine- to medium-grained gabbro, Cat Lake intrusion, intruded first by trondhjemite and then by pegmatite (that locally contains gabbro xenoliths; (UTM 327649E, 5609300N);* ***e)*** *medium-grained gabbro intruded by a granodiorite dike derived from the Maskwa Lake batholith II (unit 10; UTM 330094E, 5606632N);* ***f)*** *medium-grained gabbro dike emplaced into tonalite of the Maskwa Lake batholith I (unit 1), both rock types strongly foliated (UTM 330493E, 5607254N);* ***g)*** *foliated, fine- to medium-grained gabbro cut by medium-grained granodiorite (unit 10; UTM 323012E, 5612129N);* ***h)*** *numerous granodiorite veins to dikes of the unit 10 TTG suite that cut foliated, fine-grained gabbro at the contact (UTM 322766E, 5612170E). Abbreviations: Gb, gabbro; Pg, pegmatite; Tj, trondhjemite; TTG, tonalite-trondhjemite-granodiorite.*

is strongly magnetic. It consists essentially of plagioclase (50–60%), hornblende (30–40%; after pyroxene) and accessory magnetite and ilmenite. Secondary sericite, chlorite, epidote and biotite are common, especially within fault zones. Sporadic mineralized localities contain up to 15% disseminated chalcopyrite and pyrrhotite (±pyrite).

Unit 8 gabbroic intrusions are intruded by various granitoid rocks (units 10), such as north of Cat Lake where rocks of the Cat Lake intrusion are intruded by trondhjemite and younger pegmatite (Figure 14d). At Euclid Lake, gabbro is cut by granodiorite dikes from the Maskwa Lake batholith II (unit 10; Figure 14e). Unit 8 gabbro dikes are commonly seen to be intrusive into older granitoid rocks of unit 1 (Figure 14f).

In the Cat Creek area, unit 8 comprises fine- to medium-grained gabbro that occurs as dikes and sills in the middle part of the Mayville intrusion. The gabbroic rocks are dark green on fresh surface and characterized by plagioclase phenocrysts in a fine-grained matrix of amphibole (after pyroxene) and plagioclase. Chlorite and biotite alteration are common, whereas disseminated pyrrhotite is rare. In most cases, unit 8 rocks are nonmagnetic and appear to be undeformed, unlike the unit 7 gabbro atop the Mayville intrusion. Leucogabbro and anorthosite xenoliths occur locally in the unit 8 gabbroic intrusions, some of which display chilled margins that suggest they are likely younger than the ca. 2743 Ma Mayville intrusion. The unit 8 gabbroic intrusions occur within older leucogabbro (unit 6), as well as intercalated with metasedimentary rocks (unit 9) north of the Mayville intrusion. The gabbro is locally very similar to basalt (unit 2) in appearance but is distinguished by its intrusive relationship. At contact zones (e.g., north of Cat Creek), however, unit 8 gabbroic rocks display moderate to strong foliation and are cut by granodiorite (Figure 14g, h) of the TTG suite (unit 10; Table 1).

Cat Creek assemblage (2735.7 ±3.8 Ma): sedimentary, volcaniclastic and volcanic rocks (unit 9)

Unit 9 consists of sedimentary rocks (and derived gneisses), intercalated thin volcaniclastic beds and relatively minor mafic volcanic rocks that outcrop close to the northern margin of the Mayville intrusion, north of Cat Creek (Yang, 2012) in the northwestern part of the map area. The diverse rock association of unit 9 is termed the 'Cat Creek assemblage', whose direct contact with the Mayville intrusion, however, was not observed due to lack of exposure. The contact is inferred as faulted or tectonic (Table 1).

The main rock types in unit 9 are well-layered (1–10 cm) greywacke and siltstone (Figure 15a), fine- to medium-grained sandstone and laminated gneiss containing garnet porphyroblasts (Figure 15b–d). Matrix-supported to clast-supported polymictic conglomerate with felsic volcanic and granitoid clasts occurs locally at the base of unit 9 (Figure 15e). Volcaniclastic sandstone with intermediate to felsic volcanic clasts and feldspar, which occurs as a thin bed within unit 9, contains garnet and biotite bands and/or patches (Figure 15f). A thin bed of lapilli tuff to massive tuff up to 10 m in thickness (Figure 15g) is locally evident, but its lateral distribution is unknown. Below the lapilli tuff to tuff bed, a very coarse fragmental rock subunit containing ovoid to amoeboid fragments that are rimmed and unsorted to randomly distributed is either a debris flow or a volcanic breccia to tuff breccia (Figure 15h).

Alternating biotite-amphibole-garnet and feldspar-quartz layers within a lithic fragment–rich greywacke/sandstone bed suggest metamorphic differentiation and amphibolite-facies grade of metamorphism. Late granitoid and pegmatite dikes and veins were emplaced within this unit.

Internal contact relationships between the sedimentary, gneissic and volcaniclastic rocks in unit 9, however, are unknown because of the lack of exposure in the field. New detrital U-Pb zircon age data provide a mean of 2735.7 ±3.8 Ma for the dominant detrital zircon population in a volcaniclastic sandstone sample collected from this unit close to the northern margin of the Mayville intrusion. This age suggests that it is largely or partially derived from rocks younger than the ca. 2743 Ma 'Bird River magmatic event' (Houlé et al., 2013) because most units associated with this magmatic event are mafic–ultramafic and may not contain zircon. Unit 9 may correlate with rocks of the Peterson Creek formation in the southern part of the BRGB (Gilbert et al., 2008). Intriguingly, one exposure of unit 9 fine-grained greywacke-siltstone north of Cat Creek that is cut by pegmatite dikes (consisting mainly of K-feldspar and quartz) contains prominent amphibole and garnet porphyroblasts. In addition, the gneiss subunit is cut by late granite and pegmatite dikes, suggesting that unit 9 rocks predate the rocks of the TTG suite (unit 10).

Tonalite, trondhjemite, granodiorite (TTG) suite rocks of the Maskwa Lake batholith II (unit 10)

Granitoid rocks of the TTG suite (unit 10) are abundant south of the Cat Creek–Euclid Lake area, where they represent part of the ca. 2725 ±6 Ma Maskwa Lake batholith II (Table 1; Wang, 1993; Gilbert et al., 2008; Yang et al., 2012, 2013; Yang, 2013, 2014a; Yang and Gilbert, 2014a). This unit is also exposed south of the eastern part of the Mayville intrusion, where the granitoid rocks intrude unit 2 basalt and related gabbro (Figure 16a, b). Intrusions of the TTG suite also occur within the eastern part of the Mayville intrusion (Yang, 2012), where granitoid rocks intrude basalt of unit 2 and medium-grained gabbro of unit 8. Similar relationships were observed on the northwestern shore of Sausage Lake (see Map GR2020-1-1), where medium- to coarse-grained granodiorite (unit 10) intruded and brecciated medium-grained gabbro (unit 8; Figure 16c).

In addition to tonalite, trondhjemite and granodiorite, subordinate phases of the TTG suite include quartz diorite

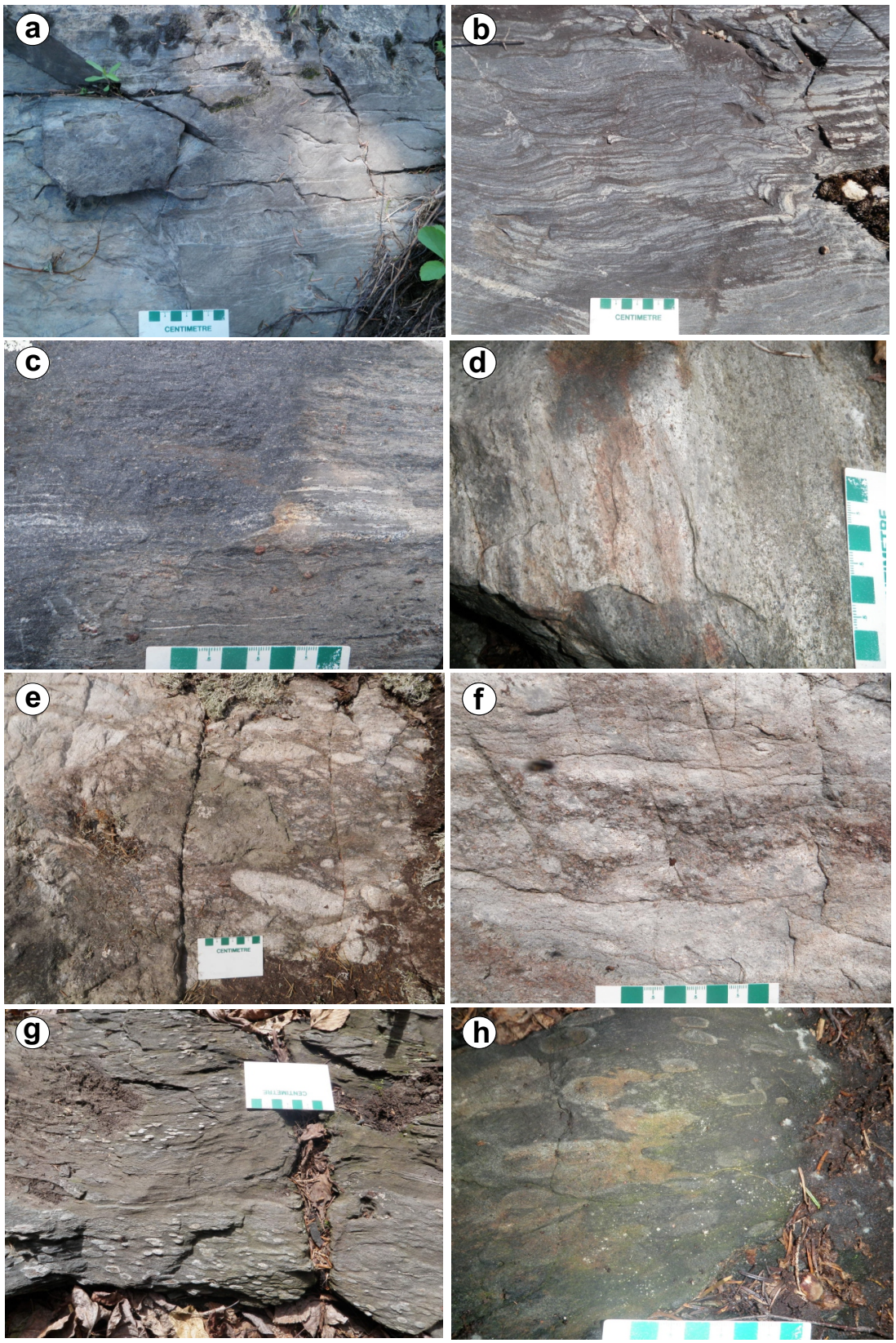

Figure 15: *Field photographs of unit 9 sedimentary, volcaniclastic and volcanic rocks, exhibiting lithological characteristics and/or field relationships, Cat Creek–Euclid Lake area:* ***a)*** *well-bedded greywacke (UTM 315176E, 5613405N);* ***b)*** *folded gneiss, containing felsic veins that are both parallel and discordant to the main foliation (UTM 312461E, 5613304N);* ***c)*** *laminated garnet-porphyroblastic greywacke (UTM 315401E, 5613350N);* ***d)*** *well-bedded siltstone and greywacke, containing disseminated pyrite (UTM 315357E, 5613415N);* ***e)*** *polymictic conglomerate with felsic volcanic and granitoid fragments (UTM 315908E, 5613436N);* ***f)*** *volcaniclastic sandstone with garnet and biotite bands and/or patches (UTM 315913E, 5613513N);* ***g)*** *lapilli tuff (UTM 315915E, 5613319N);* ***h)*** *tuff breccia to volcanic breccia or debris flow (UTM 315939E, 5613300N).*

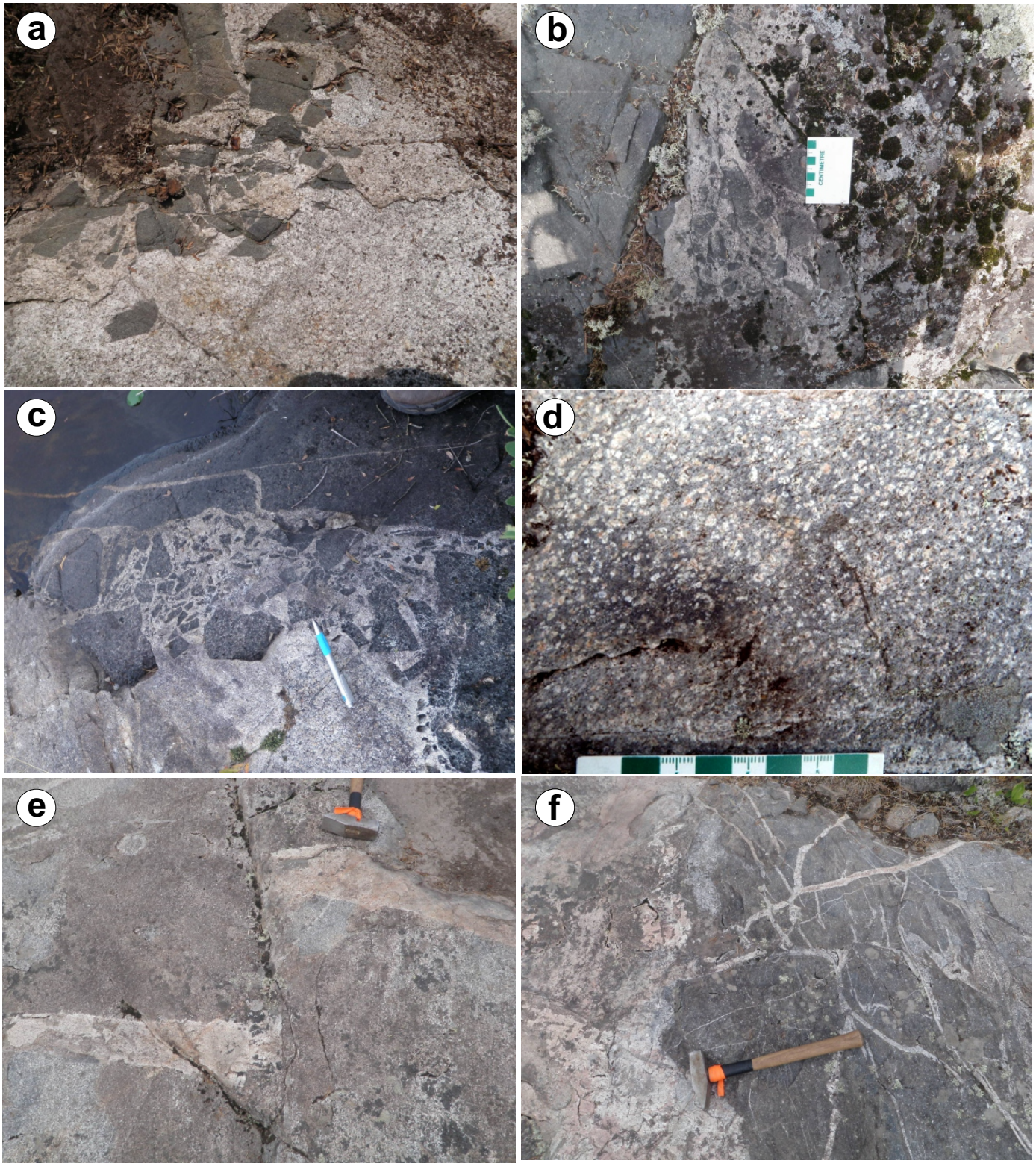

Figure 16: *Field photographs and photomicrographs of unit 10 tonalite-trondhjemite-granodiorite (TTG) suite rocks of the Maskwa Lake batholith II, showing some of the key field relationships, Cat Creek–Euclid Lake area:* ***a)*** *(view width is about 2 m) and* ***b)*** *medium-grained granodiorite intruding very fine grained basalt (unit 2) and containing basalt fragments (UTM 317746E, 5160077N);* ***c)*** *medium- to coarse-grained granodiorite, Maskwa Lake batholith II (unit 10), which intruded and brecciated medium-grained gabbro (unit 8; UTM 328104E, 5605981N);* ***d)*** *two-feldspar porphyry, Maskwa Lake batholith II (UTM 324786E, 5597364N);* ***e)*** *medium-grained tonalite cut by a granodiorite dike that is offset by a fault (sinistral sense of movement; UTM 323969E, 5608326N);* ***f)*** *large plagioclase-phyric mafic inclusion (left side of view) in tonalite cut by simple pegmatite dike and veins (UTM 323969E, 5608326N).*

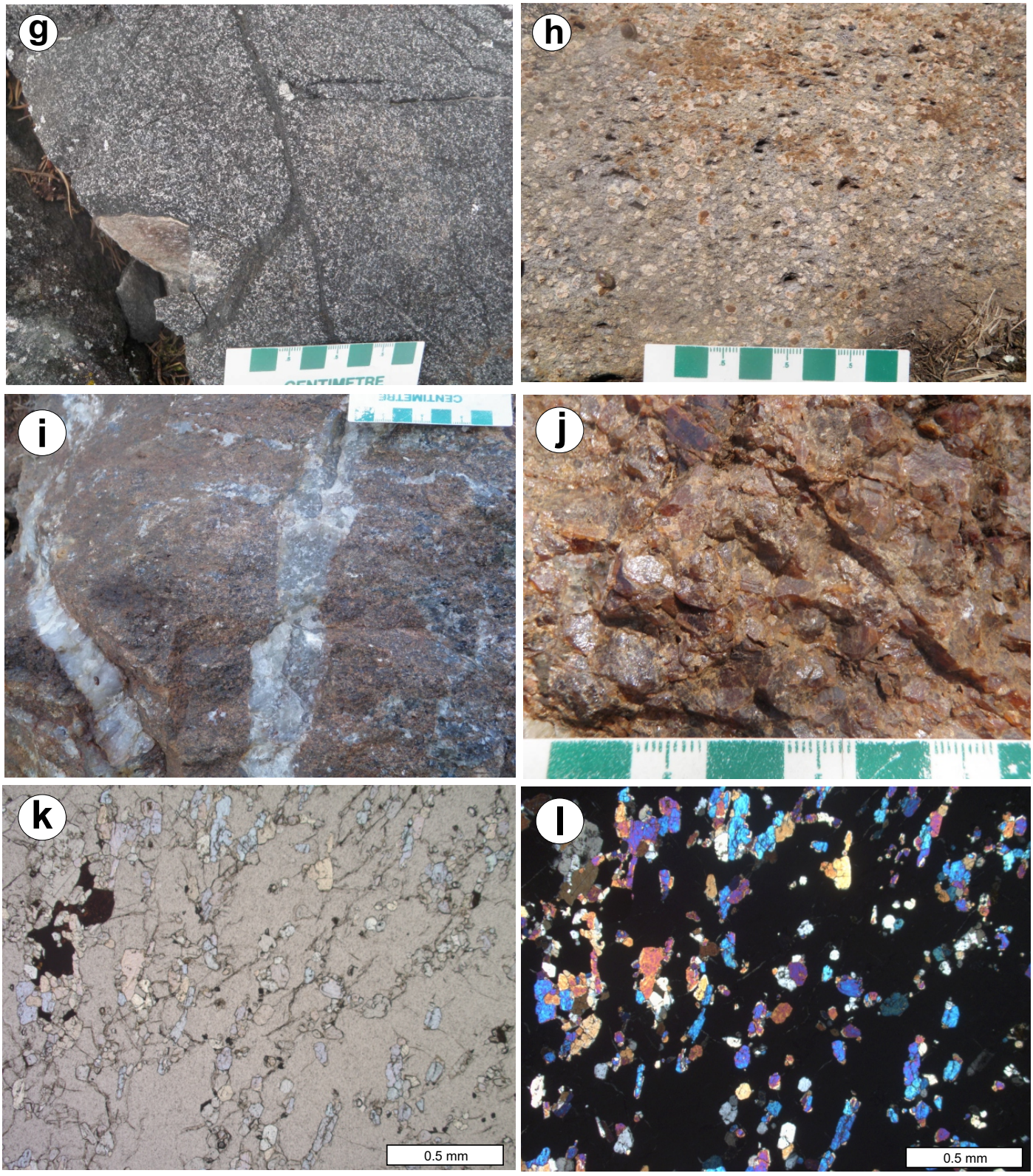

Figure 16 (continued): *Field photographs and photomicrographs of unit 10 tonalite-trondhjemite-granodiorite (TTG) suite rocks of the Maskwa Lake batholith II, showing some of the key field relationships, Cat Creek–Euclid Lake area:* ***g)*** *fine-grained gabbroic dike (up to 15 m wide) cuts unit 10 tonalite in the Maskwa Lake batholith II (UTM 327063E, 5608933E);* ***h)*** *unit 10 feldspar porphyry contains abundant plagioclase feldspar phenocrysts (UTM 326833E, 5608665N);* ***i)*** *coarse- to very coarse grained, massive scapolite-garnet skarn cut by chalcopyrite-pyrite–bearing quartz veins (UTM 328671E, 5608315N) at the Cat Lake Au-Ag mine;* ***j)*** *enlarged view of euhedral to subhedral garnet crystals in the skarn shown in Figure 16i;* ***k)*** *photomicrograph of the skarn in Figure 16i (sample 111-14-17A01;), showing clusters of diopside crystals aligned along foliation planes within large garnets (PPL);* ***l)*** *photomicrograph of the skarn in Figure 16i, showing clinopyroxene (diopside) clusters within large garnet crystals that are black due to extinction (sample 111-14-17A01; XPL). Abbreviations: PPL, plane-polarized light; XPL, cross-polarized light.*

and diorite, as well as late quartz-feldspar porphyry dikes (Figure 16d) and gabbroic dikes that postdate the other phases. Field relationships generally indicate the emplacement sequence within the TTG suite as tonalite and trondhjemite being cut by granodiorite and evolved granite, and then by associated simple pegmatite dikes and veins (i.e., comprising mainly quartz+feldspar±biotite; Figure 16e, f). Fine- to medium-grained mafic inclusions are common in rocks of the unit 10 TTG suite.

Granitoid rocks of the TTG suite are generally medium to coarse grained, weakly foliated to massive and locally porphyritic. Feldspar and quartz are the predominant minerals; K-feldspar locally accounts for more than one-third of the total feldspar content (commonly as phenocrysts), whereas mafic minerals (biotite±amphibole) are subordinate (10–20% of the rock).

Granodiorite north of Sausage Lake contains chalcopyrite-bearing quartz veins and is characterized by K-metasomatism (K-feldspar+biotite), suggesting a potential for porphyry Cu-(Au)–type mineralization. The depth of emplacement and erosion level of the granitoid intrusion could be estimated by Al-in-hornblende geobarometry (Hammarstrom and Zen, 1986; Johnson and Rutherford, 1989), but the hornblende is mostly altered, thus rendering the results calculated from this method less reliable (Yang, 2017).

Porphyritic quartz diorite and feldspar porphyry are cut by fine-grained, east-trending gabbro dikes (Figure 16g), up to 15 m wide, in the southern part of the Maskwa Lake batholith II. The porphyry is interpreted as a late-stage stock resulting from arc magmatism (Yang, 2014b). The porphyry dikes are not foliated, contain both plagioclase and Kfeldspar phenocrysts and show strong sericitic and chloritic alteration; no mafic minerals are discernible in outcrop (Figure 16d, h). Petrologically, these feldspar porphyries are similar to sanukitoids (Shirey and Hanson 1984; Yang and Gilbert, 2014a).

It is noteworthy that Cu-Au-Ag mineralization (e.g., Cat Lake Au-Ag mine; Theyer, 1994) is hosted in a skarn zone emplaced between the unit 10 granitoids and unit 2 basalt (Yang et al., 2013). The skarn is coarse to very coarse grained, composed dominantly of euhedral to subhedral garnet (Figure 16i–j) and crosscut by chalcopyrite-pyrite–bearing quartz (±carbonate) veins. Large garnet grains contain clusters of clinopyroxene (diopside) crystals that appear to align along S_2 foliation (Figure 16k–l). This skarn contains 75–80% garnet, and 15–20% diopside that is subhedral and 0.1–0.5 mm, with longer edges being subparallel foliation planes. The skarn also contains minor scapolite, ±vesuvianite, amphibole, epidote, magnetite, ilmenite, quartz, chalcopyrite, pyrrhotite, pyrite and carbonate (calcite, dolomite?). The skarn is cut by late quartz veins, consisting of fine- to medium-grained quartz with undulose extinction and containing chalcopyrite, pyrrhotite, and pyrite.

It is well known that skarn commonly occurs as a metasomatic product at the contact zone between granitoid intrusions and carbonate rocks (e.g., Siivola and Schmid, 2007). Unfortunately, no carbonate rocks were encountered nearby at the Cat Lake deposit during the course of this mapping.

Euclid Lake assemblage: sedimentary, volcaniclastic and related intrusive rocks (unit 11)

The Euclid Lake assemblage (unit 11) is composed dominantly of sedimentary rocks, intercalated thin mafic volcaniclastic sandstone beds, and mafic rocks. This unit is exposed mainly along the northeastern shore of Euclid Lake (Yang, 2013) and extending to the southeast. The unit is intruded by granitoids (unit 12) northeast of Euclid Lake and is in faulted contact with the TTG suite (unit 10) to the south (Yang, 2013; Yang et al., 2013). The main rock types are well-layered (1–10 cm) feldspathic greywacke, arkose, siltstone and oxide-facies iron formation (Figure 17a–c). The fine- to medium-grained sedimentary rocks display alternating feldspathic and mafic laminae, and are intercalated with thin beds of volcaniclastic sandstone (Figure 17a, b). Where the sedimentary rocks are folded and relatively more metamorphosed, they contain leucosome veins parallel, and locally oblique, to the main foliation (Figure 17d, e).

Gabbroic sills and/or dikes (up to 1 m thick) within the sedimentary sequence at Euclid Lake are thought to be penecontemporaneous with deposition of their hostrocks, based on consistently concordant contact relationships; these gabbroic rocks have been strongly deformed and foliated together with the sedimentary rocks (Figure 17g, h). Late pegmatitic granite dikes were emplaced within unit 11 rocks; some of these dikes were boudinaged (Figure 17f).

Northwest-trending, 1–3 m thick, oxide-facies iron formation is intercalated with fine-grained quartz-biotite schist and gneiss northwest of Euclid Lake (Theyer, 1994; Assessment File 92607, Manitoba Agriculture and Resource Development, Winnipeg). The iron formation is locally folded and disrupted, and extends discontinuously along strike for more than 350 m; it is locally mineralized with minor pyrrhotite (Theyer, 1994).

A comparison of supracrustal rock formations in the northern arm of the BRGB with those in the southern part (Gilbert et al., 2008) suggests that some of them may be correlative. Yang et al. (2012) interpreted a volcaniclastic rock (unit 9; Table 1) in the Cat Creek area of the northern arm to predate the 2742.8 ±0.8 Ma Mayville intrusion (Houlé et al., 2013). However, new detrital zircon age data provided a mean age of 2735.7 ±3.8 Ma for the dominant detrital zircon population in a volcaniclastic sandstone sample from this unit, which was collected from an outcrop close to the northern margin of the Mayville intrusion, suggesting that it probably postdates the Mayville intrusion formed by the 'Bird River magmatic event' and may correlate

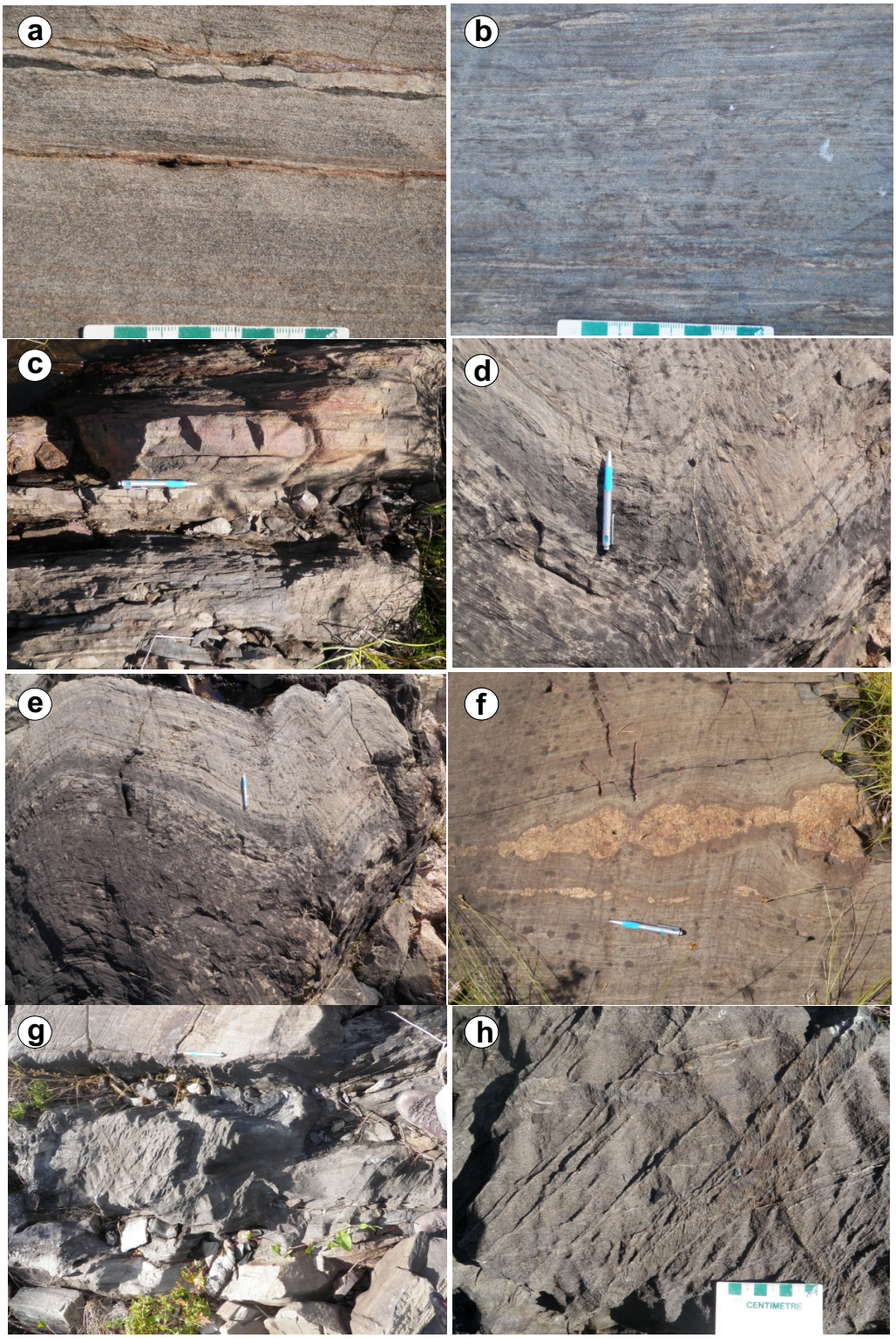

Figure 17: *Field photographs of sedimentary and volcaniclastic rocks of unit 11, showing their relationships with (inferred) syndepositional mafic rocks and younger pegmatite dikes, Cat Creek–Euclid Lake area:* ***a)*** *lithic greywacke and arkose with thin, mafic volcaniclastic sandstone and quartzite (iron formation) beds, bedding being reinforced by penetrative foliation (UTM 332040E, 5605616N);* ***b)*** *arenite and siltstone, showing feldspathic laminae and mafic layering (UTM 332040E, 5605616N);* ***c)*** *rusty banded iron formation (BIF) with strong magnetics (UTM 332040E, 5605616N);* ***d)*** *greywacke, arkose and mafic volcaniclastic sandstone, with leucosome veinlets both parallel and oblique to main foliation; this sedimentary package is cut by coarse-grained to pegmatitic granite (visible at right margin; UTM 332040E, 5605616N);* ***e)*** *M-symmetric folds in metasedimentary rocks, cut by coarse-grained to pegmatitic granite (right edge of view);* ***f)*** *greywacke intruded by boudinaged granite dike and veinlets (UTM 332040E, 5605616N);* ***g)*** *syndepositional mafic volcanic rock recrystallized to medium-grained amphibolite within unit 11 metasedimentary rocks, interpreted as intrusive, penecontemporaneous with deposition of the sedimentary host; also shows brittle deformation of early penetrative fabric (UTM 332040E, 5605616N);* ***h)*** *enlarged view of the mafic rock (medium-grained amphibolite) in Figure 17g, showing multiple generations of deformation reflected by differing orientation of fabrics.*

with rocks of the Peterson Creek formation in the main part of the BRGB (Gilbert et al., 2008; Figure 2).

In the Euclid Lake area, however, sedimentary rocks contain layers of mafic volcanic rocks and/or are intruded by thin gabbroic sills that could be related to either the 2725 Ma TTG suite or to synvolcanic gabbro within the mafic volcanic rocks; thus, a post–Euclid Lake intrusion age (i.e., post ca. 2743 Ma) cannot be ruled out for this portion of the sedimentary package at Euclid Lake.

Inconnu pluton (unit 12)

Based on field relations, mineral assemblages and textural characteristics, the Inconnu pluton (Černý et al., 1981) is subdivided into two subunits: Inconnu pluton I (subunit 12a) and Inconnu pluton II (subunit 12b). Mafic dikes cutting the Inconnu pluton are rare or absent, but metasedimentary rock xenoliths that occur in the pluton are a geological criterion to differentiate unit 12 granitoids from the unit 10 TTG suite south of the Cat Lake–Euclid Lake fault zone (Yang, 2013; Yang et al., 2013).

Inconnu pluton I (subunit 12a)

Granodiorite and granite (subunit 12a) occur in the area north of the west-northwest-trending Cat Creek–Euclid Lake fault zone, and directly north of subunit 12b gneissic granodiorite and unit 13 muscovite- and/or garnet-bearing granite (see below). Subunit 12a granitoid rocks are interpreted as early phases of the Inconnu pluton I of Černý et al. (1981), which consists mainly of coarse-grained, locally porphyritic, pinkish grey granodiorite, granite and minor monzogranite, and diorite to quartz diorite. Some of these granitoid rocks show heterogeneous texture (Figure 18a); very coarse grained to pegmatitic granite with heterogeneous texture is locally

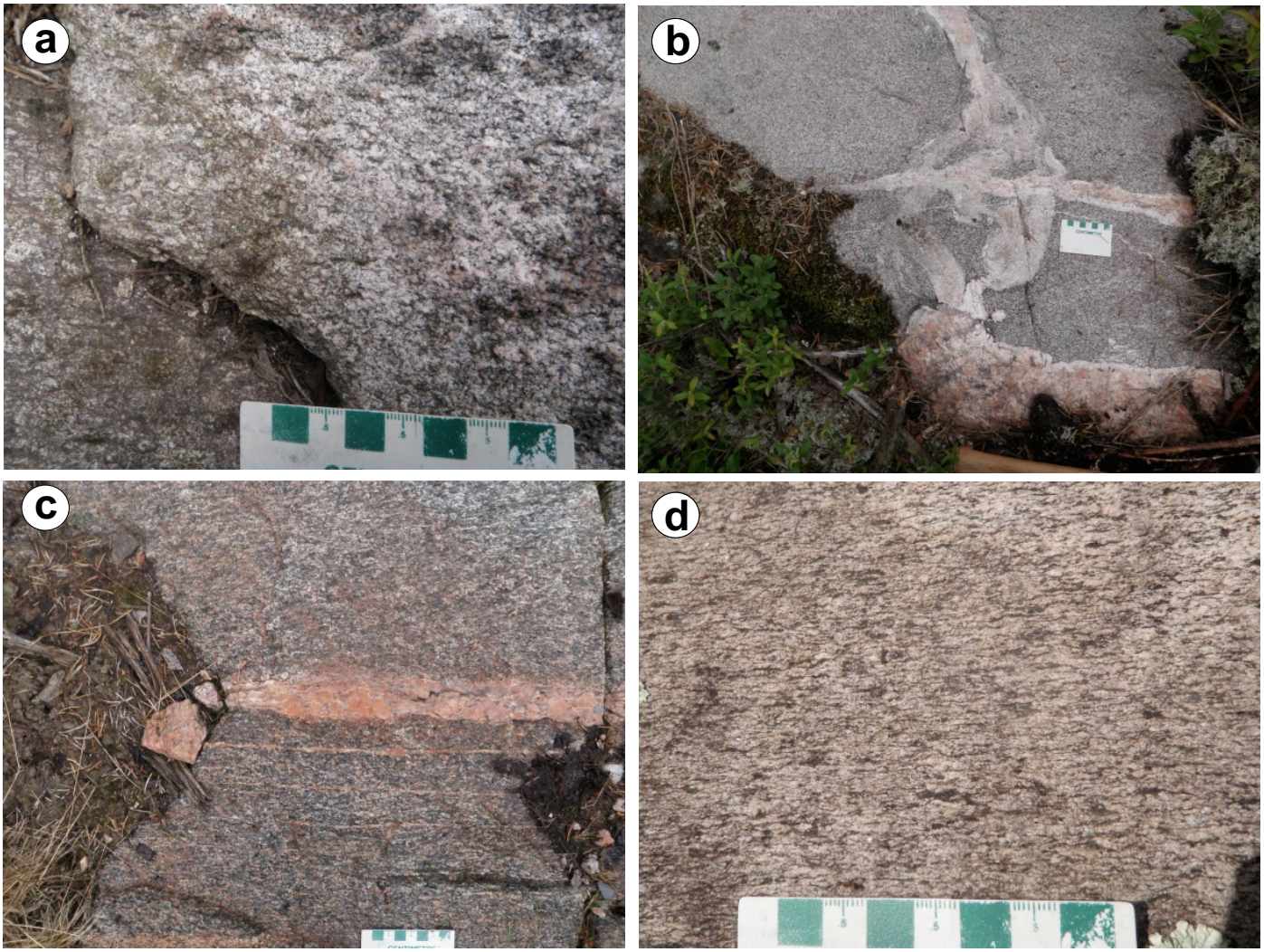

Figure 18: *Field photographs of various phases of granitoid rocks in the Inconnu pluton I (subunit 12a) and II (subunit 12b), showing some of the key features and field relationships, Cat Creek–Euclid Lake area:* ***a)*** *coarse-grained granite with heterogeneous texture (subunit 12a; UTM 333044E, 5605525N);* ***b)*** *medium-grained granodiorite cut by simple pegmatite consisting of quartz and feldspars (subunit 12a; UTM 323140E, 5612109N);* ***c)*** *gneissic granodiorite (subunit 12b) containing biotite±greenish amphibole±muscovite and associated simple pegmatite vein (UTM 332922E, 5605199N);* ***d)*** *medium-grained, strongly foliated granodiorite bearing biotite±greenish amphibole±muscovite (subunit 12b; UTM 332663E, 5605219N).*

transitional to homogeneous, massive or porphyritic varieties. The massive to weakly foliated granitoid rocks are characterized by a mineral assemblage of quartz-feldspar(s)-amphibole-biotite±muscovite. Accessory minerals are apatite, zircon, titanite, monazite ±magnetite. Late (quartz-feldspar±muscovite) pegmatite dikes are common within subunit 12a granitoid rocks. As pointed out by Černý et al. (1981), minor muscovite in some of the granite phases is the product of secondary alteration.

Inconnu pluton II (subunit 12b)

Subunit 12b granitoid rocks are confined to a narrow zone that extends from the area north of central Euclid Lake northwestward to the area north of the Trans-license road. This subunit is gradational or intrusive into granitoid rocks of subunit 12a that occur immediately north of Euclid Lake. Subunit 12b rocks were interpreted as part of the young phases of the Inconnu pluton II of Černý et al. (1981). Contacts between subunit 12b and unit 11 sedimentary rocks were not observed, but subunit 12b is assumed to be coeval with or younger than subunit 12a in terms of their spatial relation with the Cat Creek–Euclid Lake fault zone (Figure 3). Subunit 12b granitoid rocks are strongly foliated to gneissic, light grey to grey and medium grained; the mineral assemblage includes dark brown (Fe-rich) biotite±greenish amphibole±muscovite (Figure 18c, d). Micaceous, dark brown biotite stringers (1–3 mm wide) parallel to the foliation locally wrap around feldspar porphyroclasts.

Late granodiorite, granite (unit 13)

Late granodiorite and granite intrusions (e.g., Cat Creek intrusion) are closely associated with pink to grey, muscovite-garnet (±tourmaline)–bearing pegmatite bodies that cut all other map units (see below). The late granitoid rocks, which are younger than the Mayville intrusion, occur largely in the area north of, and are rare or absent south of, the Mayville intrusion. No direct contact of unit 13 granitoids with the Mayville intrusion was observed in the field, although strongly foliated, fine- to medium-grained mafic (gabbroic) xenoliths are evident in unit 13 massive granite at the northern margin of the Mayville intrusion. It is inferred that the contact is faulted.

The granitoid rocks (unit 13) are massive, fine to coarse grained and locally porphyritic; they are rarely deformed. Quartz, plagioclase and K-feldspar form approximately 90% of the granitoid rocks; muscovite, ±red garnet, ±biotite, and ilmenite are accessories (Figure 19a–c), but magnetite is rare or absent. Textural evidence of muscovite and garnet (Figure 19d–f) occurring together with an intergrowth of quartz and feldspar (Figure 19e, f) indicates that the muscovite and garnet are magmatic in origin (Kushner, 2016), which contrasts with the secondary muscovite found in subunit 12b (Černý et al., 1981). In addition, a notable physical feature of unit 13 granitoids is that they display very low magnetic-susceptibility values of $<0.1\times10^{-3}$ SI, consistent with typical S-type granites (Chappell and White, 1974, 1992, 2001) and the ilmenite-series granites defined by Ishihara (1977, 1981, 2004). The occurrence of unit 13 granites may indicate a terrane boundary zone (Yang, 2014b; Yang et al., 2019) between the English River basin to the north and the BRGB to the south.

Pegmatitic granite, pegmatite and minor aplite (unit 14)

Pegmatitic granite and pegmatite intrusions (unit 14), typically 0.5–30 m thick, are the youngest known rocks in the map area. Pegmatitic granites are composed of quartz, K-feldspar, and muscovite±tourmaline (Figure 20a, b); they occur both along and crosscutting foliations in unit 11 greywacke on the northern shore of Euclid Lake. Both simple and complex pegmatites occur in the Cat Creek–Euclid Lake area. Simple pegmatite is composed mainly of K-feldspar, plagioclase and quartz (±biotite, ±muscovite), without notable replacement textures. Complex pegmatite exhibits metasomatic texture and contains more diverse mineral assemblages (K-feldspar-quartz-albite± muscovite±garnet±tourmaline±spodumene±beryl; Figure 20c–f); graphic texture is locally evident in both simple and complex pegmatites. Where identifiable, the simple type is commonly hosted by all phases of granitoid intrusions (units 1 and 10, and subunit 12a), whereas the complex type appears to be associated only with subunit 12b and unit 13.

For a comprehensive review of pegmatites in the BRGB, the reader is referred to the very detailed descriptions in Černý et al. (1981).

Mineral chemistry

Mineral chemistry data on rocks of the Mayville intrusion (units 3–7) are presented in Tables 2–5. All analytical work was done at the University of Manitoba using a Cameca SX100 electron probe microanalyzer (EPMA). Detailed analytical conditions were briefly reported in Yang and Gilbert (2014b) and are included in DRI2020024. A brief description of the mineral chemistry of chromite, hornblende and plagioclase, as well as some other minerals, is presented in this section.

Chromite

Introduction

To demonstrate the importance of chromite for investigations of petrogenesis and mineral exploration for mafic–ultramafic rocks, it is necessary to provide a brief background on chromite studies before the results of work on the Mayville chromite are presented.

Chromite ($Fe^{2+}Cr_2O_4$) is an end member of the spinel group of minerals, whose formula is AB_2O_4 (where A is Fe^{2+}, Ni^{2+}, Mn^{2+}, Co^{2+} or Zn^{2+} in four-fold co-ordination T sites, and B is Cr^{3+}, Fe^{3+}, Al^{3+} or Ti^{4+} in six-fold co-ordination M sites; see Deer

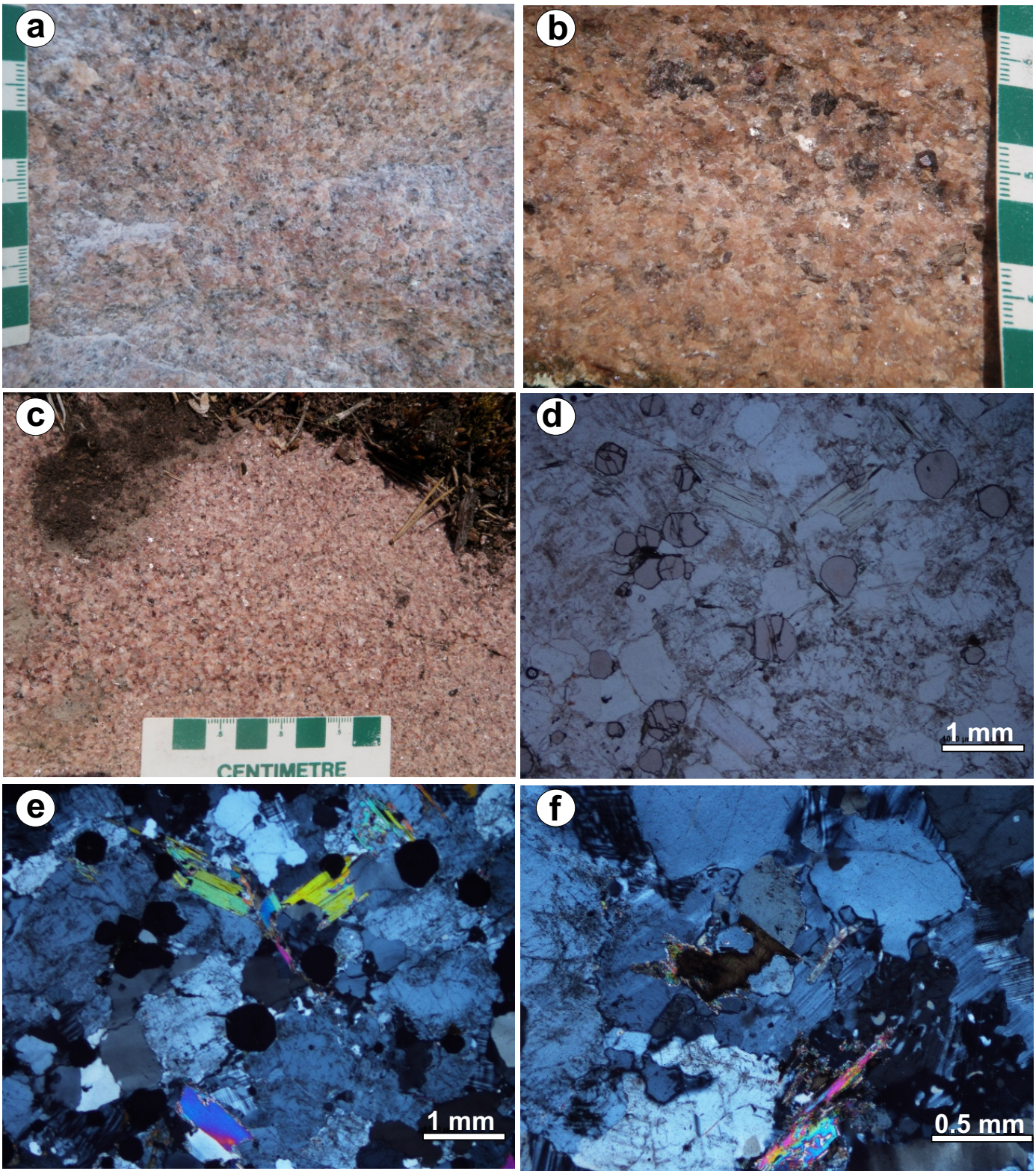

Figure 19: *Field photographs and photomicrographs of unit 13 muscovite-garnet–bearing granitoids, showing some of the key features and field relationships, Cat Creek–Euclid Lake area:* ***a)*** *massive, medium- to coarse-grained, equigranular, muscovite-garnet–bearing granite that displays a very low magnetic-susceptibility (MS) value of 0.044×10^{-3} SI (UTM 314163E, 5613775N);* ***b)*** *massive, coarse-grained, muscovite-garnet–bearing granite with a very low MS value of 0.021×10^{-3} SI (UTM 314790E, 5613829N);* ***c)*** *fine- to medium-grained garnet-muscovite–bearing granite (UTM 310217E, 5613304N);* ***d)*** *photomicrograph of muscovite-garnet–bearing granite (sample 111-15-4A01; PPL);* ***e)*** *same view as Figure 19d but under cross-polarized light (XPL);* ***f)*** *photomicrograph of muscovite-garnet–bearing granite, showing clusters of myrmekitic textures (sample 111-15-4A01; XPL). Photos d–f from Kushner (2016). Abbreviations: PPL, plane-polarized light; XPL, cross-polarized light.*

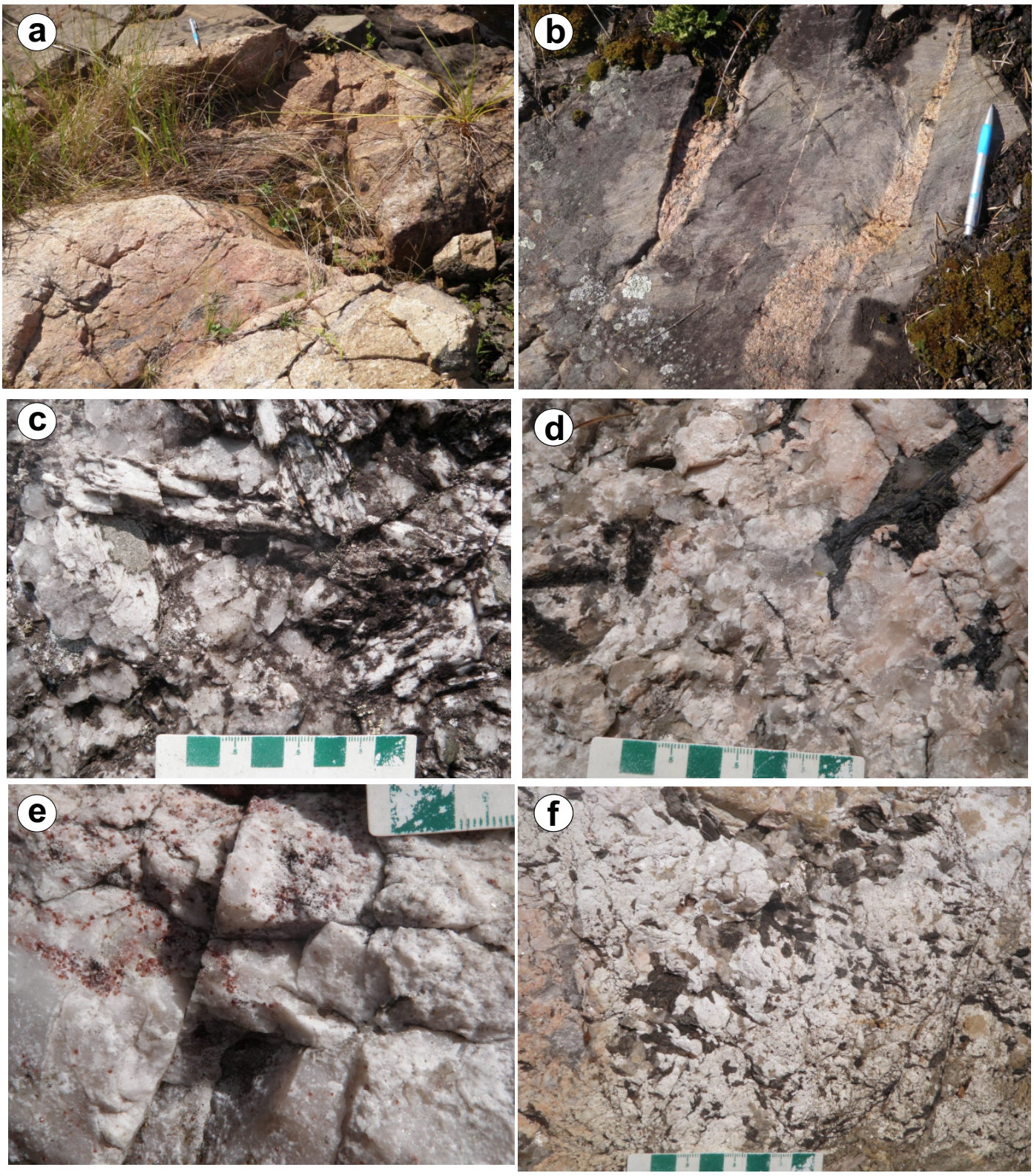

Figure 20: *Field photographs and photomicrographs of unit 14 pegmatitic granite, granitic pegmatite and minor aplite, showing some of the key features and field relationships, Cat Creek–Euclid Lake area:* ***a)*** *muscovite- and tourmaline-bearing pegmatitic granite intrusive into unit 11 sedimentary rocks (UTM 332040E, 5605616N);* ***b)*** *pegmatitic granite as veins or dikes cutting S_1 foliations (UTM 332040E, 5605616N);* ***c)*** *massive, spodumene-muscovite–bearing pegmatite (UTM 324702E, 5609789N) from a 60 cm wide dike that trends 325°;* ***d)*** *garnet-tourmaline-muscovite pegmatite (UTM 328943E, 5607872N) from a 30 m wide pegmatite dike that cuts medium-grained gabbro of unit 8;* ***e)*** *enlarged view of part of Figure 20d, showing euhedral garnet-crystal clusters;* ***f)*** *massive muscovite-bearing pegmatite (UTM 330469E, 5607231N).*

et al., 1962, 1992). Spinel-group minerals have long been used as 'petrogenetic indicators' (Irvine, 1965, 1967) because they 1) crystallize over a wide range of conditions from mafic–ultramafic magmas; 2) are among the first phase(s) to crystallize; 3) display a wide range of solid solution; and 4) are relatively refractory and resistant to alteration and metamorphism, compared to other high-temperature magmatic silicate minerals such as olivine or orthopyroxene (Bateman, 1943, 1945; Peck and Keays, 1990; Ballhaus et al., 1991; Barnes, 1998, 2000; Barnes and Roeder, 2001; Sobolev and Logvinova, 2005; Rollinson et al., 2010; Krause et al., 2011; Voigt and von der Handt, 2011; Yang and Gilbert, 2014b).

The cores of chromite crystals can retain their original magmatic chemistry at metamorphic temperatures of up to 500°C (Barnes, 1998) or even higher (Rollinson et al., 2002, 2010). Therefore, chromite chemistry has proven to be an effective tool for investigating magma types, magmatic processes and tectonic settings in metamorphosed mafic–ultramafic intrusions (Irvine, 1965; Roeder, 1994; Stowe, 1994; Barnes, 1998, 2000; Barnes and Roeder, 2001; Kamenetsky et al., 2001; Arif and Jan, 2006). The chemical composition of spinel minerals can also be used to identify Ni-mineralized and -barren mafic–ultramafic intrusions (Yang et al., 1994; Barnes and Tang, 1999; Barnes and Kunilov, 2000). Therefore, spinel is one of the best index minerals for Ni-Cu-PGE-Cr exploration. Moreover, chromite included in diamonds displays a relatively narrow Cr# range ($100\times Cr^{3+}/[Cr^{3+}+Al^{3+}]=75–90$) but variable Mg# ($100\times Mg^{2+}/[Mg^{2+}+Fe^{2+}]=50–80$), thus making it an ideal indicator mineral for diamond exploration (Sobolev and Logvinova, 2005).

Occurrences of chromite in the Mayville intrusion

Chromite occurs mostly in unit 4 rocks of the heterolithic breccia zone (HBZ) of the Mayville mafic–ultramafic intrusion (Peck et al., 1999; Yang et al., 2012; Yang and Gilbert, 2014b) as 1) chromitite bands or layers; 2) disseminations in pyroxenite and gabbro; and 3) discrete crystals in the reaction zones between leucogabbro (blocks) and ultramafic rocks in the intrusion, as described by Hiebert (2003). Chromitite layers up to 0.4 m thick, consisting of ~30–50 mode % chromite plus amphibole, chlorite and minor sulphide, occur within the upper HBZ (Figure 21a, b). Some chromite grains contain exsolution lamellae of ilmenite and/or rutile (Figure 21c), confirming the observations of Hiebert (2003). This style of chromitite is similar to that of the Bird River sill, where the Chromitiferous zone, comprising chromitite bands or layers, is also present at the top of the Ultramafic series (Scoates et al., 1986, 1989; Williamson, 1990; Sotiriou et al., 2019). Some chromitite layers in pyroxenite are strongly magnetic (Figure 21d), whereas others are lens-like rafts trapped in anorthosite that are not magnetic (Figure 21e). Disseminated chromite usually occurs in ultramafic dikes in the heterolithic breccia unit, which contains scattered disseminated pyrrhotite and chalcopyrite (Figure 21f). Some chromite crystals contain rounded inclusions of silicate melt (Figure 21g), suggesting that they crystallized from a silicate melt (magma). Compositional zoning is common in Mayville chromite (Figure 21h), indicating that it was likely buffered by the melt composition. Pyrrhotite inclusions are evident in chromite, suggesting that sulphide saturation may have occurred earlier (Hiebert, 2003; Yang et al., 2011, 2012), perhaps resulting in Ni, Cu and PGE depletion in the evolved residual magma(s).

Hiebert (2003) investigated the chemical composition of chromite from the Mayville intrusion, concluding that it is generally characterized by much lower MgO/(MgO+FeO) ratios than those in the Bird River sill (as determined by Gait, 1964). This suggests that the magmas from which the Mayville intrusion formed may have been relatively more evolved, consistent with petrological and lithogeochemical features (Theyer, 1991, 2003; Peck et al., 1999, 2000; Yang et al., 2011, 2012). Hiebert (2003) only analyzed five elements (i.e., Al_2O_3, MgO, Cr_2O_3, TiO_2, FeO) by EPMA. Full characterization of the chemistry of chromite, however, also requires analysis of NiO, CoO, MnO and ZnO (Barnes and Roeder, 2001; Rollinson et al., 2010).

In this report, 17 samples from the Mayville intrusion were collected for petrographic investigation and chemical analysis of chromite to characterize their chemical signatures and magmatic affinity, and compare them with those of chromite in the Bird River sill. The nature of the parent magma from which the Mayville intrusion formed is also assessed using chromite chemistry. Cores of refractory chromite grains may record information regarding the magma from which it crystallized, whereas rim composition of the chromite may reflect re-equilibrium with interstitial residual melt (silicate liquid; e.g., Barnes and Roeder, 2001; Rollinson et al., 2002, 2010).

Petrography

Massive, fine-grained chromitite consists of 35–50 mode % euhedral to anhedral chromite, 0.02–0.3 mm in diameter, embedded in a groundmass of serpentine and chlorite (Figure 21b). Most chromite grains are unaltered, although some display minor chloritic alteration. Some chromite crystals contain rounded silicate inclusions (Figure 21g) and others have sulphide inclusions, indicating that chromite crystallized from sulphide-saturated silicate magma(s). Compositional zonation is common, mostly with an FeO^t-enriched rim and Cr_2O_3-rich core (Figure 21h). However, reverse zoning is also evident. Opaque minerals are dominantly chromite and minor ilmenite and rutile.

Disseminated chromite also occurs in pyroxenite and gabbroic rocks from the Mayville intrusion. The ultramafic rocks are commonly coarse grained, showing adcumulus texture, and consist dominantly of hornblende (as a result of alteration of pyroxene, mostly clinopyroxene). Hornblende crystals are euhedral to subhedral and constitute more than 90% of the

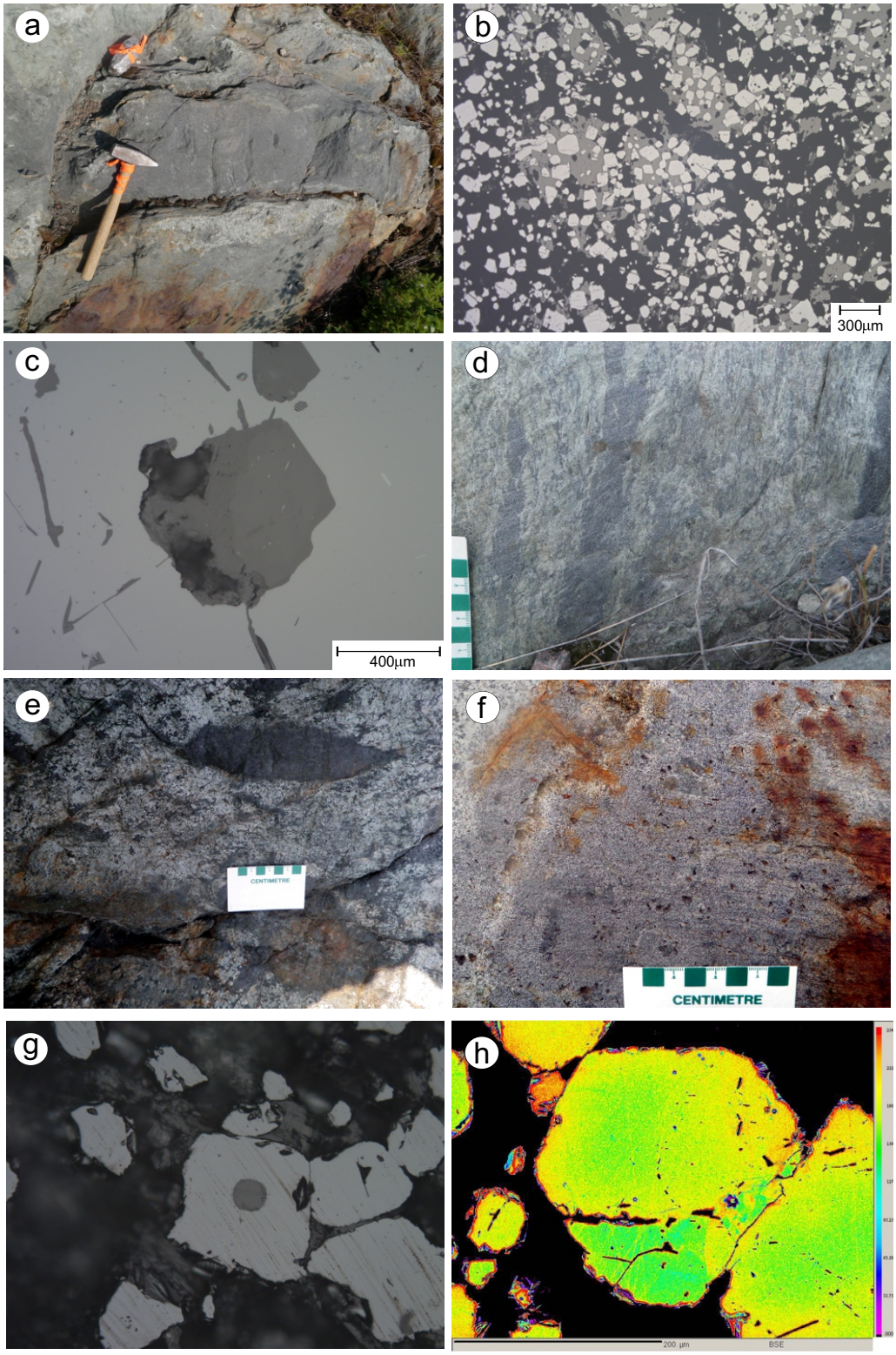

Figure 21: *Field photographs and photomicrographs of chromite occurrences and representative photomicrographs of chromite crystals in the Mayville intrusion, Cat Creek–Euclid Lake area:* ***a)*** *disrupted, ~40 cm thick, nonmagnetic chromitite band in pyroxenite from the heterolithic breccia zone (unit 4; UTM 314616E, 5612596N);* ***b)*** *photomicrograph of euhedral to subhedral chromite crystals (scale bar is 300 µm) in massive chromitite band (sample 111-12-500B1; location same as Figure 21a; RPL);* ***c)*** *photomicrograph of exsolved lamellae in a chromite crystal (sample 111-12-500B1; RPL);* ***d)*** *strongly magnetic chromitite layers in pyroxenite (UTM 314606E, 5612599N);* ***e)*** *lens-like chromitite raft in pyroxenite (UTM 314606E, 5612599N) trapped in anorthosite;* ***f)*** *disseminated chromite in an ultramafic dike from the heterolithic breccia zone that also contains scattered disseminated pyrrhotite and chalcopyrite (UTM 314616E, 5612473N);* ***g)*** *photomicrograph of spherical inclusion of silicate melt, about 25 µm in size, in a subhedral chromite crystal with resorbed edges (sample 111-12-500B1; RPL);* ***h)*** *back-scattered electron image with pseudocolour, showing compositional zonation and/or heterogeneities in chromite (sample 111-12-500B1). Abbreviation: RPL, reflected polarized light.*

mode (Yang and Gilbert, 2014b). Some hornblende grains are strongly altered to chlorite, carbonate and magnetite. Recrystallization of some grains is manifested by smaller amphibole aggregates. Disseminated chromite occurs as inclusions in hornblende grains, and pyrite and pyrrhotite are interstitial.

Chromite chemistry

Table 2 presents the chemical compositions and structural formulas of chromite in representative samples collected from the Mayville intrusion and the Bird River sill. The detailed dataset is tabulated in Tables 2_1 and 2_2 of DRI2020024.

Table 2: Chemical compositions (wt. %) and structural formulas of chromite in representative samples from the Mayville intrusion and Bird River sill, Cat Creek–Euclid Lake area, Bird River greenstone belt.

Sample:	111-12-500B1		111-11-12	111-11-20		111-11-18		111-11-21	
Intrusion:	MI		MI	BRS		BRS		BRS	
Rock type:	Chromitite		Pyroxenite	Chromitite		Chromitite		Chromitite	
Mineral:	Chromite		Chromite	Chromite		Chromite		Chromite	
No. of grains:	4		1	8		4		4	
No. of analyses:	13		1	14		5		7	
	Av.	**SD**	**Core**	**Av.**	**SD**	**Av.**	**SD**	**Av.**	**SD**
SiO_2	0.01	0.01	0.16	0.02	0.01	0.03	0.02	0.07	0.11
TiO_2	1.17	0.06	0.50	0.44	0.20	0.36	0.04	1.26	0.04
V_2O_5	0.36	0.04	0.25	0.29	0.03	0.21	0.03	0.36	0.02
Al_2O_3	12.78	0.51	17.49	16.06	2.39	17.84	0.38	14.45	0.43
Cr_2O_3	37.22	0.29	30.81	44.37	3.62	41.57	0.25	43.02	0.90
FeO^t	44.41	0.39	43.98	28.32	2.18	30.09	1.30	30.61	3.64
FeO	32.26	0.14	31.95	23.09	2.55	24.50	1.47	24.31	3.57
Fe_2O_3	13.50	0.31	13.37	5.81	1.22	6.22	0.24	7.00	0.21
MnO	0.56	0.03	0.40	0.62	0.20	0.43	0.05	0.61	0.28
MgO	1.21	0.13	0.57	6.83	1.96	6.06	0.94	6.32	2.53
CoO	0.03	0.02	0.02	0.04	0.03	0.03	0.02	0.01	0.01
NiO	0.08	0.03	0.00	0.09	0.06	0.12	0.03	0.14	0.03
ZnO	0.20	0.03	0.87	0.08	0.05	0.08	0.02	0.09	0.06
Total	99.39		96.39	97.72		97.45		97.66	
On the basis of four oxygen:									
Cr	1.034	0.011	0.868	1.182	0.119	1.106	0.006	1.159	0.007
Ti	0.031	0.002	0.013	0.011	0.005	0.009	0.001	0.032	0.001
V	0.008	0.001	0.006	0.006	0.001	0.005	0.001	0.008	0.000
Al	0.529	0.019	0.735	0.635	0.085	0.708	0.011	0.580	0.008
Fe^{3+}	0.357	0.009	0.358	0.147	0.029	0.158	0.006	0.180	0.008
Fe^{2+}	0.948	0.007	0.952	0.651	0.082	0.690	0.045	0.694	0.113
Mn	0.017	0.001	0.012	0.018	0.006	0.012	0.001	0.018	0.008
Mg	0.063	0.007	0.030	0.341	0.091	0.304	0.045	0.319	0.121
Co	0.001	0.001	0.001	0.001	0.001	0.001	0.001	0.000	0.000
Ni	0.002	0.001	0.000	0.002	0.002	0.003	0.001	0.004	0.001
Zn	0.005	0.001	0.023	0.002	0.001	0.002	0.000	0.002	0.001
$Cr/(Cr^{3+}+Al^{3+}+Fe^{3+})$	0.538	0.006	0.443	0.602	0.058	0.561	0.003	0.604	0.004
$Fe^{3+}/(Cr^{3+}+Al^{3+}+Fe^{3+})$	0.186	0.005	0.183	0.075	0.015	0.080	0.003	0.094	0.004
$Al/(Cr^{3+}+Al^{3+}+Fe^{3+})$	0.276	0.010	0.375	0.324	0.044	0.359	0.005	0.303	0.004
$Fe^{3+}/(Fe^{2+}+Fe^{3+})$	0.274	0.004	0.274	0.186	0.045	0.186	0.015	0.208	0.026
$Mg/(Mg^{2+}+Fe^{2+})$	0.063	0.007	0.031	0.343	0.088	0.306	0.045	0.314	0.116
$Fe^{2+}/(Mg^{2+}+Fe^{2+})$	0.937	0.007	0.969	0.657	0.088	0.694	0.045	0.686	0.116
$Cr/(Cr^{3+}+Al^{3+})$	0.661	0.010	0.542	0.650	0.052	0.610	0.005	0.666	0.004

Abbreviations: Av., average; BRS, Bird River sill; Core, position of grain; MI, Mayville intrusion; SD, standard deviation.

Nomenclature of spinel-group minerals used in this report strictly follows the recommendations of the International Mineralogical Association (Nickel, 1992). Spinel minerals are named based on the most abundant trivalent cations: chromite (dominated by Cr^{3+}), spinel (Al^{3+}) or magnetite (Fe^{3+}). Accordingly, spinel minerals in the Mayville intrusion and the Bird River sill are chromite that is dominated by Cr^{3+} (Table 2). Chromite in the Mayville intrusion has a maximum Cr/Fe^{t} ratio of 1.1, whereas that in the Bird River sill varies up to 1.8. These ratios are well within the range of stratiform chromite deposits associated with layered mafic–ultramafic intrusions but much lower than those of podiform chromite deposits related to ophiolite suites (Stowe, 1994).

It is worth noting that chromite in the Bird River sill displays a range of Mg# from 19 to 50 but maintains a narrow, relatively high range of Cr# (52–76). In contrast, chromite in the Mayville intrusion has a larger range of Cr# (31–83), with only a small and lower variation in Mg# (10–23).

Chemical composition of chromite in the Mayville intrusion and the Bird River sill is well portrayed in a set of compositional diagrams suggested by Barnes and Roeder (2001), based on two common projections of the spinel prism of Stevens (1944). The Cr^{3+}-Al^{3+}-Fe^{3+} ternary diagram (Figure 22) represents the projection onto the end face of the prism; diagrams (not shown) of $Cr^{3+}/(Cr^{3+}+Al^{3+})$ and $Fe^{3+}/(Fe^{3+}+Cr^{3+}+Al^{3+})$ versus Fe# (i.e., $Fe^{2+}/(Mg^{2+}+Fe^{2+})$ represent their mutual relations to Fe#. Plots (not shown) of TiO_2 versus $Fe^{3+}/(Fe^{3+}+Cr^{3+}+Al^{3+})$ and versus Fe# are also used to explore their compositional variations.

Two populations of chromite are evident on the Cr^{3+}-Al^{3+}-Fe^{3+} ternary diagram (Figure 22). One group displays an Fe-Ti trend and exhibits characteristics of enriched Fe^{3+}. The other group, together with the data from the Bird River sill, displays a Rum trend, indicating the similarity between the two intrusions in terms of chromite chemistry, although the data from the Bird River sill lack the Fe-Ti trend. This suggests that chromite crystallized from magmas of tholeiitic affinity that may have differentiated by means of fractional crystallization in a continental-crust setting (cf. Barnes and Roeder, 2001). These combined trends are interpreted to be the result of reaction between cumulus chromite crystals and evolving interstitial silicate melt. This is consistent with the observations of Barnes and Roeder (2001), who pointed out that the Rum trend is commonly restricted to layered mafic intrusions and is attributed to reaction between cumulus chromite, trapped intercumulus liquid, plagioclase and olivine.

Moreover, some of the chromite in chromitite from the Bird River sill displays relatively low Fe^{3+} content (Figure 21). Because the ratio of chromite to the trapped silicate liquid (melt) is so high in chromitite, the effect of the reaction between chromite and interstitial liquid on the composition of chromite may be less pronounced. Thus, chromitite is more likely to reflect the primary composition of liquidus chromite.

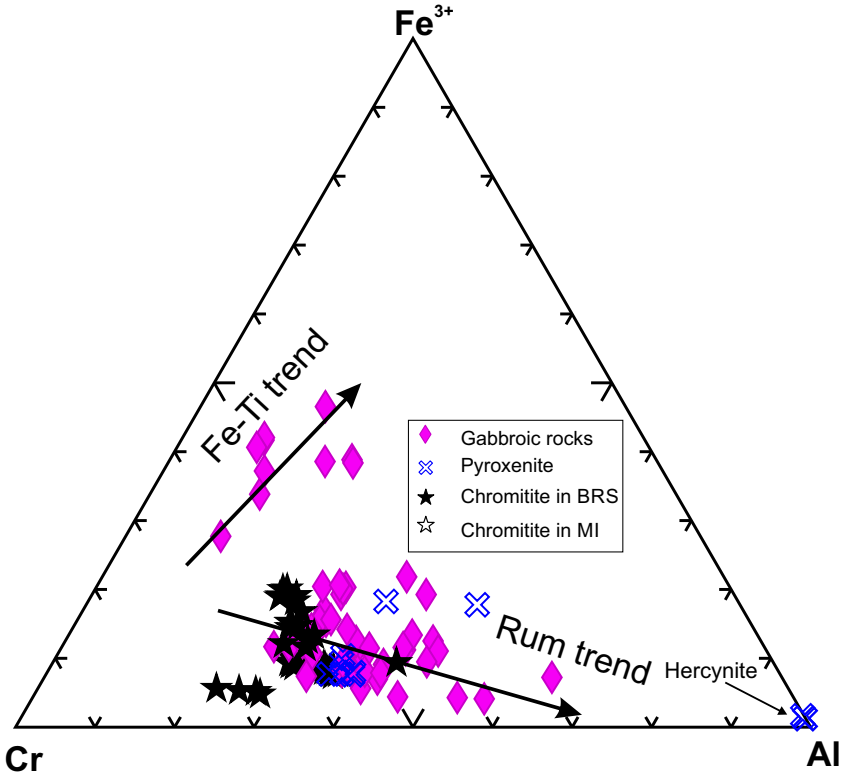

Figure 22: *Ternary plot of Cr^{3+}-Al^{3+}-Fe^{3+} in chromite from the Mayville intrusion (MI) and Bird River sill (BRS) in the Bird River greenstone belt. Data are from Gait (1964), Hiebert (2003) and this study. Arrows show the Fe-Ti trend and Rum trend, as defined by Barnes and Roeder (2001). The data for chromite in gabbroic rocks and pyroxenite are from the Mayville intrusion.*

On a plot of Cr# (Cr/[Cr+Al]) versus Fe# (Fe^{2+}/[Mg+Fe^{2+}]; Figure 23), chromite from the Mayville intrusion appears to resemble that in Archean anorthosite complexes of Rollinson et al. (2010), showing a continuous trend, but it is distinctly different from that of the Bird River sill. The Mayville intrusion chromite displays variable Cr# but relatively narrow and higher Fe#. The Bird River sill chromite, however, has relatively constant Cr# but variable and relatively lower Fe#, which may be due to the late-stage metamorphic effect, as proposed by Scoates et al. (1986). However, at a fixed Cr#, the Mayville chromite has a higher Fe# and lower Mg# than chromite from the Bird River sill that had formed from relatively primitive magma(s) (i.e., higher Mg#), consistent with their geochemical signatures based on bulk-rock molar MgO/(FeO+MgO) ratios (Yang et al., 2011, 2012). This strongly suggests that the parental magmas of both the Mayville intrusion and the Bird River sill are dominantly tholeiitic in affinity but evolved via different paths (i.e., the Mayville intrusion being more evolved than the Bird River sill).

In this study, hercynite ($Fe^{2+}Al_2O_4$) was not observed in samples from the Mayville intrusion, although it was reported to be present as disseminations in a pyroxenite sample by Hiebert (2003). Hercynite displays the lowest Cr# and relatively lower Fe#. This mineral belongs to a distinct population in mineral chemistry, as shown in Figures 22 and 23. The hercynite grains occur as disseminations in a matrix of amphibole and chlorite (Hiebert, 2003), suggesting that it may not be primary and perhaps formed during later alteration or metamorphism (e.g., Deer et al., 1962, 1992). Evidence of magmatic hercynite is very rare (Kamenetsky et al., 2001), so the petrogenetic implications are not discussed further in this report.

A diagram (not shown) of Fe# versus Fe^{3+}/(Fe^{3+}+Cr+Al) indicates that the values for chromite from the Mayville intrusion are very low (<20 in most cases), comparable to those from the Bird River sill, and seem to increase with fractionation. This suggests that the parental magmas from which chromite crystallized might be relatively reduced, favouring the formation of sulphide minerals (Roeder, 1994). The Fe-numbers, however, are generally higher but less variable than those from the Bird River sill, consistent with the conclusion that the Mayville intrusion is more evolved than the BRS (Yang et al., 2011, 2012). A plot (not shown) of Mg# (Mg/Mg+Fe^{2+}) versus Fe^{3+}/(Fe^{3+}+Cr+Al) indicates that the Mayville intrusion chromite has much lower Mg# (<20), whereas chromite in the Bird River sill has higher and more variable Mg# (20–50). Again, chromite from chromitite in the Bird River sill is broadly similar to that in chromitite from continental mafic intrusions, as compiled by Barnes and Roeder (2001), with relatively low Fe^{3+}/(Fe^{3+}+Cr+Al) ratios and a range in Fe#.

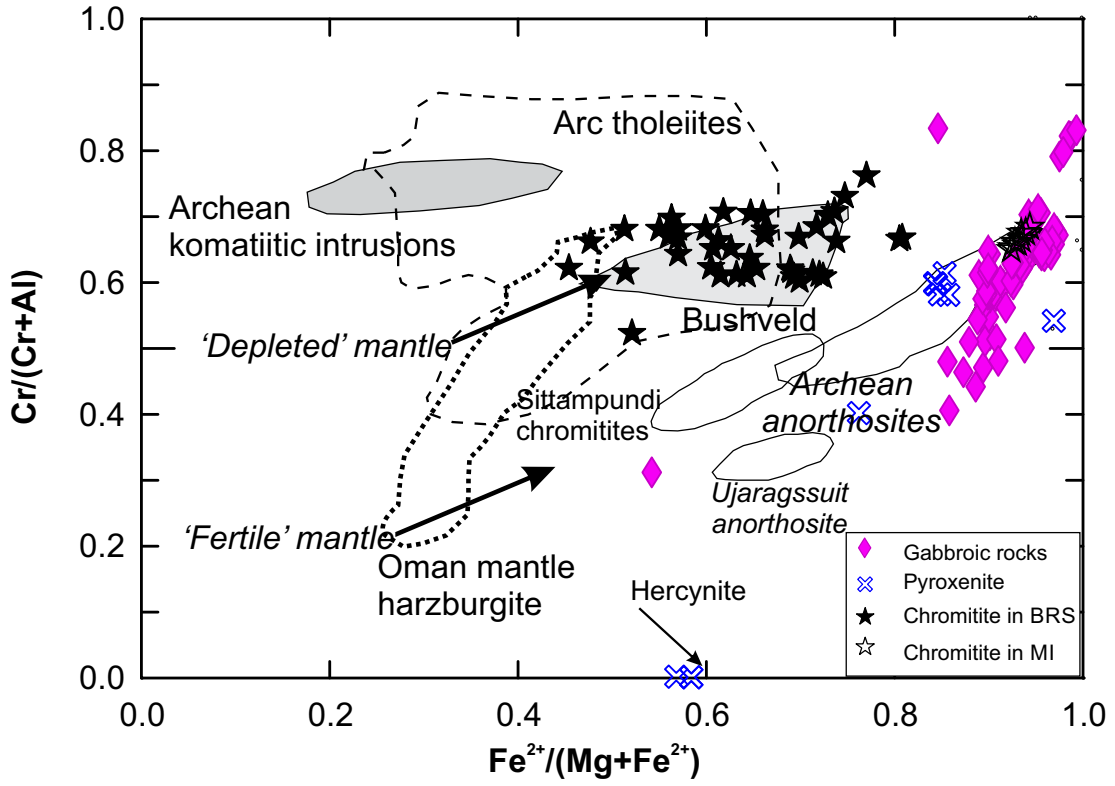

Figure 23: *Plot of Cr# versus Fe# of chromite from the Mayville intrusion (MI) and Bird River sill (BRS). Data sources and symbols as in Figure 22. Hercynite has the lowest Cr# (=0). Shown for comparison are the fields of chromite in arc tholeiite (Barnes and Roeder, 2001), the Oman ophiolite from the 'fertile' mantle harzburgite (dotted outline; Le Mée et al., 2004), and Archean komatiitic intrusions, Bushveld complex, Archean anorthosites, Ujaragssuit anorthosite and Sittampundi chromitite (Rollinson et al., 2010). The heavy arrows show the evolution of melts from aluminous (fertile) mantle in the Archean and from less aluminous (depleted) mantle in recent arcs (after Rollinson et al., 2010).*

Titanium oxide (wt. %) contents (not shown; see also Figure 22) increase with increasing atomic $Fe^{3+}/(Fe^{3+}+Cr+Al)$ ratios and Fe# in chromites from the Mayville intrusion and the Bird River sill, a typical Fe-Ti trend commonly evident in continental mafic intrusions elsewhere, as indicated in Barnes and Roeder (2001). Chemically, chromites from these two intrusions are indistinguishable in terms of their $Fe^{3+}/(Fe^{3+}+Cr+Al)$ ratios, but the Mayville chromite has higher Fe#, as described above. In addition, most of the chromite has relatively low TiO_2 (<1.5 wt. %; Table 2). These values are higher than those in podiform chromite (<0.3 wt. %) associated with ophiolite (e.g., Duke, 1983), but they are consistent with those crystallized from tholeiitic magmas (Kamenetsky et al., 2001) elsewhere and with the conclusions based on lithogeochemical characteristics of the Mayville intrusion (Peck et al., 2000, 2002; Yang et al., 2011, 2012).

It is known that trivalent (Al, Cr) and tetravalent (Ti) cations in magmatic spinel-group minerals are reluctant to exchange with those in olivine during post-entrapment re-equilibration because these cations have low diffusivity in olivine compared to Mg^{2+} and Fe^{2+}. Consequently, Al_2O_3 and TiO_2 contents of spinel minerals are largely controlled by magma composition, as suggested by Kamenetsky et al. (2001), a characteristic that can be used to discriminate geodynamic settings in which the magmas formed. For example, low-Al–low-Ti spinel is related to island-arc magmas, whereas low-Al–high-Ti spinel is associated with rifting magmas in large igneous provinces. Chromites in both the Mayville intrusion and the Bird River sill are relatively low in Al_2O_3 and TiO_2 (Table 2) and most plot in the fields of island arc and MORB (Figure 24) with transitional features. The core compositions of chromite define a narrow range that largely straddles the boundary of island-arc magmas (ARC) and MORB, which may be compatible with a back-arc setting. According to the study of Kamenetsky et al. (2001), spinel minerals from modern back-arc environments also exhibit transitional compositions, spanning those for island arc and MORB. They suggested that back-arc magmas form in complex settings that may involve diverse melting conditions and subduction-related magma components. However, a more complicated situation is evident for the Mayville intrusion chromite dataset, which may be attributed to the effect of metamorphism and/or alteration. For example, Barnes (2000) and Rollinson et al. (2002) noticed that metamorphism at mid-amphibolite– to granulite-facies conditions may modify chromite chemistry, leading to enrichment in Ti^{4+}, Fe^{3+}/Fe^{2+} and Al^{3+}.

It is noteworthy that Al/Mg ratios increase with decreasing Mg# in chromite from the Mayville intrusion and the Bird River sill (Figure 25). This diagram shows that the Mayville intrusion chromites have higher Al/Mg ratios but lower Mg# than the Bird River sill chromites, suggesting that the Mayville intrusion

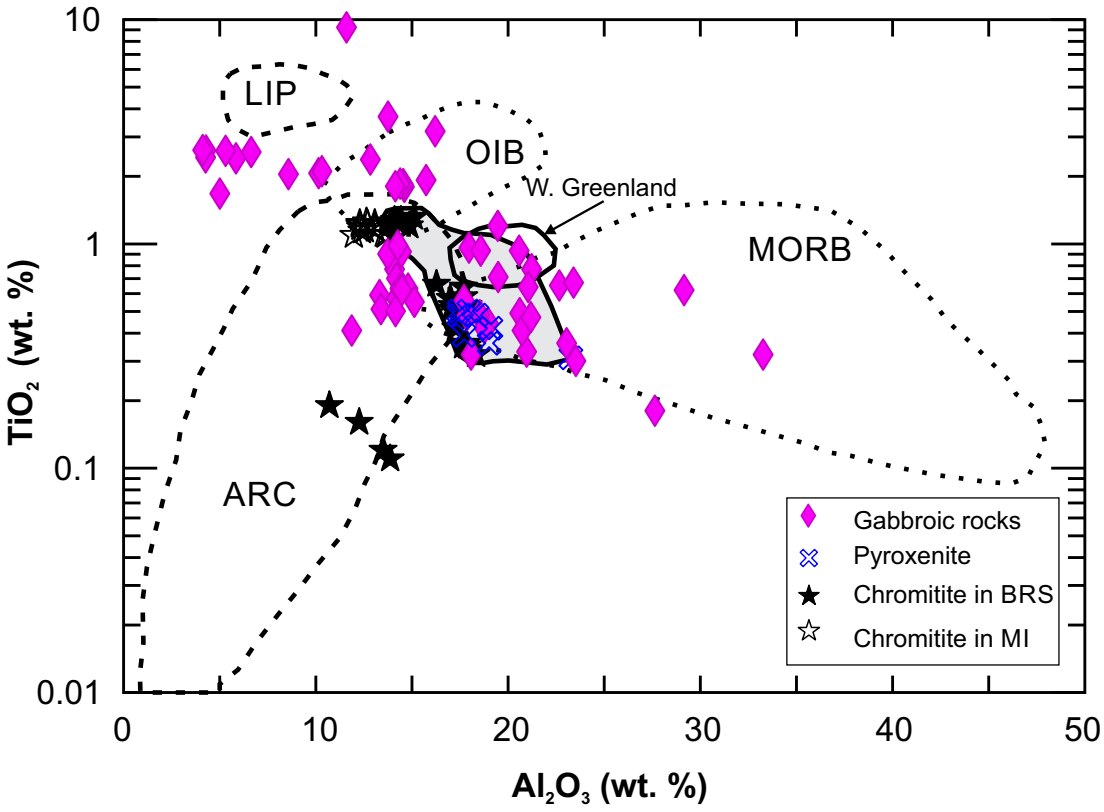

Figure 24: *Plot of TiO_2 versus Al_2O_3 content (wt. %) of chromite from the Mayville intrusion (MI) and Bird River sill (BRS). The shaded area denotes core compositions. The discrimination fields of chrome-spinel inclusions trapped in primitive olivine (Fo>84) from mid-ocean–ridge basalt (MORB), oceanic-island basalt (OIB), large igneous provinces (LIP), island-arc magmas (ARC) and west Greenland are from Kamenetsky et al. (2001). Data sources and symbols as in Figure 22.*

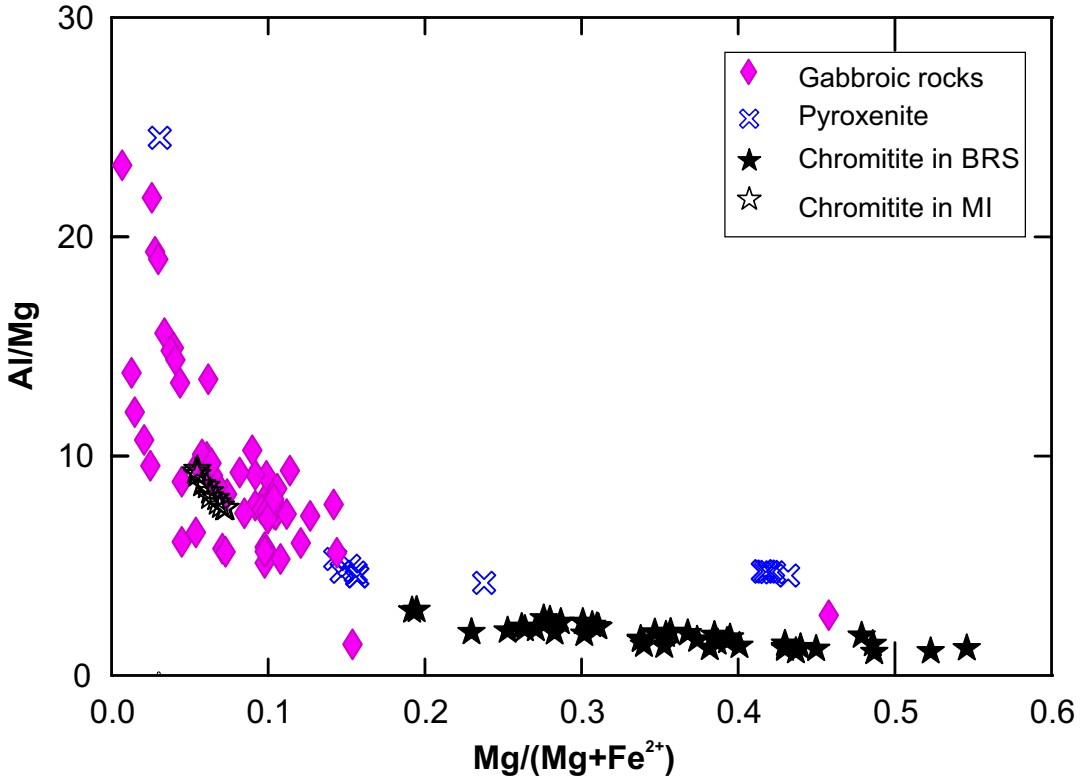

Figure 25: *Plot of Al/Mg versus Mg# (Mg/[Mg+Fe^{2+}]) in chromite from the Mayville intrusion (MI) and Bird River sill (BRS). Data sources and symbols as in Figure 22.*

is more evolved than the Bird River sill. Again, this is consistent with the prior lithogeochemical studies mentioned above (e.g., Peck et al., 2000, 2002; Yang et al., 2011, 2012), although the ultramafic unit (pyroxenite) in the Mayville intrusion displays a trend similar to that of the Bird River sill. These chemical characteristics of chromite may reflect a petrogenetic linkage between the two intrusions. Given that their ages overlap within uncertainty (i.e., Mayville intrusion at 2742.8 ±0.8 Ma per Houlé et al., 2013; BRS at 2743.0 ±0.5 Ma per Scoates and Scoates, 2013), they were likely produced either from partial melting of a common, heterogeneous mantle source or via fractional crystallization of similar parental magma derived from a subcontinental lithospheric mantle. In the former case, the Mayville intrusion requires a more fertile mantle source, whereas the Bird River sill requires a depleted-mantle source. In the latter scenario, the Mayville intrusion may have been sourced from a more fractionated parental magma compared to that of the Bird River sill. The EPMA analyses showing 'abnormal' compositions may be attributed to the effects of metamorphism or alteration.

Hiebert (2003) concluded that the Mayville intrusion and Bird River sill were probably comagmatic, in accord with the conclusions of Macek (1985a). However, the compositional differences between the two chromite populations suggest apparent differences in magmatic processes.

Minor oxides, such as V_2O_5, NiO, CoO, ZnO and MnO, in chromite were also analyzed in this study, but no anomalous values were noted (Table 2). However, the Mayville intrusion chromite exhibits relatively lower NiO contents than that of the Bird River sill. Because sulphide saturation led to Ni depletion in the silicate melt from which the chromite crystallized, this relative depletion of Ni in the Mayville intrusion chromite suggests that it is prospective for magmatic Ni mineralization (e.g., Barnes and Tang, 1999), manifested in the occurrences of Ni-Cu sulphide mineralization in the M2 deposit (Figure 6).

Plagioclase

The chemical compositions and structural formulas of plagioclase in representative samples from the Mayville intrusion are given in Table 3. Detailed data on plagioclase chemistry are tabulated in Tables 3_1 and 3_2 of DRI2020024. Plagioclase in unit 3 gabbro to melagabbro has average An contents ranging from 66.1 to 75.1, categorizing it as labradorite to bytownite. In unit 4 heterolithic breccia, plagioclase is highly calcic with An contents of 79.0–85.0, making it bytownite. Notably, unit 5 anorthosite has alkali-feldspar with very low An content (2.1–3.8), which is abnormal for Archean anorthosite (e.g., Ashwal, 1993). Plagioclase in unit 5 gabbroic anorthosite has an average An content of 63.8, categorizing it as labradorite. In unit 6 leucogabbro, plagioclase displays a consistent highly calcic signature, with average An content of 78.5–89.5 (Table 3), typical of Archean anorthosite (Ashwal, 1993). Plagioclase in unit 7 gabbro, however, has a low An content of 18.3, making it

Table 3: Chemical compositions (wt. %) and structural formulas of plagioclase in representative samples from the Mayville intrusion, Cat Creek–Euclid Lake area, Bird River greenstone belt.

Sample:	111-12-514A1		111-12-594A1		111-11-14		111-11-16		111-11-17		111-12-541A1		111-12-541A1	111-12-632A1		111-12-461A1		111-12-538A1		111-12-628A1		111-12-677A1		111-12-621A1	
Rock:	Gabbro		Melagabbro		Leucograbbro		Anorthosite		Pyroxenite		Anorthosite		Anorthosite	Gabbroic anorthosite		Leucogabbro		Leucograbbro		Leucograbbro		Anorthosite		Gabbro	
Unit:	3		3		4		4		4		5		5	5		6		6		6		6		7	
Mineral:	Plagioclase		Plagioclase		Plagioclase		Plagioclase		Plagioclase		K-feldspar		Albite	Plagioclase		Plagioclase		Plagioclase		Plagioclase		Plagioclase		Plagioclase	
No. of grains:	2		5		2		4		3		1		1	4		3		3		2		3		5	
No. of analyses:	15		15		7		12		6		5		1	21		12		6		7		10		10	
	Av.	**SD**	**Av.**	**SD**	**Av.**	**SD**	**Av.**	**SD**	**Av.**	**SD**	**Av.**	**SD**	83 / 1 .	**Av.**	**SD**	**Av.**	**SD**	**Av.**	**SD**	**Av.**	**SD**	**Av.**	**SD**	**Av.**	**SD**
SiO_2	51.43	3.92	48.48	2.44	47.49	1.00	45.95	0.59	48.16	2.57	62.92	8.02	66.43	51.51	1.34	44.94	0.56	47.91	0.93	48.07	0.37	47.40	1.32	64.11	0.73
TiO_2	0.02	0.02	0.01	0.02	0.01	0.01	0.02	0.03	0.01	0.02	0.02	0.01	0.02	0.01	0.01	0.00	0.01	0.01	0.01	0.02	0.02	0.01	0.01	0.01	0.02
Al_2O_3	30.91	2.44	32.23	1.64	33.37	0.59	33.95	0.53	33.00	1.72	25.12	5.27	21.47	30.44	0.57	34.58	0.42	33.01	0.67	33.26	0.16	32.83	0.84	23.17	0.66
FeO	0.07	0.03	0.07	0.04	0.07	0.04	0.02	0.02	0.07	0.03	0.21	0.35	0.00	0.04	0.03	0.06	0.04	0.10	0.05	0.06	0.02	0.10	0.10	0.09	0.03
MnO	0.01	0.01	0.01	0.01	0.01	0.01	0.00	0.01	0.01	0.01	0.01	0.02	0.01	0.00	0.01	0.01	0.01	0.01	0.01	0.01	0.01	0.01	0.01	0.01	0.01
MgO	0.00	0.00	0.00	0.00	0.00	0.00	0.00	0.00	0.00	0.00	0.64	0.79	0.01	0.00	0.00	0.00	0.00	0.03	0.08	0.01	0.02	0.01	0.04	0.00	0.00
CaO	13.84	3.05	15.64	2.03	16.83	0.74	17.59	0.67	16.29	2.03	0.62	0.29	1.35	13.38	0.76	18.50	0.49	16.26	1.25	16.52	0.38	16.25	1.07	3.96	0.54
Na_2O	3.93	1.78	2.86	1.16	2.04	0.42	1.71	0.35	2.39	1.23	4.65	2.23	10.88	4.19	0.46	1.20	0.29	2.30	0.38	2.33	0.18	2.41	0.61	9.66	0.37
K_2O	0.03	0.02	0.02	0.01	0.01	0.00	0.01	0.01	0.01	0.01	5.09	2.41	0.43	0.02	0.00	0.00	0.00	0.12	0.26	0.01	0.01	0.09	0.20	0.16	0.18
Total	100.26	0.31	99.34	0.54	99.83	0.56	99.25	0.65	99.93	0.49	99.29	2.37	100.62	99.60	0.69	99.30	0.45	99.74	0.69	100.33	0.45	99.13	0.67	101.19	0.88
On the basis of 32 oxygen:																									
Si	9.331	0.605	8.937	0.392	8.730	0.143	8.526	0.106	8.829	0.414	11.170	1.047	11.608	9.402	0.171	8.358	0.091	8.809	0.167	8.790	0.042	8.778	0.204	11.212	0.107
Al	6.621	0.595	7.005	0.384	7.230	0.138	7.425	0.099	7.133	0.417	5.302	1.319	4.421	6.551	0.167	7.580	0.088	7.152	0.147	7.168	0.031	7.167	0.197	4.775	0.115
Fe	0.011	0.004	0.011	0.007	0.011	0.006	0.003	0.002	0.011	0.004	0.032	0.055	0.000	0.006	0.005	0.010	0.007	0.015	0.008	0.009	0.003	0.016	0.016	0.013	0.005
Ti	0.002	0.003	0.002	0.003	0.001	0.001	0.002	0.004	0.001	0.002	0.002	0.002	0.003	0.001	0.001	0.000	0.001	0.001	0.002	0.003	0.003	0.002	0.002	0.001	0.002
Cr	0.000	0.000	0.000	0.000	0.000	0.000	0.000	0.000	0.000	0.000	0.000	0.000	0.000	0.000	0.000	0.000	0.000	0.000	0.000	0.000	0.000	0.000	0.000	0.000	0.000
Mn	0.001	0.001	0.001	0.002	0.002	0.001	0.001	0.001	0.001	0.002	0.002	0.003	0.001	0.001	0.001	0.001	0.001	0.001	0.002	0.001	0.002	0.002	0.002	0.001	0.001
Mg	0.000	0.000	0.000	0.000	0.000	0.000	0.000	0.000	0.000	0.000	0.176	0.221	0.003	0.000	0.000	0.000	0.000	0.009	0.021	0.002	0.004	0.004	0.011	0.000	0.000
Ca	2.699	0.622	3.091	0.410	3.316	0.159	3.496	0.130	3.202	0.419	0.116	0.055	0.253	2.618	0.168	3.685	0.099	3.202	0.239	3.237	0.070	3.225	0.218	0.742	0.100
Ba	0.000	0.000	0.000	0.000	0.000	0.000	0.000	0.000	0.000	0.000	0.000	0.000	0.000	0.000	0.000	0.000	0.000	0.000	0.000	0.000	0.000	0.000	0.000	0.000	0.000
Na	1.376	0.610	1.021	0.402	0.726	0.146	0.615	0.128	0.848	0.432	1.581	0.756	3.686	1.481	0.153	0.431	0.103	0.819	0.136	0.824	0.065	0.863	0.218	3.276	0.136
K	0.007	0.004	0.005	0.003	0.002	0.001	0.003	0.003	0.003	0.003	1.171	0.582	0.096	0.004	0.001	0.001	0.001	0.028	0.062	0.002	0.002	0.022	0.047	0.036	0.040
X_{Ab}	0.337	0.150	0.248	0.098	0.180	0.037	0.149	0.031	0.209	0.105	0.502	0.264	0.914	0.361	0.038	0.105	0.025	0.203	0.036	0.203	0.016	0.210	0.052	0.808	0.029
X_{Or}	0.002	0.001	0.001	0.001	0.000	0.000	0.001	0.001	0.001	0.001	0.460	0.281	0.024	0.001	0.000	0.000	0.000	0.007	0.016	0.000	0.000	0.005	0.012	0.009	0.010
X_{An}	0.661	0.151	0.751	0.099	0.820	0.037	0.850	0.032	0.790	0.106	0.038	0.021	0.063	0.638	0.039	0.895	0.025	0.790	0.046	0.797	0.016	0.785	0.054	0.183	0.025

Abbreviations: Av., average; SD, standard deviation.

oligoclase. Again, this is uncommon for Archean anorthosite and likely due to late alteration.

When plotting all plagioclase chemical data (DRI2020024, Table 3_2) on an Ab-Or-An diagram (Figure 26a), a compositional gap(s) in the plagioclase is evident between An<30 and An>50. Also, a few alkali-feldspar points stand out and display a large but discontinuous Or range. A histogram of An contents in plagioclase (Figure 26b) shows a bimodal distribution that is highly skewed toward high An values (~80–90), indicative of a compositional gap between An ~30–40, similar to Figure 26a. Plagioclase with higher An content is interpreted to reflect a primary magmatic signature, whereas plagioclase with low An content, together with the presence of alkali feldspar, may be the result of late hydrothermal alteration and/or metamorphism. Ashwal (1993) had similar findings for plagioclase in the Archean Bad Vermilion Lake anorthosite and likewise attributed the low An content of plagioclase to hydrothermal alteration and/or metamorphism. Interestingly, Phinney et al. (1985)

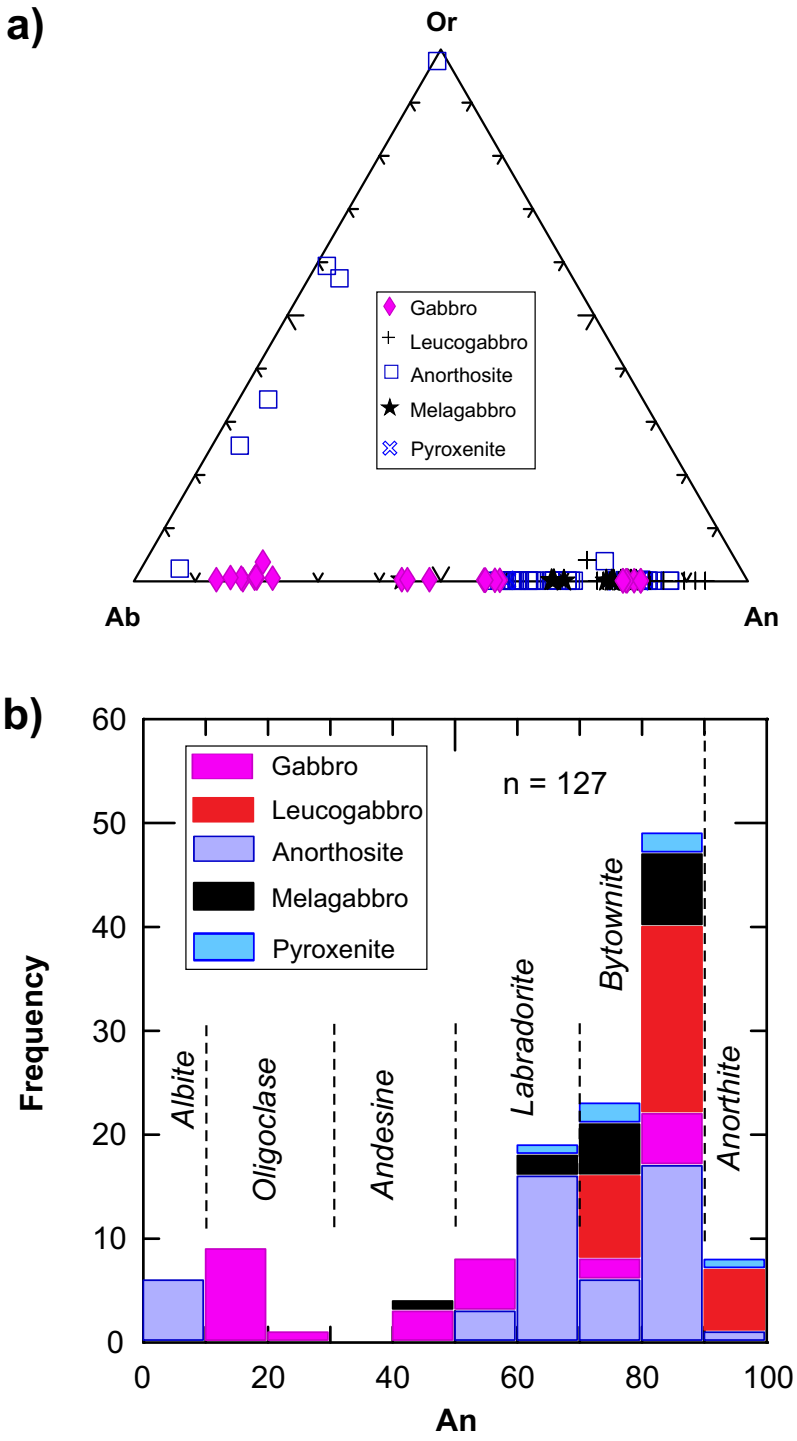

Figure 26: *Chemical composition of feldspar in representative samples from the Mayville intrusion, Bird River greenstone belt:* ***a)*** *Ab-Or-An plot;* ***b)*** *histogram of An contents (mole %) in plagioclase.*

noticed that megacrystic plagioclase from the Bird River sill anorthosite displayed complicated rim zonings with discrete compositional steps in An content at 73–75, 55–57, 38–40 and 23–25.

Amphibole

The chemical compositions and structural formulas of amphibole in representative samples from the Mayville intrusion are given in Table 4. Detailed data on amphibole chemistry determined by EPMA are tabulated in Tables 4_1 and 4_2 of DRI2020024. Mineral formula calculations are based on 23 oxygens, and ferric/ferrous ratios were calculated using 13-cation normalization and charge balance (Leake et al., 1997). Water contents were calculated on the basis of stoichiometry.

According to the amphibole classification scheme of Leake et al. (1997, 2003), amphibole in various units of the Mayville intrusion is calcic amphibole characterized by Σ(Ca+Na) on $M_4 \geq 1.00$ with $Na < 0.5$, and $Ca \geq 1.5$ on M_4 (Table 4). The calcic amphibole is mostly magnesian and falls mainly into the field of magnesiohornblende, although some of the analyses extend into the fields of ferrohornblende, ferrotschermakite and tschermakite (Figure 27). Amphibole in each unit displays positive correlation between $Mg/(Mg+Fe^{2+})$ ratios and Si values, consistent with a typical fractionation trend of tholeiitic magmas. A notable population of amphibole in sample 111-12-621A1, collected from unit 7 gabbro, has lower $Mg/(Mg+Fe^{2+})$ ratios and Si values, typical of ferrohornblende (Figure 27), strongly suggesting evolved characteristics of the tholeiitic magmas. This amphibole further displays $(Na+K)_A \geq 0.5$ with $Ti < 0.5$, which is assigned compositionally to ferro-edenite (Leake et al., 1997).

Chemical zonation in each individual amphibole grain is not evident in terms of variations in Mg# ($Mg/[Mg+Fe^{2+}]$) and Fe# ($Fe^{2+}/[Mg+Fe^{2+}]$). For instance, eight analyses from rim, core and core to rim on amphibole grain #3 in sample 111-12-632A1 (Table 4; DRI2020024) show consistent Mg# (0.58–0.67) and Fe# (0.33–0.42) values, suggesting compositional homogeneity throughout the grain. Generally, calcic amphibole from the Mayville intrusion has relatively low TiO_2 contents, ranging from 0.15 to 0.88 wt. % and reflecting a reduced nature for the tholeiitic magmas consistent with very low $Fe^{3+}/(Fe^{3+}+Fe^{2+})$ ratios (0.01–0.06; Table 4).

Crystallization pressures, calculated using the Al-in-hornblende geobarometer of Johnson and Rutherford (1989), are 3.3–4.1 kb for unit 3, 4.2–4.4 kb for unit 4, 4.1 kb for unit 5, 2.1–5.0 kb for unit 6 and 4.3 kb for unit 7 (Table 4). Application of a revised Al-in-hornblende geobarometer proposed by Mutch et al. (2016) raised the calculated pressures by up to 0.6 kb. Such a large range of pressures, from 2.1 to 5.0 kb, recorded in Mayville intrusion amphibole cannot represent emplacement pressures because the difference in relative altitude (elevation) of the exposed intrusion is less than 100 m (i.e., ~0.03 kb), but may instead reflect regional metamorphism and rapidly differential terrane exhumation.

More recently, Sotiriou et al. (2020) suggested that primary magmatic hornblende occurs in the various units of the Mayville intrusion, making the parental magma hydrous tholeiite derived from partial melting of depleted mantle in a back-arc setting. This is largely consistent with the main conclusion of this study.

Epidote group minerals

The mineral chemistry of epidote-group minerals from the Mayville intrusion is similar to clinozoisite (Table 5), and their detailed data are listed in Tables 5_1 and 5_2 of DRI2020024. The epidote-group minerals likely formed by low-grade metamorphism (i.e., ranging from greenschist to epidote-amphibolite facies; Deer et al., 1962, 1992).

Chlorite

Chlorite minerals are classified as ripidolite in terms of chemical composition (Table 5), with an average Mg# of 57.0 that is typical of a metamorphic product at greenschist facies.

Ilmenite

The presence of ilmenite in units 3 and 7 gabbroic rocks (Table 5) is consistent with tholeiitic magmas that are relatively reduced in terms of redox condition. This may have facilitated sulphide saturation in the tholeiitic magmas, consistent with the occurrence of pyrrhotite blebs in various units of the Mayville intrusion, as described above.

Geochemistry

Major (wt. %) and trace-element (ppm) contents of 194 samples collected from the Cat Creek–Euclid Lake area were analyzed using the 4-Lithores package at Activation Laboratories Ltd. (Actlabs) in Ancaster, Ontario. Detailed analytical procedures and methods were described in Anderson (2013) and Polat et al. (2016), and may also be found at www.actlabs.com. Precious metals (Au, Pt, Pd; ppb) in some of the samples were also analyzed using fire assay (standard grade) at Actlabs. The geochemical compositions of representative samples for each map unit are presented in Table 6. Detailed data on the geochemical compositions (and elemental ratios as well as petrochemical parameters) of all 194 whole-rock samples are tabulated in Tables 6_1 and 6_2 of DRI2020024.

Remarks on the geochemical studies of granitoids

In addition to supracrustal rocks, the Cat Creek–Euclid Lake area is underlain by various phases of granitoid rocks that are grouped into five map units (units 1, 10, 12, 13 and 14; Table 1) that record a diverse geodynamic history from Meso- to Neoarchean. In the context of granitoid study, it is neces-

Table 4: Chemical compositions (wt. %) and structural formulas of amphibole in representative samples from the Mayville intrusion, Cat Creek–Euclid Lake area, Bird River greenstone belt.

Sample:	111-12-514A1		111-12-594A1		111-11-14		111-11-16		111-11-17		111-12-632A1		111-12-461A1		111-12-538A1		111-12-628A1		111-12-677A1		111-12-621A1	
Rock:	Gabbro		Melagabbro		Leucograbbro		Anorthosite		Pyroxenite		Gabbroic anorthosite		Leucogabbro		Leucograbbro		Leucograbbro		Anorthosite		Gabbro	
Unit:	3		3		4		4		4		5		6		6		6		6		7	
Mineral:	Amphibole		Amphibole		Amphibole		Amphibole		Amphibole		Amphibole		Amphibole		Amphibole		Amphibole		Amphibole		Amphibole	
No. of grains:	2		3		2		4		4		4		5		3		2		3		5	
No. of analyses:	10		10		8		8		9		19		15		8		8		10		9	
	Av.	**SD**	**Av.**	**SD**	**Av.**	**SD**	**Av.**	**SD**	**Av.**	**SD**	**Av.**	**SD**	**Av.**	**SD**	**Av.**	**SD**	**Av.**	**SD**	**Av.**	**SD**	**Av.**	**SD**
SiO_2	45.45	0.96	46.37	1.59	44.29	2.38	47.40	3.94	45.62	2.66	46.84	2.85	45.62	4.02	47.67	1.55	48.78	3.62	48.09	1.37	41.60	0.32
TiO_2	0.49	0.04	0.49	0.06	0.44	0.06	0.32	0.14	0.49	0.10	0.40	0.12	0.64	1.42	0.43	0.08	0.15	0.16	0.51	0.07	0.88	0.05
Al_2O_3	10.08	0.87	9.12	1.18	10.21	1.75	10.57	4.94	10.60	2.78	10.38	3.19	11.43	4.74	7.81	1.69	8.70	4.65	7.61	1.39	9.89	0.23
Cr_2O_3	0.00	0.00	0.00	0.00	0.00	0.00	0.00	0.00	0.00	0.00	0.00	0.00	0.00	0.00	0.00	0.00	0.00	0.00	0.00	0.00	0.00	0.00
Fe_2O_3	0.47	0.35	0.42	0.29	3.35	0.92	0.68	0.34	1.46	0.55	0.18	0.13	0.35	0.25	0.21	0.21	0.47	0.32	0.68	0.80	2.00	0.17
FeO	16.86	0.65	14.25	0.61	16.43	0.45	12.32	2.91	13.61	0.41	12.77	0.83	14.21	2.04	13.80	1.06	15.11	2.44	15.40	1.13	24.55	0.24
MnO	0.21	0.02	0.27	0.01	0.23	0.01	0.26	0.14	0.24	0.04	0.24	0.03	0.26	0.12	0.24	0.03	0.43	0.22	0.35	0.02	0.50	0.04
MgO	10.54	0.54	12.59	0.84	9.00	1.14	15.23	2.97	11.75	1.54	13.43	1.72	12.99	2.69	13.29	0.95	14.80	2.84	11.83	0.85	5.06	0.17
CaO	12.01	0.25	12.22	0.14	11.27	0.69	8.97	3.94	11.55	0.15	11.71	0.21	10.26	2.69	12.29	0.15	8.28	3.86	12.12	0.06	10.75	0.07
BaO	0.00	0.00	0.00	0.00	0.00	0.00	0.00	0.00	0.00	0.00	0.00	0.00	0.00	0.00	0.00	0.00	0.00	0.00	0.00	0.00	0.00	0.00
Na_2O	0.96	0.08	0.99	0.13	1.09	0.15	1.26	0.63	1.11	0.31	1.25	0.40	1.27	0.55	0.79	0.20	0.96	0.52	0.65	0.12	1.68	0.10
K_2O	0.29	0.05	0.22	0.05	0.15	0.05	0.10	0.05	0.16	0.06	0.14	0.07	0.18	0.11	0.30	0.05	0.08	0.05	0.35	0.06	0.50	0.02
H_2O	1.99	0.02	2.00	0.02	1.82	0.07	2.04	0.02	1.96	0.05	2.05	0.02	2.03	0.05	2.02	0.01	2.05	0.02	2.00	0.04	1.82	0.01
Cl	0.02	0.00	0.02	0.01	0.55	0.17	0.09	0.04	0.21	0.10	0.02	0.01	0.05	0.03	0.01	0.01	0.02	0.01	0.03	0.02	0.29	0.02
F	0.03	0.03	0.02	0.02	0.01	0.02	0.01	0.02	0.01	0.02	0.00	0.01	0.00	0.01	0.01	0.02	0.03	0.03	0.04	0.07	0.01	0.01
-O=Cl	0.00	0.00	0.00	0.00	0.12	0.04	0.02	0.01	0.05	0.02	0.00	0.00	0.01	0.01	0.00	0.00	0.00	0.00	0.01	0.00	0.07	0.00
-O=F	0.01	0.01	0.01	0.01	0.00	0.01	0.00	0.01	0.01	0.01	0.00	0.00	0.00	0.00	0.00	0.01	0.01	0.01	0.02	0.03	0.00	0.01
Total	99.38	0.27	98.98	1.11	98.72	1.36	99.21		98.72	1.07	99.39	0.42	99.27	1.37	98.85	0.65	99.82	0.60	99.65		99.45	
On the basis of 23 oxygen:																						
Si	6.793	0.115	6.874	0.153	6.736	0.251	6.87	0.53	6.776	0.321	6.835	0.357	6.695	0.469	7.042	0.209	7.076	0.494	7.103	0.159	6.558	0.026
^{IV}Al	1.207	0.115	1.126	0.153	1.264	0.251	1.13	0.53	1.224	0.321	1.165	0.357	1.305	0.469	0.958	0.209	0.924	0.494	0.897	0.159	1.442	0.026
T site	8.000	0.000	8.000	0.000	8.000	0.000	8.00	0.00	8.000	0.000	8.000	0.000	8.000	0.000	8.000	0.000	8.000	0.000	8.000	0.000	8.000	0.000
^{VI}Al	0.569	0.052	0.470	0.077	0.572	0.099	0.67	0.32	0.636	0.189	0.626	0.204	0.686	0.415	0.403	0.095	0.566	0.308	0.428	0.092	0.396	0.028
Ti	0.055	0.005	0.055	0.007	0.050	0.008	0.03	0.02	0.055	0.012	0.044	0.014	0.070	0.155	0.048	0.009	0.016	0.017	0.057	0.008	0.105	0.005
Fe^{3+}	0.018	0.014	0.016	0.011	0.147	0.046	0.03	0.01	0.059	0.024	0.007	0.005	0.013	0.010	0.008	0.008	0.018	0.012	0.027	0.034	0.083	0.007
Cr	0.000	0.000	0.000	0.000	0.000	0.000	0.00	0.00	0.000	0.000	0.000	0.000	0.000	0.000	0.000	0.000	0.000	0.000	0.000	0.000	0.000	0.000
Fe^{2+}	2.148	0.078	1.803	0.083	2.372	0.089	1.55	0.32	1.815	0.101	1.574	0.116	1.774	0.224	1.723	0.138	1.872	0.289	1.960	0.102	3.416	0.026
Mn	0.026	0.002	0.034	0.002	0.029	0.002	0.03	0.02	0.030	0.005	0.029	0.004	0.033	0.014	0.030	0.003	0.052	0.027	0.044	0.002	0.067	0.005
Mg	2.184	0.118	2.622	0.154	1.829	0.225	2.69	0.08	2.406	0.304	2.720	0.323	2.424	0.250	2.788	0.214	2.477	0.067	2.484	0.181	0.934	0.035
C site	5.000	0.000	5.000	0.000	5.000	0.000	5.00	0.00	5.000	0.000	5.000	0.000	5.000	0.000	5.000	0.000	5.000	0.000	5.000	0.000	5.000	0.000

Abbreviations: Av., average; SD, standard deviation.

Table 4 (continued): Chemical compositions (wt. %) and structural formulas of amphibole in representative samples from the Mayville intrusion, Cat Creek–Euclid Lake area, Bird River greenstone belt.

Sample:	111-12-514A1		111-12-594A1		111-11-14		111-11-16		111-11-17		111-12-632A1		111-12-461A1		111-12-538A1		111-12-628A1		111-12-677A1		111-12-621A1	
Rock:	Gabbro		Melagabbro		Leucograbbro		Anorthosite		Pyroxenite		Gabbroic anorthosite		Leucogabbro		Leucograbbro		Leucograbbro		Anorthosite		Gabbro	
Unit:	3		3		4		4		4		5		6		6		6		6		7	
Mineral:	Amphibole		Amphibole		Amphibole		Amphibole		Amphibole		Amphibole		Amphibole		Amphibole		Amphibole		Amphibole		Amphibole	
No. of grains:	2		3		2		4		4		4		5		3		2		3		5	
No. of analyses:	10		10		8		8		9		19		15		8		8		10		9	
	Av.	**SD**	**Av.**	**SD**	**Av.**	**SD**	**Av.**	**SD**	**Av.**	**SD**	**Av.**	**SD**	**Av.**	**SD**	**Av.**	**SD**	**Av.**	**SD**	**Av.**	**SD**	**Av.**	**SD**
On the basis of 23 oxygen:																						
Mg	0.164	0.049	0.160	0.025	0.211	0.149	0.60	0.62	0.196	0.042	0.201	0.042	0.414	0.418	0.140	0.051	0.722	0.598	0.121	0.027	0.255	0.018
Fe^{2+}	0.000	0.000	0.000	0.000	0.000	0.000	0.00	0.00	0.000	0.000	0.000	0.000	0.000	0.000	0.000	0.000	0.000	0.000	0.000	0.000	0.000	0.000
Mn	0.000	0.000	0.000	0.000	0.000	0.000	0.00	0.00	0.000	0.000	0.000	0.000	0.000	0.000	0.000	0.000	0.000	0.000	0.000	0.000	0.000	0.000
Ca	1.836	0.049	1.840	0.025	1.789	0.149	1.40	0.62	1.804	0.042	1.799	0.042	1.586	0.418	1.860	0.051	1.278	0.598	1.879	0.027	1.745	0.018
Na	0.000	0.000	0.000	0.000	0.000	0.000	0.00	0.00	0.000	0.000	0.000	0.000	0.000	0.000	0.000	0.000	0.000	0.000	0.000	0.000	0.000	0.000
B site	2.000	0.000	2.000	0.000	2.000	0.000	2.00	0.00	2.000	0.000	2.000	0.000	2.000	0.000	2.000	0.000	2.000	0.000	2.000	0.000	2.000	0.000
Ca	0.087	0.019	0.102	0.032	0.047	0.062	-0.00	0.04	0.035	0.040	0.033	0.018	0.035	0.038	0.085	0.035	0.011	0.012	0.038	0.027	0.070	0.027
Na	0.280	0.023	0.286	0.039	0.321	0.046	0.35	0.18	0.319	0.092	0.353	0.115	0.363	0.160	0.225	0.057	0.271	0.147	0.185	0.037	0.513	0.031
K	0.056	0.010	0.041	0.010	0.029	0.010	0.02	0.01	0.030	0.012	0.026	0.012	0.033	0.021	0.056	0.010	0.016	0.010	0.067	0.011	0.100	0.004
Asite	0.423	0.048	0.428	0.072	0.397	0.079	0.37	0.18	0.384	0.115	0.412	0.129	0.431	0.201	0.366	0.088	0.298	0.163	0.290	0.060	0.684	0.020
Cl	0.004	0.001	0.005	0.002	0.143	0.045	0.02	0.01	0.053	0.026	0.005	0.002	0.012	0.009	0.003	0.001	0.004	0.003	0.009	0.004	0.078	0.004
F	0.014	0.015	0.011	0.011	0.004	0.008	0.01	0.01	0.006	0.009	0.002	0.004	0.001	0.003	0.005	0.008	0.014	0.013	0.019	0.034	0.005	0.006
OH	1.982	0.014	1.984	0.011	1.853	0.046	1.97	0.01	1.941	0.024	1.993	0.005	1.987	0.010	1.992	0.008	1.982	0.012	1.973	0.034	1.917	0.007
Si	6.79	0.11	6.87	0.15	6.74	0.25	6.87	0.53	6.78	0.32	6.84	0.36	6.69	0.47	7.04	0.21	7.08	0.49	7.10	0.16	6.56	0.03
$Mg/(Mg+Fe^{2+})$	0.52	0.02	0.61	0.03	0.46	0.04	0.68	0.01	0.59	0.04	0.65	0.04	0.61	0.04	0.63	0.03	0.63	0.01	0.57	0.03	0.26	0.01
Fe#	0.48	0.02	0.40	0.02	0.55	0.04	0.32	0.01	0.42	0.05	0.35	0.04	0.39	0.04	0.37	0.03	0.37	0.01	0.43	0.03	0.75	0.01
$Fe^{3+}/(Fe^{3+}+Fe^{2+})$	0.01	0.01	0.01	0.01	0.06	0.02	0.02	0.01	0.03	0.01	0.00	0.00	0.01	0.01	0.00	0.00	0.01	0.01	0.01	0.02	0.02	0.00
P (kb)[(1)]	4.1		3.3		4.3		4.2		4.4		4.1		5.0		2.3		2.8		2.1		4.3	

[(1)] Pressures estimated by Ai-in-hornblende barometer of Johnson and Rutherford (1989)

Abbreviations: Av., average; SD, standard deviation.

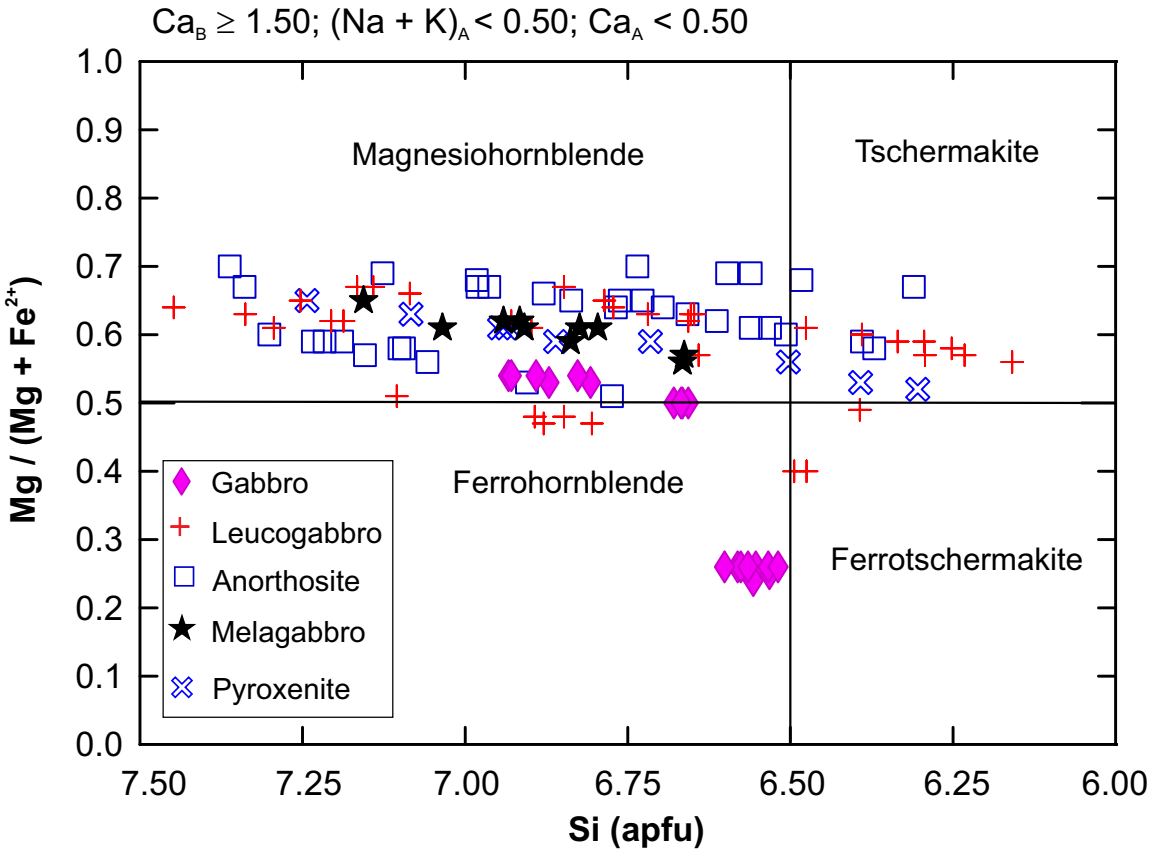

Figure 27: *Chemical classification diagram (after Leake et al., 1997) for amphibole in representative samples from the Mayville intrusion, Bird River greenstone belt. Abbreviation: apfu, atoms per formula unit.*

Table 5: Chemical compositions of ilmenite, chlorite and epidote from the Mayville intrusion, Cat Creek–Euclid Lake area, Bird River greenstone belt.

Sample:	**111-11-02**	**111-12-621A1**	**111-12-541A1**		**111-12-541A1**	
Mineral:	Ilmenite	Ilmenite	Chlorite		Epidote	
Rock:	Melagabbro	Gabbro	Anorthosite			
Unit:	3	7	5		5	
No. of grains:	1	1	3		3	
No. of analyses:	1	1	10		14	
	Core	Core	Av.	SD	Av.	SD
SiO_2	0.00	0.06	25.65	1.09	39.50	4.57
TiO_2	52.43	51.59	0.12	0.22	0.02	0.02
Al_2O_3	0.01	0.08	21.00	0.62	28.33	2.54
FeO	46.97	45.82	22.75	1.65	2.33	1.70
MnO	1.33	1.67	0.25	0.03	0.06	0.06
MgO	0.13	0.03	16.91	1.07	0.19	0.49
CaO	na	0.03	0.08	0.12	23.56	3.52
Na_2O	na	0.10	0.01	0.01	0.08	0.18
K_2O	na	0.04	0.00	0.00	0.25	0.70
F	na	0.04	0.01	0.02	0.01	0.02
Cl	na	0.05	0.03	0.01	0.00	0.01
Total	100.85	99.51	86.79		94.33	

Abbreviations: Av., average; Core, grain centre; na, not analyzed; SD, standard deviation.

sary to briefly review the current understanding of petrology and major-element geochemistry of granitoid rocks (Clarke, 1992; Frost et al., 2001; Yang, 2007; Frost and Frost, 2008; Winter, 2010). Based on major-element composition of granitoid rocks, their magmatic affinities can be divided into 1) subalkaline or alkaline series (that is further subdivided into calcic, calcalkaline, alkaline and peralkaline) in terms of alkalinity; 2) metaluminous, peraluminous and peralkaline in terms of the aluminum saturation index; and 3) magnesian and ferroan, based on Fe*. However, this report will not review advances in granitoid petrogenesis using trace-element and radiogenic-isotope geochemistry because there are numerous references dealing with this topic (e.g., Allègre and Minster, 1978, Hanson, 1978; O'Nions et al., 1979; DePaolo, 1981, 1988; Pearce et al., 1984; Whalen et al., 1987; Eby, 1990; Chappell and White, 2001; Ishihara, 2004; Zhang et al., 2006; Hildebrand et al., 2018; Whalen and Hildebrand, 2019; Clemens et al., 2020).

Scaillet et al. (2016) reviewed the studies of experimental petrology on the formation of granite magmas containing 3–7% H_2O^{melt} that are inversely correlated with pre-eruptive temperatures (700° to >950°C) but unrelated to redox conditions. They showed that granites are readily subdivided into peraluminous (A/CNK>1.1), metaluminous (1.1>A/CNK>1, A/NK>1) and peralkaline (A/NK<1) classes based on molar ratios of A/CNK and A/NK (i.e., Al/[2Ca+Na+K] and Al/[Na+K], respectively), which display different mineralogy and have distinctively different petrogenesis. Although the scheme of Scaillet et al. (2016) is slightly different from that of Clarke (2019), whose classification is similar to that of Maniar and Piccoli (1989) in terms of peraluminosity, the results (i.e., peraluminosity) obtained by the two methods are almost the same.

Peraluminous granites are derived mainly from partial melting of continental sedimentary rocks; metaluminous granites require input from both continental and mantle materials; and peralkaline granites (and rhyolites) are formed by protracted differentiation or small degrees of partial melting of basalt, with limited crustal contribution. High-pressure experiments suggest that Archean TTG suites require partial melting of basaltic rocks in equilibrium with garnet at very high pressures of 10–30 kb (e.g., Moyen and Martin, 2012; Scaillet et al., 2016).

Peraluminous granites characterized by the occurrence of minerals rich in aluminum, such as cordierite, garnet, muscovite, tourmaline, hercynite ($Fe^{2+}Al_2O_4$) to gahnite ($ZnAl_2O_4$), andalusite or sillimanite, occur in three geological settings: thickened continental crust as a result of continental collision (e.g., Himalayas); continental arc (e.g., Peruvian Andes); and post-orogenic environments (e.g., the Devonian terranes of eastern Australia). In leucogranite (FeO^t <1.5%), Mn-rich garnet (spessartine) occurs only in late-stage derivatives; this contrasts with the higher temperature, almandine-type garnet present in more mafic peraluminous granites. Muscovite occurs in S-type leucogranites but only crystallizes under high pressure (>3.5 kb), although it is also a late-crystallizing mineral at lower $f(O_2)$ (Scaillet et al., 2016).

Metaluminous granitoids and dacites to rhyolites normally occur in subduction-zone settings, although they are also present in anorogenic zones and hotspots. Mixing of magmas from both crust and mantle sources is common, although metaluminous silicic magmas may have been directly derived from partial melting of igneous rocks in continental crust.

Peralkaline silicic magmatic rocks occur mostly in rift zones, back-arc settings or hotspot environments. They are associated with basalts of transitional affinity between those of MORB and alkali basalts, thus forming bimodal volcanic provinces. Peralkaline silicic rocks result from processes involving differentiation from mantle-derived magmas, with marginal inputs from crustal materials. The A-type granites are not necessarily peralkaline, but can be metaluminous or even peraluminous. Although A-type granites are ambiguous in genesis, they are commonly rich in alkalis, anhydrous and emplaced into an anorogenic setting (Loiselle and Wones, 1979; Whalen et al., 1987; Eby, 1990; Yang, 2007; Yang et al., 2008) or within-plate settings (Pearce et al., 1984; Whalen et al., 1987) to plate boundaries (Bonin, 2007).

Thus far, only metaluminous (e.g., units 1, 10, 12) and peraluminous (e.g., units 1, 13, 14) granitoid rocks, but no peralkaline varieties, have been found in the Cat Creek–Euclid Lake area.

Unit 1: basement granitoid rocks

Classification

Based on major-element composition, unit 1 granitoid rocks are dominantly within the fields of granodiorite and granite in the total alkalis versus SiO_2 (TAS) diagram, although one sample plots in each of the quartz diorite and monzonite fields (Figure 28a). All samples are subalkaline, based on the definition of Irvine and Baragar (1971), and most are calcic in terms of alkalinity, except for a few that plot in the calc-alkalic and alkali-calcic fields (Figure 28b). Based on the Fe* index proposed by Frost et al. (2001), unit 1 granitoids are dominantly magnesian, although a few evolved phases fall into the ferroan field (Figure 28c). On the Shand index plot (Figure 28d), unit 1 granitoids are weakly to moderately peraluminous, although a sheared granite (sample 111-13-190C01; solid red reverse triangle on Figure 28d) that was called muscovite-biotite schist in terms of texture and mineral assemblage in the field is strongly peraluminous due to the presence of secondary muscovite. In addition, sample 111-13-221A01 is metaluminous. Using an aluminum saturation index (ACNK) of 1.1 as the boundary for differentiating I-type (<1.1) from S-type (>1.1) granites (Figure 28d; Chappell and White, 1974), unit 1 granitoids are of I-type and therefore most likely derived from partial melting of igneous source rocks that typically contain titanite and apatite

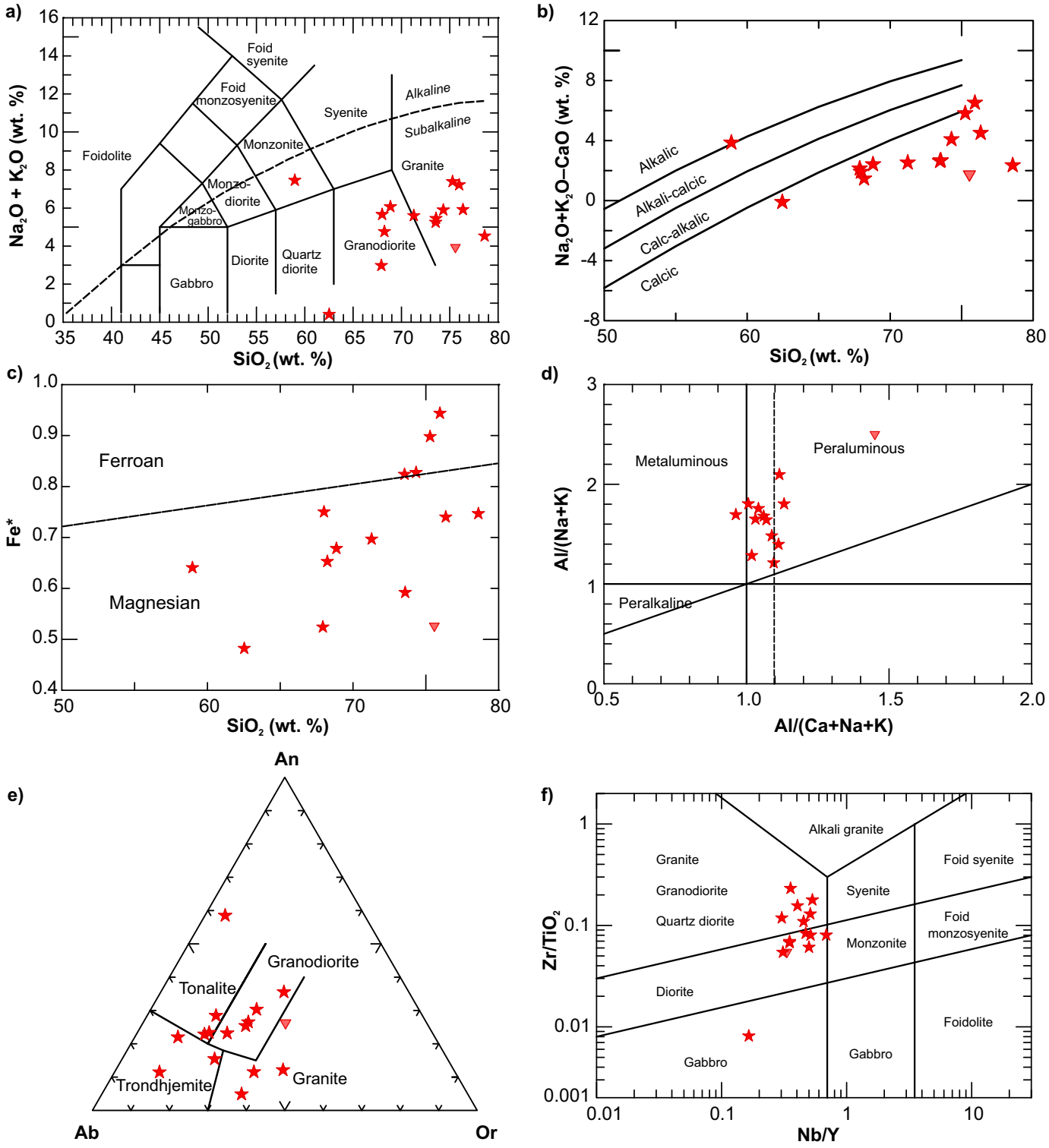

Figure 28: *Chemical classification of unit 1 granitoid rocks from the Cat Creek–Euclid Lake area:* ***a)*** *total alkalis (Na_2O+K_2O) versus SiO_2 (TAS; wt. %) diagram (fields from Middlemost, 1994); boundary between alkaline and subalkaline series from Irvine and Baragar (1971);* ***b)*** *plot of MOLI (i.e., $Na_2O+K_2O–CaO$) vs. SiO_2; wt. %; after Frost et al., 2001);* ***c)*** *classification of ferroan versus magnesian granitoids ($Fe^*=FeO^t/(FeO^t+MgO)$; wt. %; from Frost et al., 2001);* ***d)*** *Shand index plot (fields from Maniar and Piccoli, 1989); ACNK=$Al_2O_3/(CaO+Na_2O+K_2O)$, ANK=$Al_2O_3/(Na_2O + K_2O)$, moles; vertical dashed line indicates ACNK=1.1, a key parameter discriminating S- and I-type granites (Chappell and White, 1974);* ***e)*** *Ab-An-Or ternary diagram (fields from Barker, 1979);* ***f)*** *plot of Zr/TiO_2 versus Nb/Y (after Pearce, 1996). Note: solid red reverse triangle indicates muscovite-biotite schist sampled from a shear zone cutting unit 1 granitoid.*

(e.g., Bruand et al., 2020). More interestingly, unit 1 granitoid rocks display a range of lithologies from tonalite, trondhjemite, granodiorite (TTG) to granite (Figure 28e), typical of Archean TTG suites (Barker, 1979). This is also consistent with the observation on the TAS (total alkalis vs. silica) diagram (Figure 28a) that unit 1 granitoid rocks span a wide compositional space.

Unit 1 granitoid rocks display a range of values from 0.01 to 3.48 on the Rittmann Serial Index ($\sigma=[Na_2O+K_2O]^2/[SiO_2-43]$; Table 6_2 of DRI2020024; Rittmann, 1973), suggesting that they are calcic to calcalkaline (Yang, 2007). This is consistent with the classification results obtained in Figure 28b and is also confirmed by variation in Nb/Y ratios of the unit 1 granitoids that are consistently less than 0.7 on the Zr/TiO_2 versus Nb/Y plot (Figure 28f), typical of subalkaline affinity (Pearce, 1996). In addition, unit 1 granitoid rocks exhibit varied Zr/TiO_2 ratios that are mostly higher than 0.05, reflecting relatively evolved characteristics (Figure 28f), although sample 111-12-28B01 falls into the field of unevolved gabbro.

Trace-element geochemistry

Unit 1 granitoid rocks have low Rb (up to 180 ppm), relatively high Sr (up to 196 ppm) and Ba (up to 5080 ppm) contents, with low Rb/Sr ratios that are mostly <1 (Table 6_2 of DRI2020024), suggesting limited magmatic fractionation after separation from the source magma. However, unit 1 granitoids display variable K/Rb ratios that range from 116 to 563 but are mostly higher than 200, indicating that their sources were unevolved to moderately evolved (cf. Blevin, 2004). This is consistent with low to moderately abundant transitional elements (e.g., Cr, Co, Ni) in unit 1 granitoids.

Chondrite-normalized rare-earth element (REE) patterns of unit 1 granitoid rocks show moderately to strongly light-REE–enriched and heavy-REE–depleted profiles, mostly with small negative Eu anomalies. as indicated by the Eu/Eu* values of 0.33–0.94. Some granite samples, however, do not have Eu anomalies (Eu/Eu*=0.97–1.00; Figure 29a). The abundances of REE vary remarkably, ranging from a few up to 650 times

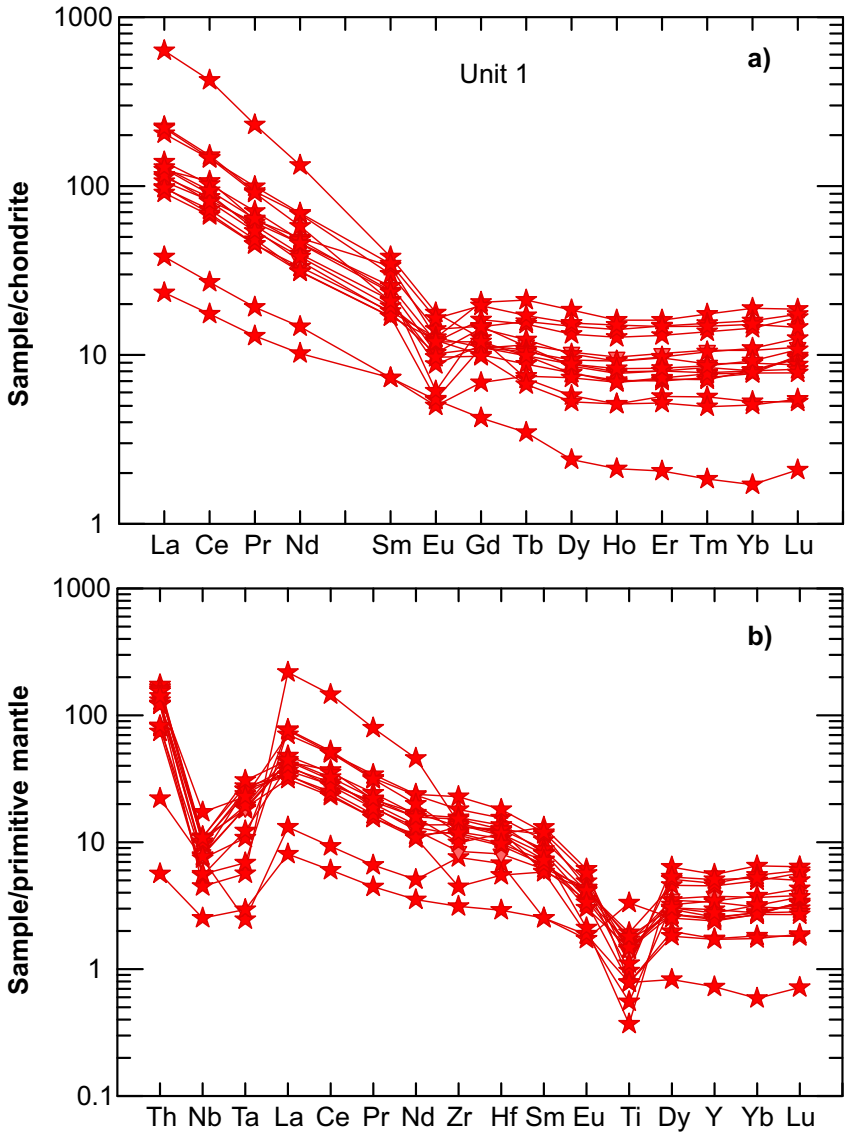

Figure 29: *Trace-element profiles for unit 1 granitoid rocks from the Cat Creek–Euclid Lake area:* ***a)*** *chondrite-normalized rare-earth–element plot;* ***b)*** *primitive-mantle–normalized extended trace-element plot (normalizing values from Sun and McDonough, 1989).*

the chondrite values. Also, LREE and HREE are moderately to strongly fractionated, manifested by chrondrite-normalized ratios of $(La/Yb)_N$ ranging from 3 to 120. Intra-HREE fractionation, however, is relatively weak, with $(Gd/Yb)_N$ ratios ranging from 0.9 to 2.5 (Table 6_2 of DRI2020024).

Primitive-mantle–normalized extended trace-element profiles of unit 1 granitoid rocks show that they are enriched in incompatible elements, with pronounced negative Nb, Ta and Ti anomalies (Figure 29b). This is a typical arc signature, suggesting that unit 1 granitoids may have been formed in an arc-type setting (e.g., Rollinson, 1993; Pearce and Peate, 1995; Yang et al., 2008). On the Pearce et al. (1984) discrimination diagram, all samples from unit 1 granitoids fall in the field of volcanic granitoids (Figure 30a). On the plot of log τ versus log σ (not shown), all samples from unit 1 granitoids fall in the field of orogenic belts and island arcs. Note that $\tau=(Al_2O_3–Na_2O)/TiO_2$ (Gottini, 1968) and ranges from 28.86 to 90.05 (Table 6_2 of DRI2020024), consistent with characteristics of granitoids from unevolved to moderately evolved source(s) suggested by the moderate to high K/Rb ratios described above.

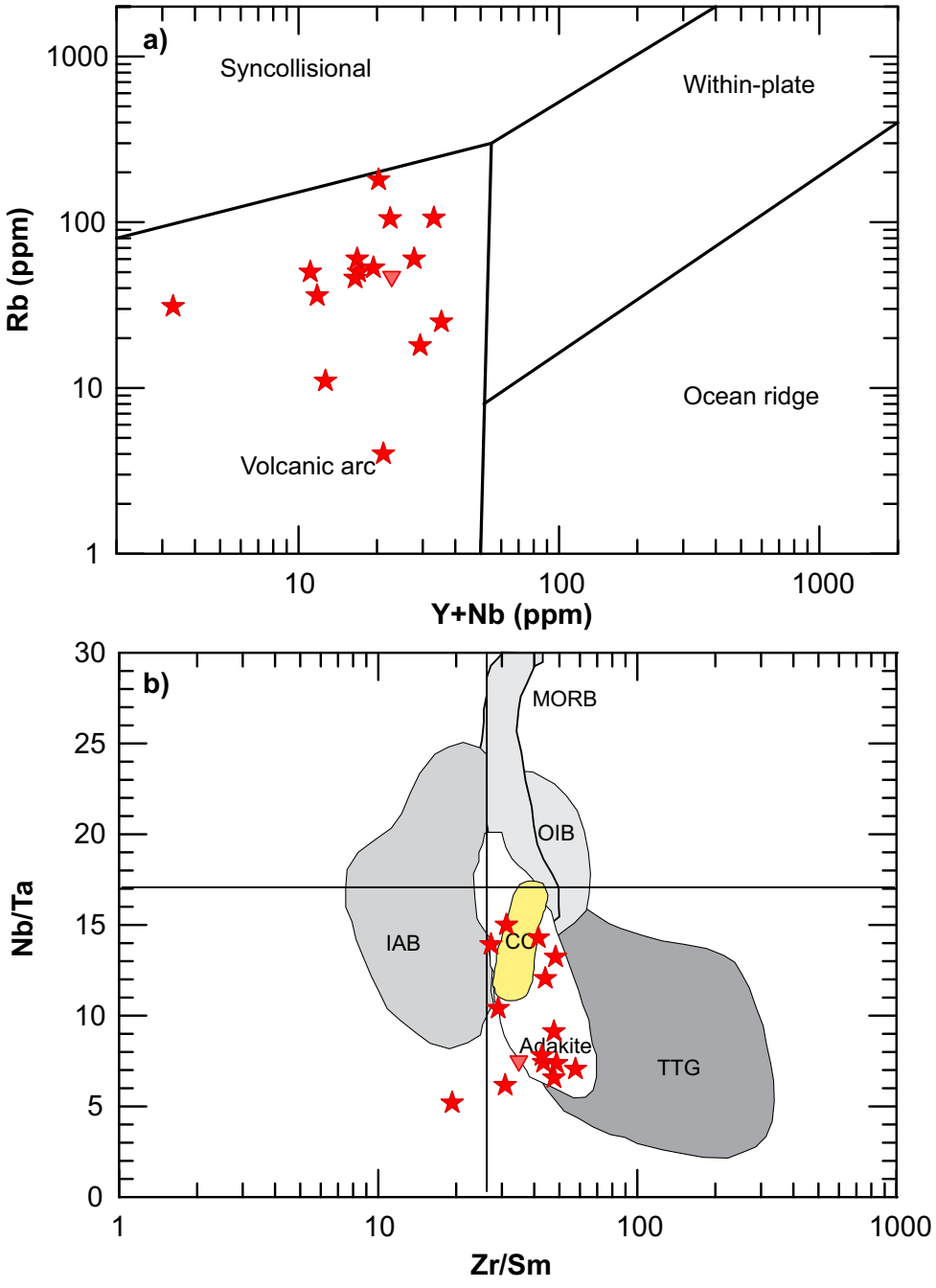

Figure 30: *Tectonomagmatic discrimination diagram for unit 1 granitoid rocks from the Cat Creek–Euclid Lake area:* ***a)*** *plot of (Y+Nb) versus Rb (after Pearce et al., 1984);* ***b)*** *plot of Zr/Sm versus Nb/Tb (after Foley et al., 2002); primitive-mantle Na/Ta and Zr/Sm ratios are 17.4 and 25.2, respectively (Sun and McDonough, 1989). Abbreviations: CC, continental crust; IAB, island-arc basalt; MORB, mid-ocean–ridge basalt; OIB, ocean-island basalt; TTG, tonalite-granodiorite-trondhjemite.*

On the plot of Nb/Ta versus Zr/Sm (Figure 30b), unit 1 granitoid rocks display relatively low Nb/Ta ratios (<17.4) and high Zr/Sm ratios (>25.2) when compared to primitive mantle, MORB, ocean-island basalt and island-arc basalt, and are more similar to Archean TTG and/or adakite (Foley et al., 2002). This suggests that the granitoids from unit 1 may have been derived from partial melting of amphibolite (Foley et al., 2002) in a volcanic-arc environment. However, on the plot of Sr/Y versus La/Yb, unit 1 granitoid rocks can be subdivided into two groups: one with Sr/Y<10 and La/Yb<20 located in the non-TTG field, and the other with 50>Sr/Y>10 and La/Yb>20, located in the low-pressure TTG field (Figure 31; Moyen and Martin, 2012). Relatively low La/Yb and Sr/Y ratios in the granitoids can be explained by plagioclase fractionation in a closed system, which consequently leads to moderately negative Eu anomalies (Figure 29a). Alternatively, partial melting of the source region may have taken place at relatively shallow crustal levels and involving plenty of plagioclase (e.g., juvenile mafic crustal material).

It is noteworthy that TTG can be subdivided into low, medium and high subtypes in terms of heavy REE (HREE) contents. These subtypes correspond to high-, medium- and low-pressure partial melting, respectively, of the source region (Moyen, 2011; Moyen and Martin, 2012). The TTG subtype with low HREE concentration (Moyen, 2011), low Nb and Ta, and high Sr displays a geochemical signature of modern adakite, requiring the TTG melt to be in equilibrium with a significant amount of garnet and some rutile in a source region where plagioclase is absent or unstable under high pressure (>15 kb). The absence of plagioclase in the source region (residue), where it is unstable because of P–T conditions, or the absence of physical separation of plagioclase from the ascending magma in a closed system (e.g., shallow magma chamber; Prouteau et al., 1999) is required to preserve the geochemical characteristics of adakite-type melts inherited from putative slab melting (Defant and Drummond, 1990; Drummond and Defant, 1990). In contrast, the 'low-pressure' TTG group (Moyen, 2011) shows high HREE, Nb and Ta but lower Sr, consistent with the presence of plagioclase in the source region (residues) but a smaller amount of garnet and no rutile. The 'medium pressure' group falls in between. Plagioclase, rutile and garnet are strongly pressure dependent, so the three subtypes of TTG can be interpreted in terms of depth of partial melting that implicitly takes place in an arc environment linked to plate subduction.

Unit 1 granitoid rocks are comparable to the low-pressure subtype of TTG proposed by Moyen and Martin (2012), which may exhibit the geochemical characteristics of non-TTG owing to differentiation (Figure 31), likely involving plagioclase (Figure 29) in a closed system. In addition, these granitoids generally display calcic, magnesian and weakly to moderately peraluminous affinities. These features, together with constraints from trace-element geochemistry, suggest that unit 1 granitoids may have been generated by partial melting of

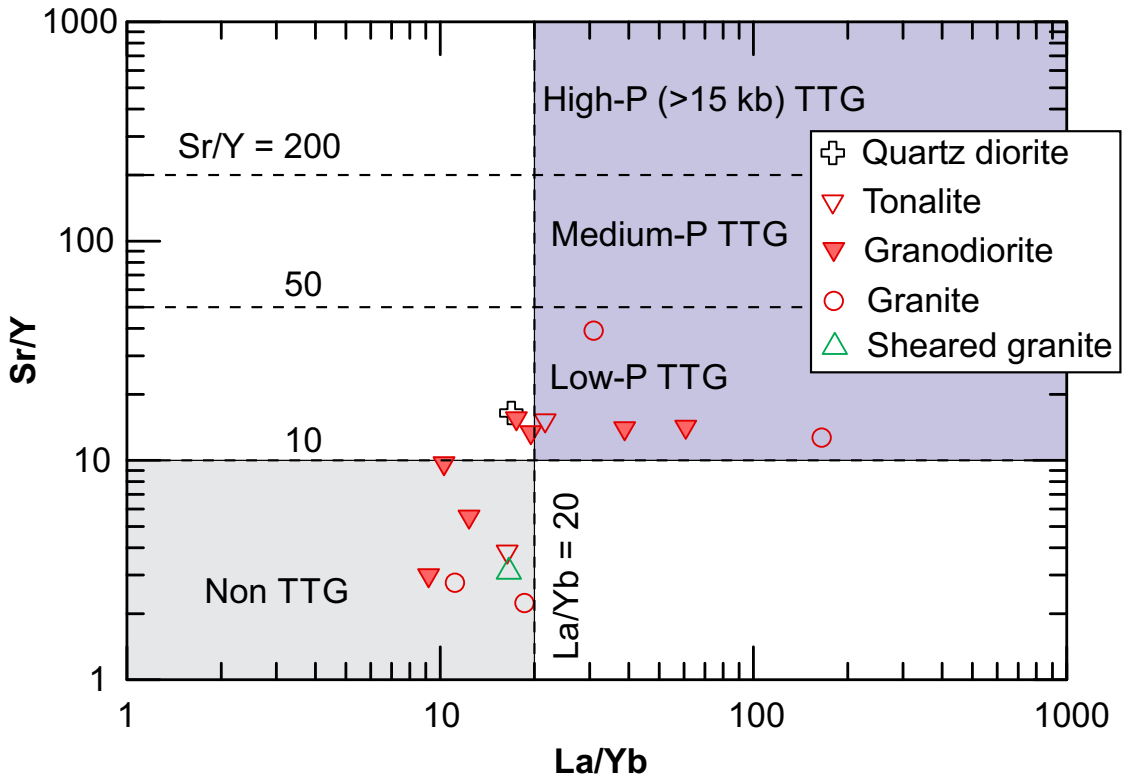

Figure 31: *Plot of La/Yb versus Sr/Y for unit 1 granitoid rocks from the Cat Creek–Euclid Lake area. The boundary between Sr/Y and La/Yb ratios used to define TTG and subtypes is from Moyen and Martin (2012). Abbreviation: TTG, tonalite-trondhjemite-granodiorite.*

amphibolites derived from mafic protoliths at relatively low pressure in an arc-like setting (e.g., Windley and Garde, 2009; Bruand et al., 2020), together constituting part of a newly formed continental basement in the BRGB.

Unit 2: MORB-type basalt and synvolcanic gabbro

Major- and trace-element characteristics

Unit 2 MORB-type basalt and related synvolcanic gabbro are dominated by basaltic (or basic) composition according to the TAS classification (Le Bas et al., 1986), although few samples fall into the fields of basaltic andesite, basaltic trachyandesite and picrobasalt (Figure 32a). These basalts (unit 2) and gabbros (subunit 2a) display a normal and narrow range of SiO_2 (46.01–50.83 wt. %) and MgO (5.67–8.13 wt. %), but a large range of total alkalis (0.25–3.20 wt. %; Table 6; Table 6_2 of DRI2020024); the increase in SiO_2 with increasing total alkalis is consistent with a common compositional trend of magmatic fractionation (e.g., Winter, 2010). Sample 111-14-12B01 (Table 6_2 of DRI2020024), which was collected from the contact

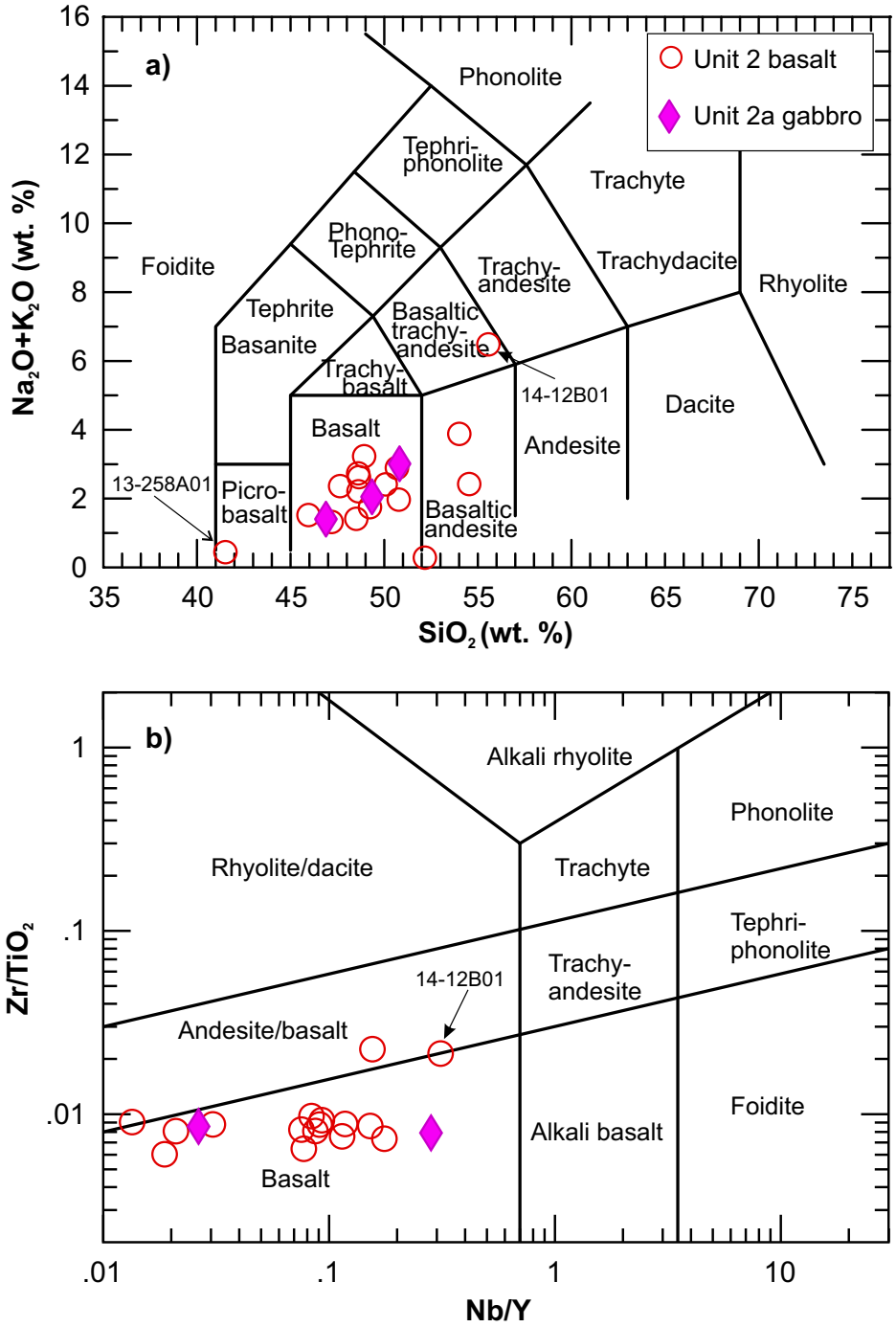

Figure 32: *Geochemical classification of unit 2 MORB-type basalt and synvolcanic gabbro from the Cat Creek–Euclid Lake area:* ***a)*** *total alkalis (Na_2O+K_2O; wt. %) versus SiO_2 (wt. %) diagram (TAS; after Le Bas et al., 1986);* ***b)*** *plot of Zr/TiO_2 versus Nb/Y (after Pearce, 1996). Note that the prefix '111' has been omitted from sample 111-14-12B01; the same practice may be applied to other figures in this report.*

zone where the basalt intruded and fragmented the unit 1 basement granitoid rocks (Figure 4c), has abnormally high total alkalis and is therefore thought to have been severely contaminated by the basement granitoids. Consequently, it is enriched in Na_2O+K_2O up to 6.45 wt. % and SiO_2 up to 55.62 wt. % (Figure 32a; Table 6_2 of DRI2020024). Another outlier is sample 111-13-258A01, which displays ultrabasic composition (Figure 32a) with low SiO_2 (41.58 wt. %) and total alkalis (0.41 wt. %) but high MgO (12.94 wt. %), and can be classified as picrobasalt based on the IUGS Subcommission nomenclature of Le Bas et al. (1986). Three samples plot in the field of basaltic andesite, having a relatively narrow range in SiO_2 but a large range in total alkalis (Figure 32a).

On the plot of high-field-strength–element (HFSE) ratios, unit 2 basalt and subunit 2a gabbro samples have consistently low Zr/TiO_2 but varied Nb/Y ratios and are mainly within the field of basalt (Figure 32b); only one sample plots in the andesite/basalt field and two straddle the border between the basalt and andesite/basalt fields. These generally agree with the results of discrimination based on the TAS diagram (Figure 32a). Low and varied Nb/Y ratios (0.01–0.34) of all the unit 2 mafic rocks suggest that they are subalkaline (Pearce, 1996), which is also supported by, and consistent with, the result based on the classification scheme of Irvine and Baragar (1971).

The unit 2 subalkaline mafic rocks are dominantly tholeiitic, but basalt sample 111-14-12B01, which is strongly contaminated by unit 1 granitoids, is calcalkaline in terms of FeO^t/MgO versus SiO_2 (wt. %; Figure 33a). Similarly, using HFSE ratios (i.e., Th/Yb versus Zr/Y; see Ross and Bédard, 2009) to discriminate

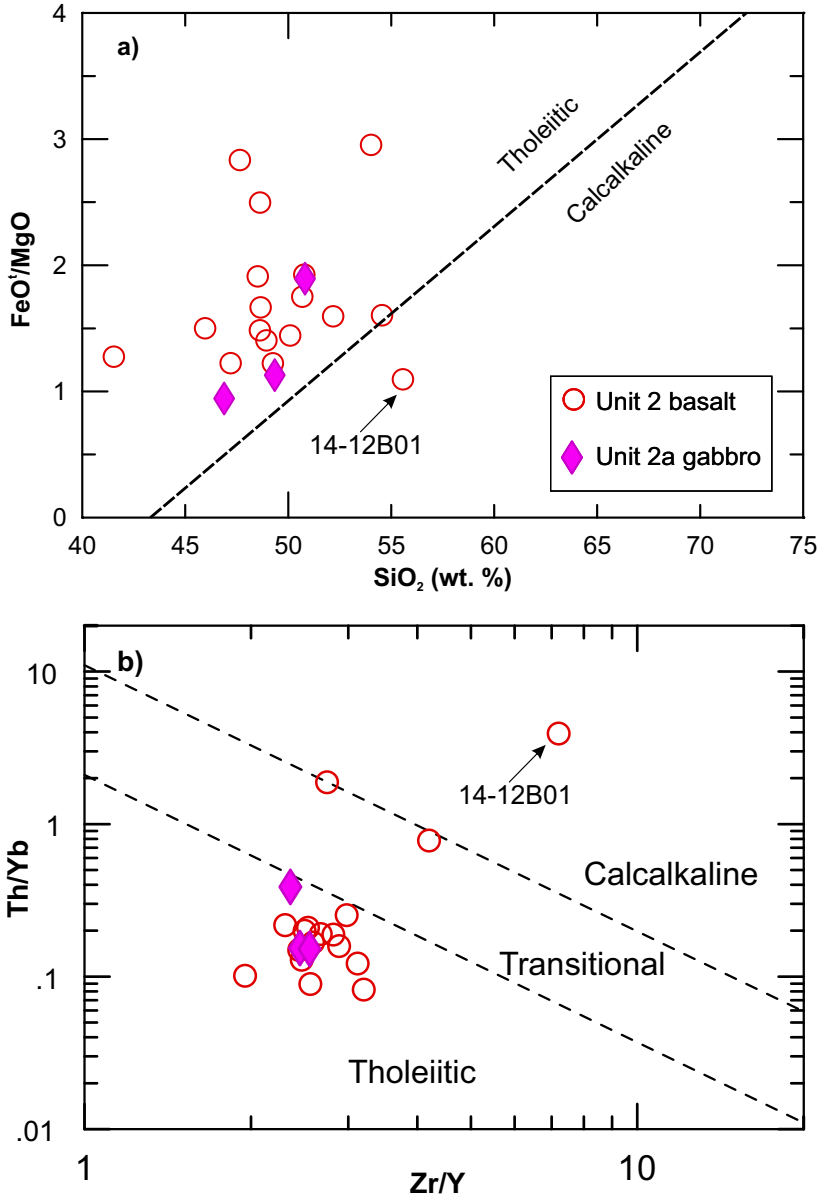

Figure 33: *Discrimination diagrams for whole-rock samples of unit 2 MORB-type basalt and synvolcanic gabbro from the Cat Creek–Euclid Lake area:* ***a)*** *FeO^t/MgO versus SiO_2 (wt. %; boundary between tholeiitic and calcalkaline series from Miyashiro, 1974);* ***b)*** *Th/Yb versus Zr/Y (boundaries between tholeiitic, transitional and calcalkaline from Ross and Bédard, 2009).*

magmatic affinities indicates that the unit 2 rocks are predominantly tholeiitic (Figure 33b). However, sample 111-14-12B01 plots in the calcalkaline series and two other samples plot on the boundary between the calcalkaline and transitional series due to elevated Th/Yb ratios that are interpreted to be the result of crustal contamination and/or input of melts from slab subduction (e.g., Pearce, 1983, 2008; Pearce and Peate, 1995).

More importantly, unit 2 mafic rocks could be divided into two subgroups in terms of TiO_2 concentration: high (>1.5 wt. %) and low (<1.5 wt. %) TiO_2 mafic rocks. On the plot of TiO_2 (wt. %) versus Mg#, there is a compositional gap between these two subgroups (Figure 34a). Within the low TiO_2 subgroup, the TiO_2 contents decrease with increasing Mg#, consistent with the compositional trend produced by partial melting of the upwelling mantle at different depths (i.e., deep melting forms basaltic melt with high TiO_2 and low Mg#, whereas shallow melting creates melt with low TiO_2 and high Mg#; Pearce, 2008). Alternatively, the degree of the mantle partial melting may have been different for the two subgroups of magmas. The most contaminated sample (111-14-12B01) exhibits a lower Mg#, off the differentiation trend, although its TiO_2 remains unaffected by crustal contamination (Figure 34a). This suggests that the melting depth could have played a major part

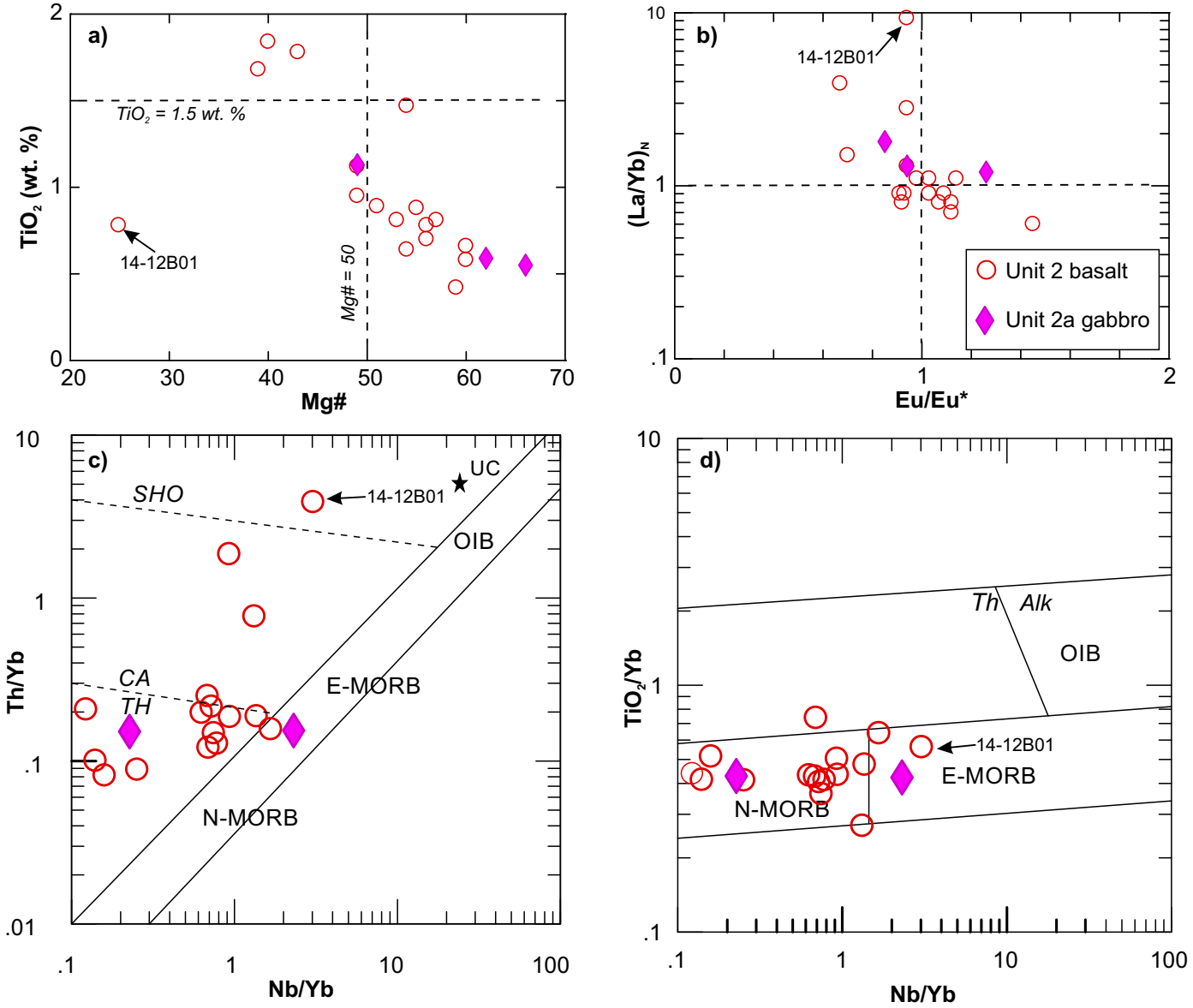

Figure 34: *Geochemical plots for rocks of unit 2 MORB-type basalt and subvolcanic gabbro from the Cat Creek–Euclid Lake area:* ***a)*** *TiO_2 (wt. %) versus Mg# (Mg#=molar MgO/[MgO+FeO^t]); note that two subgroups of mafic rocks are evident (i.e., high TiO_2 and low TiO_2);* ***b)*** *$(La/Yb)_N$ versus Eu/Eu*; see strongly contaminated basalt, as indicated by sample 14-12B01, with a considerably elevated chondrite-normalized $(La/Yb)_N$ value of 9.3 and slightly negative Eu anomaly; chondrite-normalizing values from Sun and McDonough (1989);* ***c)*** *Th/Yb versus Nb/Yb, and* ***d)*** *TiO_2/Yb versus Nb/Yb. Abbreviations: alk, alkaline; CA, calcalkaline; E-MORB, enriched mid-ocean–ridge basalt; N-MORB, normal mid-ocean–ridge basalt (mantle array for oceanic basalts from Pearce, 2008); OIB, ocean-island basalt; SHO, shoshonitic; Th, tholeiitic; UC, upper continental crust, indicated by solid black star (data from Taylor and McLennan, 1985).*

in controlling the composition of mafic melts (rocks). Furthermore, despite the effect of crustal contamination manifested by the decrease in Mg# and increase in $(La/Yb)_N$, most of the samples display relatively constant Eu/Eu* values (within 1.0 ±0.2; Figure 34b). However, a few samples (i.e., three basalts and one gabbro) display Eu/Eu* values considerably beyond this threshold, suggesting that plagioclase may have occurred either as a fractionating phase or as a cumulus phase (see 'REE patterns' section).

The presence of old sialic crust could be reflected by the composition of Archean supracrustal mafic volcanics (e.g., Whyman and Kerrich, 2010). The decrease in Mg# and increase in $(La/Yb)_N$ and Th/Yb ratios (Figure 34a–c) suggest that these rocks may have been contaminated (e.g., sample 111-14-12B01) when the mafic magmas ascended and percolated through the basement, as represented by unit 1 granitoids with similar Th/Yb ratios (~5.0) to that of the upper continental crust (4.9; Taylor and McLennan, 1985). Other samples that are less or not contaminated by crust display much lower $(La/Yb)_N$ (<1) and Th/Yb ratios but relatively higher Mg# (>50; Figure 34a–c). Crustal contamination would have likely changed magmatic affinities of the samples from tholeiitic to calcalkaline or even to shoshonitic (e.g., the most contaminated sample, 111-14-12B01; Figure 34c). However, most of the samples have low Zr/Y ratios (<3.0; Table 6_2 of DRI2020024), identical to those from the Northern MORB-type formation of Gilbert et al. (2008), which was likely emplaced in an oceanic-arc to back-arc setting (e.g., Pearce, 1983, 2008; Gorton and Schandl, 2000). Again, the most contaminated sample (111-14-12B01) has high Zr/Y (7.2) and Nb/Yb (3.1) ratios, ruling out derivation from an enriched mantle (e.g., enriched MORB; Fitton et al., 1997; Figure 34d).

Most of the unit 2 mafic rocks have constant TiO_2/Yb ratios (Figure 34d), regardless of whether or not they interacted with the crust (see 'REE patterns' section), suggesting that they may have been derived from partial melting at similar mantle levels. This may be evidence for fairly constant lithosphere thickness (e.g., Pearce, 2008). Therefore, it is suggested that the subgroupings of unit 2 mafic rocks based on TiO_2 concentrations (Figure 34a) are most likely due to differing degrees of partial melting of the mantle (i.e., the high-Ti melts formed by a relatively low degree of partial melting).

REE patterns

Chondrite-normalized REE patterns of unit 2 mafic rocks display fairly flat LREE-depleted and -enriched patterns (Figure 35), except for the most contaminated sample (111-14-12B01). As such, these rocks can be divided into two subgroups on the basis of chondrite-normalized $(La/Yb)_N$ ratios: LREE-depleted patterns with $(La/Yb)_N$ ratios <1 and LREE-enriched patterns with $(La/Yb)_N$ ratios >1. Both subgroups have no slightly positive or negative Eu anomalies. The most crustally contaminated sample (111-14-12B01) has the most enriched LREE pattern, with a $(La/Yb)_N$ ratio of 9.3 (Figures 34b, 35b). All subunit 2a gabbros (n=3) fall into the LREE-enriched subgroup with $(La/Yb)_N$ values of 1.2–1.8, suggesting that they are only slightly enriched in LREE. There appears to be a negative correlation between the ratios of $(La/Yb)_N$ and Eu/Eu* (Figure 34b), which is likely due to fractional crystallization of plagioclase under relatively reduced conditions (cf., Rollinson, 1993). The most contaminated sample (111-14-12B01) has only a slightly negative Eu anomaly, as indicated by its Eu/Eu* value of 0.94. Also, it is noted that $(Gd/Yb)_N$ ratios remain relatively constant between 0.9 and 1.3 (Table 6; Table 6_2 of DRI2020024), except for sample 111-14-12B01, which has a ratio of 1.6 as a result of strong crustal contamination. A plot of La/Sm ratio against La (ppm) for unit 2 mafic rocks (not shown) displays a linear relationship, suggesting that these rocks may have been formed by batch partial melting of the mantle (e.g., Allègre and Minster, 1978; Rollinson, 1993).

Unit 2 mafic rocks are generally identical in terms of their REE patterns to those of the Northern MORB-type formation proposed by Gilbert et al. (2008) in the southern limb of the BRGB. Other characteristic parameters of lithogeochemistry also point to their similarities (see below). Therefore, unit 2 appears to correlate well with the Northern MORB-type formation based on lithogeochemistry.

Extended trace-element patterns

The primitive-mantle–normalized extended trace-element patterns for unit 2 mafic rocks in Figure 36 can be used to divide this unit into two subgroups in terms of $(La/Yb)_N$ ratios (i.e., a depleted and an enriched pattern). The depleted subgroup of unit 2 mafic rocks displays fairly flat patterns, with trace-element abundances 2–9 times higher (Figure 36a; Table 6; Table 6_2 of DRI2020024) than the primitive mantle of Sun and McDonough (1989), whereas the enriched subgroup has an enriched pattern, with trace-element concentrations 2–65 times higher than the primitive mantle (Figure 36b). Both depleted and enriched trace-element profiles display notable to significant negative Nb, Ta and Ti anomalies, typical of oceanic island-arc to back-arc volcanic rocks (Pearce and Peate, 1995; Pearce, 2008; Anderson, 2013). Thorium is strongly enriched in the enriched subgroup, particularly in the most contaminated sample (111-14-12B01; Figure 36b). Generally, these trace-element patterns are comparable to those of the most primitive arc mafic rocks of the Northern MORB-type formation (Gilbert et al., 2008) in the southern limb of the BRGB (e.g., Polat and Kerrich, 2001; Whyman and Kerrich, 2010; Sotiriou et al., 2019, 2020).

However, a gabbro sample (111-12-726A01) in subunit 2a shows an abnormally large positive Ta anomaly, in addition to a slightly positive Nb anomaly (Figure 36b). This distinct feature contrasts with other samples in the enriched subgroup

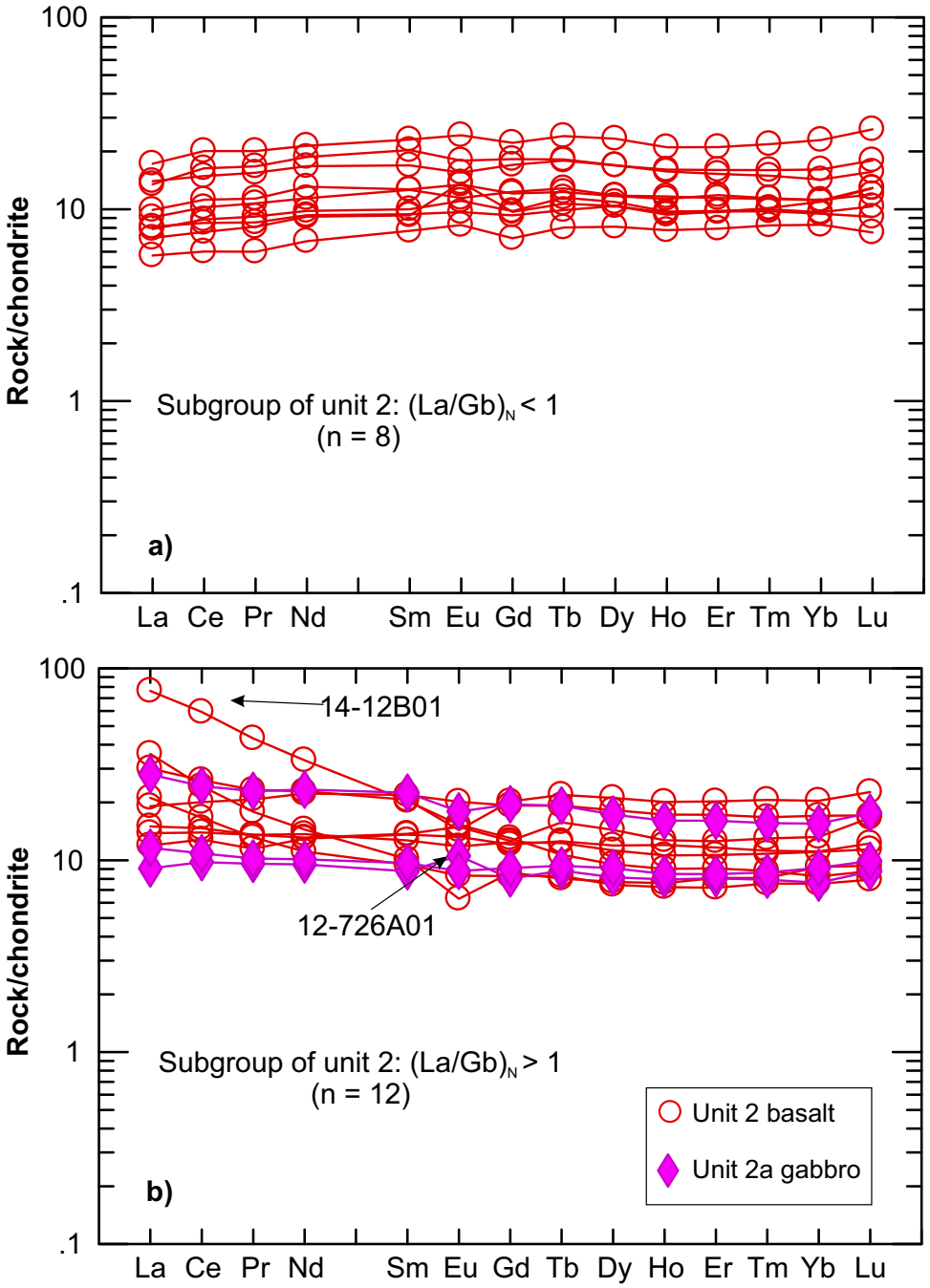

Figure 35: *Trace-element profiles for unit 2 MORB-type basalt and synvolcanic gabbro from the Cat Creek–Euclid Lake area:* ***a)*** *LREE-depleted pattern with* $(La/Yb)_N$ *ratios < 1;* ***b)*** *LREE-enriched pattern with* $(La/Yb)_N$ *ratios > 1. Note that* $(La/Yb)_N$ *is a chondrite-normalized ratio. Normalizing values from Sun and McDonough (1989).*

and may indicate the presence of a cumulus Ta (Nb)–bearing mineral (e.g., rutile, ilmenite) in the sample. In addition, this gabbro sample also has a slightly positive Eu anomaly (see Figure 35b), indicative of the presence of cumulus plagioclase.

In summary, unit 2 MORB-type basalt and synvolcanic gabbro are mainly tholeiitic, dominated chemically by basaltic composition, and can be divided into two subgroups: high TiO_2 (>1.5 wt. %)–low Mg# (<50) and low TiO_2 (<1.0 wt. %)–high Mg# (>50), which appear to be unrelated, respectively, to LREE-enriched ($[La/Yb]_N$ > 1.0) and LREE-depleted ($[La/Yb]_N$ < 1.0) subgroupings. This geochemical fingerprint is consistent with the observation that these mafic rocks of unit 2 could have been affected by crustal contamination, requiring the presence of crustal basement in the Bird River belt (e.g., unit 1 granitoid rocks in the Maskwa Lake batholith I). The unit 2 rocks were likely formed by partial melting of slightly depleted mantle (see 'Sm-Nd isotope systematics' section), and some must have been affected by crustal contamination to some extent during emplacement. Therefore, this unit is interpreted to have been emplaced in an oceanic-arc to back-arc setting adjacent to a

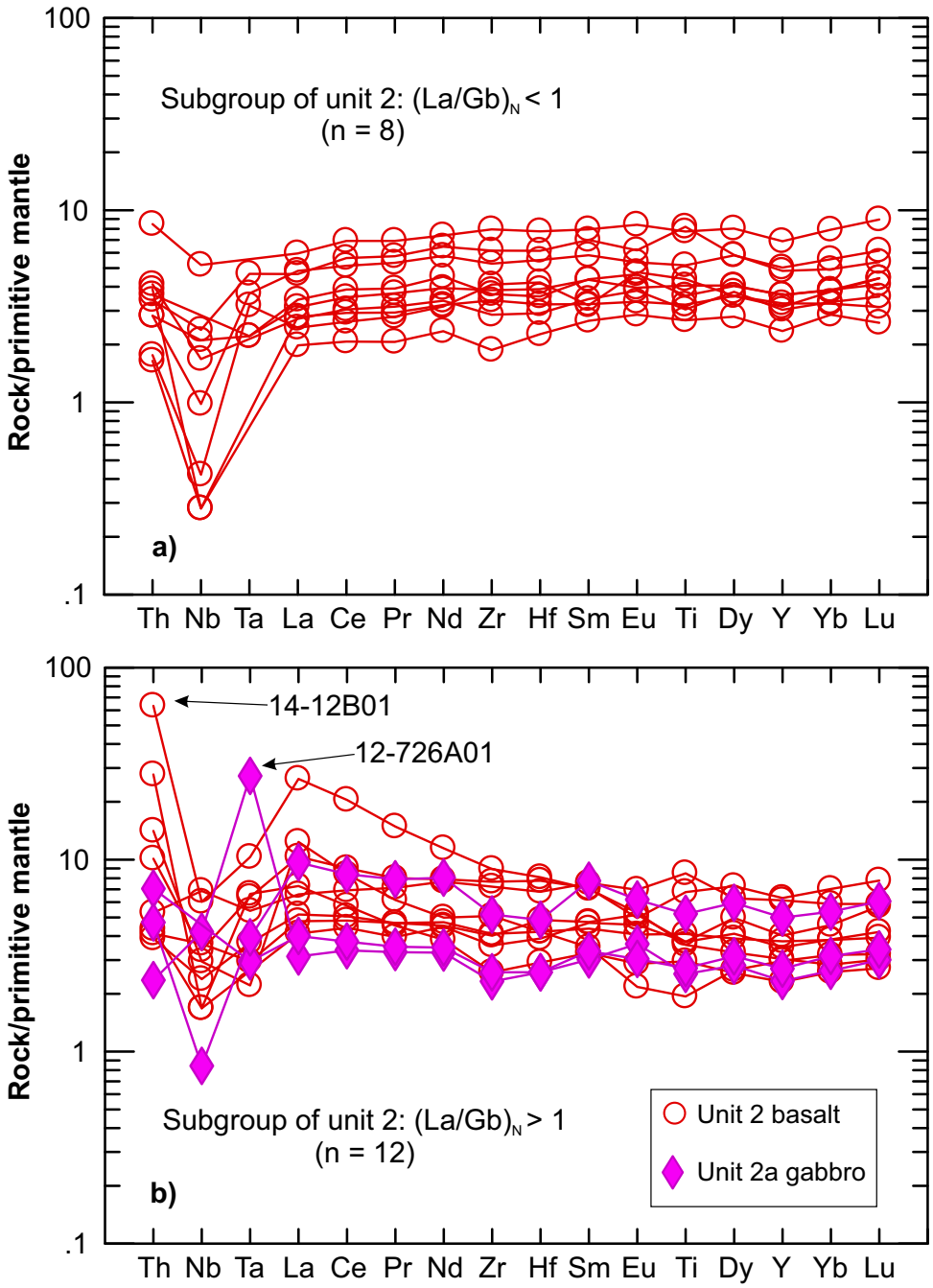

Figure 36: *Primitive-mantle–normalized, extended trace-element distribution patterns for unit 2 MORB-type basalt and synvolcanic gabbro from the Cat Creek–Euclid Lake area:* ***a)*** *depleted pattern with $(La/Yb)_N$ ratios < 1;* ***b)*** *enriched pattern with $(La/Yb)_N$ ratios > 1. Normalizing values from Sun and McDonough (1989).*

continental margin (e.g., Yang et al., 2012). In addition, unit 2 mafic rocks are geochemically comparable to the Northern MORB-type formation of Gilbert et al. (2008) in the southern limb of the BRGB, both representing remnants of a magmatic, arc-related supracrustal sequence.

Units 3–7: Mayville intrusion

The geochemical characteristics of the Mayville intrusion were discussed in Yang et al. (2011, 2012) based on previously published data (Peck et al., 2000) and the data acquired during the course of this bedrock mapping. The major conclusion was that the Mayville intrusion may have been formed from multiple injections of tholeiitic magmas derived from partial melting of the lithospheric mantle. These magmas were interpreted to have undergone assimilation and fractional crystallization (AFC) processes during emplacement in an extensional setting characterized by a relatively thin crust (Yang et al., 2011, 2012). In this section, additional whole-rock geochemical data (Table 6; Table 6_2 of DRI2020024) are presented to

help assess the petrogenesis and geodynamic setting of the Mayville intrusion in terms of field relationships established by the bedrock mapping.

Classification

Based on the TAS diagram, the Mayville intrusion is composed dominantly of gabbroic rocks, although a few samples from units 4, 6, and 7 extend to ultrabasic and dioritic varieties (Figure 37a). All samples have relatively low total alkali (Na_2O+K_2O) contents (Table 6; for details, see Table 6_2 of DRI2020024) and can be attributed to the subalkaline series defined by Irvine and Baragar (1971). There is a general trend of increasing total alkali content with increasing SiO_2, except that the samples from unit 3 show a negative correlation.

Application of the cation normative plagioclase-orthopyroxene-clinopyroxene ternary classification plot proposed by Streckeisen (1976) indicates that most of the unit 3 samples

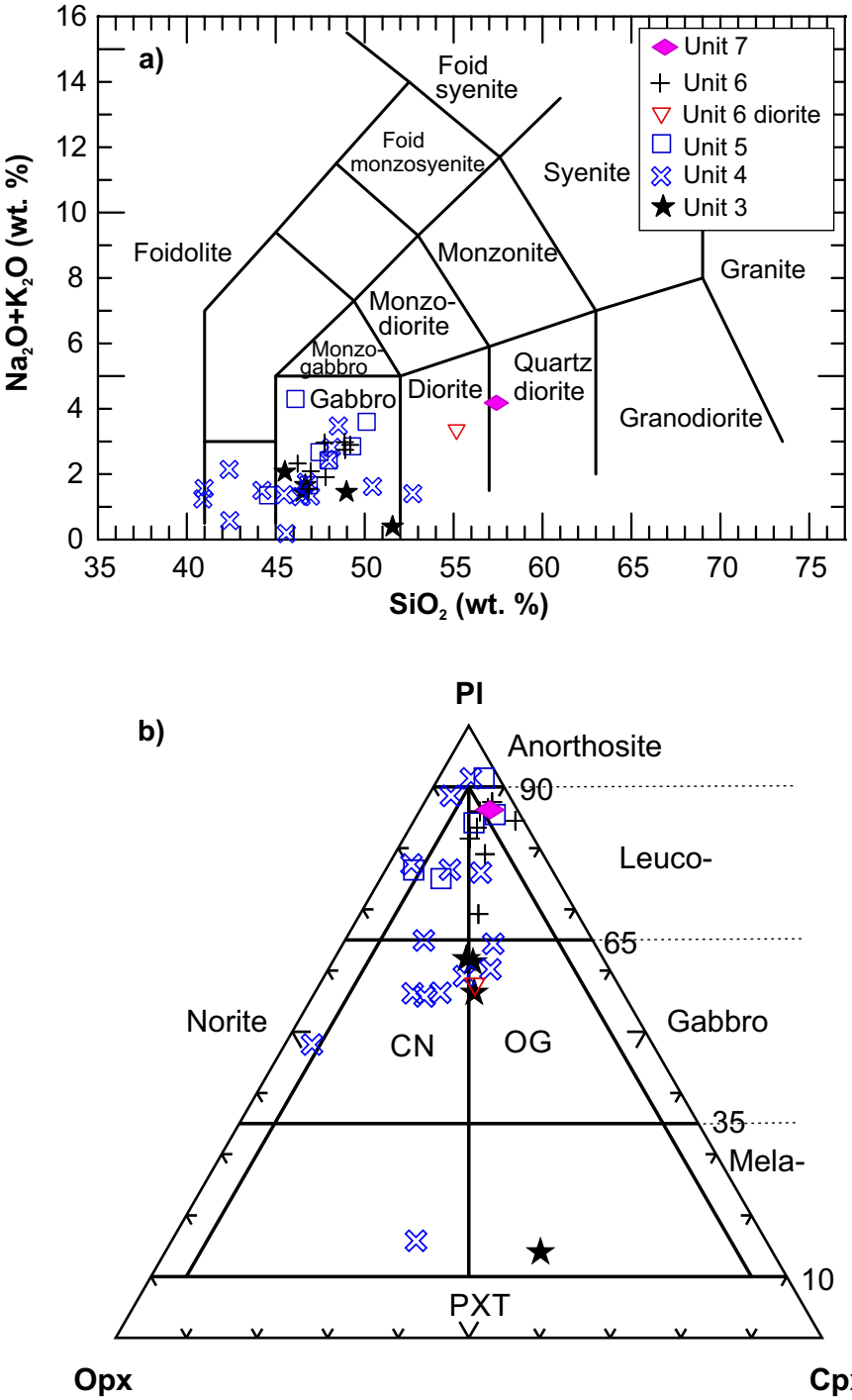

Figure 37: *Chemical classification of the Mayville intrusion (units 3–7):* ***a)*** *total alkalis (Na_2O+K_2O wt. %) versus silica (SiO_2 wt. %) diagram (TAS; after Middlemost, 1994);* ***b)*** *cation-normative Pl-Cpx-Opx ternary plot (modified from Streckeisen, 1976). Abbreviations: CN, clinopyroxene norite; Cpx, clinopyroxene; OG, orthopyroxene gabbro; Opx, orthopyroxene; Pl, plagioclase; PXT, pyroxenite.*

are normal gabbronorite and one is an orthopyroxene melagabbronorite (Figure 37b). In addition, unit 4 samples span from gabbronorite and leucogabbronorite to anorthosite and orthopyroxene melagabbronorite, consistent with the field occurrences of heterolithic breccia formed by multiple injections of mafic to ultramafic magmas (Yang et al., 2011, 2012). Chemically, unit 5 consists of leuconorite, leucogabbronorite and anorthosite, whereas unit 6 comprises leucogabbronorite and leucogabbro (Figure 37b). Unit 7 is leucogabbro, although it falls in the field of quartz diorite on the TAS diagram.

All rocks of units 3–7 of the Mayville intrusion are subalkaline in magmatic affinity and dominantly tholeiitic, although some fall in the calcalkaline field (Figure 38a, b). Unit 7 gabbro has a high FeO^t/MgO ratio of 8.5, which places it outside the plot area (Figure 38a) due to magmatic differentiation, as suggested by Miyashiro (1974), but it is tholeiitic based

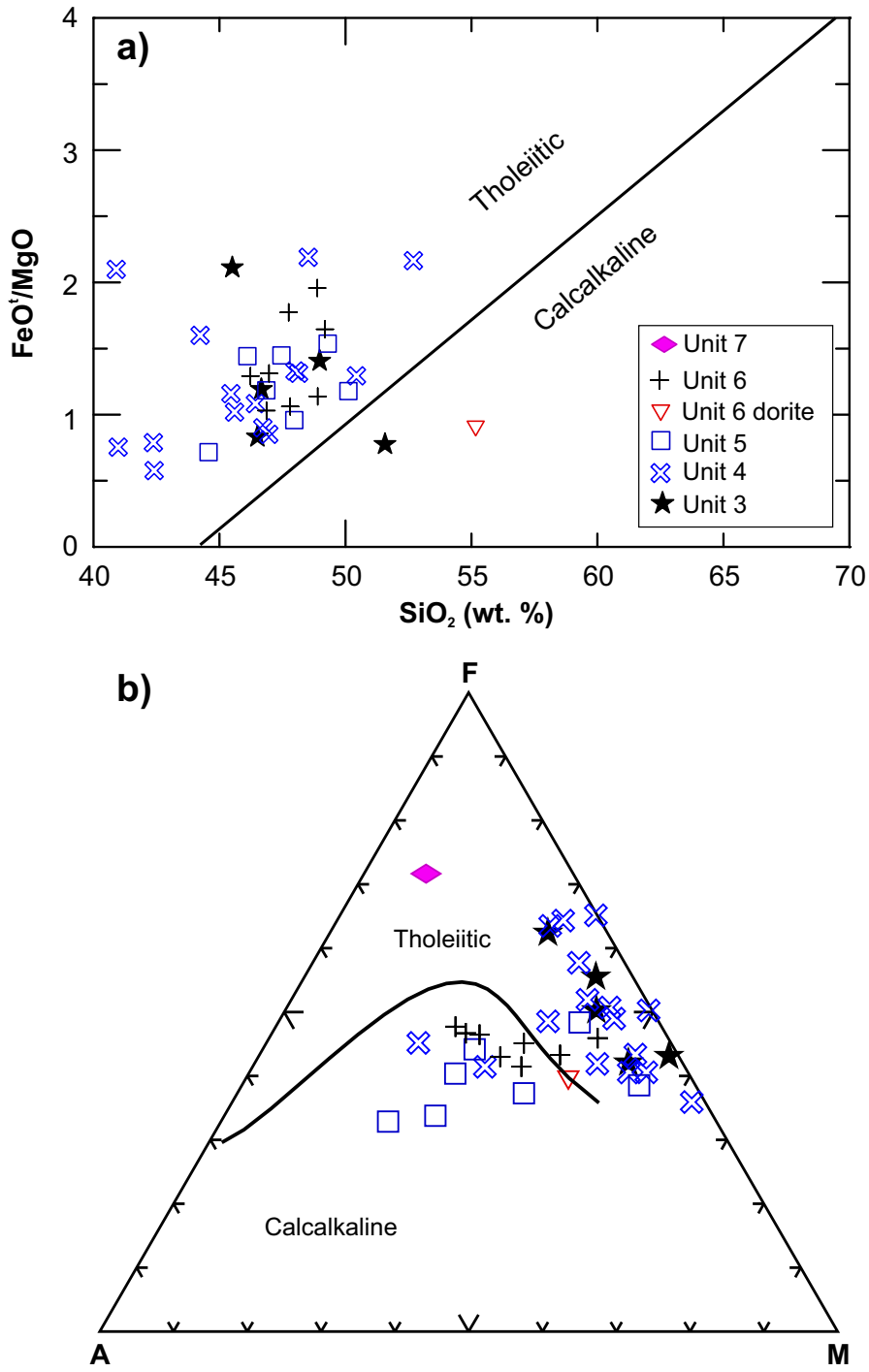

Figure 38: *Geochemical discrimination diagrams for rocks of the Mayville intrusion (units 3–7):* ***a)*** *FeO^t/MgO versus SiO_2 (wt. %; boundary between tholeiitic and calcalkaline rock series from Miyashiro, 1974);* ***b)*** *AFM diagram, showing the division of tholeiitic and calcalkaline series (after Irvine and Baragar, 1971). Abbreviations: A, Na_2O+K_2O; F, FeO^t, (total Fe as FeO); M, MgO. All values in wt. %.*

on the discrimination factor. Samples from unit 3, together with a large part of the samples from units 4 and 7, align parallel to the MgO-FeO^t side of the AFM diagram (Figure 38b), consistent with the common trend of tholeiitic magmas that evolved under relatively reduced condition (e.g., Miyashiro, 1974; Yang et al., 2011; Sotiriou et al., 2020). However, some of the samples from units 4, 5 and 6 fall into the calcalkaline field (Figure 38b), which is interpreted as an effect of crustal contamination to some extent.

There is no doubt that the chemical composition of a magmatic rock, particularly of mafic–ultramafic composition, can be readily altered by hydrothermal processes, chemical weathering and/or metamorphism (e.g., Rollinson, 1993; Syme, 1998). In order to address this problem, Hattie et al. (2007) proposed a new Th versus Co discrimination diagram (Figure 39a). Most of the samples from the Mayville intrusion plot in the island-arc tholeiite (IAT) field on this diagram and vary from basaltic to dacitic in composition, as suggested by the decrease in Co concentration. This reflects a fractional crystallization process controlled by separation of sulphide minerals (e.g., pyrrhotite) from the residual tholeiitic magmas. Most samples have relatively low Th contents (<0.2 ppm) that increase with decreasing Co content, consistent with the process of magmatic fractionation. Three samples plot as calcalkaline and one sample (111-12-544A01) as high K, which is interpreted to be the result of crustal contamination (e.g., AFC process). Sample 111-12-544A01 was collected from a 5 m wide dike cutting a very coarse grained leucogabbro phase of unit 6, which is likely unrelated to the Mayville intrusion despite being spatially associated with the intrusion.

Whole-rock samples from the Mayville intrusion are dominantly tholeiitic based on the plot of Th/Yb versus Zr/Y ratios proposed by Ross and Bédard (2009), despite the presence of a few samples falling in the fields of transitional to calcalkaline series (Figure 39b). The outliers are likely attributed to the crustal contamination mentioned previously, leading to elevated Th contents. Notably, the Mayville intrusion exhibits a large range of Zr/Y ratios within a relatively narrow Th/Yb range (except for those affected by crustal contamination), strongly suggesting its derivation from partial melting of the upper mantle (i.e., a sub-arc lithospheric mantle). This interpretation is consistent with a positive correlation between these ratios (Figure 39b).

Mafic and ultramafic rocks of the Mayville intrusion are characterized by low Zr/TiO_2 and Nb/Y ratios (Table 6; for detail, see Table 6_2 of DRI2020024), typical for the subalkaline series (Figure 39c) and consistent with a magmatic-arc setting (Syme, 1998; Syme et al., 1999). Low ratios of Nb/Y, Zr/TiO_2 and Zr/P_2O_5 (the latter not shown) suggest the Mayville intrusion has a tholeiitic rather than calcalkaline petrogenetic affinity. These three ratios involving HFSE correlate positively with one another, although the data points are fairly scattered, indicating that magmatic evolution was associated with a distinct AFC trend, as described above (Yang et al., 2011). Only a few gabbroic samples plot outside the basalt field in Figure 39c, probably due to the effect of crustal contamination. Because the HFSE are fairly stable and would not be readily remobilized by metamorphism and alteration, the classification of the Mayville intrusion rocks described here is considered reliable and also consistent with the patterns in the AFM diagram (Figure 38b). Unit 3 rocks appear to have a positive correlation between the Zr/TiO_2 and Nb/Y ratios (Figure 39c), whereas they seem to have a negative correlation between the total alkalis and SiO_2 contents (Figure 37a). Such geochemical relationships are likely ascribed to one of two scenarios: 1) crustal contamination; or 2) the magma(s) being derived from a lower degree melting of the mantle source (e.g., Pearce, 2008). The authors of this study prefer the first scenario.

In summary, the parental magmas of the Mayville intrusion are mainly subalkaline and tholeiitic, and may have been contaminated by crustal material during emplacement into a magmatic-arc environment, consistent with the AFM, Th/Ta versus Yb, and Zr/TiO_2 versus Nb/Y discrimination diagrams (Irvine and Baragar, 1971; Pearce, 1996; Syme, 1998; Syme et al., 1999; Gorton and Schandl, 2000; Yang et al., 2011, 2012). Due to the presence of magmatic hornblende in the intrusion, Sotiriou et al. (2020) postulated that the parental magma was hydrous tholeiitic in composition, favourable for the generation of calcic plagioclase, as indicated in Archean anorthosite in magmatic-arc to back-arc settings.

REE patterns and extended trace-element profiles

Chondrite-normalized REE patterns and primitive-mantle–normalized extended trace-element profiles of rocks from units 3–7 of the Mayville intrusion are presented in Figure 40. Gabbronorite and clinopyroxene melagabbronoritic rocks of unit 3 display dominantly flat REE patterns with either slightly negative or positive Eu anomalies, except for pyroxenite sample 111-13-226A01, which shows an LREE-enriched pattern without a notable Eu anomaly (Figure 40a). Similarly, these rocks exhibit flat extended trace-element profiles, with either negative or positive Nb, Ta, Zr and Hf anomalies, and low but varied trace-element concentrations ranging from 0.3 to 10 times the primitive-mantle values (Figure 40b). These features are consistent with magmatic fractionation plus crustal assimilation (i.e., AFC process; Yang et al., 2011, 2012). Accumulation of plagioclase plus Fe-Ti (±Zr) oxides (e.g., ilmenite, rutile and baddeleyite?) can explain the fact that some of the samples display positive Nb, Ta, Zr and Hf anomalies.

Unit 4 rocks display relatively flat REE patterns similar to those of unit 3, although unit 4 comprises diverse lithologies, except for the massive chromitite sample that shows much lower REE contents but a slightly enriched pattern with a notable trough in the middle (Figure 40c). Both the cumulative phases (e.g., pyroxenite, anorthosite) and the common

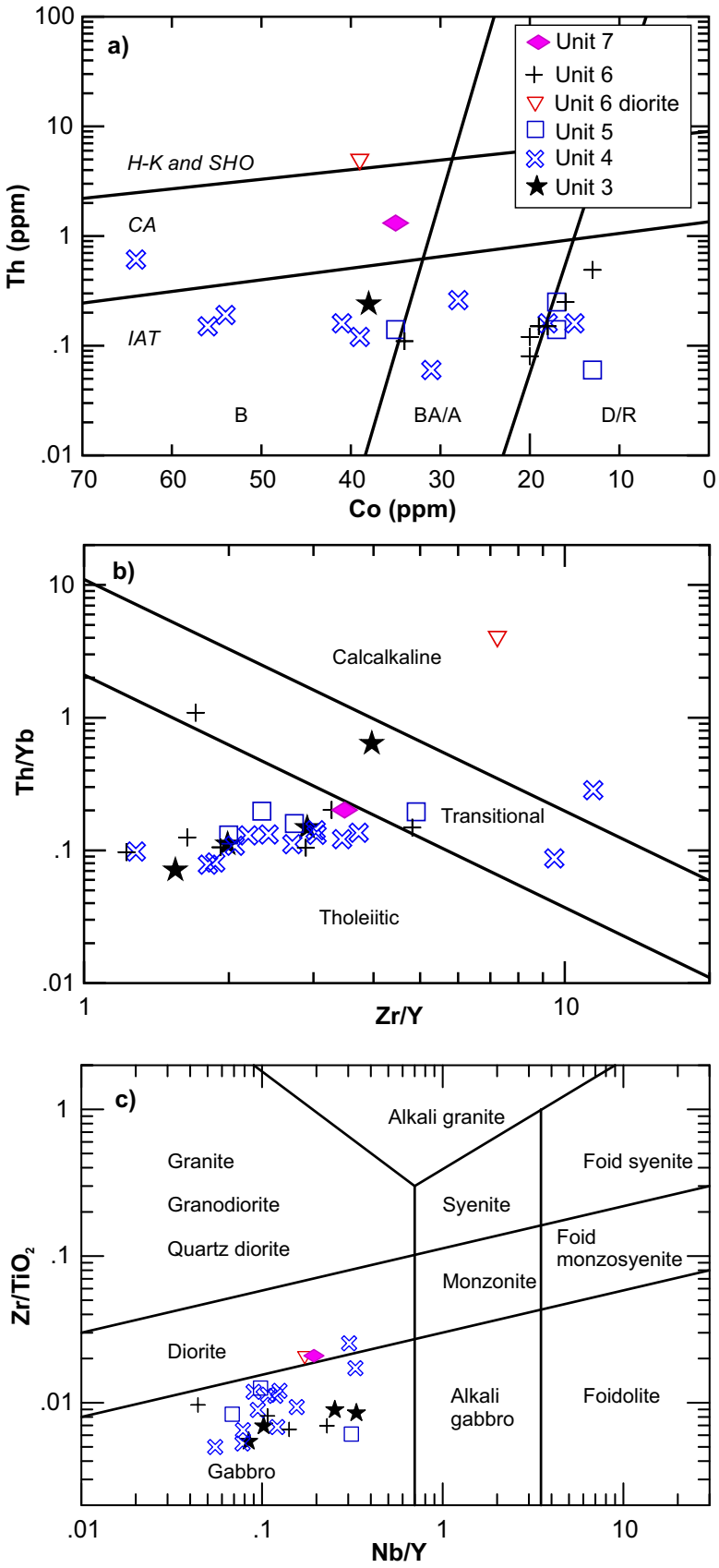

Figure 39: *Trace-element discrimination diagrams for rocks of the Mayville intrusion (units 3–7):* ***a)*** *Th versus Co (field boundaries after Hattie et al., 2007);* ***b)*** *Th/Yb versus Zr/Y (boundaries between tholeiitic, transitional and calcalkaline series from Ross and Bédard, 2009);* ***c)*** *Zr/TiO_2 versus Nb/Y (Pearce, 1996), widely used as an immobile-element discriminator equivalent to the TAS (total alkalis vs. silica) diagram (Rollinson, 1993); TiO_2 values quoted in ppm when calculating Zr/TiO_2 ratios. Rock series abbreviations: H-K and SHO, high-K calcalkaline and shoshonite; IAT, island-arc tholeiite. Rock type abbreviations: A, andesite; B, basalt; BA, basaltic andesite; D, dacite; R, rhyolite.*

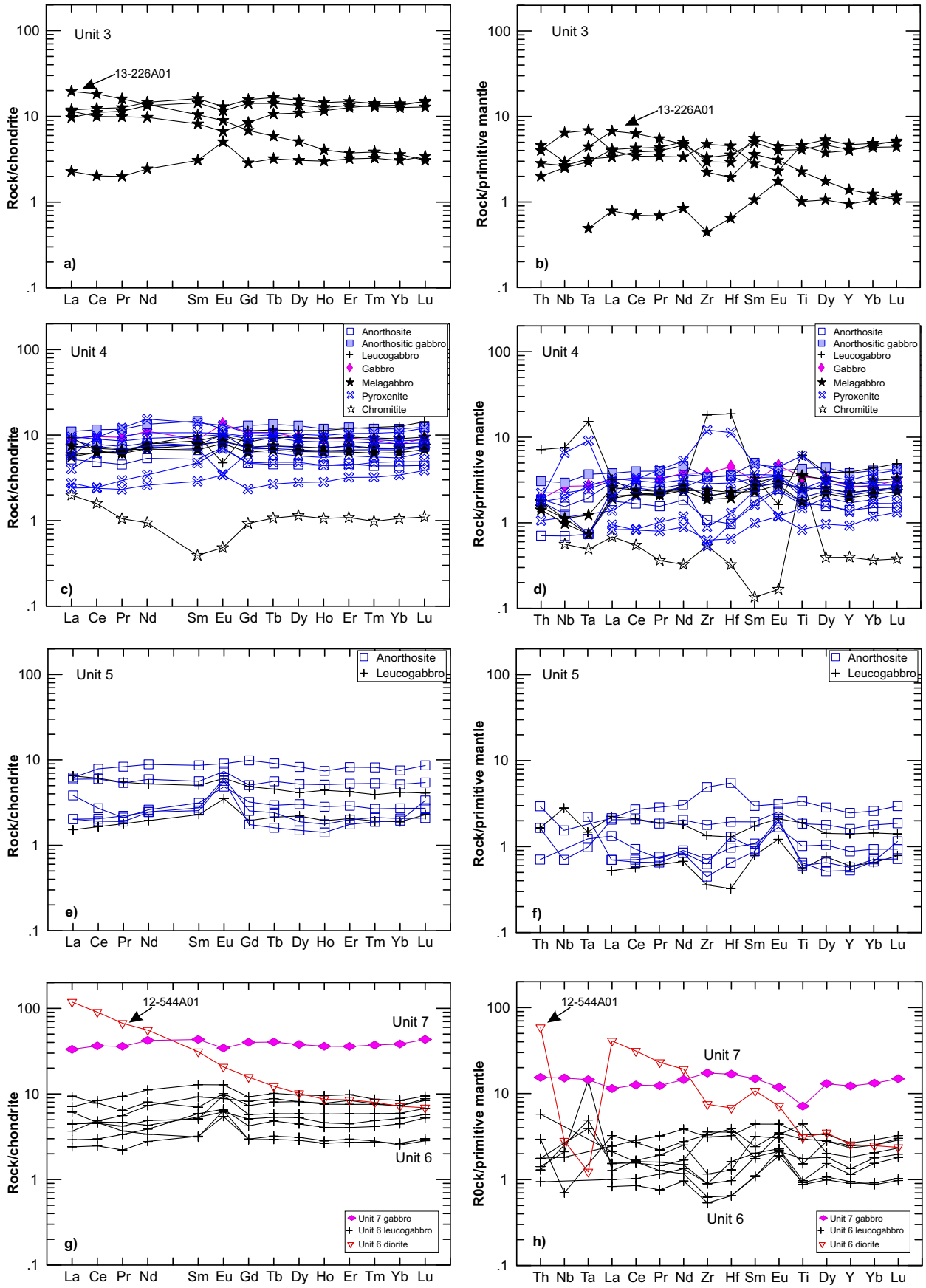

Figure 40: *Chondrite-normalized rare-earth–element patterns and primitive-mantle–normalized extended trace-element profiles of rocks from the Mayville intrusion:* ***a)*** *and* ***b)*** *for unit 3;* ***c)*** *and* ***d)*** *for unit 4;* ***e)*** *and* ***f)*** *for unit 5;* ***g)*** *and* ***h)*** *for units 6 and 7. Normalizing values from Sun and McDonough (1989).*

fractionated phases (e.g., leucogabbro) are manifested by the presence or absence of positive or negative Eu anomalies related to evolvement of plagioclase (e.g., Rollinson, 1993). On the primitive-mantle–normalized, extended trace-element profiles, these unit 4 mafic–ultramafic rocks also display either positive or negative anomalies for Nb, Ta, Zr and Hf, similar to those observed in rocks of unit 3. Similar trace-element compositions and REE patterns strongly suggest that they may have been derived from similar mantle source(s). More importantly, individual REE patterns of unit 4 rocks are subparallel, suggesting that the intrusion may have formed by multiple batches of magma derived from a common magma chamber where fractional crystallization took place, probably involving all constituent minerals except plagioclase as fractionating phases. One pyroxenite sample displays distinctive LREE depletion and a slight negative Eu anomaly; this rock may either be a cumulate phase or have crystallized from a late phase of ultramafic magma. Field evidence shows that the pyroxenite cuts leucogabbro, thus favouring the latter interpretation.

Leucogabbro to anorthositic rocks in unit 5 are more or less similar in REE patterns and extended trace-element profiles, although some show positive and others negative Eu, Nb, Ta, Zr and Hf anomalies (Figure 40c, d). These are interpreted to have formed by processes similar to those previously proposed for units 3 and 4. Some of the samples have slightly negative Nb (Ta) anomalies (Figure 40b, d, f), suggesting that they may have formed in a back-arc type of setting. In contrast, a sample (111-12-544A01) collected from a quartz diorite dike cutting unit 6 shows a significantly LREE-enriched and HREE-depleted pattern without a Eu anomaly; it also exhibits pronounced negative Nb, Ta, Zr, Hf, and Ti anomalies (Figure 40g, h), resulting in a strong magmatic-arc signature (e.g., Pearce, 2008). Although gabbroic rocks of unit 7 have relatively higher REE and trace-element concentrations, they cannot be distinguished in REE and extended trace-element profiles (Figure 40g, h) from the rocks of units 3–6. Elevated REE and trace-element abundances are most likely due to magmatic fractionation.

The trace-element (including REE) characteristics collectively suggest that the Mayville intrusion formed by multiple batches of magma derived from a common magma chamber where fractional crystallization took place, probably involving all constituent minerals except plagioclase as fractionating phases. Melagabbro, characterized by moderate negative Eu anomalies, may be an exception in this model because it appears to represent a residual phase following fractionation of plagioclase. This is interpreted to indicate that the magma(s) was/were probably derived from a relatively shallow depleted mantle that underwent a high degree of partial melting. Plagioclase may have been absent in the fractionating phases that led to anorthosite, leucogabbro, gabbro and pyroxenite in the Mayville intrusion, but it is present as a constituent mineral in these rocks. The extended trace-element profiles are consistent with mafic–ultramafic rocks derived from a magmatic-arc to back-arc system, where arc-related magmas were generated by decompression melting in the mantle wedge augmented by fluid and/or magma additions from the subducting lithospheric slab (Pearce and Peate, 1995; Tatsumi and Eggins, 1995; Mantle and Collins, 2008).

Contamination of tholeiitic magma by continental crustal materials would influence the geochemical signature of the magma because the crustal rocks have relatively higher primitive-mantle–normalized ratios of $(Th/Yb)_{PM}$ (20–100), elevated $(Nb/Yb)_{PM}$ (2–15) and greater Th enrichment relative to Nb compared to juvenile magma (Lightfoot et al., 1990; Keays and Lightfoot, 2010; Yuan et al., 2012). A geochemical model of simple mixing between N-MORB magma and upper continental crust was carried out to test the hypothesis that the Mayville intrusion was emplaced in an extensional environment at a continental margin (Yang et al., 2012). The model suggests that about 5–10% contamination by continental crust is required to elevate the $(Th/Yb)_{PM}$, $(Nb/Yb)_{PM}$ and $(Th/Nb)_{PM}$ ratios in N-MORB magma to the values observed in the Mayville intrusion. This contamination is thought to be important for triggering sulphide saturation in tholeiitic magmas (e.g., Naldrett, 2004).

Unit 8: gabbroic rocks

Samples from unit 8 fall mainly in the field of gabbro on the TAS diagram (not shown), although a few from the New Manitoba Mine intrusion (NMMI; Yang et al., 2013) fall into the ultrabasic field (44.0–44.7 wt. % SiO_2) and one (56.9 wt. % SiO_2) into the diorite field (Table 6_2 of DRI2020024). Gabbroic samples from the Cat Lake intrusion display consistent SiO_2 contents ranging from 49.1 to 51.0 wt. %. Similarly, other unit 8 samples are restricted within an SiO_2 range of 48.1–51.0 wt. %. As an affiliation (Table 1), gabbroic rocks of unit 8 are attributed to the subalkaline series defined by Irvine and Baragar (1971) because of relatively low alkali contents (Table 6; Table 6_2 of DRI2020024). On an AFM diagram (Figure 41a), all unit 8 gabbroic samples are exclusively tholeiitic. They align along the F-M side of the AFM diagram, consistent with the fractionation trend of tholeiitic magmas elsewhere under relatively reduced conditions (e.g., Miyashiro, 1974; Winter, 2010).

Based on the Th/Yb versus Zr/Y diagram, unit 8 gabbroic rocks are dominantly tholeiitic (Figure 41b), consistent with the discrimination result from the AFM diagram. Two samples (111-13-096A01 and 111-12-703A01) show higher Th/Yb and Zr/Y ratios, probably reflecting the effect of crustal contamination. This is also manifested in the plot of Zr/TiO_2 versus Nb/Y, although all samples with relatively low Nb/Y ratios (<0.7) are located exclusively in the gabbro field (Figure 41c) with subalkaline affinity (Pearce, 1996).

Figure 42 shows chrondrite-normalized REE patterns and primitive-mantle–normalized extended trace-element profiles for unit 8 gabbroic rocks. Generally, these rocks have similar,

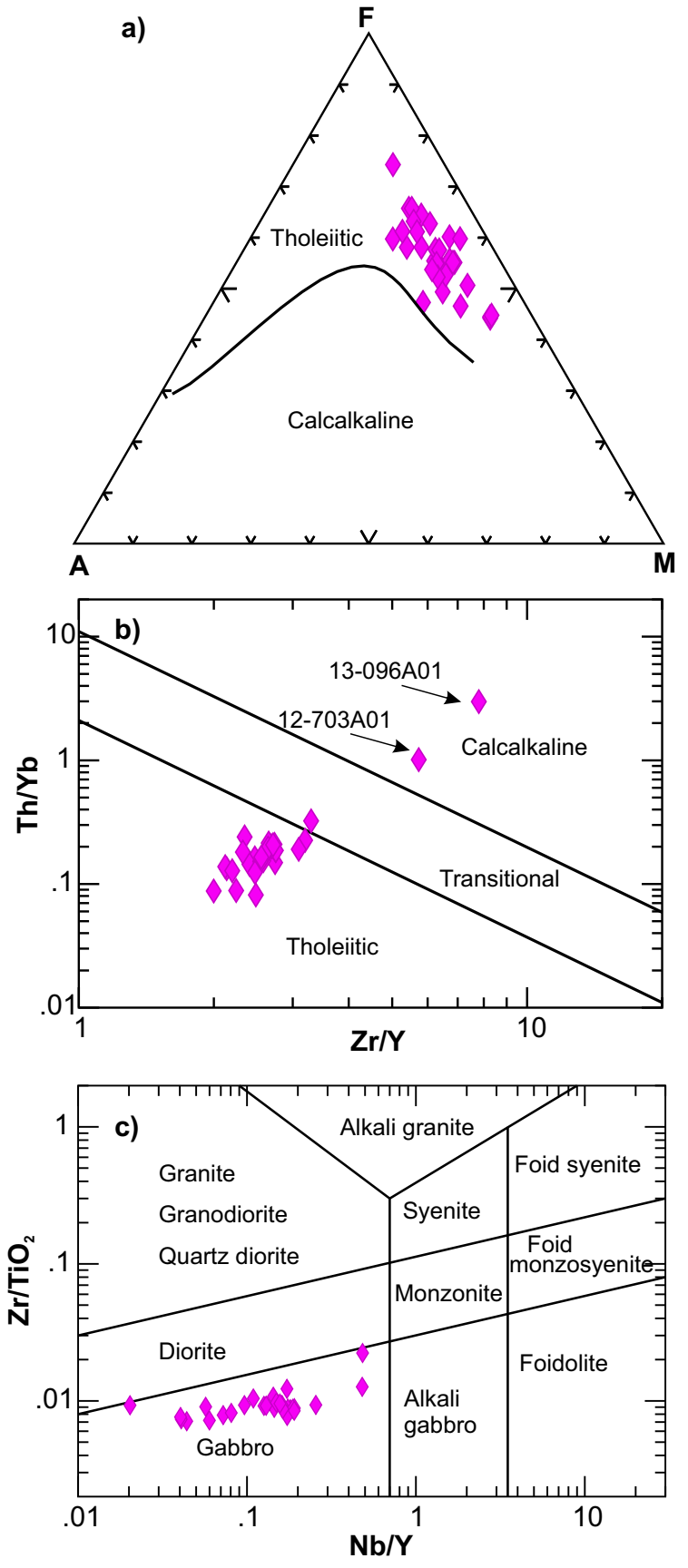

Figure 41: *Geochemical discrimination diagrams for gabbroic rocks of unit 8 from the Cat Creek–Euclid Lake area:* ***a)*** *AFM diagram, showing the division of tholeiitic and calcalkaline series (after Irvine and Baragar, 1971);* ***b)*** *Th/Yb versus Zr/Y ratios (boundaries between tholeiitic, transitional and calcalkaline from Ross and Bédard, 2009);* ***c)*** *Zr/TiO_2 versus Nb/Y ratios (from Pearce, 1996), widely used as an immobile element equivalent to the TAS (total alkalis versus silica) diagram (Rollinson, 1993). Abbreviations: A, Na_2O+K_2O; F, FeO^t (total Fe as FeO); M, MgO. All values in wt. %.*

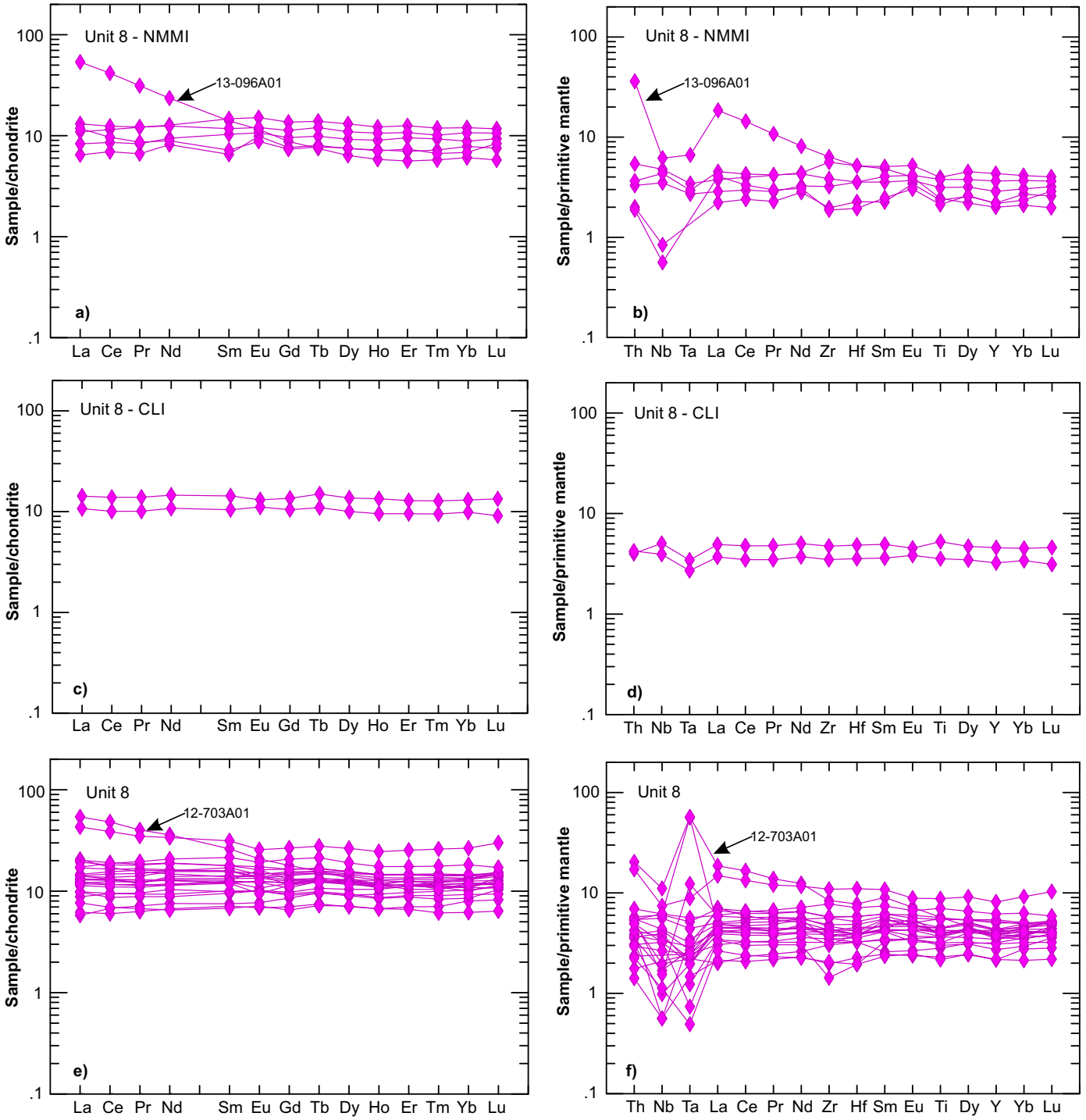

Figure 42: *Chondrite-normalized rare-earth–element patterns and primitive-mantle–normalized, extended trace-element profiles for unit 8 gabbroic rocks from the Cat Creek–Euclid Lake area:* ***a)*** *and* ***b)*** *for the New Manitoba Mine intrusion (NMMI);* ***c)*** *and* ***d)*** *for the Cat Lake intrusion (CLI);* ***e)*** *and* ***f)*** *for other unit 8 rocks. Normalizing values from Sun and McDonough (1989).*

flat REE patterns with or without very slight Eu anomalies and display 5–20 times chondrite-normalized REE values. They also exhibit similar extended trace-element profiles with relatively low HFSE concentrations that are ~5–10 times higher than primitive-mantle values (Sun and McDonough, 1989). Exceptions are evident for two samples (111-13-096A01 and 111-12-703A01) that show LREE-enriched patterns with REE abundances up to 50 times the normalized values (Figure 42a, e). Again, these characteristics are attributed to crustal contamination, which is also apparent in the trace-element profiles that show either pronounced Nb, Ta and Ti negative anomalies or even a positive Ta anomaly (Figure 42b, f). Accumulation or separation of Fe-Ti oxide minerals (e.g., ilmenite, rutile) can explain the geochemical characteristics.

To further test the effect of crustal contamination on the geochemistry of unit 8 rocks, application of a primitive-mantle–normalized $(Cu/Zr)_{PM}$ versus $(Nb/Th)_{PM}$ ratio plot (e.g., Lightfoot et al., 1990) suggests that some of these rocks may have been influenced by crustal contamination, leading to significantly decreased $(Nb/Th)_{PM}$ ratios (Figure 43). Simultaneously, such a process may also have resulted in sulphide melt saturation (that would form sulphide minerals, such as chalcopyrite and pyrrhotite, upon cooling and solid-solution fractionation and exsolution), segregation, accumulation and settling down, which is common for tholeiitic magmas (chambers or conduits; e.g., Lightfoot et al., 1990; Peck et al., 2001, 2002; Naldrett, 2004; Lightfoot, 2016). Notably, both sulphide accumulation and removal are manifested in the New Manitoba Mine intrusion, as shown by the dashed outline and sample 111-13-96A01 in Figure 43.

Unit 9: Cat Creek assemblage rocks

Unit 9 metasedimentary rocks, represented by greywackes, have intermediate to felsic composition, with SiO_2 contents ranging from 61.22 to 70.69 wt. % and total alkali contents ranging from 4.81 to 5.40 wt. % (Table 6_2 of DRI2020024), placing them in the andesite and dacite fields on the TAS diagram (Figure 44a). They are relatively rich in Na_2O, with K_2O/Na_2O ratios of 0.56–0.79, suggesting derivation from an arc-like provenance. These greywackes display low Nb/Y ratios (<0.7), with Zr/TiO_2 ratios comparable to those commonly seen in arc basalt or andesite (Figure 44b) and consistent with their source rocks being subalkaline arc-like volcanic rocks. A La-Th-Sc ternary discrimination diagram for greywackes (not shown), proposed by Bhatia and Cook (1986), indicates that these samples fall in the field of either continental island arcs (three samples) or oceanic island arcs (one sample), confirming that their provenance could be a volcanic arc.

The volcaniclastic rocks from unit 9 display chemical compositions similar to that of greywacke on a TAS diagram, despite extending to a lower SiO_2 content (54.94 wt. %), and a positive correlation between SiO_2 and total alkali contents (Figure 44a). The volcaniclastic rocks also have low K_2O/Na_2O ratios (0.33–0.77) that are relatively enriched in Na_2O (Table 6_2 of DRI2020024). This suggests that the volcaniclastic rocks (e.g., lapilli tuff and volcaniclastic sandstone), together with the greywacke, may have inherited their subalkaline signature from volcanic-arc rocks. Again, on a plot of Zr/TiO_2 versus Nb/Y, unit 9 volcaniclastic rocks have compositions similar to those of the greywackes, with low Nb/Y ratios (<0.7) and a range of Zr/TiO_2 values comparable to those of basalt to andesite (Figure 44b).

More interestingly, unit 9 greywackes and volcaniclastic rocks exhibit very similar chondrite-normalized REE patterns (Figure 45a) and primitive-mantle–normalized trace-element profiles (Figure 45b). These rocks show LREE-enriched and relatively HREE-depleted patterns with slightly negative to no Eu anomalies. One volcaniclastic sample and one greywacke sam-

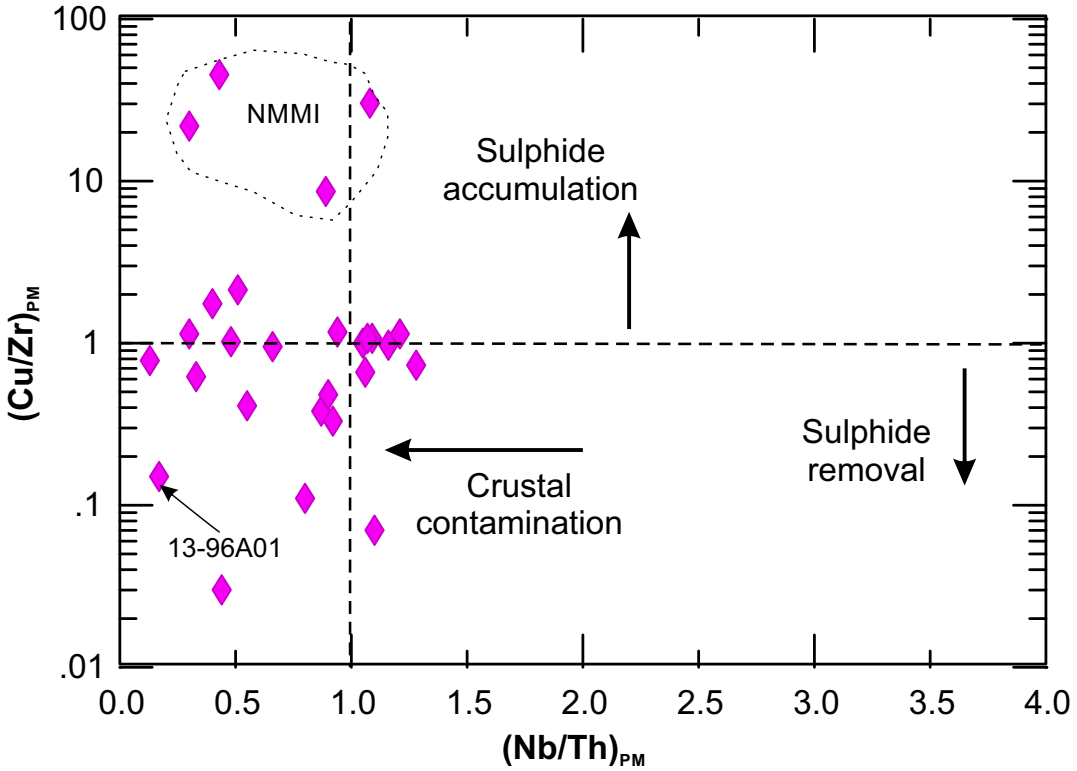

Figure 43: *Plot of $(Cu/Zr)_{PM}$ versus $(Nb/Th)_{PM}$ for unit 8 gabbroic rocks; dashed line outlines some of the samples from the New Manitoba Mine intrusion (NMMI). Primitive-mantle–normalized values from McDonough and Sun (1995).*

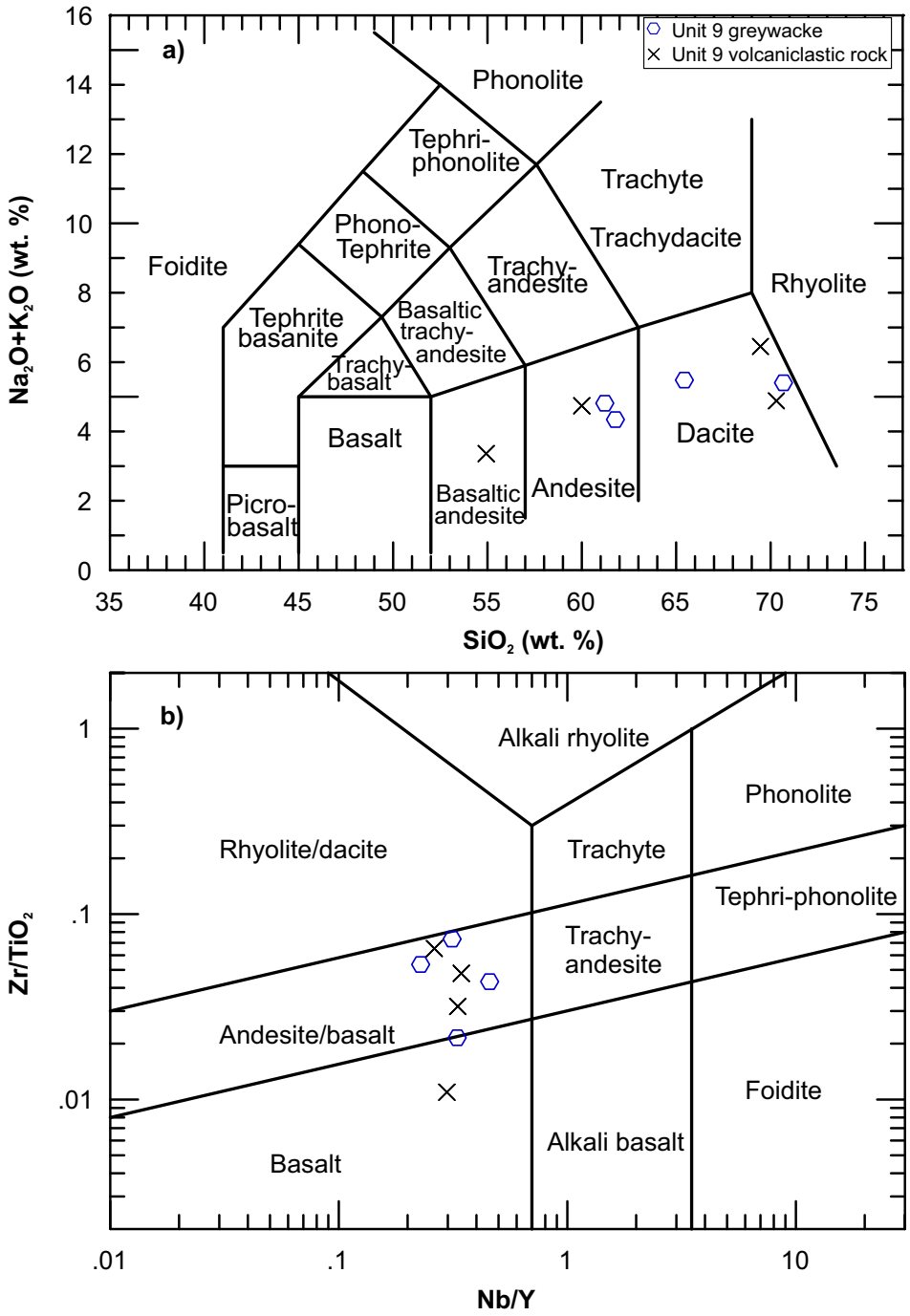

Figure 44: *Geochemical characteristics of unit 9 Cat Creek assemblage rocks from the Cat Creek–Euclid Lake area:* ***a)*** *total alkalis versus SiO_2 diagram (TAS; after Le Bas et al., 1986);* ***b)*** *Zr/TiO_2 versus Nb/Y (from Pearce, 1996).*

ple appear to be less fractionated between the LREE and HREE, likely because of their compositional differences compared to the other samples. This is also manifested in the extended trace-element profiles that these two samples display, with much less pronounced Nb, Ta and Ti negative anomalies compared to the other samples, which inherited more typical arc signatures (Figure 45b; e.g., Rollinson, 1993; Pearce, 2008).

Geochemical characteristics of the greywackes and volcaniclastic rocks from the unit 9 Cat Creek assemblage suggest that they may have a volcanic-arc provenance.

Unit 10: TTG suite rocks, including the Maskwa Lake batholith II

Classification

Based on their major-element compositions, unit 10 TTG suite rocks range from granite, granodiorite and quartz diorite to gabbro on the TAS diagram (Figure 46a), and can be grouped into felsic and mafic compositions. Field relationships indicate that the felsic rocks were cut by mafic rocks, although they are all subalkaline based on the definition by Irvine and Baragar

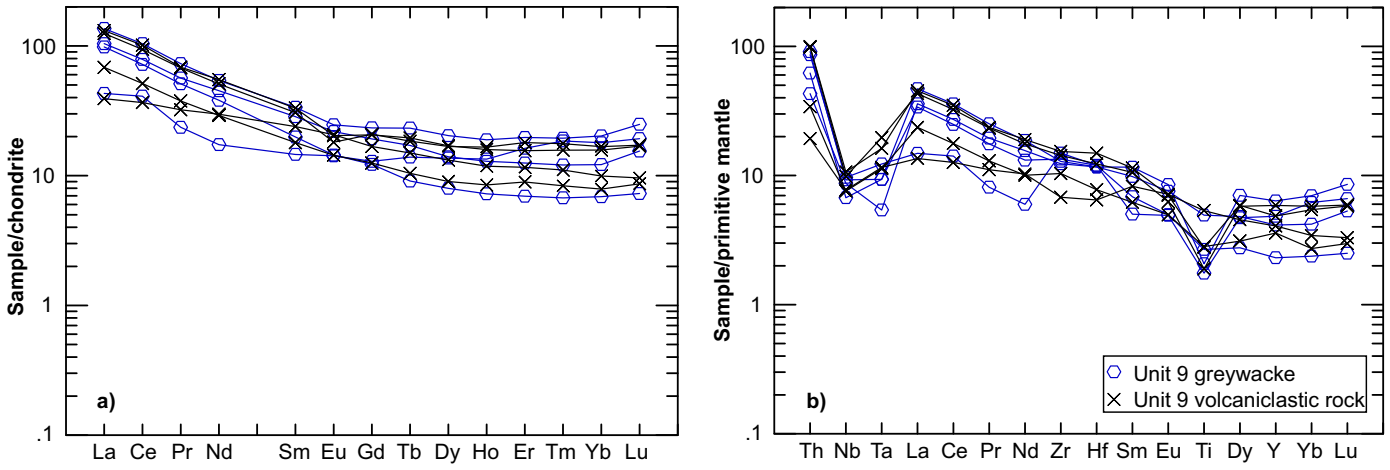

Figure 45: *Rare-earth–element patterns of unit 9 Cat Creek assemblage rocks from the Cat Creek–Euclid Lake area:* ***a)*** *chondrite-normalized, rare-earth–element profiles;* ***b)*** *primitive-mantle–normalized, extended trace-element profiles. Normalizing values from Sun and McDonough (1989).*

(1971). Most are calcic, although a few samples are calc-alkalic (Figure 46b). Based on the index of Fe* proposed by Frost et al. (2001), unit 10 granitoids are dominantly magnesian, although a few samples from evolved phases fall into the ferroan field (Figure 46c). On the Shand index plot, they are metaluminous to weakly peraluminous. Only a few, more evolved, samples are moderately to strongly peraluminous (Figure 46d). Using an aluminum saturation index ACNK of 1.1 as the boundary to differentiate I-type (<1.1) from S-type (>1.1) granites (Chappell and White, 1974, 1992, 2001), unit 10 granitoids are of I-type, which is interpreted to be derived from partial melting of igneous source rocks. More interestingly, unit 10 granitoid rocks display a range of lithological types, from tonalite, trondhjemite and granodiorite (TTG) to granite (Figure 46e), typical of Archean TTG suites (Barker, 1979). This is consistent with the observation on the TAS diagram (Figure 46a) that unit 10 granitoid rocks span a wide compositional range.

Unit 10 granitoid rocks display a range of σ values from 0.60 to 2.05 but are all below 3.5 (Table 6_2 of DRI2020024), suggesting that they are calcic to calcalkaline (Yang, 2007). This is consistent with the classification result in Figure 46b and is also confirmed by Nb/Y ratios consistently less than 0.7 for the unit 10 granitoids (Figure 46f), typical of subalkaline affinity (Pearce, 1996). One sample (111-12-477C01) has an Nb/Y ratio of 0.98, likely reflecting the effect of crustal contamination. In addition, unit 10 granitoid rocks exhibit varied Zr/TiO_2 ratios that are mostly higher than 0.05, reflecting relatively evolved characteristics (Figure 46f). Again, similar to the TAS diagram classification, two groups of unit 10 rocks are evident based on their felsic and mafic compositions.

Trace elements

Except for gabbro dikes, unit 10 granitoid rocks have relatively low Rb (up to 286 ppm) and Sr (up to 263 ppm), and high Ba (up to 1102 ppm); Rb/Sr ratios range from 0.1 to 6.6 (Table 6_2 of DRI2020024), suggesting extensive magmatic fractionation. Unit 10 granitoids display varied K/Rb ratios, ranging from 32 to 681 and generally higher than 200, reflecting sources that were unevolved to moderately evolved (Blevin, 2004). This is consistent with low to moderately abundant transitional elements (e.g., Cr, Co, Ni) in these rocks.

Figure 47 shows chondrite-normalized REE patterns of unit 10 granitoid rocks, which are plotted on the basis of rock types (i.e., gabbro, quartz diorite, feldspar porphyry, tonalite, granodiorite and granite). Relative to the granitoid rocks of unit 10, the gabbros have lower REE abundances and display flat to slightly LREE-enriched patterns with slightly negative to positive Eu anomalies (Figure 47a). One sample (111-13-137B01) even exhibits an LREE-depleted pattern without a notable Eu anomaly and is elevated in TiO_2 (1.24 wt. %). Quartz diorite shows moderately to strongly LREE-enriched and HREE-depleted profiles, with small negative to positive Eu anomalies, as indicated by Eu/Eu* values of 0.89–1.11 (Figure 47b). Rare-earth element abundance increases from gabbro to quartz diorite to granitoid compositions. Tonalite, granodiorite and granite all display very similar LREE-enriched and HREE-depleted patterns with variably negative Eu anomalies, indicated by Eu/Eu* values of 0.21–0.94 (Figure 47d–f). This suggests that plagioclase may have played a role in their magmatic evolution, leading to bulk-REE concentrations varying from tens to hundreds of times chondrite-normalized values and La/Yb ratios varying from ~6 to 31 (Table 6_2 of DRI2020024). Feldspar porphyry samples are generally similar to the other granitoids in terms of their REE patterns (Figure 47c). A garnet skarn sample (Figure 47b) displays an LREE-depleted pattern with notable positive Eu anomaly, although it has a much lower bulk-REE content.

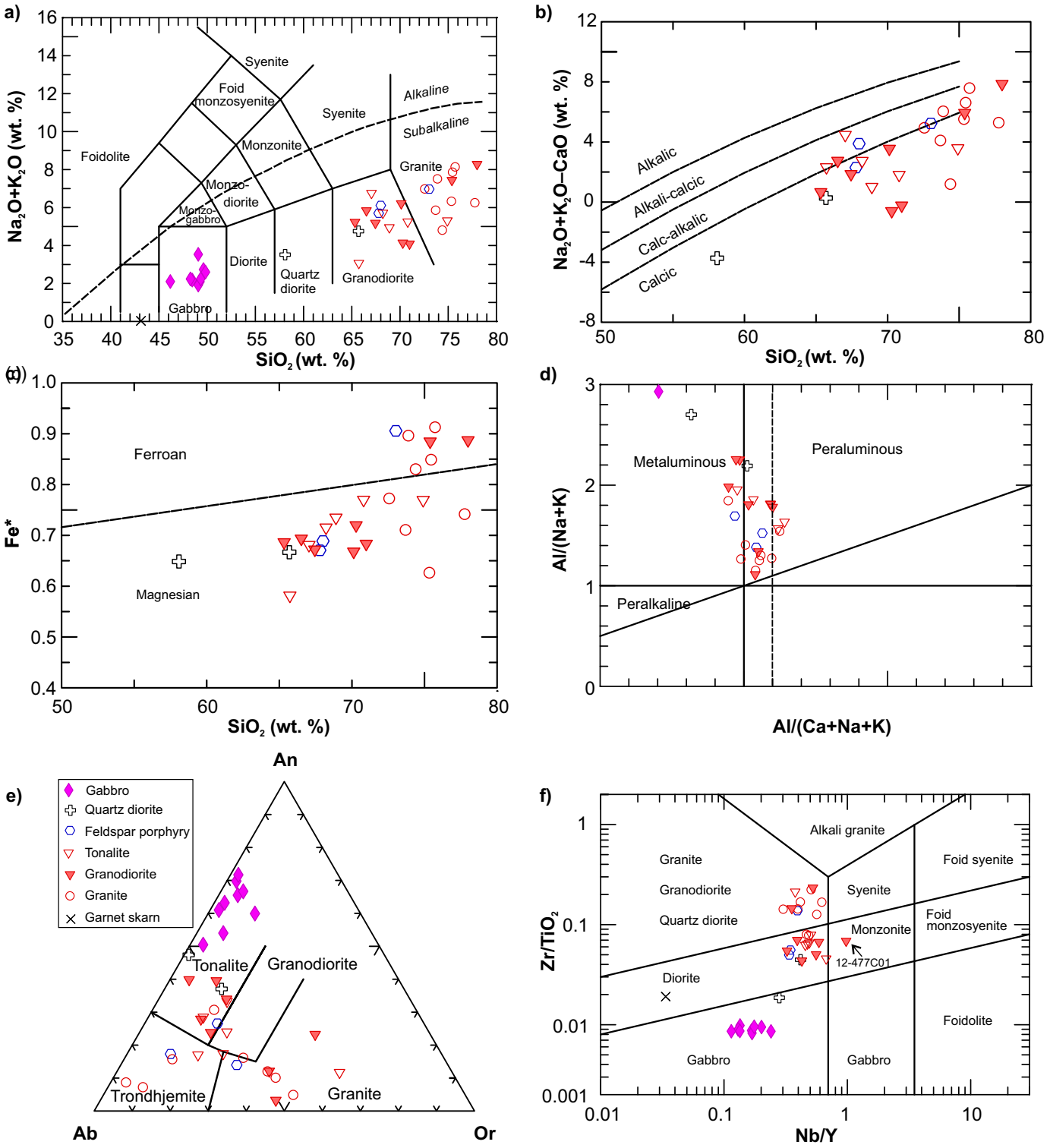

Figure 46: *Chemical classification of unit 10 granitoid rocks and related rocks from the Cat Creek–Euclid Lake area:* ***a)*** *total alkalis (Na_2O+K_2O, wt. %) versus SiO_2 (wt. %) diagram (i.e., TAS; fields from Middlemost, 1994; boundary between alkaline and subalkaline series from Irvine and Baragar, 1971);* ***b)*** *MOLI ($Na_2O+K_2O–CaO$, wt. %) versus SiO_2 (wt. %; after Frost et al., 2001);* ***c)*** *classification of ferroan versus magnesian granitoids (from Frost et al., 2001); $Fe^*=FeO^t/(FeO^t+MgO)$;* ***d)*** *Shand index (fields from Maniar and Piccoli, 1989); $ACNK=Al_2O_3/(CaO+Na_2O+K_2O)$, $A/NK=Al_2O_3/(Na_2O+K_2O)$, units in moles; vertical dashed line indicates ACNK=1.1, a key parameter discriminating S- and I-type granites (Chappell and White, 1974);* ***e)*** *Ab-An-Or ternary diagram (fields from Barker, 1979);* ***f)*** *Zr/TiO_2 versus Nb/Y (after Pearce, 1996).*

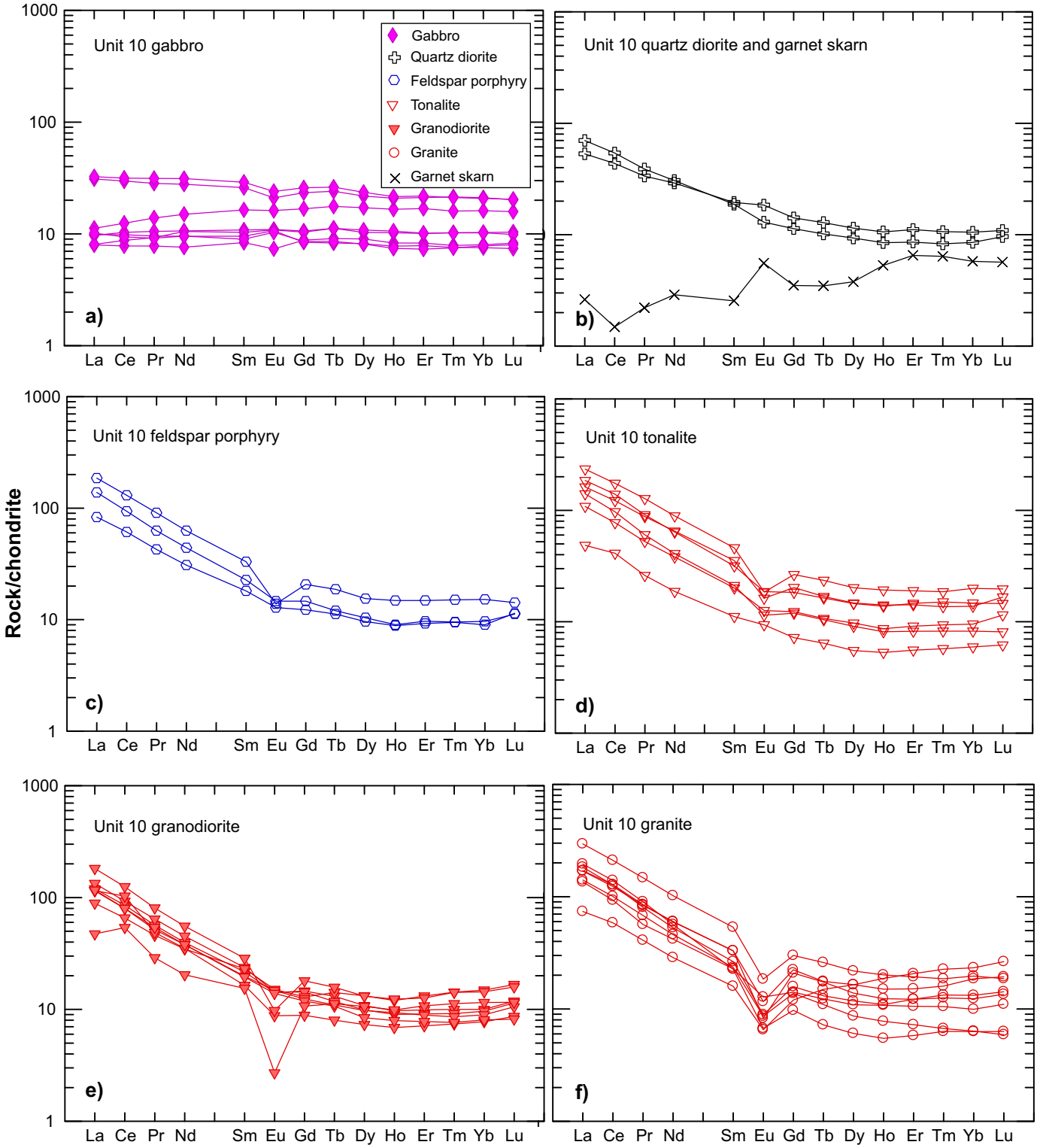

Figure 47: *Chondrite-normalized rare-earth element patterns for unit 10 granitoid rocks from the Cat Creek–Euclid Lake area. Normalizing values from Sun and McDonough (1989).*

Figure 48 shows primitive-mantle–normalized extended trace-element profiles of unit 10 granitoid rocks, revealing that they are enriched in incompatible elements and have pronounced negative Nb, Ta and Ti anomalies. This is a typical arc signature, suggesting that unit 10 granitoids may have formed in a magmatic-arc setting (e.g., Prouteau et al., 1999, 2001; Pearce et al., 2005; Anderson, 2013). Again, unit 10 gabbros, which occur as dikes cutting granitoids, have lower trace-element abundances and flat profiles with or without Nb, Ta and Ti anomalies. A garnet skarn sample (Figure 48b) displays

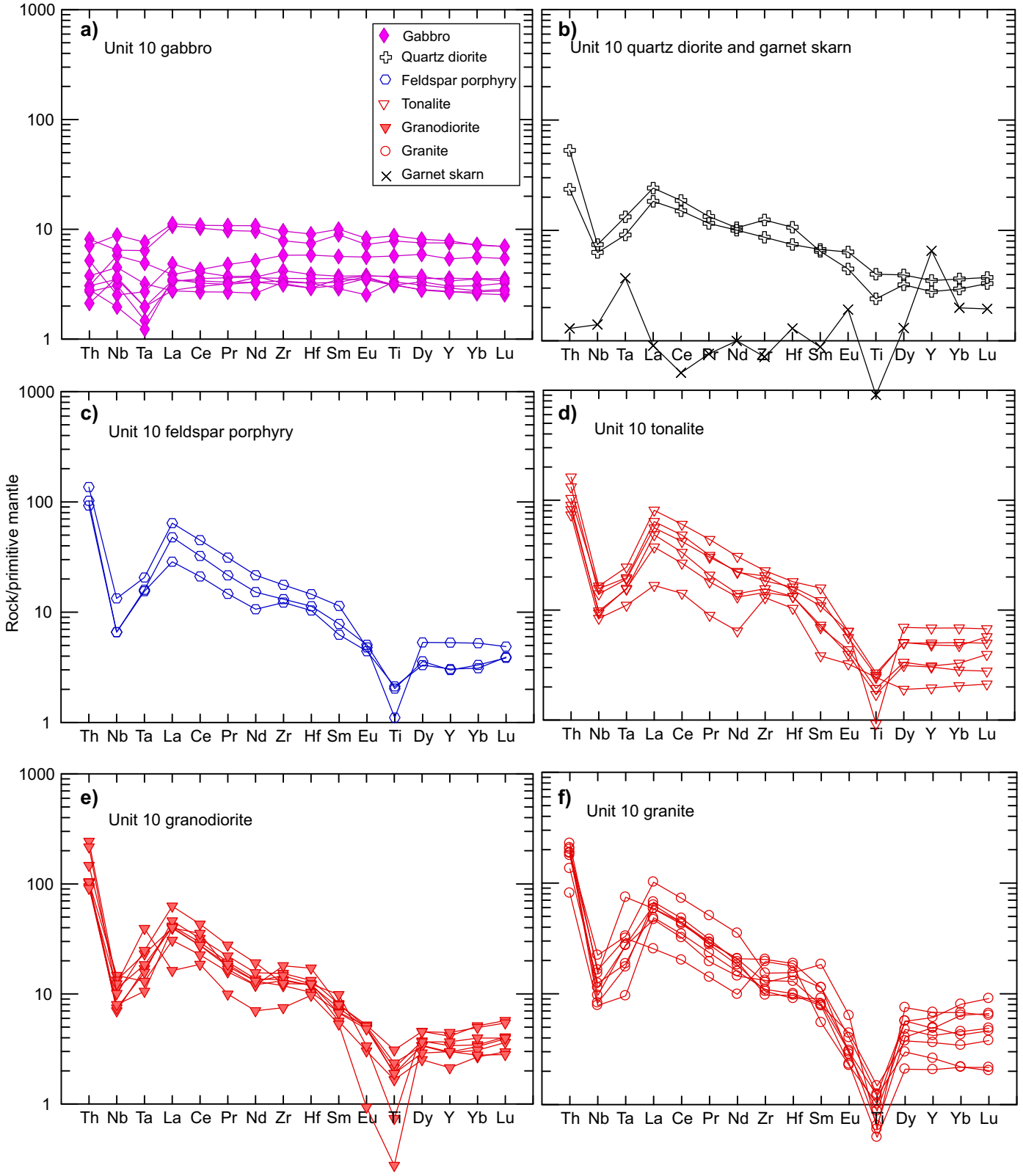

Figure 48: *Primitive-mantle–normalized extended trace-element plots for unit 10 granitoid rocks from the Cat Creek–Euclid Lake area. Normalizing values from Sun and McDonough (1989).*

much lower trace-element concentrations characterized by a zigzag profile, suggesting that it was formed by metasomatism resulting from its intrusion into calcareous sedimentary rock (e.g., limestone).

On the Pearce et al. (1984) discrimination diagram, all samples of unit 10 granitoids plot in the field of volcanic granitoids (Figure 49a) except sample 111-12-279c, which has a Rb content of 286 ppm as a result of amphibole fractionation (cf. Clarke, 1992; Yang et al., 2008). On the plot of log τ versus log σ (not shown), all granitoid samples fall into the field of orogenic belts and island arcs. Note that $\tau=(Al_2O_3–Na_2O)/TiO_2$ (Gottini, 1968) and ranges from 13.88 to 151.23 (see Table 6_2

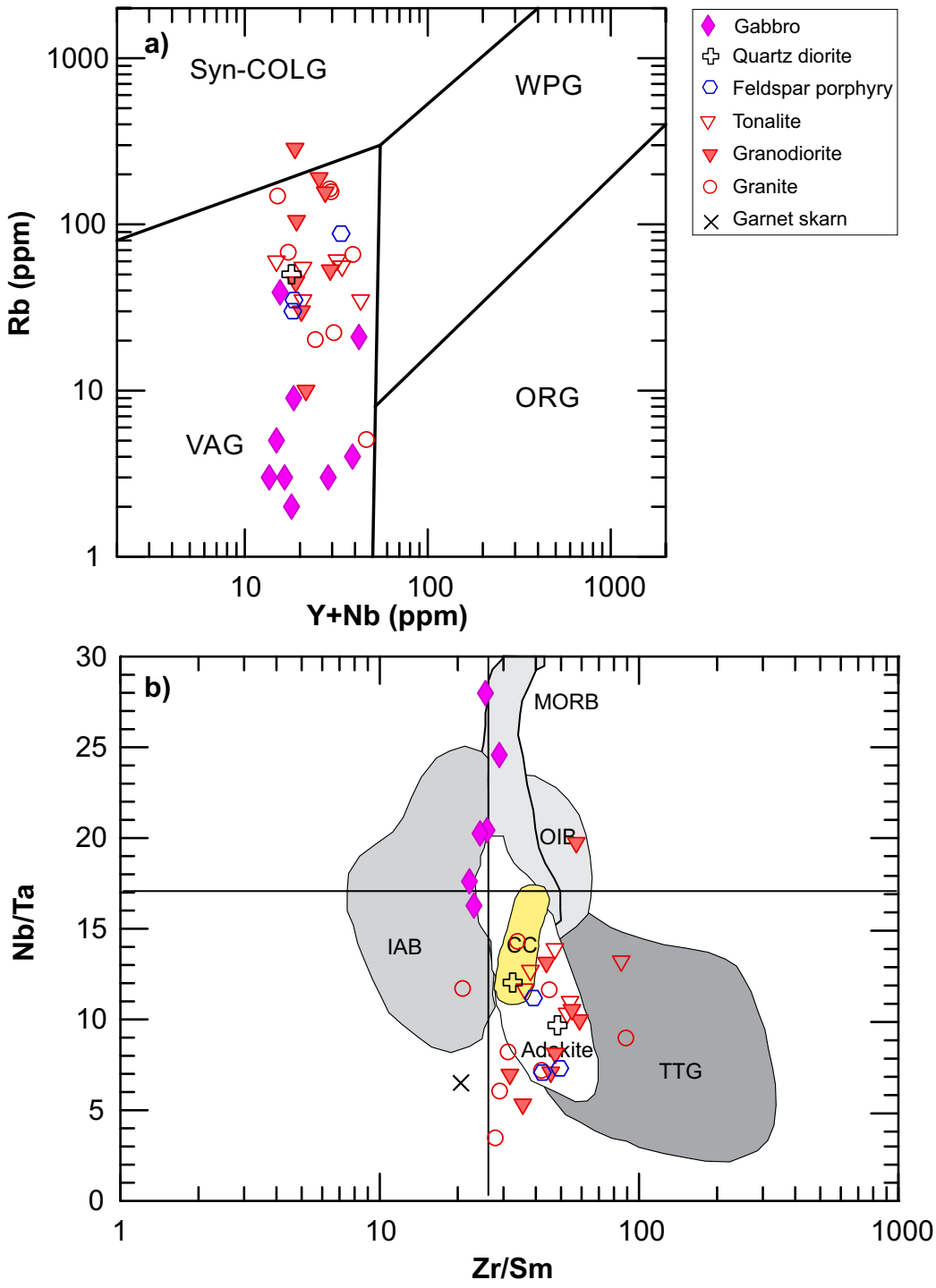

Figure 49: *Tectonomagmatic discrimination diagram for unit 10 granitoid rocks from the Cat Creek–Euclid Lake area:* ***a)*** *(Y+Nb) versus Rb (after Pearce et al., 1984);* ***b)*** *Zr/Sm versus Nb/Tb (after Foley et al., 2002); primitive-mantle Nb/Ta and Zr/Sm ratios are 17.4 and 25.2, respectively (Sun and McDonough, 1989). Abbreviations: CC, continental crust; IAB, island-arc basalt; MORB, mid-ocean–ridge basalt; OIB, ocean-island basalts; ORG, ocean-ridge granitoid; syn-COLG, syncollisional granitoid; TTG, tonalite-trondhjemite-granodiorite; VAG, volcanic-arc granitoid; WPG, within-plate granitoid.*

of DRI2020024), which is consistent with characteristics of unevolved to strongly evolved granitoids. Also, these chemical features are suggested by moderate to high K/Rb ratios, as mentioned previously.

On the plot of Nb/Ta versus Zr/Sm (Figure 49b), unit 10 granitoid rocks display relatively low Nb/Ta ratios (<17.4) and high Zr/Sm ratios (>25.2) compared to primitive mantle, MORB, ocean-island basalt and island-arc basalt, and are more similar to Archean TTG and/or adakite (Foley et al., 2002). This suggests that they may have been derived from partial melting of amphibolite (Foley et al., 2002) in a volcanic-arc environment. However, on a plot of Sr/Y versus La/Yb (Figure 50), most of the unit 10 granitoid samples form a group with Sr/Y < 10 and La/Yb < 20 (i.e., the field of non-TTG), and only a few samples with 50 > Sr/Y > 10 and La/Yb > 20 are attributed to low-pressure TTG (Moyen and Martin, 2012). Relatively low La/Yb and Sr/Y ratios in the granitoids can be explained by plagioclase fractionation, which also leads to moderately negative Eu anomalies (Figure 48).

Since Sr is readily remobilized in granitoid rocks, the abundance of HFSE is preferred as a means of discriminating rock types and tectonic environments (e.g., Whalen et al., 1987). In terms of geodynamic settings, Whalen and Hildebrand (2019) proposed a set of trace-element concentrations and ratios to discriminate granitoid rocks formed by arc magmatism (pre-collisional), slab failure (post-accretion or post-collisional; Hildebrand et al., 2018) and A-type (late post-collisional or anorogenic). First, A-type granitoids contain higher Nb+Y (>60 ppm) and Ta+Yb (>6 ppm) than slab-failure– and arc-related counterparts. Secondly, granitoids produced by slab-failure magmatism have geochemical signatures of Sr/Y >20 (although this is not diagnostic), Nb/Y >0.4, Ta/Yb >0.3, La/Yb >10, Gd/Yb >2 and Sm/Yb >2.5, whereas arc-related rocks have lower ratios than slab-failure ones. Thirdly, these ratios are applicable to metaluminous granitoid rocks with SiO_2 ranging from 55 to 70 wt. %. Application of the discrimination diagrams of Whalen and Hildebrand (2019) indicates that most unit 10 granitoid samples fall in the field of slab-failure granitoids and/or straddle the boundary between arc-related and slab-failure–related granitoids (Figure 51). No A-type granites, however, were identified in the unit 10 TTG suite.

Some of the unit 10 granitoid rocks are comparable to the low-pressure TTG subtype proposed by Moyen and Martin (2012), which may have exhibited the geochemical characteristics of non-TTG owing to extensive differentiation (Figure 50). In addition, these granitoids generally display calcic, magnesian and weakly to moderately peraluminous affinities. These features, together with constraints from trace-element geochemistry, suggest that unit 10 granitoids may have been generated by partial melting of amphibolites derived from mafic protoliths at relatively low pressure in an arc-related to slab-failure setting. Underplating of mafic mantle-derived magmas could have triggered partial melting of the lower crustal amphibolites to form unit 10 granitoids and, due to tectonism, some of the mafic magmas may have ascended to emplace into the

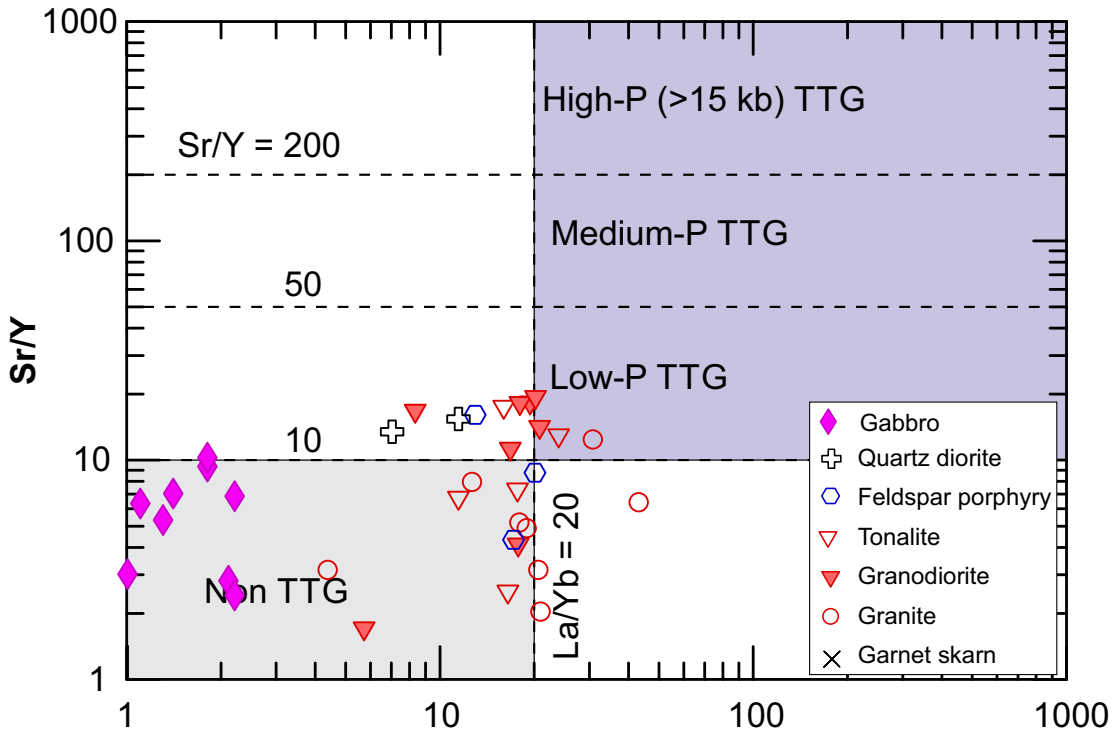

Figure 50: *Discrimination plot of La/Yb versus Sr/Y in unit 10 granitoid rocks from the Cat Creek–Euclid Lake area. Boundaries used to define TTG types from Moyen and Martin (2012). Abbreviation: TTG, tonalite-trondhjemite-granodiorite.*

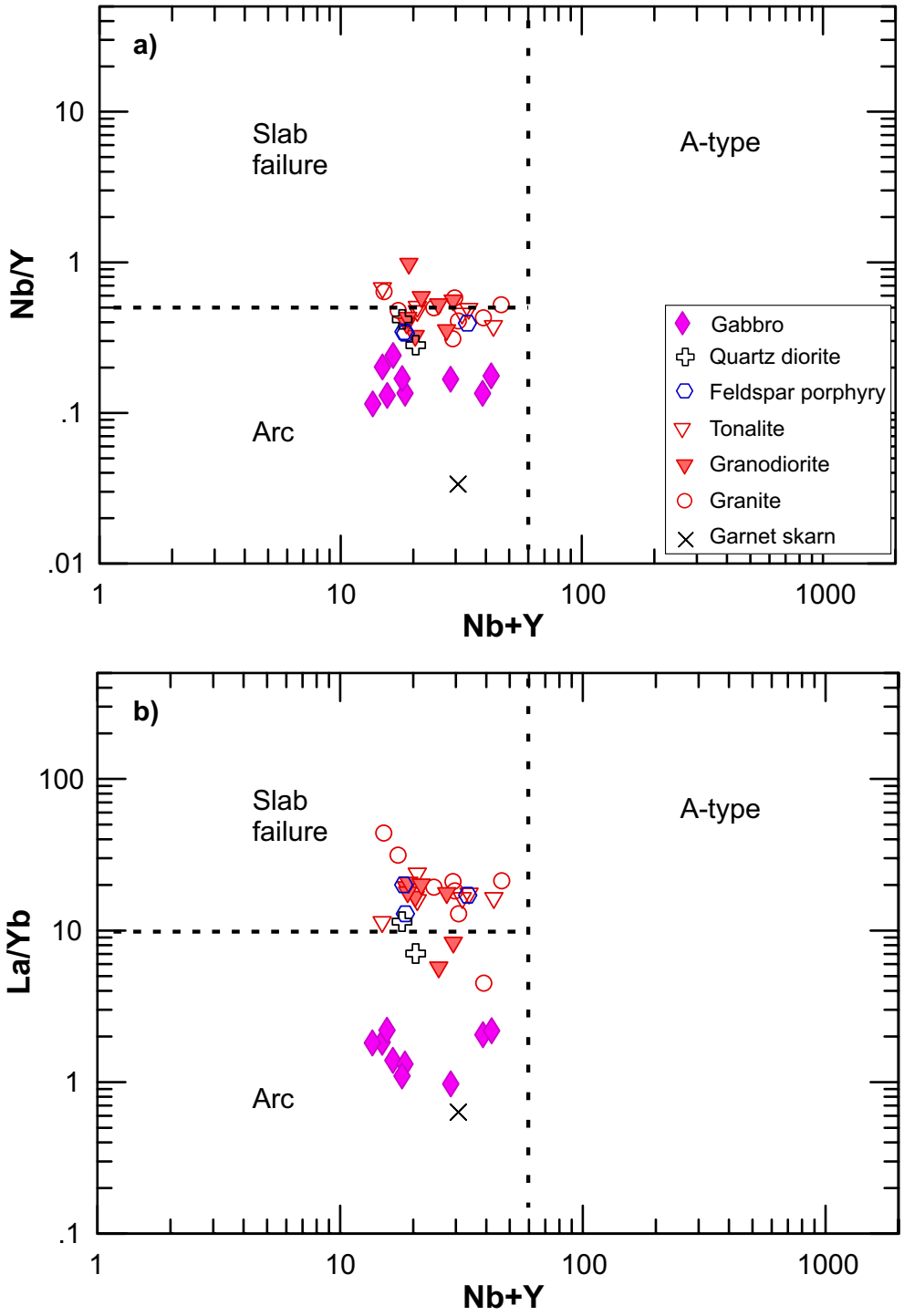

Figure 51: *Discrimination plots of Nb/Y versus Nb+Y (ppm) and La/Yb versus Nb+Y (ppm) for unit 10 granitoid rocks from the Cat Creek–Euclid Lake area. Boundaries for slab-failure, arc and A-type granitoids from Whalen and Hildebrand (2019).*

unit 10 granitoids along pre-existing structures to form slightly younger gabbroic dikes.

Unit 11: Euclid Lake assemblage rocks

Major-element data for unit 11 rocks (Table 6; Tables 6_1 and 6_2 of DRI2020024) indicate that three sandstone samples plot in the dacite field, one amphibolite sample in the basaltic andesite field and two mafic volcanic samples in the basalt field on the TAS diagram (not shown) of Le Bas et al. (1986). Trace-element data reveal that these samples fall in the andesite/basalt field on the Zr/TiO_2 versus Nb/Y classification diagram (not shown) of Pearce (1996) and in the volcanic-arc granitoid field on the (Y+Nb) versus Rb diagram (not shown) of Pearce et al. (1984). Together, these characteristics suggest that the Euclid Lake assemblage rocks were likely derived from local arc-related rocks.

The three sandstone samples collected from this unit 11 have similar and consistent REE patterns, showing LREE enrichment and HREE depletion without notable Eu anomalies (Figure 52a). These sandstones have pronounced Nb, Ta and Ti negative anomalies (Figure 52b), similar to arc-related rocks.

The amphibolite samples display similar REE and trace-element profiles to the sandstone samples, although they appear more differentiated between LREE and HREE and display notably negative Zr and Hf anomalies (Figure 52a, b).

Two samples of mafic-volcanic rocks show slightly different REE and trace-element patterns: one has relatively enriched LREE and the other depleted LREE, although both the profiles are flat; and one has notably negative Ta, Zr and Hf anomalies, whereas the other does not.

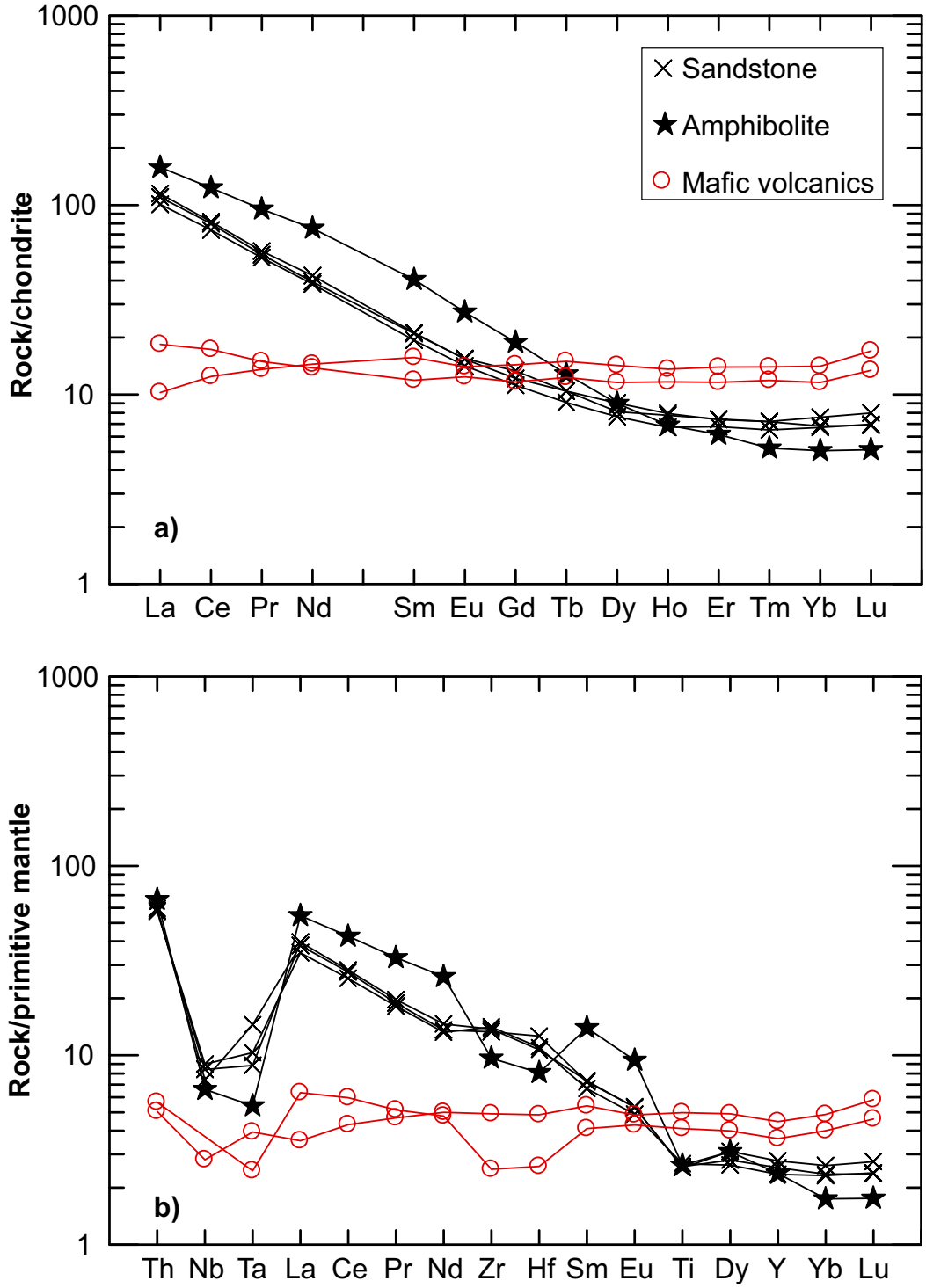

Figure 52: *Trace-element patterns of Euclid Lake assemblage rocks from the Cat Creek–Euclid Lake area:* ***a)*** *chondrite-normalized rare-earth element profiles;* ***b)*** *primitive-mantle–normalized extended rare-earth–element profiles. Normalizing values from Sun and McDonough (1989).*

Unit 12: Inconnu pluton

Major elements

Based on major-element compositions, unit 12 granitoid rocks of the Inconnu pluton include a variety of rock types, ranging from granite, granodiorite and quartz diorite to monzonite on the TAS diagram, all of which belong to the subalkaline series (Figure 53a) of Irvine and Baragar (1971). Although these rocks are mostly calc-alkalic in terms of alkalinity (Figure 53b), a few samples fall into the fields of calcic and even alkalic (e.g., one aplite sample), suggesting that unit 12 rocks may represent diverse magmas, which requires further discussion. Based on the index of Fe* proposed by Frost et al. (2001), unit 12 granitoids are dominantly magnesian, although the aplite sample falls into the ferroan field (Figure 53c). Notably, the samples display a roughly linear relationship on the plot of Fe* versus SiO_2, consistent with a magmatic differentiation trend. On the Shand index plot, unit 12 granitoid rocks are metaluminous to weakly peraluminous (Figure 53d). Only two samples are moderately to strongly peraluminous; one of these, sample 111-13-170D01, was collected from a very coarse grained to pegmatitic granite dike cutting Euclid Lake assemblage (unit 11) greywacke on the north shore of Euclid Lake (see below). Using an aluminum saturation index (ACNK) of 1.1 as the boundary to differentiate I-type (<1.1) from S-type (>1.1) granites (Chappell and White, 1974, 1997, 2001), unit 12 granitoids, except for the pegmatitic granite, are of I-type and interpreted to be derived from partial melting of igneous source rocks. On a CIPW normative Ab-An-Or plot (Figure 53e), these rocks display a range of lithological types from tonalite, trondhjemite and granodiorite to granite, similar to Archean TTG suite rocks (Barker, 1979). This is also consistent with the observation on the TAS diagram (Figure 53a) that they span a wide compositional range. Again, a magmatic differentiation trend of the calc-alkalic series is well exhibited on Figure 53f, consistent with the characteristics shown on Figure 53b and c.

Unit 12 granitoid rocks have relatively narrow σ values ranging from 1.44 to 3.18 (Table 6_2 of DRI2020024), suggesting that they are calcalkaline (Yang, 2007). This is consistent with the classification result obtained with Figure 53b.

On the TAS diagram (Figure 53a), the pegmatitic granite sample (11-13-170D01), as mentioned above, plots in the granite field, which is subalkaline, and it plots on the boundary between calcic and calc-alkalic series (Figure 53b). This sample plots on the boundary between magnesian and ferroan granitoids (Figure 53c; defined by Frost et al., 2001) and has a very high ACNK value of 1.29 (Figure 53d), which is attributed to strongly peraluminous granite, as defined by Clarke (2019). Thus, it is an S-type granite in origin (Yang et al., 2019). However, this granite is rich in Na_2O (5.98 wt. %) compared to K_2O (0.31 wt. %), resulting in a K_2O/Na_2O ratio of 0.05, and must therefore contain a very high CIPW normative albite content (54.9%). As a result, it plots in the trondhjemite field (Figure 53e), consistent with the differentiation trend of calcic granitoids (Figure 53f; see Whalen and Frost, 2013). The Na enrichment of this granite is atypical compared to K-rich S-type granitoids from the Lachlan fold belt (Chappell and White, 1974, 1992, 2001). Remarkably, this granite sample exhibits very high concentrations of Be (195 ppm), Nb (95.5 ppm) and Ta (290 ppm), probably enough to constitute rare-metal ore. Notably, it is depleted in transitional elements (e.g., Cr, Ni, Co) and REEs (see Table 6_2 of DRI2020024).

Trace elements

Figure 54a (Pearce, 1996) is used to classify volcanic rocks, is thought (Rollinson, 1993) to be equivalent to the TAS diagram proposed by Le Bas et al. (1986), and is also applied to the classification of intrusive rocks (Middlemost, 1994). Unit 12 granitoids display a roughly linear relationship between ratios of Zr/TiO_2 and Nb/Y, extending from the field of andesite through trachyandesite and trachyte to rhyolite, except for highly evolved samples such as aplite and pegmatitic granite. Such a trend is interpreted to be the result of magmatic differentiation of subalkaline magmas with Nb/Y ratios of <0.7 (Figure 54a; Pearce, 1996). However, this interpretation has difficulty explaining some of the samples with high Nb/Y ratios (>0.7), which require either upper crustal contamination or addition of magmas derived from much deeper sources. Compositional constraints favour the former interpretation because these granitoid rocks are poor in transition elements (e.g., Ni, Co, Cr). In addition, Zr/TiO_2 ratios higher than 0.05 in the unit 12 granitoid rocks indicate that they are relatively evolved (Figure 54a), consistent with K/Rb ratios as low as 42. The ratios ranging from 42 to as much as 515 (Table 6_2 of DRI2020024) likely reflect heterogeneity of the source regions.

On the Pearce et al. (1984) discrimination diagram, most of the samples of unit 12 granitoid plot in the field of volcanic-arc granitoids (Figure 54b) and a few extend to the field of syncollisional granitoids. The pegmatitic granite (sample 111-170D01) plots in the ocean-ridge granitoid field, indicating that it is much depleted in Rb. In contrast, the aplite sample has a much higher Rb content and thus plots in the syncollisional granitoid field. These two extremes strongly suggest that these rocks may have formed by different processes: one leading to Rb (432 ppm) enrichment in the aplite, and the other resulting in Rb (5 ppm) depletion in the pegmatitic granite (see also Table 6_2 of DRI2020024). This is also indicated by the distinct K_2O/Na_2O ratios of 2.21 and 0.05 of the pegmatitic granite and aplite, respectively, suggesting that they may have followed different fractionation paths (e.g., Scaillet et al., 2016) under relatively low pressures (e.g., Yang, 2017).

Figure 55a and b show chondrite-normalized REE patterns of unit 12 granitoid rocks that were grouped into subunits 12a and 12b based on their field relationships (Table 1). Granitoid rocks of subunit 12a (Figure 55a) display LREE-enriched pat-

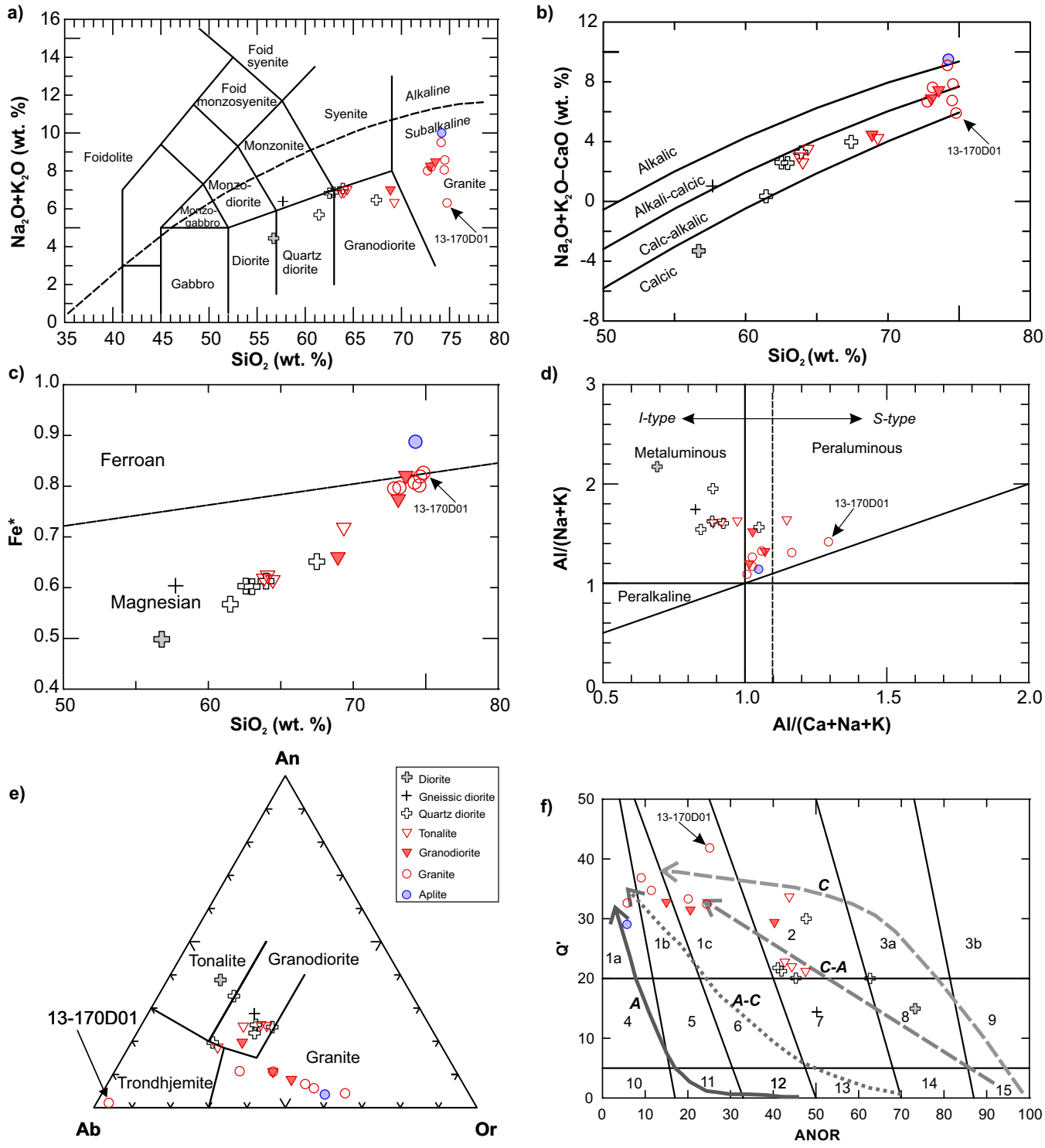

Figure 53: *Chemical classification of unit 12 granitoid rocks from the Cat Creek–Euclid Lake area:* ***a)*** *total alkalis (Na_2O+K_2O, wt. %) versus SiO_2 (wt. %) diagram (i.e., TAS; fields from Middlemost, 1994; boundary between alkaline and subalkaline series from Irvine and Baragar, 1971);* ***b)*** *MOLI (Na_2O+K_2O–CaO; wt. %) versus SiO_2 (wt. %; after Frost et al., 2001);* ***c)*** *classification of ferroan versus magnesian granitoids (from Frost et al., 2001; $Fe^*=FeO^t/(FeO^t+MgO)$;* ***d)*** *Shand index plot (fields from Maniar and Piccoli, 1989); $ACNK=Al_2O_3/(CaO+Na_2O+K_2O)$, $A/NK=Al_2O_3/(Na_2O+K_2O)$, units in moles; vertical dashed line indicates ACNK=1.1, a key parameter discriminating S- from I-type granites (Chappell and White, 1974);* ***e)*** *Ab-An-Or ternary diagram (fields from Barker, 1979);* ***f)*** *CIPW normative Q' versus ANOR diagram (after Streckeisen and Le Maitre, 1979); Q'=CIPW normative 100*Qz/(Qz+Or+Ab+An); ANOR=CIPW normative 100*An/(An+Or). Rock-unit abbreviations: 1a, alkali-feldspar granite; 1b, syenogranite; 1c, monzogranite; 2, granodiorite; 3a, tonalite; 3b, calc-tonalite; 4, alkali-feldspar quartz syenite; 5, quartz syenite; 6, quartz monzonite; 7, quartz monzodiorite; 8, quartz diorite; 9, quartz gabbro; 10, alkali-feldspar syenite; 11, syenite; 12, monzonite; 13, monzogabbro; 14, diorite; 15, gabbro. Coarse dashed and solid lines with arrows indicate interpreted differentiation trends of different magmatic suites (after Whalen and Frost, 2013): A, alkali; A-C, alkali-calcic; C, calcic; C-A, calc-alkalic. Mineral abbreviations: Ab, albite; An, anorthite; Or, orthoclase; Qz, quartz.*

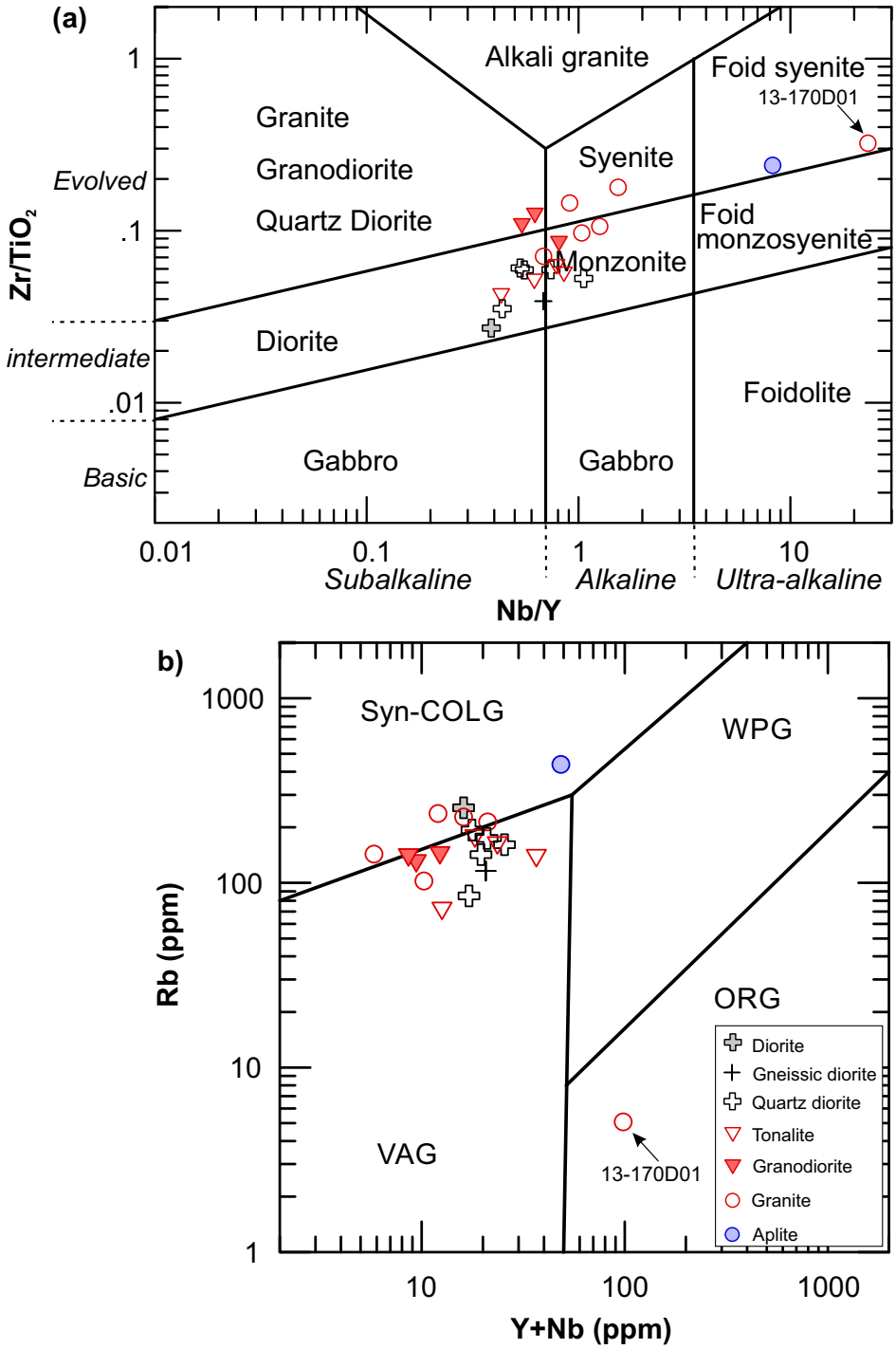

Figure 54: *Trace-element discrimination diagram for unit 12 granitoid rocks from the Cat Creek–Euclid Lake area:* ***a)*** *Zr/TiO_2 versus Nb/Y (after Pearce, 1996);* ***b)*** *(Y+Nb) versus Rb (after Pearce et al., 1984). Abbreviations: ORG, ocean-ridge granitoid; Syn-COLG, syncollisional granitoid; VAG, volcanic-arc granitoid; WPG, within-plate granitoid.*

terns with slightly negative to positive Eu anomalies, and their LREE/HREE ratios decrease with increasing degree of differentiation. It is noted that the aplite sample has the lowest REE abundance and LREE/HREE ratio, which likely resulted from magmatic fractionation. Subunit 12b rocks (Figure 55b) are characterized by LREE-enriched and HREE-depleted patterns with notably negative Eu anomalies. The negative Eu anomalies become pronounced with differentiation, and the patterns in the HREE portion become concave. The pegmatitic granite (sample 111-170D01) displays much lower REE abundance and a slightly LREE-enriched pattern with a more pronounced Eu negative anomaly compared with other subunit 12b samples, suggesting these may have different origins.

Figure 55c and d shows primitive-mantle–normalized, extended trace-element profiles of unit 12 granitoid rocks, revealing that they are enriched in incompatible elements with

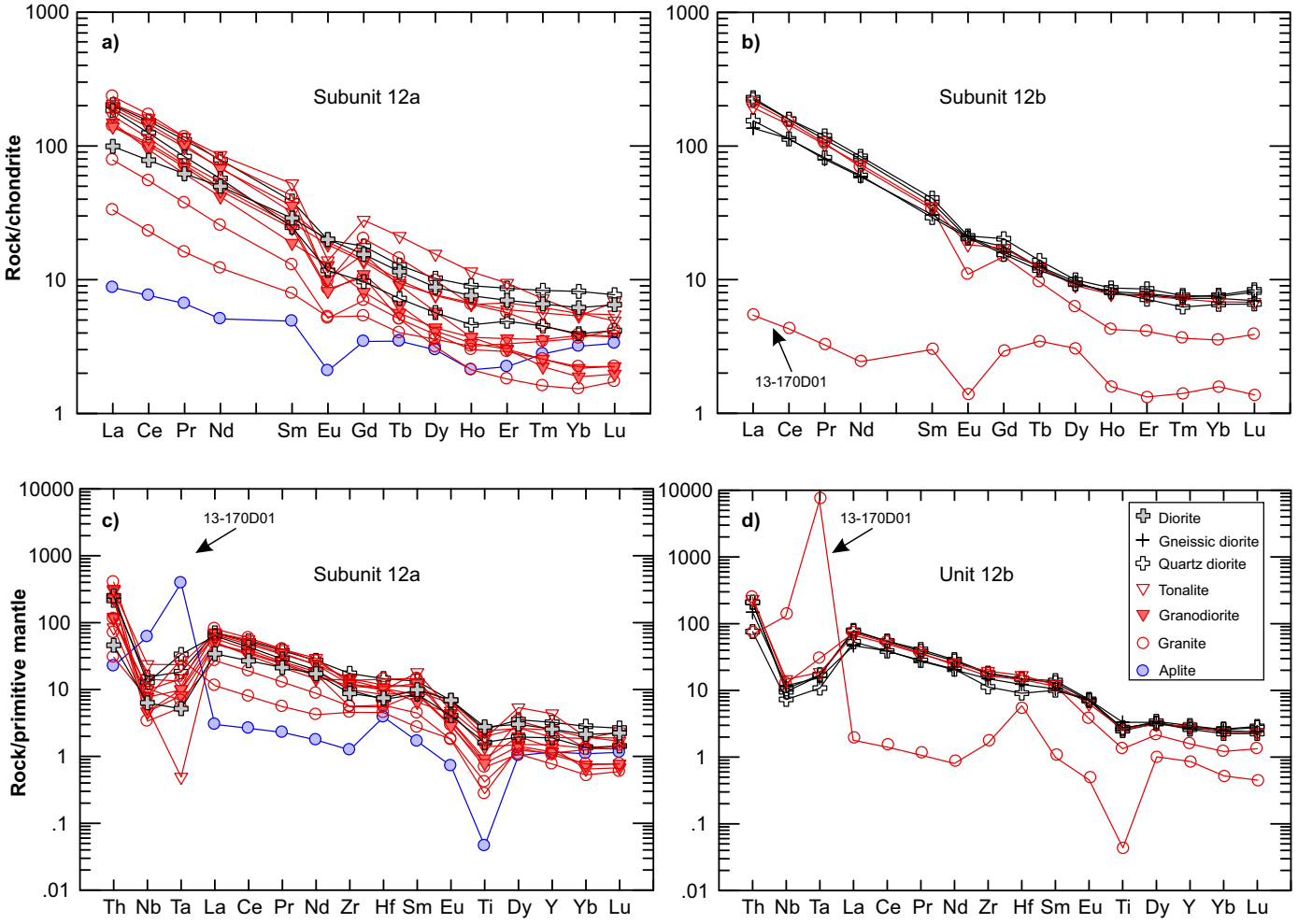

Figure 55: *Chondrite-normalized rare-earth element patterns (**a, b**) and primitive-mantle–normalized extended trace-element plots (**c, d**) for unit 12 granitoid rocks from the Cat Creek–Euclid Lake area. Normalizing values from Sun and McDonough (1989).*

pronounced negative Nb, Ta and Ti anomalies, except for the aplite sample in subunit 12a and the pegmatitic granite sample in subunit 12b. These exceptions are characterized by their much higher Nb and Ta abundances and thus display positive anomalies.

Figure 56a shows a scattered distribution of unit 12 granitoid rocks on a plot of Nb/Ta versus Zr/Sm, ranging from MORB to TTG although most of the samples plot in the fields of TTG and adakite. These rocks have relatively low Nb/Ta ratios (<17.4) and high Zr/Sm ratios (>25.2) compared to primitive mantle, MORB, ocean-island basalts and island-arc basalts, and are more similar to Archean TTG and/or adakite (Foley et al., 2002). This suggests that unit 12 granitoid rocks may have been derived from partial melting of amphibolite (Foley et al., 2002) in a volcanic-arc setting. Interestingly, the pegmatitic granite and aplite show very low Nb/Ta ratios, likely due to extreme fractionation aided by internal fluids in the magmatic system (Yang et al., 2019). On a plot of Sr/Y versus La/Yb (Figure 56b), most of the unit 12 granitoid samples represent medium- to low-P TTG based on their Sr/Y ratios that range from 10 to 200 and La/Yb ratios that are >20 (Moyen and Martin, 2012). Relatively low La/Yb and Sr/Y ratios in granitoids can be explained by plagioclase fractionation, which also leads to moderately negative Eu anomalies (Figure 55a, b).

Units 13 and 14

Major elements

Most of the whole-rock samples from units 13 and 14 generally have high SiO_2 contents and plot in the granite field of the TAS diagram (Figure 57a), but two samples from unit 13 fall in the granodiorite field and just above the boundary between granodiorite and quartz syenite (Table 6; Table 6_2 of DRI2020024). These rocks all belong to the subalkaline series. On the MALI versus SiO_2 (wt. %) plot of Frost et al. (2001), these subalkaline granitic rocks are mostly alkali-calcic to calc-alkalic, although two samples are well within the calcic field (Figure 57b).

The Rittmann Serial Index (σ; Rittmann, 1973) values for samples of units 13 and 14 granitic rocks range from 1.87 to 3.03, suggesting the calcalkaline series (Yang, 2007); only two samples have lower σ values of 0.47–0.81, which places

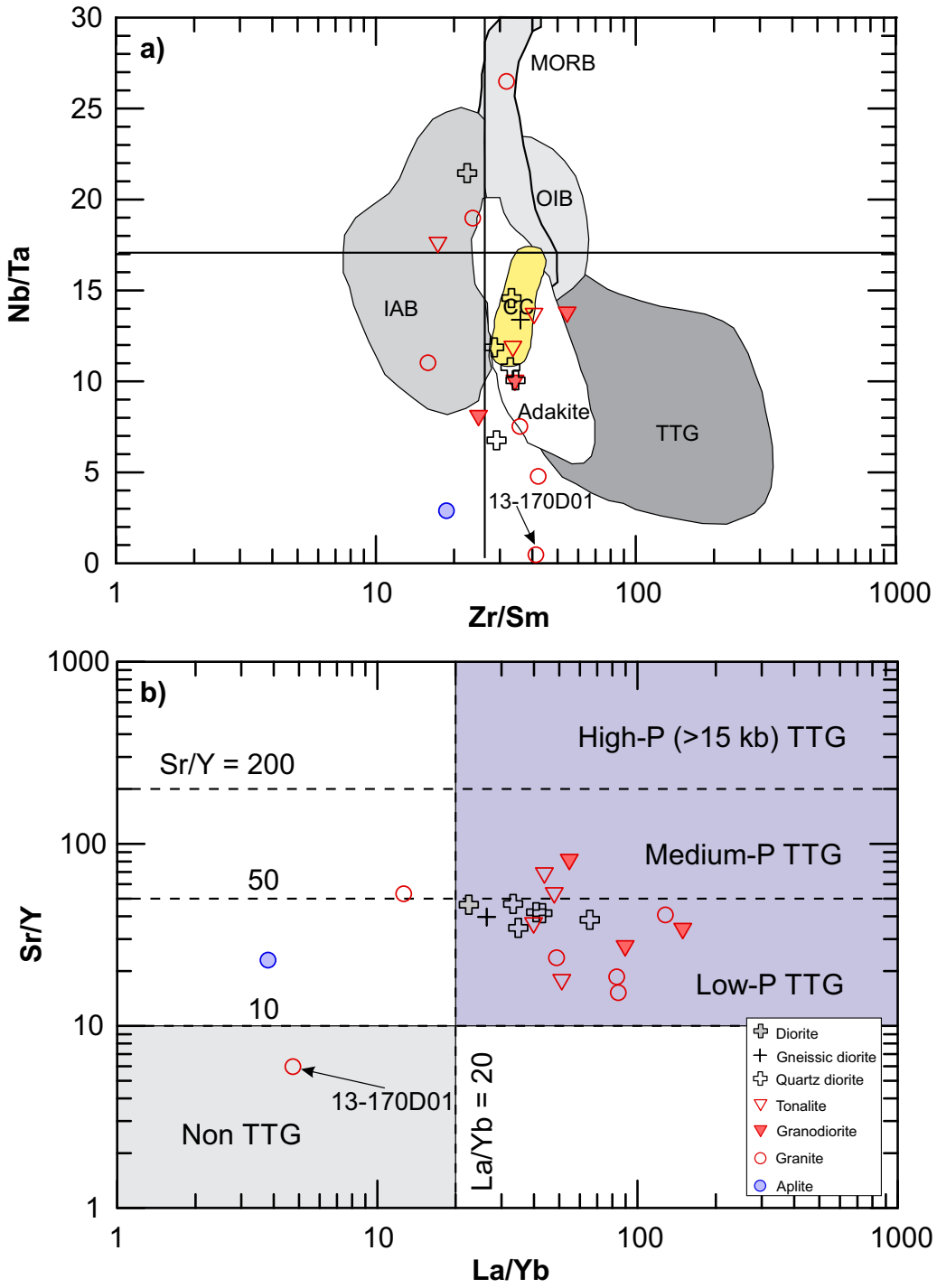

Figure 56: *Trace-element discrimination diagram for unit 12 granitoid rocks from the Cat Creek–Euclid Lake area:* ***a)*** *Zr/Sm versus Nb/Tb (after Foley et al., 2002); primitive-mantle Na/Ta and Zr/Sm ratios are 17.4 and 25.2, respectively (Sun and McDonough, 1989);* ***b)*** *La/Yb versus Sr/Y; boundary between Sr/Y and La/Yb ratios used to define TTG and subtypes from Moyen and Martin (2012). Abbreviations: CC, continental crust; IAB, island-arc basalt; MORB, mid-ocean–ridge basalt; OIB, ocean-island basalt; TTG, tonalite-trondhjemite-granodiorite.*

them in the calcic series (Table 6_2 of DRI2020024). These observations agree with the results shown in Figure 57b. On the K_2O versus SiO_2 plot (not shown), units 13 and 14 rocks plot within the medium- to high-K fields of the calcalkaline series (Peccerillo and Taylor, 1976); this assignment is supported by the fact that they are mostly enriched in K_2O relative to Na_2O (Table 6; Table 6_2 of DRI2020024).

Unit 13 granitoids and unit 14 granitic pegmatite and aplite are S-type granites that are dominantly ferroan, but some samples plot in the magnesian field (Figure 57c), suggesting that intra-intrusion magmatic differentiation may have caused such compositional variation (Clarke, 1992). These granitoid rocks are moderately to strongly peraluminous (Figure 57d), which is typical for S-type granites (Chappell and White, 1974, 2001;

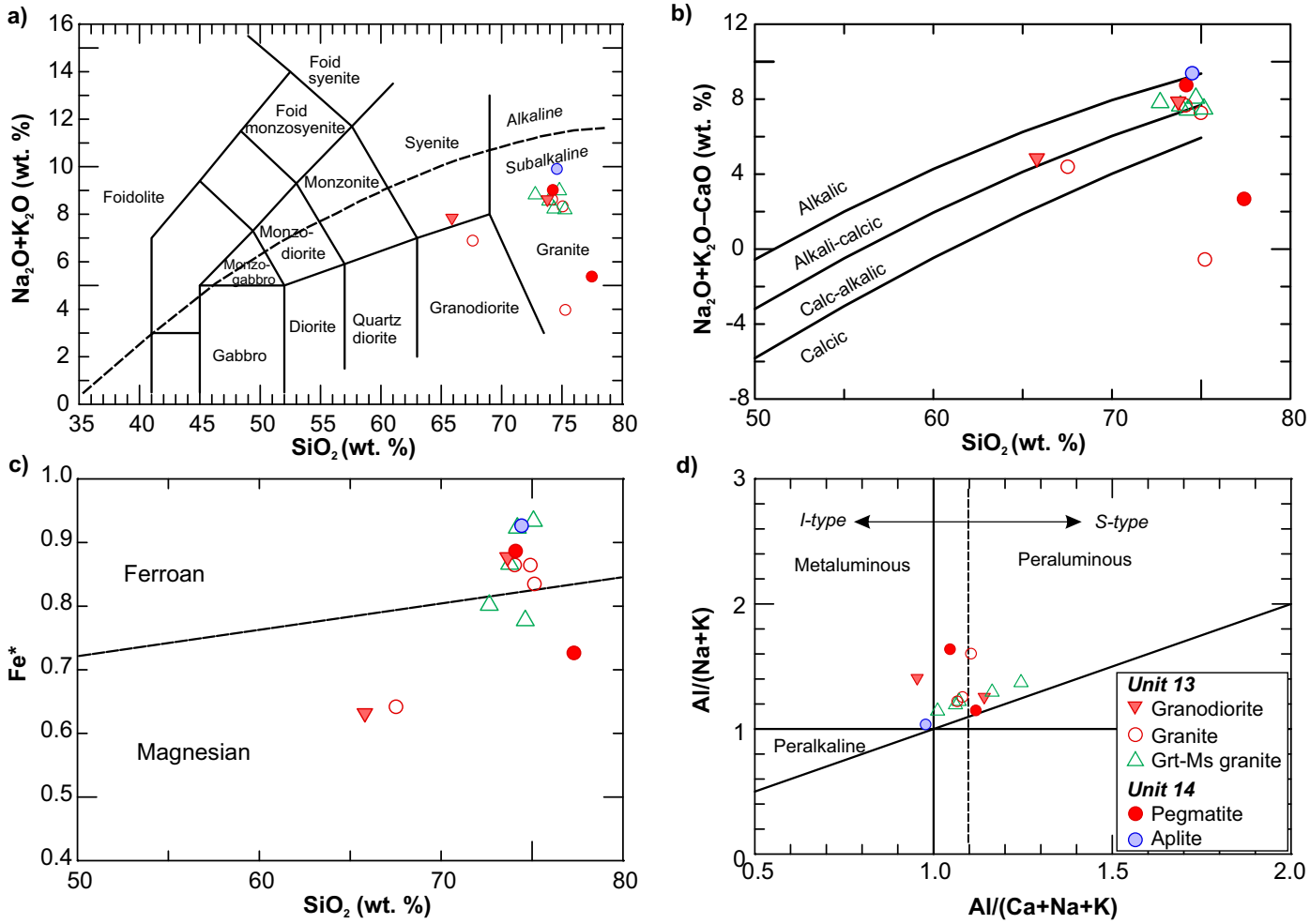

Figure 57: *Chemical classification of units 13 and 14 granitoid rocks from the Cat Creek–Euclid Lake area:* ***a)*** *total alkalis (Na_2O+K_2O, wt. %) versus SiO_2 (wt. %) diagram (i.e., TAS; fields from Middlemost, 1994); boundary between alkaline and subalkaline series from Irvine and Baragar (1971);* ***b)*** *MOLI (Na_2O+K_2O–CaO, wt. %) vs. SiO_2 (wt. %; after Frost et al., 2001);* ***c)*** *classification of ferroan versus magnesian granitoids ($Fe^*=FeO^t/(FeO^t+MgO$; from Frost et al., 2001);* ***d)*** *Shand index plot (fields from Maniar and Piccoli, 1989); ACNK=$Al_2O_3/(CaO+Na_2O+K_2O)$, A/NK=$Al_2O_3/(Na_2O+K_2O)$, units in moles; vertical dashed line indicates ACNK=1.1, a key parameter discriminating S- and I-type granites (Chappell and White, 1974). Abbreviations: Grt, garnet; Ms, muscovite.*

Clarke, 1992, 2019; Yang et al., 2019). The unit 14 aplite sample and a unit 13 granodiorite sample are metaluminous, further indicating intra-intrusion differentiation.

Trace elements

Unit 13 granitoid rocks display varied abundances of large-ion lithophile elements (e.g., Rb, Cs, Sr, Ba) and relatively low concentrations of transition metals (e.g., Co, Ni; Table 6 and Table 6_2 of DRI2020024). Unit 14 pegmatite and aplite are strongly enriched in Be, Rb, Cs, Nb and Ta, similar to those in the LCT pegmatites of Černeý and Ercit (2005), which are genetically related to S-type granites.

Most of the samples from units 13 and 14 have low Sr (<400 ppm) and low Yb (<2 ppm) contents (Figure 58a; Table 6_2 of DRI2020024), suggesting that their parental magmas may have formed at medium pressures from sources with a granulite-facies residue comprising plagioclase, pyroxene ±garnet (Zhang et al., 2006). They contrast with typical TTG suite rocks that display much higher Sr and low Yb, and formed at higher pressures in a source region with appreciable amounts of garnet but no plagioclase (Martin et al., 2005; Zhang et al., 2006; Moyen and Martin, 2012). Negative Eu anomalies and low Sr/Y and La/Yb ratios in the S-type granites (Figure 58b) suggest that they require the presence of plagioclase in their source magma but the absence of garnet at relatively low to moderate pressures (e.g., Castillo et al., 1999; Zhang et al., 2006; Moyen and Martin, 2012). Furthermore, intrapluton and interpluton variations in both Eu/Eu* and Gd/Yb ratios (Figure 58b) suggest that units 13 and 14 granites and related pegmatite and aplite likely originated from such heterogeneous sources.

REE patterns

Chondrite-normalized REE patterns of unit 13 granitoids display LREE enrichment relative to HREE with variable nega-

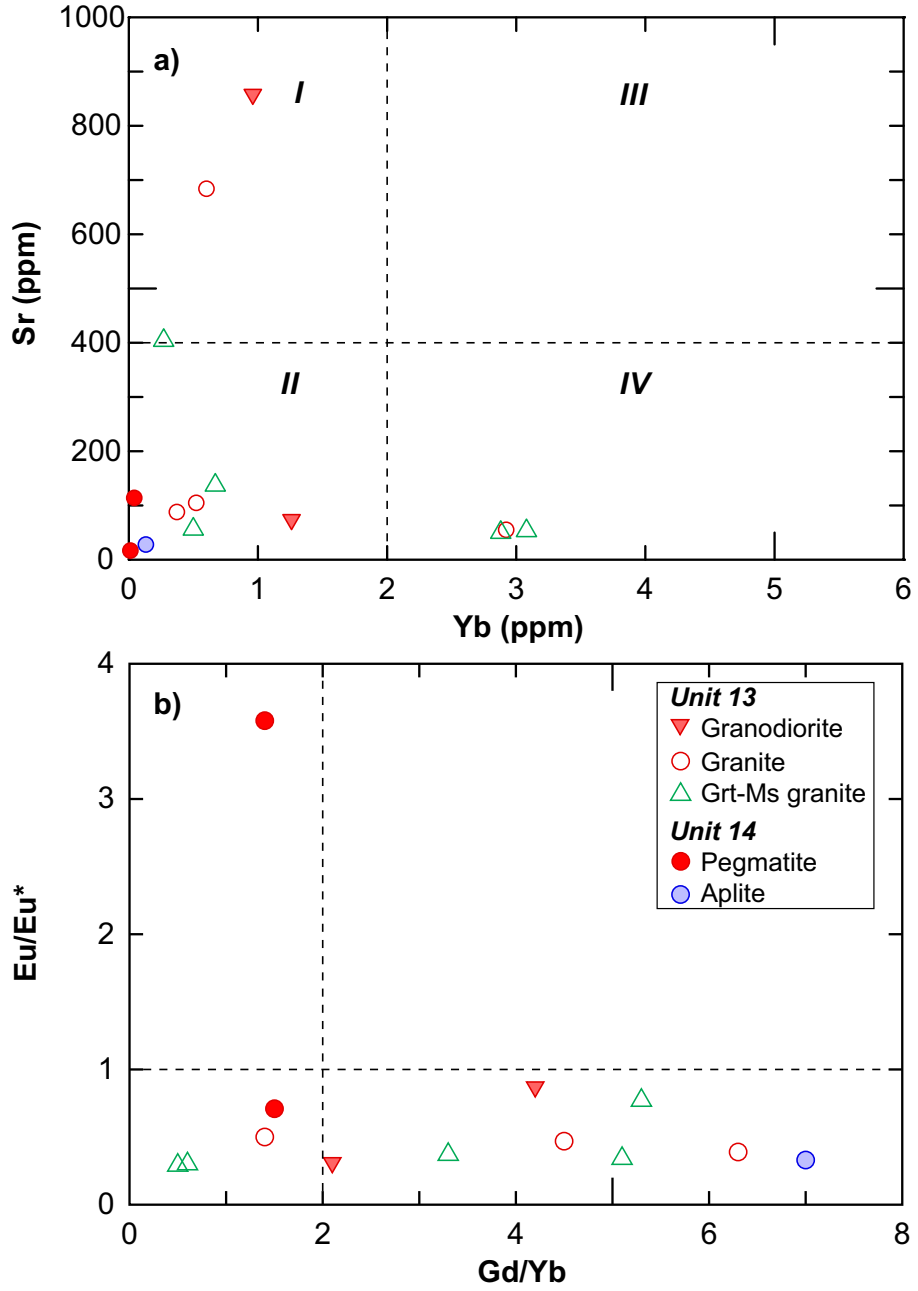

Figure 58: *Discriminant diagrams of elemental abundances and ratios for units 13 and 14 granitoid rocks from the Cat Creek–Euclid Lake area:* ***a)*** *Sr (ppm) versus Yb (ppm); fields I–IV from Zhang et al. (2006);* ***b)*** *Eu/Eu* versus Gd/Yb. Field abbreviations: I, granitoids with high Sr and Yb contents (magmas derived from high-pressure sources in equilibrium with eclogite-facies residues); II, granitoids with low Sr and low Yb contents (magmas derived from moderate-pressure sources in equilibrium with granulite-facies residues); III, granitoids with high Sr and high Yb contents (magmas from low-pressure sources in equilibrium with amphibolite-facies residues); IV, granitoids with low Sr and high Yb contents (magmas from very low pressure sources in equilibrium with gabbroic residues such as modern middle-ocean-ridge). Mineral abbreviations: Grt, garnet; Ms, muscovite.*

tive Eu anomalies (Eu/Eu*=0.29–0.87; Figure 59a; Table 6_2 of DRI2020024). Unit 14 aplite shows an REE pattern similar to unit 13, but pegmatites from unit 14 display much lower REE abundances with LREE enrichment and slightly negative to pronounced positive Eu anomalies. These geochemical characteristics suggest that the sources of the rocks in units 13 and 14 did not have a garnet residue and formed at shallower depths than the I-type granitoids of the TTG suite, which were derived from deeper magma sources containing an appreciable amount of garnet (e.g., Martin et al., 2005; Moyen and Martin, 2012).

Extended trace-element patterns

On primitive-mantle–normalized multi-element plots (Figure 59b), unit 13 granitoid rocks show relative enrichments in Th, LREE, Zr and Hf, with pronounced negative Nb, Ta and Ti anomalies. Unit 14 pegmatite and aplite samples have much

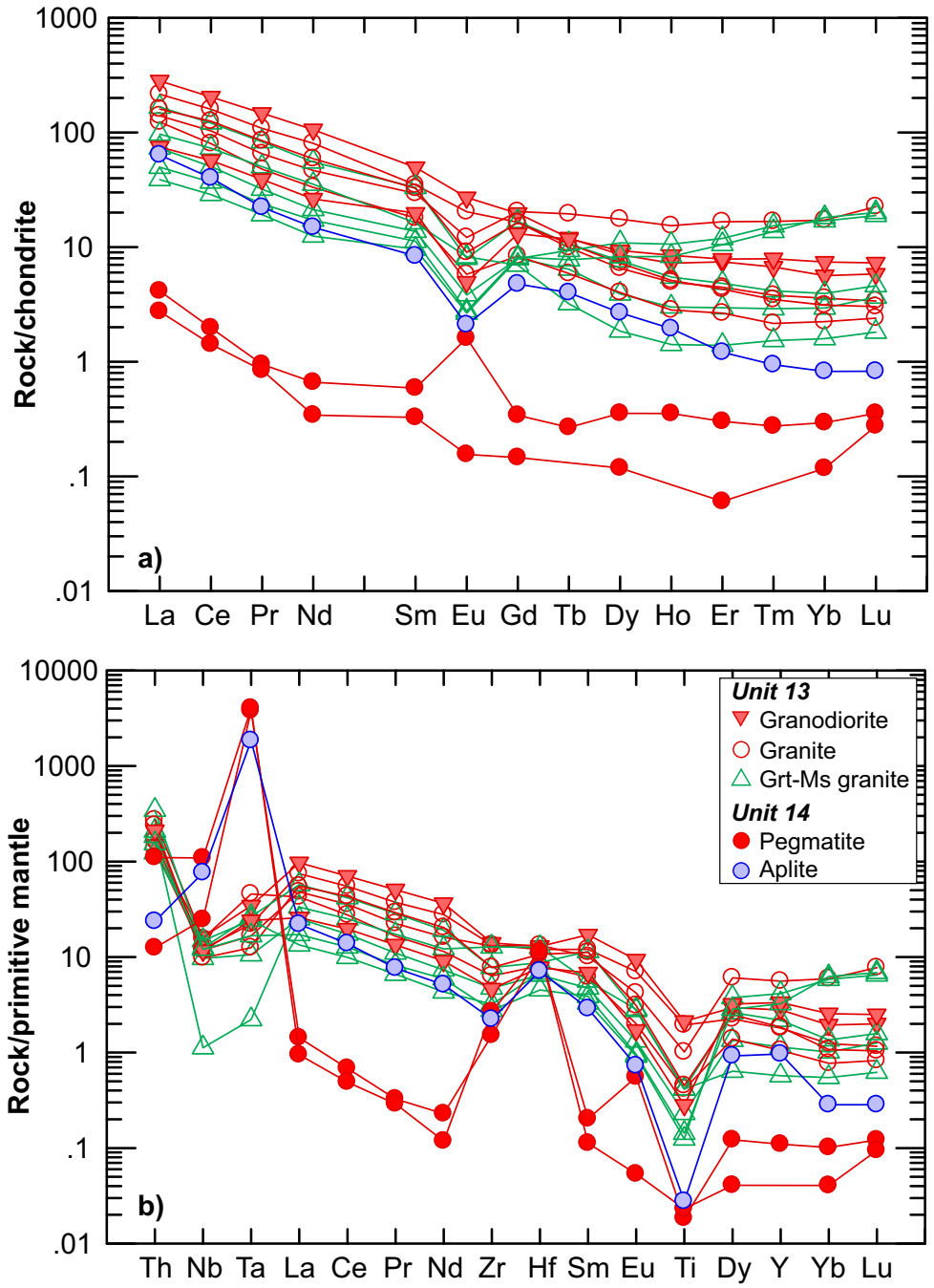

Figure 59: *Chondrite-normalized rare-earth element patterns* ***a)*** *and primitive-mantle–normalized extended trace-element plots* ***b)*** *for units 13 and 14 rocks from the Cat Creek–Euclid Lake area. Normalizing values from Sun and McDonough (1989). Abbreviations: Grt, garnet; Ms, muscovite.*

higher Nb (up to 77.7 ppm) and Ta (up to 164 ppm), and lower values for the other HFSE (Table 6_2 of DRI2020024), with enormously positive Nb and Ta anomalies and positive Zr and Hf anomalies. All of this suggests that these rare metals are strongly enriched because of high differentiation, which is also indicated by very low Nb/Ta ratios of <1 (Figure 60a). These Nb/Ta ratios are much lower than that of the upper continental crust (13.3; Rudnick and Gao, 2010) and also lower than those of less evolved S-type granites (6.0–6.0) from the Inconnu pluton (Yang et al., 2019). Such low Nb/Ta ratios, and the enrichment in Nb and Ta, require extreme fractional crystallization of micas aided by internal fluid (cf., Dostal and Chatterjee, 2000; Yang et al., 2008; Stepanov et al., 2014). As pointed out by Ballouard et al. (2016), interaction of peraluminous S-type granites with internal subsolidus magmatic fluids would not only differentiate Nb from Ta, but also decrease Nb/Ta ratios to <5. Notably, unit 14 rocks also show pronounced positive Zr and Hf anomalies with low Zr/Hf ratios (<12; Figure 60a), which are much lower than that of the upper continental crust (36.4; Rudnick and Gao, 2010) and lower than those of less

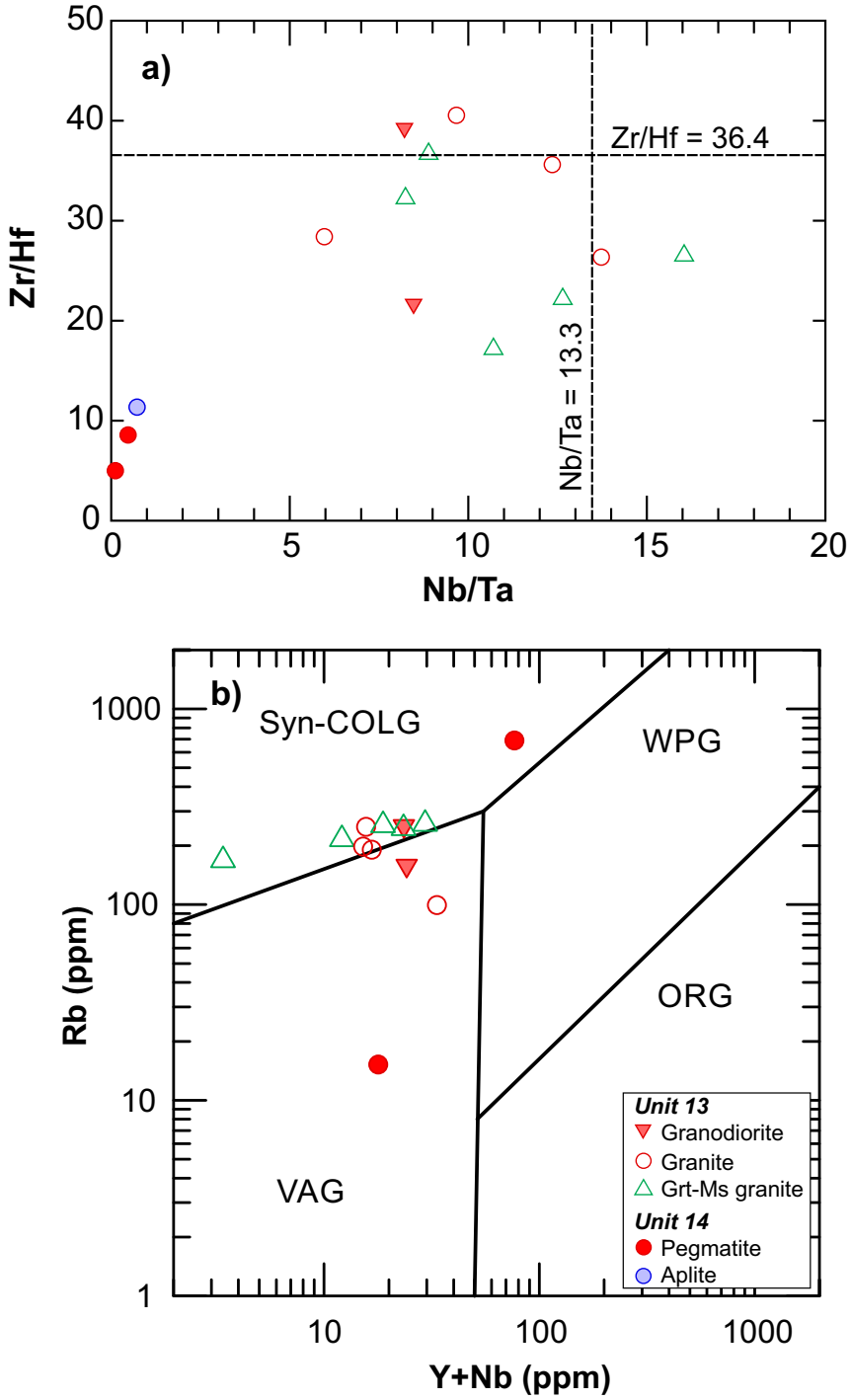

Figure 60: *Discriminant diagrams of elemental abundances and elemental ratios for units 13 and 14 rocks from the Cat Creek–Euclid Lake area:* ***a)*** *Zr/Hf versus Nb/Ta (Na/Ta ratio of 13.3 and Zr/Hf ratio of 36.4 in the upper continental crust from Rudnick and Gao, 2010);* ***b)*** *(Y+Nb) versus Rb (after Pearce et al., 1984). Abbreviations: Grt, garnet; Ms, muscovite; ORG, ocean-ridge granitoid; syn-COLG, syncollisional granitoids; VAG, volcanic-arc granitoid; WPG, within-plate granitoid.*

evolved S-type granites (17.1–36.7) from the Inconnu pluton (Yang et al., 2019). Linnen and Keppler (2002) suggested that a decrease in Zr/Hf ratios of peraluminous granites may result from zircon fractionation. Positive Zr and Hf anomalies in the S-type pegmatitic granite and muscovite pegmatite suggest that they could contain notable amounts of zircon as one of the accumulating phases.

Unit 13 granitoids plot mostly in the field of syncollisional granitoids defined by Pearce et al. (1984), although two samples, together with a pegmatite sample of unit 14, fall in the field of volcanic-arc granitoids (Figure 60b), which may be the result of K-feldspar (±biotite) fractionation. This indicates that unit 13 granitoid rocks are S-type, formed in a thickened-crust setting due to terrane collision (Yang et al., 2019).

Summary

In summary, lithogeochemical data demonstrate a typical signature of arc-related volcanic to volcaniclastic rocks and derived sedimentary rocks that constitute the supracrustal rock suites of units 2, 9 and 11. Intrusive rocks comprise unit 1 basement granitoids displaying arc affinities; units 3–7 Mayville mafic–ultramafic intrusion and unit 8 gabbroic rocks that show broad geochemical commonalities related to arc- to back-arc settings; unit 10 TTG and rocks of the unit 12 Inconnu pluton emplaced in a volcanic setting; unit 13 S-type granites formed in a collisional setting; and unit 14 pegmatitic and aplitic rocks associated with various granitoid intrusions.

Sm-Nd isotope systematics

Twenty whole-rock samples were selected for analysis of Sm-Nd isotopic composition at the University of Alberta. These samples are grouped into three classes in terms of their field relationships: the Mayville intrusion (units 3–7), volcanics and related synvolcanic gabbroic rocks (unit 2), and granitoid rocks (unit 1 granitoid basement and unit 10 TTG rocks). Detailed analytical procedures followed the approach described previously in Böhm et al. (2007) and Anderson (2013), which are also summarized in DRI2020024. The Sm-Nd isotopic data provided in Table 7 and Table 7 of DRI2020024 are used to identify the source(s) of these rocks and to assess plausible petroge-

Table 7: Sm-Nd isotopic data for representative whole-rock samples, Cat Creek–Euclid Lake area, Bird River greenstone belt.

Sample	UTM		Rock type	Sm (ppm)	Nd (ppm)	$^{147}Sm/^{144}Nd$[2]	$^{143}Nd/^{144}Nd$[3]	Err.[4] (2σ)	T_{DM}[5] (Ga)	T[6] (Ma)	$\varepsilon_{Nd}{}^{T}$[7]	Sm/Nd	$f^{Sm/Nd}$[8]	$\varepsilon_{Nd}{}^{0}$[9]	$T_{2\text{-}DM}$[10] (Ga)
	Easting[1]	Northing[1]													
Mayville mafic-ultramafic intrusion (units 3 to 7)															
111-12-604A01	315405	5612665	Gabbro	1.95	5.98	0.1970	0.51272	0.00001	n/a	2743	1.6	0.33	0.001	1.7	
111-12-621A01	313613	5613265	Magnetic gabbro,	6.80	20.0	0.2053	0.51286	0.00001	n/a	2743	1.4	0.34	0.044	4.4	
111-12-461A01	314150	5612506	Leucogabbro	0.67	2.08	0.1932	0.51267	0.00001	n/a	2743	1.8	0.32	-0.018	0.6	
111-12-547A01	319578	5611716	Golf-ball anorthosite	0.41	1.33	0.1844	0.51266	0.00001	n/a	2743	4.8	0.30	-0.063	0.4	
111-12-669A01	312453	5612101	Pyroxenite	0.47	1.22	0.2319	0.51337	0.00001	n/a	2743	1.8	0.38	0.179	14.2	
111-13-226A01	329665	5607285	Pyroxenite	1.43	6.22	0.1388	0.51166	0.00000	3.04	2743	1.4	0.23	-0.294	-19.1	
111-12-594A01	315139	5612633	Melagabbro	4.05	21.6	0.1137	0.51112	0.00001	3.09	2743	-0.3	0.19	-0.422	-29.6	
111-13-171A01	332361	5605049	Leucogabbro	0.714	2.36	0.1830	0.51249	0.00001	n/a	2743	1.9	0.30	-0.070	-2.9	
Mafic-ultramafic rocks (unit 2)															
111-12-485A01	313872	5611665	Basalt	2.21	6.73	0.1987	0.51273	0.00001	n/a	2743	1.1	0.33	0.010	1.8	
111-12-490A01	313809	5610578	Basalt	1.50	4.44	0.2039	0.51283	0.00001	n/a	2743	1.2	0.34	0.037	3.7	
111-13-056B01	325837	5609534	Basalt	3.26	10.1	0.1947	0.51265	0.00001	n/a	2743	0.9	0.32	-0.010	0.2	
111-13-108A01	324595	5608749	Gabbro	1.93	5.91	0.1971	0.51272	0.00001	n/a	2743	1.5	0.33	0.002	1.6	
111-13-170B01	332033	5605618	Gabbro (amphibolite)	6.01	34.34	0.1057	0.51102	0.00001	3.01	2743	0.5	0.17	-0.462	-31.7	
111-13-244A01	328803	5607798	Gabbro	1.01	3.03	0.2022	0.51282	0.00001	n/a	2743	1.7	0.33	0.028	3.6	
Granitoids															
Unit 10 TTG															
111-13-041A01	323868	5609811	Tonalite	4.73	29.3	0.0975	0.51081	0.00001	3.07	2725	-0.9	0.16	-0.504	-35.7	2.97
111-13-142B01	326107	5609209	Feldspar porphyry	5.15	29.7	0.1047	0.51099	0.00001	3.02	2725	0.0	0.17	-0.468	-32.2	2.89
111-13-167A01	332944	5605444	Granite	6.44	36.4	0.1071	0.51105	0.00001	3.00	2725	0.5	0.18	-0.455	-30.9	2.85
Unit 1 basement granitoids															
111-13-149A01	327619	5606634	Granodiorite	2.88	23.7	0.0735	0.51042	0.00001	2.97	2832	1.6	0.12	-0.626	-43.4	2.91
111-13-051A01	323968	5608315	Granite	5.31	59.31	0.0542	0.51005	0.00001	2.96	2832	1.5	0.09	-0.725	-50.5	2.86
111-13-211A01	328790	5606444	Tonalite	3.67	21.89	0.1013	0.51091	0.00001	3.03	2832	1.1	0.17	-0.485	-33.7	2.89

Abbreviation: n/a, not applicable.
[1] UTM co-ordinates (Zone 15, NAD83)
[2] Estimated error is better than 0.5%
[3] Normalized to $^{146}Nd/^{144}Nd = 0.7219$; external precision based on repeat La Jolla Nd standard runs
[4] Analytical uncertainty
[5] Depleted mantle Nd model ages calculated according to the model of DePaolo (1981); T_{DM} not calculated for samples with $^{147}Sm/^{144}Nd > 0.14$
[6] Known or inferred age
[7] ε_{Nd} values at the known or inferred age (T) calculated using present-day chondritic ratios of $^{143}Nd/^{144}Nd = 0.512638$ and $^{147}Sm/^{144}Nd = 0.1967$
[8] Fractionation factor (Rollinson, 1993)
[9] ε_{Nd} values at present calculated using present-day chondritic ratios of $^{143}Nd/^{144}Nd = 0.512638$ and $^{147}Sm/^{144}Nd = 0.1967$
[10] Two-stage depleted mantle Nd model ages calculated according to the model of Liew and Hofmann (1988)

netic processes (e.g., crustal contamination; O'Nions et al., 1979; DePaolo, 1981, 1988; Rollinson, 1993).

Results

Whole-rock samples of the Mayville intrusion yielded $^{147}Sm/^{144}Nd$ isotope ratios of 0.1137–0.2319 and $^{143}Nd/^{144}Nd$ isotope ratios of 0.511120–0.513365 (Table 7). Plotting the samples (n=8) on a bivariate diagram results in a collinear data array (not shown), which returns an errorchron corresponding to an age of 2776 +110/–240 Ma with an initial $^{143}Nd/^{144}Nd$ ratio of 0.50912 ±0.00024 (or with an $\varepsilon_{Nd}^{isochron,t}$ value of +1.6), based on a robust regression calculation using the Isoplot 3.70 program (Ludwig, 2008). Within its large uncertainty, this errorchron age is roughly consistent with the U-Pb zircon age of 2742.8 ±0.8 Ma for the Mayville intrusion (Houlé et al., 2013). The Mayville intrusion samples have a relatively small range of ε_{Nd}^{t} values (+1.4 to +1.9), except for two samples (–0.3 for melagabbro sample 111-12-594A01 and +4.8 for 'golf-ball' anorthosite sample 111-12-547A01; Table 7). This strongly indicates that the Mayville intrusion's parental magma(s) was derived from a depleted-mantle source, although some minor degree of crustal contamination or mantle heterogeneity cannot be ruled out (Sotiriou et al., 2019, 2020). Two depleted-mantle model ages (T_{DM}) for Mayville intrusion samples with measured $^{147}Sm/^{144}Nd$ ratios smaller than 0.14 (Table 7) yielded ~ 3.1–3.0 Ga, suggesting that the magma(s) may have been separated from the mantle source around that time (DePaolo, 1981, 1988; Figure 61). Interestingly, the Mayville intrusion samples display a large range of the fractionation factor $f^{Sm/Nd}$ (Rollinson, 1993), from –0.48 to +0.18, indicating that these samples may have evolved along two different paths: one group to positive $\varepsilon_{Nd}^{t=0}$ values (+0.4 to +14.2) and the other to negative values (–29.6 to –2.9). Such Sm-Nd isotopic systematics require further discussion (see 'Discussion' section).

Six samples collected from unit 2 volcanic rocks and related synvolcanic gabbroic rocks display a narrow range of ε_{Nd}^{t} values between +0.4 and +1.7, suggesting that these rocks, similar to those from the Mayville intrusion, may have been derived from a depleted-mantle source. One sample yielded a depleted-mantle model age of ca. 3.0 Ga. Positive fractionation factor ($f^{Sm/Nd}$; Rollinson, 1993) values of 0.002–0.04 indicate that most of the samples evolved to positive $\varepsilon_{Nd}^{t=0}$ values, consistent with their LREE-depleted patterns, akin to modern MORB. Gabbro (amphibolite) sample 111-13-170B01 has a negative $f^{Sm/Nd}$ value of –0.46, indicating that it evolved to a highly negative value of $\varepsilon_{Nd}^{t=0}$ (= –31.7). An errorchon for the unit 2 samples using robust regression yielded a poorly defined age of 2830 +300/–1800 Ma with an initial $^{143}Nd/^{144}Nd$ ratio of 0.50904 ±0.00080 (or with $\varepsilon_{Nd}^{isochron,t}$ value of +1.6).

Six granitoid samples, three from unit 1 basement rocks and three from unit 10 TTG rocks, yielded positive ε_{Nd}^{t} values ranging from +0.09 to +1.8 (Table 7), indicating that they may

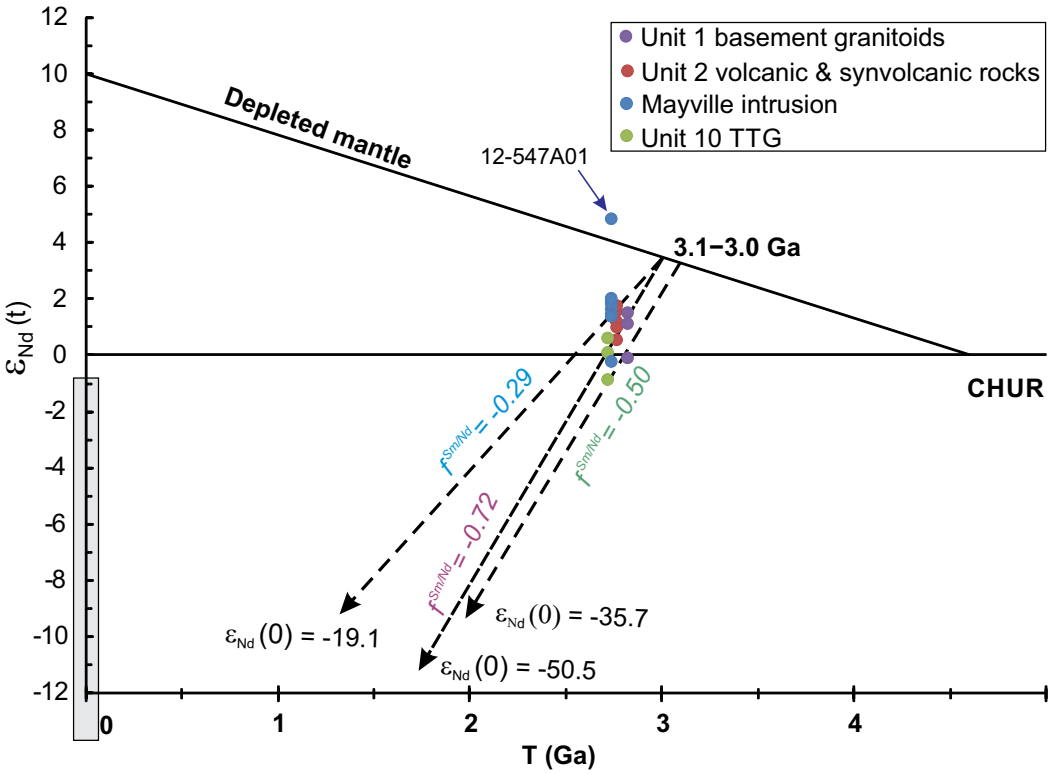

Figure 61: *Time (t) versus ε_{Nd} evolution diagram for whole-rock samples from the Cat Creek–Euclid Lake area. $f^{Sm/Nd}$ denotes fractionation factor (Rollinson, 1993). Note that 'golf-ball' anorthosite sample 111-12-547A01 plots above the depleted-mantle evolution line defined by Goldstein et al. (1984), likely related to heterogeneity of the depleted-mantle source. Grey box on the y-axis denotes values of $\varepsilon_{Nd}^{t=0}$ at present.*

have been derived from a protolith akin to a depleted-mantle source (or juvenile crustal material) that was separated from the mantle at ca. 3.1–3.0 Ga, as indicated by their depleted-mantle model ages (Table 7). However, these samples display consistently highly negative $f^{Sm/Nd}$ values ranging from –0.46 to –0.72, corresponding to highly negative $\varepsilon_{Nd}^{t=0}$ values of –30.9 to –50.5 at present (Figure 61), which is consistent with their LREE-enriched patterns. Linear regression of these six samples returned an errorchron age of 2880 +880/–230 Ma with an initial $^{143}Nd/^{144}Nd$ ratio of 0.50902 ±0.00046 (or with $\varepsilon_{Nd}^{isochron,t}$ value of +2.6).

Figure 62 presents a plot of Th/Yb ratios against ε_{Nd}^{t}, in which the Th/Yb ratios are used as an index for crustal contamination (e.g., Parks et al., 2014). The sample data points are clearly scattered, although the mafic samples, including those from the Mayville intrusion, have low to very low Th/Yb ratios (mostly <1.0). One gabbroic sample (111-170B01) has a Th/Yb ratio of 6.6, which is interpreted to be the result of crustal contamination. The granitoid samples have much higher Th/Yb ratios, all >2 (up to 50), suggesting that they were derived from a source region dominated by crustal material. More significantly, there is no correlation between the Th/Yb ratios and ε_{Nd}^{t} for the Mayville intrusion samples, indicating that their parental basaltic magmas are of arc-like origin, likely related to oceanic-plate subduction. Most of the Mayville intrusion samples, together with the unit 2 volcanic and synvolcanic gabbroic rocks, appear to have Th/Yb ratios that decrease with increasing ε_{Nd}^{t} values (Figure 62), pointing to a crustal contamination trend, possibly with the basement granitoids of unit 1 as the contaminant. This is also supported by the field observations and trace-element compositions previously described.

It needs to pointed out that the golf-ball anorthosite sample 111-12-547A01 has a very low Th/Yb ratio of 0.07 and a very high ε_{Nd}^{t} value of +4.8 (Table 7; Figure 62), above the depleted-mantle evolution line (Figure 61). The consistent relationship recorded by this sample between the Th/Yb and ε_{Nd}^{t} values provides evidence for the presence of a more depleted mantle and no crustal contamination. Thus, the depleted-mantle source must have been heterogeneous, sub-arc lithospheric mantle.

Furthermore, the Sm/Nd ratio is another index for measuring LREE fractionation of magmatic rocks. The Sm/Nd ratios for samples of the Mayville intrusion are 0.19–0.38 (average 0.30), for unit 2 volcanic and associated synvolcanic gabbroic rocks they are 0.17–0.34 (average 0.30), for unit 10 TTG they are 0.16–0.18 (average 0.17) and for unit 1 basement granitoids they are 0.09–0.17 (average 0.13). The Sm/Nd ratios are positively correlated with $f^{Sm/Nd}$ (Table 7). Most samples from the Mayville intrusion and unit 2 mafic rocks have Sm/Nd ratios higher than that of upper continental crust (0.19; Goldstein et al., 1984) and average continental crust (0.195; Rudnick and Gao, 2010) but lower than the primitive mantle (0.33) and N-type MORB (0.36; Sun and McDonough, 1989). All granitoid samples have Sm/Nd ratios lower than average

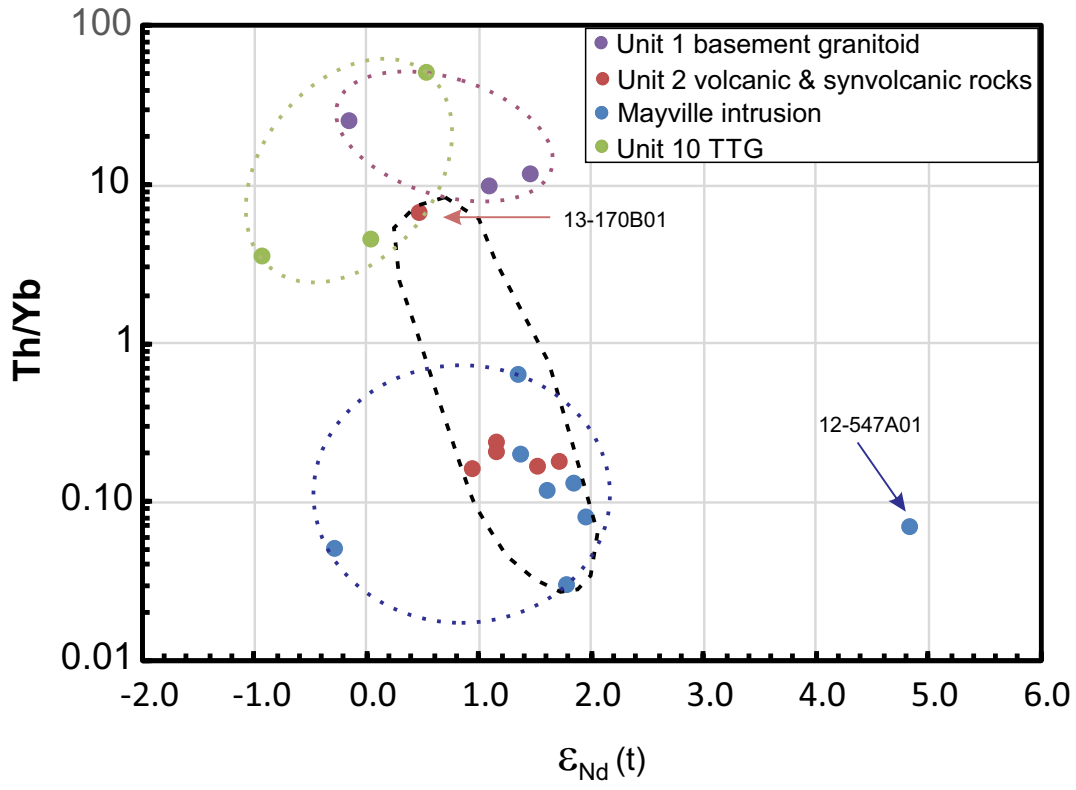

Figure 62: *Plot of Th/Yb ratios versus ε_{Nd}^{t} for whole-rock samples from the Cat Creek–Euclid Lake area.*

continental crust. Consequently, those mafic samples with Sm/Nd ratios <0.20 (Table 7) were likely contaminated by the unit 1 basement granitoids.

Discussion

In summary, the Sm-Nd isotopic data reveal that the parental magmas of the Mayville intrusion (units 3–7) and mafic volcanic and synvolcanic gabbroic rocks (unit 2) may have been derived from a depleted-mantle source, and that the magmas extracted from the mantle at ca. 3.1–3.0 Ga were likely arc related and contaminated to some extent by the granitoid basement (unit 1). Consequently, a juvenile crust formed via crust-mantle differentiation (Hawkesworth and Kemp, 2006; Frisch et al., 2011; Lee et al., 2011). Furthermore, it is noteworthy that unit 10 TTG and unit 1 basement granitoids may have been derived from a juvenile crustal source that had also separated from a depleted mantle, likely oceanic lithosphere (e.g., Babuška and Plomerová, 2020), at ca. 3.1–3.0 Ga. This is further constrained by the high T-P phase equilibrium relationship that has the granitic melts in impossible direct chemical equilibrium with the depleted mantle (e.g., Clarke, 1992; Scaillet et al., 2016; Yang, 2017; Clemens, 2018; Hildebrand et al., 2018; Clemens et al., 2020; Yang et al., 2020). Thus, the granitoids with positive ε_{Nd}^{t} values must have been derived from partial melting of juvenile crustal material, likely of an amphibolite source as constrained by lithogeochemical characteristics described above. However, calculation of single-stage depleted-mantle Nd model ages (Table 7) could not discern the difference in source regions between the mafic rocks (i.e., the Mayville intrusion of units 3–7, and unit 2 basalt and associated synvolcanic gabbro) and granitoid rocks (i.e., unit 1 granitoid basement and unit 10 TTG suite).

Therefore, it is necessary to use either a two-stage depleted-mantle Nd model (see Liew and Hofmann, 1988; Janoušek, 1999) to constrain the evolution of juvenile crustal source(s) or short-lived crustal material derived from the mantle (Hanson, 1978). The calculation indicates that the two-stage Nd model ages for unit 10 TTG rocks range from 2.97 to 2.85 Ga, whereas unit 1 basement granitoids range from 2.91 to 2.86 Ga (Table 7). This suggests that the unit 10 TTG may have been derived from a slightly older, juvenile crustal source than that of unit 1 basement granitoids. The source rock(s) of unit 10 TTG may have slightly longer duration of cumulative time (~130 m.y.) after differentiating (or separating) from the depleted mantle at ca. 3.1–3.0 Ga, as constrained by the depleted Nd model ages (or single-stage Nd model ages; Table 7; DePaolo, 1981, 1988), than that of unit 1 granitoids (~100 m.y.). This explanation is also consistent with the requirements of the high P-T experiments mentioned above, clarifying the limit of using single-stage Nd model ages to investigate the difference in source rocks between the Archean mafic rocks and the granitoid rocks.

U-Pb zircon geochronology

A whole-rock sample, each weighing ~10 kg, was selected from each of units 9, 11 and 13 for U-Pb zircon age determination to constrain absolute ages and critical age relationships of the lithostratigraphic units in the map area. Zircon mineral separation and isotopic analysis were conducted at the University of Alberta using isotope dilution thermal ionization–mass spectrometry (ID-TIMS) and laser-ablation, multicollector, inductively coupled plasma–mass spectrometry (LA-MC-ICP-MS) techniques. Detailed analytical procedures were reported previously by Anderson (2013) and Martins et al. (2019), and are also described in DRI2020024.

Results

The U-Pb zircon age results are summarized in Table 8. Detailed isotopic analyses are tabulated in Tables 8_1, 8_2, 8_3 and 8_4 of DRI2020024. These ages, together with the ages of the mafic–ultramafic intrusions acquired by the TGI-4 project in collaboration with the Geological Survey of Canada (Houlé et al., 2013, 2015), help to establish the temporal relationships of the map units and provide further insight into the tectonic evolution of the northern arm of the BRGB.

Figure 63 shows frequency histograms of concordant $^{207}Pb/^{206}Pb$ ages (Ma) for zircon grains analyzed by LA-MC-ICP-MS from two samples: a) a volcaniclastic sandstone sample (111-12-707A01) collected from the Cat Creek assemblage of unit 9; and b) a garnet-muscovite granite sample (111-15-4A01) taken from a unit 13 granite intrusion. The probability-density distribution of the ages is also shown by the red curves for these two samples. A large number of zircon grains was retrieved from sample 111-12-707A01. These grains display various shapes, typically with eroded corners, although euhedral to subhedral crystals are also evident (see inset photos in

Table 8: Results of U-Pb zircon age determinations for selected map units in the Cat Creek–Euclid Lake area, Bird River greenstone belt.

Map unit	Sample	UTM (Zone 15N, NAD83)		Rock type	Age (Ma)	Method	Interpretation
		Easting	Northing				
9	111-12-707A01	315346	5613416	Volcaniclastic sandstone	2736 ±4	LA-MC-ICP-MS	Deposition of volcanic sediments
13	111-15-4A01	314872	5613733	Garnet-muscovite granite	2733 ±10	LA-MC-ICP-MS	Maximum emplacement/crystallization
11	111-15-1A01	332044	5605608	Arenite	2657.1 ±7.4	ID-TIMS	Maximum age of deposition

Abbreviations: ID-TIMS, isotope dilution–thermal ionization mass spectrometry; LA-MC-ICP-MS, laser-ablation, multicollector, inductively coupled plasma–mass spectrometry.

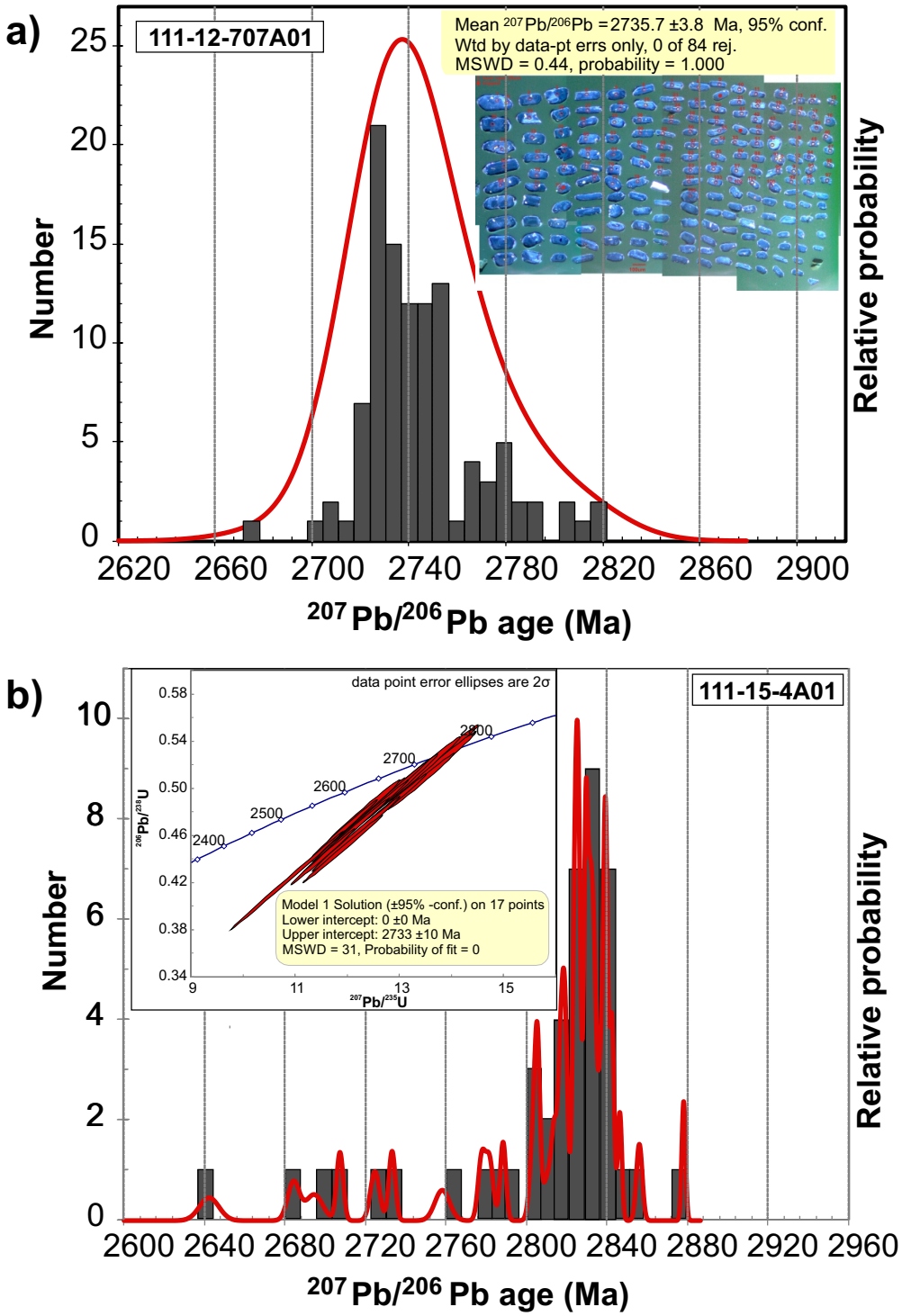

Figure 63: *Frequency histograms of $^{207}Pb/^{206}Pb$ ages (Ma) for zircon grains analyzed by LA-MC-ICP-MS for:* ***a)*** *volcaniclastic sandstone (sample 111-12-707A01), collected from the Cat Creek assemblage of unit 9 (inset photo of zircon grains); and* ***b)*** *garnet-muscovite granite (sample 111-15-4A01), taken from unit 13 granite intrusion (inset concordia diagram of 17 zircon grains with <20% discordance). Red curves indicate probability-density distribution of the ages. Abbreviation: MSWD, mean square of weighted deviates.*

Figure 63a). In total, 105 zircon grains were analyzed by LA-MC-ICP-MS (Table 8_2 of DRI2020024), yielding a weighted mean $^{207}Pb/^{206}Pb$ age of ~2736 ±4 Ma (Figure 63a).

The garnet-muscovite granite sample (111-15-4A01) was collected from a unit 13 granite intrusion to determine its emplacement or crystallization age. However, the results of LA-MC-ICP-MS analyses (Table 8_3 of DRI2020024) returned a complex spectrum of $^{207}Pb/^{206}Pb$ age data that exhibits multiple peaks or modes, as indicated by the probability-density distribution of the ages (Figure 63b). The presence of inherited zircons is evident, including Mesoarchean $^{207}Pb/^{206}Pb$ ages ranging from 2873 ±6 to 2803 ±9 Ma, much older than the sur-

rounding rocks based on field relations. Four least-discordant analyses (<5%) have $^{207}Pb/^{206}Pb$ ages ranging from 2752 ±6 to 2731 ±10 Ma, with a weighted mean $^{207}Pb/^{206}Pb$ age of 2746 ±16 Ma (MSWD of 6.0). In comparison, 17 zircon analyses that were <20% discordant yielded a weighted mean $^{207}Pb/^{206}Pb$ age of 2733 ±10 Ma (see inset concordia diagram in Figure 63b). Eight zircon grains with younger $^{207}Pb/^{206}Pb$ ages ranging from 2133 ±31 to 2558 ±11 Ma and high discordance (≥55%; see Table 8_3 of DRI2020024) may be attributed to new zircon growth or, more likely, to significant loss of radiogenic Pb due to one or more, unknown, late thermal events (e.g., Anderson, 2013).

The arenite sample (111-15-1A01) was collected from the unit 11 Euclid Lake assemblage on the northern shore of Euclid Lake, where this unit is cut by a Ta-Nb–enriched pegmatitic granite dike (subunit 12b; for geochemical composition, see the granite sample 111-13-170D01 in Table 6_2 of DRI2020024). Although this bulk sample weighted ~10 kg, only a few zircon grains were retrieved. Isotope dilution–thermal ionization mass spectrometry analyses of the few detrital zircons are listed in Table 8_4 of DRI2020024. The zircon grains, which have Th/U ratios of 0.02–0.59, were likely derived from eroded felsic igneous rocks (e.g., Kirkland et al., 2015). Although the number of analyses was limited, a large range of $^{207}Pb/^{206}Pb$ ages was obtained for these detrital zircons: 2847.1 ±0.6 to 2657.1 ±7.4 Ma (Table 8_4 of DRI2020024).

Interpretation

The Cat Creek assemblage (unit 9) is interpreted to have been deposited at a maximum age of ca. 2736 Ma, which is slightly younger than the ca. 2743 Ma Mayville intrusion (Houlé et al., 2013). This volcano-sedimentary package could be temporally comparable to the ca. 2734 Ma Peterson Creek formation (Gilbert et al., 2008) in the southern arm of the BRGB, although the Cat Creek lacks the extensive dacitic to rhyolitic flows present in the Peterson Creek. The Cat Creek assemblage occurs at the terrane boundary between the BRGB to the south and the English River basin to the north (Figure 2), so the felsic flows could have been removed by tectonic erosion if a correlation with the Peterson Creek formation is considered. The terrane boundary is defined by the Cat Lake–Euclid Lake fault zone (Duguet et al., 2009; Yang et al., 2013). If this interpretation is correct, then it is reasonable to assign the Cat Creek assemblage to a supracrustal assemblage of the BRGB.

The concordant $^{207}Pb/^{206}Pb$ age of ca. 2733 Ma obtained from sample 111-15-4A01 is interpreted as the maximum emplacement or crystallization age of the unit 13 garnet-muscovite–bearing granite intrusion (unit 13). This granite is S-type in origin, meaning that it was likely formed by partial melting of thickened crust in a terrane collision zone (Yang, 2014b; Yang et al., 2019). In the western Superior province, S-type granites were emplaced mainly during the period between 2720 and 2664 Ma (Anderson, 2013; Yang et al., 2019). However, the presence of the Mesoarchean inherited zircons suggests that the source region of S-type granites may have had notable heterogeneities, likely due to interaction of tectonically distinct blocks at the collision zone.

The youngest concordant $^{207}Pb/^{206}Pb$ age of ca. 2657 Ma is thought to represent the maximum sedimentation age of the Euclid Lake assemblage sedimentary rocks, which also is significantly younger than the ca. 2697 Ma Flanders Lake formation arenite and the ca. 2712 Ma Booster Lake formation turbidite (see Gilbert et al., 2008) in the southern limb of the BRGB. This suggests that, based on the above geochronological constraints, the Euclid Lake assemblage (unit 11) likely cannot be correlated with the Flanders Lake and Booster Lake formations in the southern limb of the BRGB as previously thought (e.g., Černý et al., 1981). Therefore, this assemblage is likely a distinct stratigraphic entity, possibly attributed to the English River basin (Stott et al., 2010). Alternatively, if it is assigned as a part of the BRGB, it must have been deposited after or over the Flanders Lake and Booster Lake formations. The authors prefer the latter scenario because of the occurrences of intercalated arc-like mafic rocks in the Euclid Lake assemblage. Basically, such mafic rocks are uncommon or absent in the English River basin (Stott et al., 2010) sedimentary rocks that have a minimum depositional age of ca. 2698 Ma, as indicated by cutting granite intrusions (Corfu et al., 1995; Percival et al., 2006a, 2012).

More importantly, some very coarse grained to pegmatitic granites (to pegmatites) cutting the Euclid Lake assemblage sedimentary rocks display significant Nb and Ta (and likely Li; Table 6_2 of DRI2020024) mineralization, implying that rare-metal, fertile, S-type granites and related pegmatites may be younger than 2657 Ma in the Cat Creek–Euclid Lake area. Thus, such geological constraints from detailed bedrock mapping, aided by the lithogeochemical and geochronological data presented in this report, demonstrate that exploration targeting for rare metals can be considerably focused in the region. This approach could also be extended to other regions for targeting of rare metals associated with granitic pegmatites. The Tanco rare-metal pegmatites in the southern limb of the BRGB were dated at ca. 2660–2640 ±7 Ma (Baadsgaard and Černý, 1993; Gilbert et al., 2008; Camacho et al., 2012; Brown et al., 2017), thus making pegmatites up to 2660 Ma in age favourable exploration targets for rare metals in the BRGB.

Structural geology

The Cat Creek–Euclid Lake map area, situated in the northern arm of the BRGB, is in fault (tectonic) contact with the southern boundary of the English River basin to the north (Figures 2, 3). The west-northwest-trending Cat Lake–Euclid Lake fault zone (CLELFZ), thought to be coincident with this tectonic zone, cuts through and/or is manifested by high-strain

zone(s) within gneissic, peraluminous and strongly foliated and mylonitic granitoid rocks (e.g., subunit 12b and unit 13; Yang et al., 2013). The northwest-trending penetrative foliation in this area dips steeply to the south. Deformation fabrics suggest a north-side-up sense of dextral-normal, oblique-slip shear, consistent with the observations by Gilbert et al. (2008), Duguet et al. (2009) and Yang et al. (2013).

Two major types of contacts have been identified at the southern margin of the northern limb of the BRGB: 1) intrusive contacts indicated by unit 2 MORB-type basalt cutting and brecciating the basement granitoids (Maskwa Lake batholith I) of unit 1, as well as the unit 2 basalt and related synvolcanic gabbro (subunit 2a) cut by the unit 10 TTG suite; and 2) structural (or fault-bounded) contacts manifested by the southern wall of the CLELFZ cutting through units 1 and 10 granitoid rocks, particularly on the southeastern shore or side of Cat Lake and Euclid Lake (Figures 2, 3).

At least three generations of deformation structures (D_1–D_3) are evident in the Cat Creek–Euclid Lake area (Yang et al., 2012, 2013) on the basis of overprinting and cutting relationships between different generations of mesoscopic deformation fabrics. Similarly, three phases of deformation events were also recorded in various fault-bounded domains of supracrustal rocks in the southern limb of the BRGB (Trueman, 1980; Gilbert et al., 2008; Duguet et al., 2009). This leads to a plausible structural correlation of the northern and southern limbs of the BRGB in terms of the structural characteristics, styles and relationships. Also, it suggests that they may have been influenced by similar tectonic regimes: 1) north-south compression associated with terrane juxtaposition, 2) east-trending transpression and shearing coeval with diapiric emplacement (or doming) of granitoid plutons, represented mainly by the Maskwa Lake batholith II (unit 10); and 3) northwest- and northeast-oriented transcurrent shearing to transtension, likely related to relaxation of collided tectonic blocks (e.g., the pop-up structures suggested by Gilbert et al., 2008 and Duguet et al., 2009; angular breccias at contact zones) and emplacement of unit 13 granite intrusions.

D_1 structures

Primary structures (S_0) are manifested by 1) primary bedding of the sedimentary rocks (i.e., units 9 and 11; Table 1) north of Cat Creek and on the northern shore of Euclid Lake; 2) primary igneous layering, particularly in units 5 and 6 rocks of the Mayville intrusion; and 3) lava-flow contacts revealed in unit 2 MORB-type basalt. These primary structures are mostly overprinted and transposed, mainly by D_2 fabrics (e.g., S_2 foliation), which may have changed their original orientation as shown in a stereographic projection (Figure 64).

A limited number of observations (n=28) on the primary bedding (S_0) of the sedimentary rocks in units 9 and 11 display varied strikes of 047–186° and dip angles of 40–87°, with an average of 65° (Figure 64a, b). The rose diagram indicates that 18.5% of the observed bedding strikes between 131 and 140°, although it was folded by regional open folds that are likely attributed to D_3 deformation (Figure 64a, b). Bedding dips are consistently to the south and relatively shallow (see below).

Primary igneous layering was discernible and recorded in the gabbroic anorthosite to anorthosite (unit 5) and leucogabbro to gabbroic anorthosite (unit 6) of the Mayville intrusion. Although it has been overprinted by younger structures, the primary layering displays flow banding, as shown by varied grain sizes and compositional variation in mineralogy. The igneous layering ranges in strike mainly from 052 to 095°, except for one measurement of 158° (Figure 64b, c), with dips of 46–90° to the south. The rose diagram shows that 31.6% of the primary igneous layering strikes 051–060° (Figure 64b), and dip angles average 76°, steeper than the sedimentary bedding north of the Mayville intrusion when comparing the projections of poles to the primary structures (Figure 64b, c).

On the basis of pillow tops, unit 2 MORB-type basalt generally youngs to the north; the lava-flow contacts strike dominantly 091–100° although varying in a large range of 010–275°, and dipping 45–90° (average 83°) to the south (Figure 64e). Therefore, the unit 2 basalt is structurally overturned, making the flow contacts mostly subvertical to vertical and steeper than the primary igneous layering in the Mayville intrusion rocks. This igneous layering, in turn, is steeper than the sedimentary bedding in units 9 and 11, suggesting apparent (rheological) differences in response to tectonic stress by these lithostratigraphic units.

However, only a few outcrops show that the primary structures mentioned previously are folded by D_1 upright folds, where S_1 foliation is subparallel to the axial planes (Figure 65a). Some of the S_0 bedding in unit 9 volcaniclastic rocks is folded by D_1 folds (i.e., F_1 folds), resulting in S_1 foliations (Figure 65b). The S_1 foliation was overprinted by F_2 folds, forming axial S_2 foliation in unit 1 basement granitoids (south of the New Manitoba mine; Figure 65c). On the stereographic-net projection, these S_1 foliation planes strike 040°–060° in the Cat Creek area, whereas one measurement of S_1 strikes 155° and dips 85° to the southwest in the Euclid Lake area (Figure 66a).

In the northern portion of the Cat Creek area, part of the unit 9 sedimentary rocks are gneissic in texture and contain abundant garnet, biotite and amphibole, typically exhibiting a gneissosity (S_{1-2}) that overprints and transposes the bedding (S_0). This contrasts with the unit 11 sedimentary rocks on the northern shore of Euclid Lake, where graded bedding is well preserved but gneissosity, garnet and biotite are absent, suggesting differences in metamorphic grade and strain. The Cat Creek area is of amphibolite facies, while the Euclid Lake area is of upper-greenschist facies. This suggests that a relatively deeper portion of the greenstone belt may have been exposed in the Cat Creek area than in the Euclid Lake area.

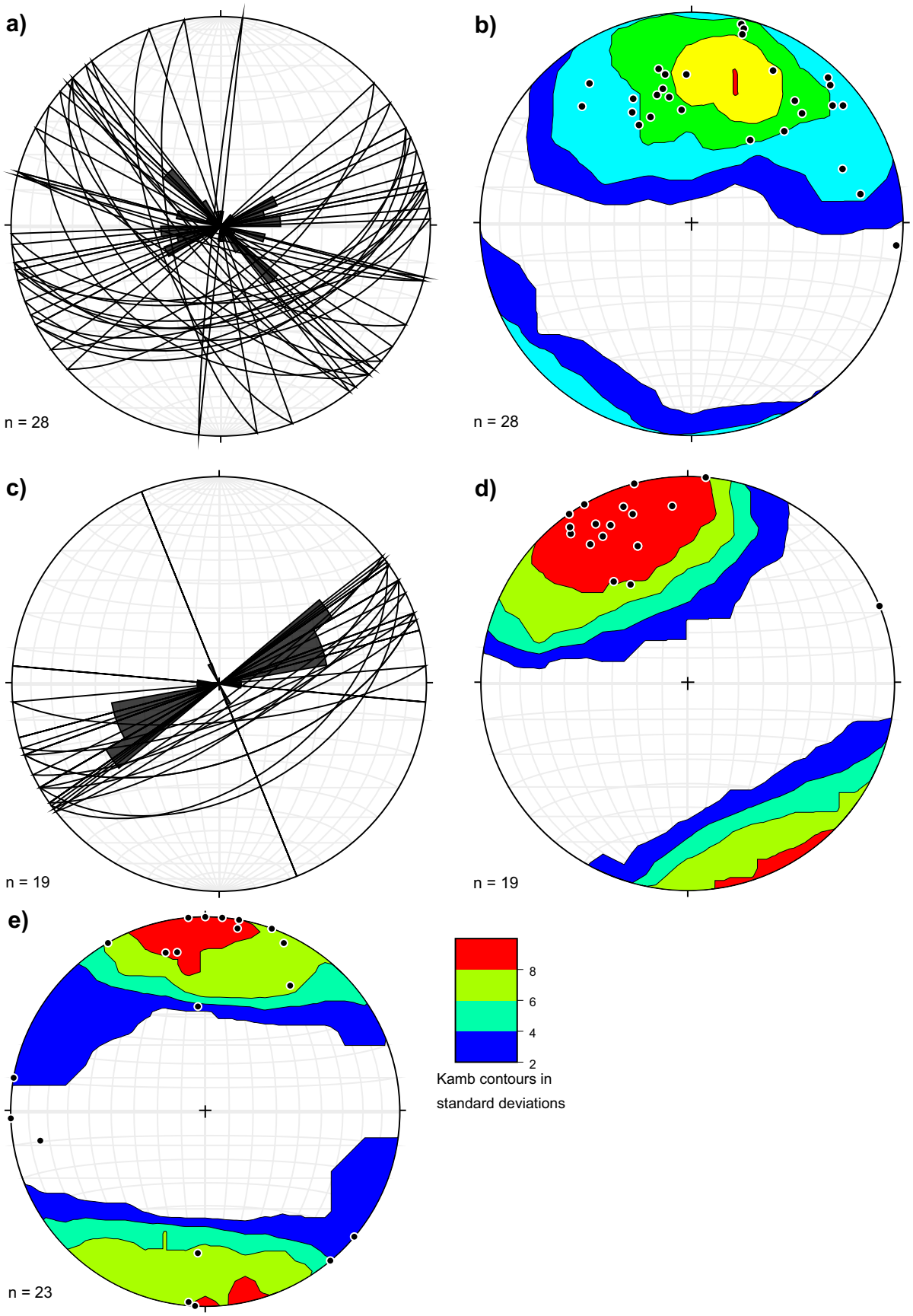

Figure 64: *Lower-hemisphere, equal-area stereographic projections (and rose diagrams) of primary structures (S_0), as well as poles to the primary structures, in the Cat Creek–Euclid Lake area:* ***a)*** *and* ***b)*** *sedimentary bedding;* ***c)*** *and* ***d)*** *primary igneous layering;* ***e)*** *lava-flow contacts. Note: Kamb contours in standard deviations; n, number of measurements (or data points).*

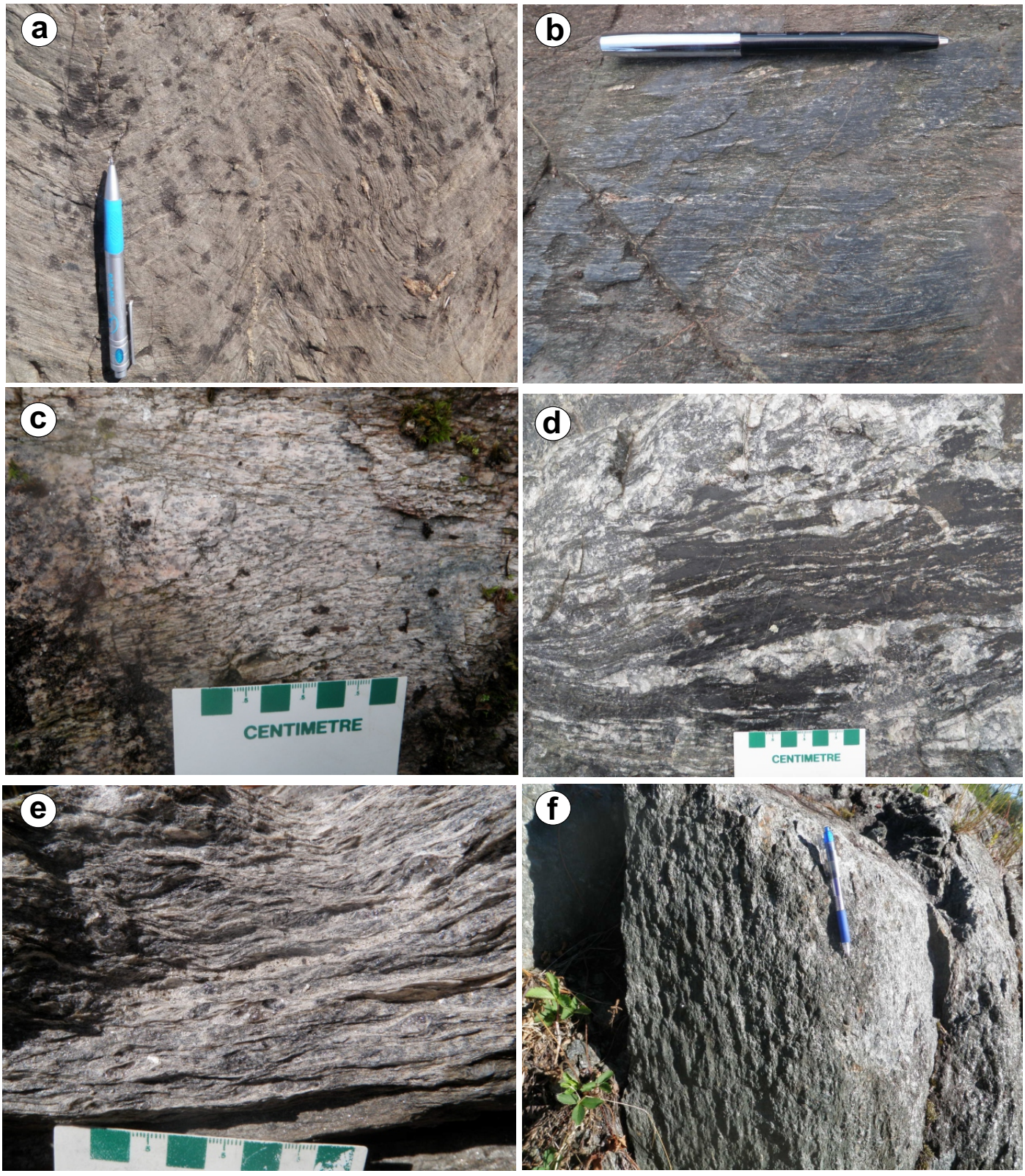

Figure 65: *Field photographs showing characteristics of D_1–D_3 structures in the Cat Creek–Euclid Lake area:* ***a)*** *unit 11 greywacke sedimentary bedding (S_0) folded by F_1 fold, and late granite veins present along S_1 plane, north shore of Euclid lake;* ***b)*** *S_0 folded by F_1 folds, leading to north-west-striking axial S_1 foliation observed in unit 9 volcaniclastic rocks, north of Cat Creek;* ***c)*** *S_1 overprinted by F_2 fold, forming axial S_2 foliation in unit 1 granitoid, south of the New Manitoba mine;* ***d)*** *sheared quartz veins (dextral movement) and boundins related to D_2 deformation event, northeast of Cat Lake;* ***e)*** *sheared unit 1 granitoids at the Cat Lake–Euclid Lake fault zone, with shear bands and 'S-C' fabrics suggestive of dextral movement, small island in the central part of Euclid Lake;* ***f)*** *stretching lineation L_2, indicative of north-side-up movement, south of Cat Creek.*

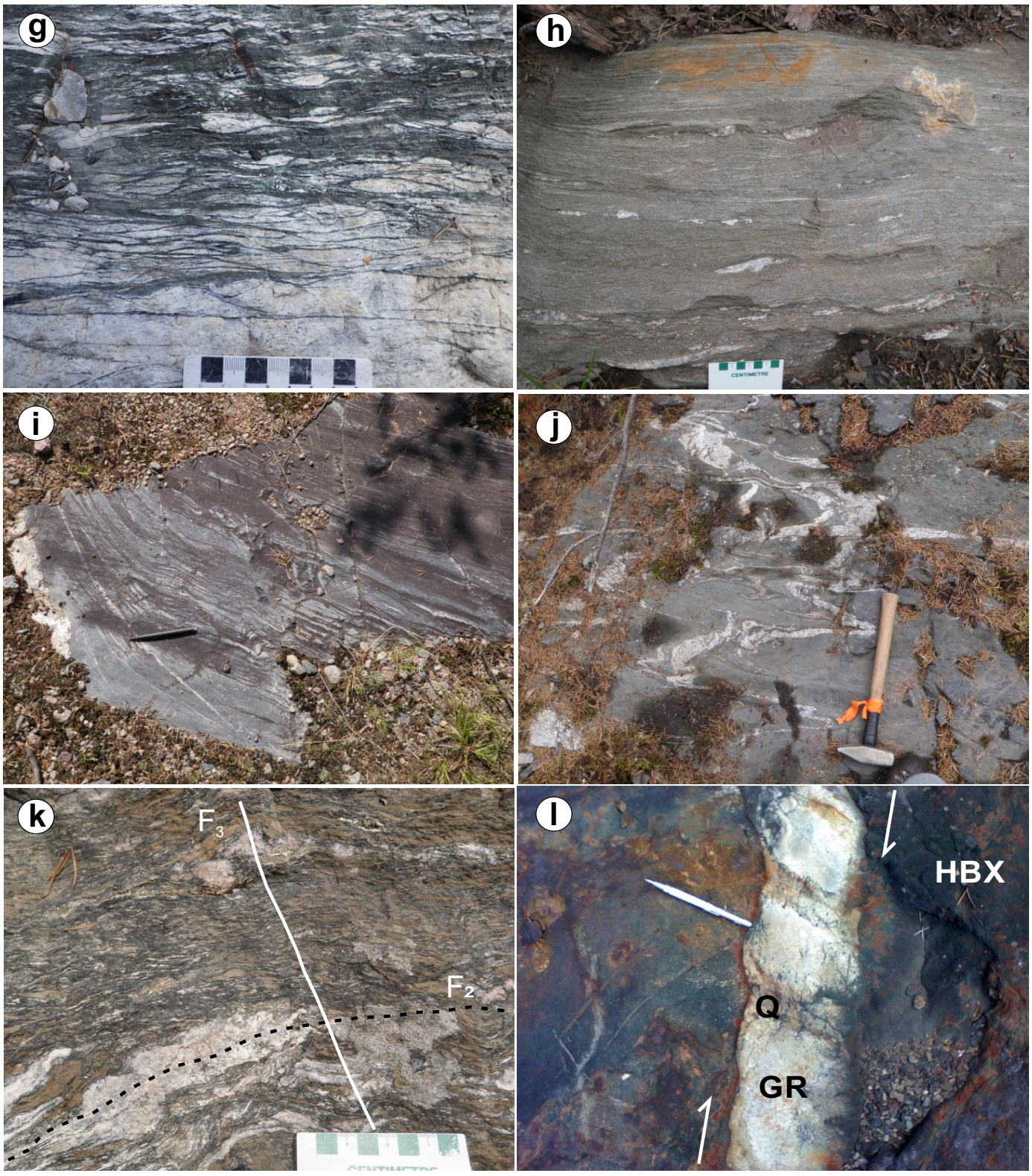

Figure 65 (continued): *Field photographs showing characteristics of D_1–D_3 structures in the Cat Creek–Euclid Lake area:* ***g)*** *dextral brittle-ductile shear zone (D_2; central part of the photo) cutting unit 14 pegmatite, which was overprinted by a sinistral shearing (D_3) during late exhumation (upper and lower portions of the photo) at the Irgon mine, north of Cat Lake;* ***h)*** *bedding transposed by S_2 foliation along which asymmetric sigmoidal boudinaged quartz is indicative of dextral movement, north of Cat Creek;* ***i)*** *'S'-folds formed by D_3, resulting in northeast-trending S_3 foliation in unit 9 volcaniclastic rocks, northwest of Cat Creek;* ***j)*** *unit 2 pillow basalt intruded by unit 10 tonalite veins/dikes, which were folded to form northeast-trending $S_{2/3}$ foliation, north of Cat Creek;* ***k)*** *isoclinal folds (F_2) refolded into open folds by F_3, south of the New Manitoba mine;* ***l)*** *right-lateral en échelon quartz veins within a unit 10 granitoid dike that cuts unit 4 heterolithic breccia at the M2 deposit (magnetic pen ~15 cm long and pointing north). Abbreviations: GR, granitoid; HBX, heterolithic breccia; Q, quartz vein.*

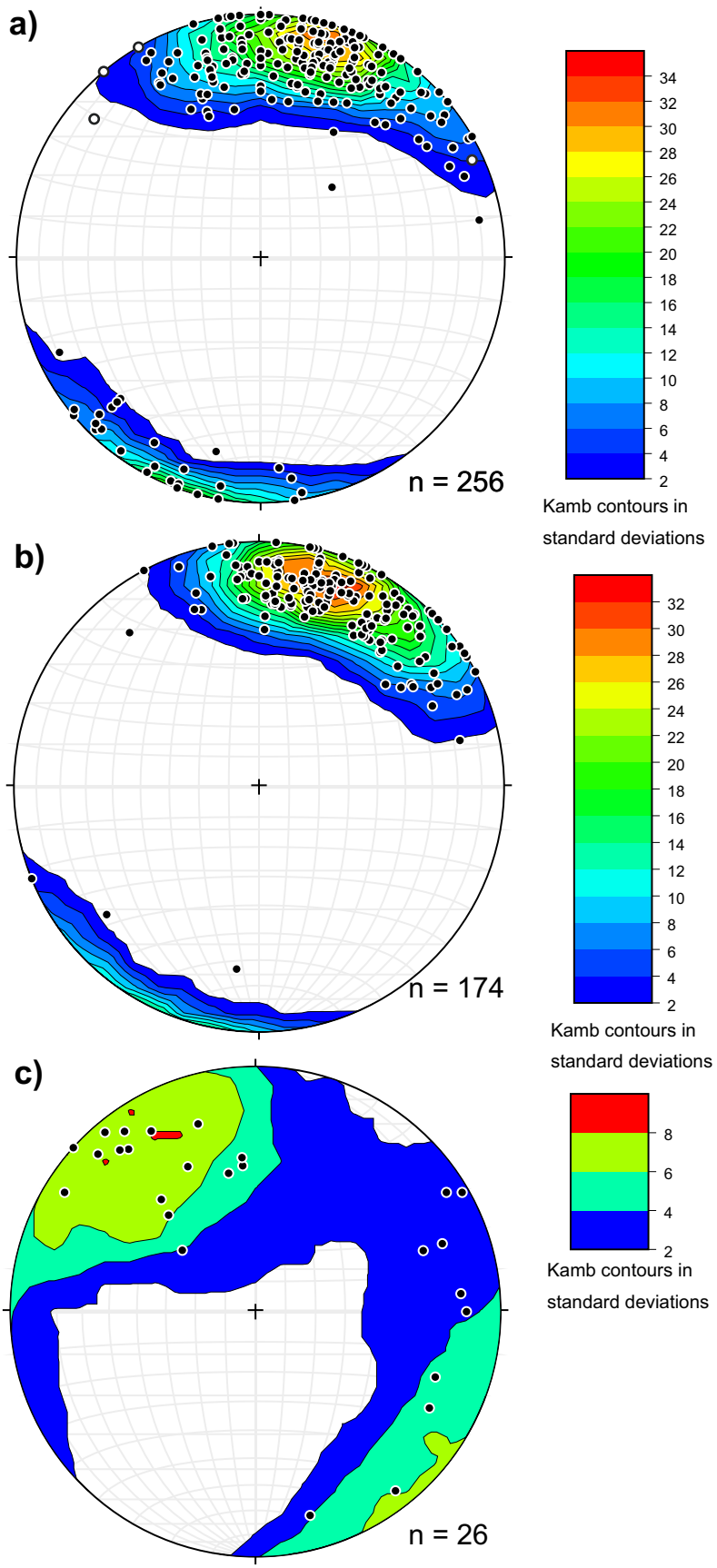

Figure 66: *Lower-hemisphere, equal-area stereographic projections of the poles to foliations of D_1–D_3 structures in the Cat Creek–Euclid Lake area:* ***a)*** *S_1 (open circle; n=4) and S_2 (solid circle; n=252);* ***b)*** *main foliation S (n=174) not assigned to generation of deformation but most likely attributed to S_2;* ***c)*** *S_3 foliation (n=26). Note: Kamb contours are in standard deviations; n, number of measurements (or data points).*

D_2 structures

The D_2 deformation structures display a complex pattern, with north-side-up shearing associated with some back-thrusting (south-side-up offset), similar to the D_2 structures found in the southern limb of the BRGB (Gilbert et al., 2008; Duguet et al., 2009). Kinematic indicators suggest that the orientation of the shear zones varies from sinistral for those that trend northeast to dextral for those that trend southeast. These two anastomosed sets of shear zones accommodated relative movements and rotation among the fault-bounded rock units (e.g., south of Cat Creek and on the southern shores of Cat and Euclid lakes; see Figure 65d–f), suggestive of transpressive tectonics. In places, such features as stretching lineation (L_2), penetrative foliation (S_2) and kinematic indicators suggest that a vertical component of movement was present along the major shearing plane(s).

A dextral brittle-ductile shear zone (D_2) cutting unit 14 pegmatite (Figure 65g) at the Irgon mine north of Cat Lake was overprinted by a late sinistral shearing (D_3), suggesting that such structural overprinting may have taken place synchronously with or during terrane exhumation. North of Cat Creek, primary bedding (S_0) was completely transposed by S_2 foliation, along which asymmetric sigmoidal boudinaged quartz is indicative of dextral movement (Figure 65h). The data points of poles to penetrative foliation (S_2) assigned to D_2 deformation, presented in Figure 66a, indicate that most of the foliations strike east-southeast and dip subvertically to the south. However, some S_2 planes dip steeply to the north. Such variation in dip direction of the S_2 foliations is consistent with a general anticlinal fold structure that is also reflected by the slight convergence between the opposite dips of the foliation planes in the two limbs of an anticlinal fold. Although 174 measurements of penetrative foliation were not assigned to a particular deformation generation in the field, plotting these foliations on the stereonet (Figure 66b) shows very similar patterns to that of S_2 foliations (Figure 66a).

Minor folds with 'Z' asymmetry in the Euclid Lake area display varying degrees of closure (or openness of the folds) and become tighter in the axial area, which is likely due to dextral shearing of the CLELFZ.

D_3 structures

The structures of D_3 deformation are related to northwest- and northeast-oriented transcurrent shearing to transtension, likely caused by relaxation of collided tectonic blocks and emplacement of unit 13 granite intrusions and associated granitic pegmatites. The D_3 structures are characterized by moderately open folds (Figure 65i–k) and associated transcurrent shears (e.g., locally indicated by the occurrence of en échelon quartz veins; Figure 65l). Resultant S_3 foliations show variations in strike and dip on the plot of poles to foliation planes (Figure 66c), likely influenced by emplacement of granite intrusions and terrane exhumation. Based on their orientations and overprinting relationships, northwest- and northeast-trending faults (Figure 3) are interpreted to be associated with D_3 deformation. The northwest-trending faults, striking from 300° to 330°, cut and offset the primary igneous layering (Figure 64b) in rocks of the Mayville intrusion at a high angle.

The northeast-trending faults, with strikes ranging from 25° to 40°, are relatively rare in the Cat Creek area. These faults are parallel to the S_3 foliations in nearby outcrops. One major northeast-trending fault lies east of the M_2 deposit (Figure 3; Yang, 2014a). However, the northeast-trending faults are more common in the Euclid Lake area than the Cat Creek area (Yang, 2013). The map pattern indicates a north-northeast-oriented, open regional fold attributed to the D_3 event that is also manifested by subparallel axial S_3 foliation.

Tectonic evolution

The structural features in the Cat Creek–Euclid Lake area are similar to those in the southern arm of the BRGB in that they are characterized by steep to subvertical structures, anastomosing shear zones displaying down-dip lineations, and subvertical movements (Gilbert et al., 2008; Duguet et al., 2009). Such structural kinematic movements are remarkably common in most greenstone belts (e.g., Polat and Kerrich, 2001, 2002; Lin, 2005). Figure 67 illustrates the current tectonic configuration of the lithostratigraphic units described in this report. The following is a summary of the tectonic evolution recorded in the rock units and related to the three generations of structures (D_1–D_3) in the Cat Creek–Euclid Lake area on the northern arm of the BRGB.

- Formation of the Mesoarchean Maskwa Lake batholith I (unit 1), which becomes the basement to the BRGB; the D_1–D_3 structures are present (although the absolute ages are unknown, the D_1/D_2 event(s) is thought to predate unit 11 but postdate unit 9, occurring between ca. 2736 and 2657 Ma; D_3 might be coeval with unit 13 granites and unit 14 pegmatites, ca. 2650 Ma)
- Production of MORB-type basalt and synvolcanic intrusive gabbroic rocks (unit 2) in a magmatic-arc to back-arc setting; the D_1–D_3 structures are present
- Continuation of extension in the arc to back-arc regime to generate the ca. 2743 Ma Mayville intrusion (units 3–7) and related gabbroic intrusions (unit 8; e.g., New Manitoba Mine intrusion); subsequently, formation of the 2736 Ma Cat Creek assemblage (unit 9); the D_1–D_3 structures are present
- Extensive arc plutonism and emplacement of the Neoarchean Maskwa Lake batholith II, consisting of TTG (unit 10); deposition of the ca. 2660 Ma Euclid Lake assemblage (unit 11) via volcano-sedimentary processes; the D_2 and D_3 structures are present
- Arc- to continent collision between the Winnipeg River and North Caribou terranes to generate units 12 and 13

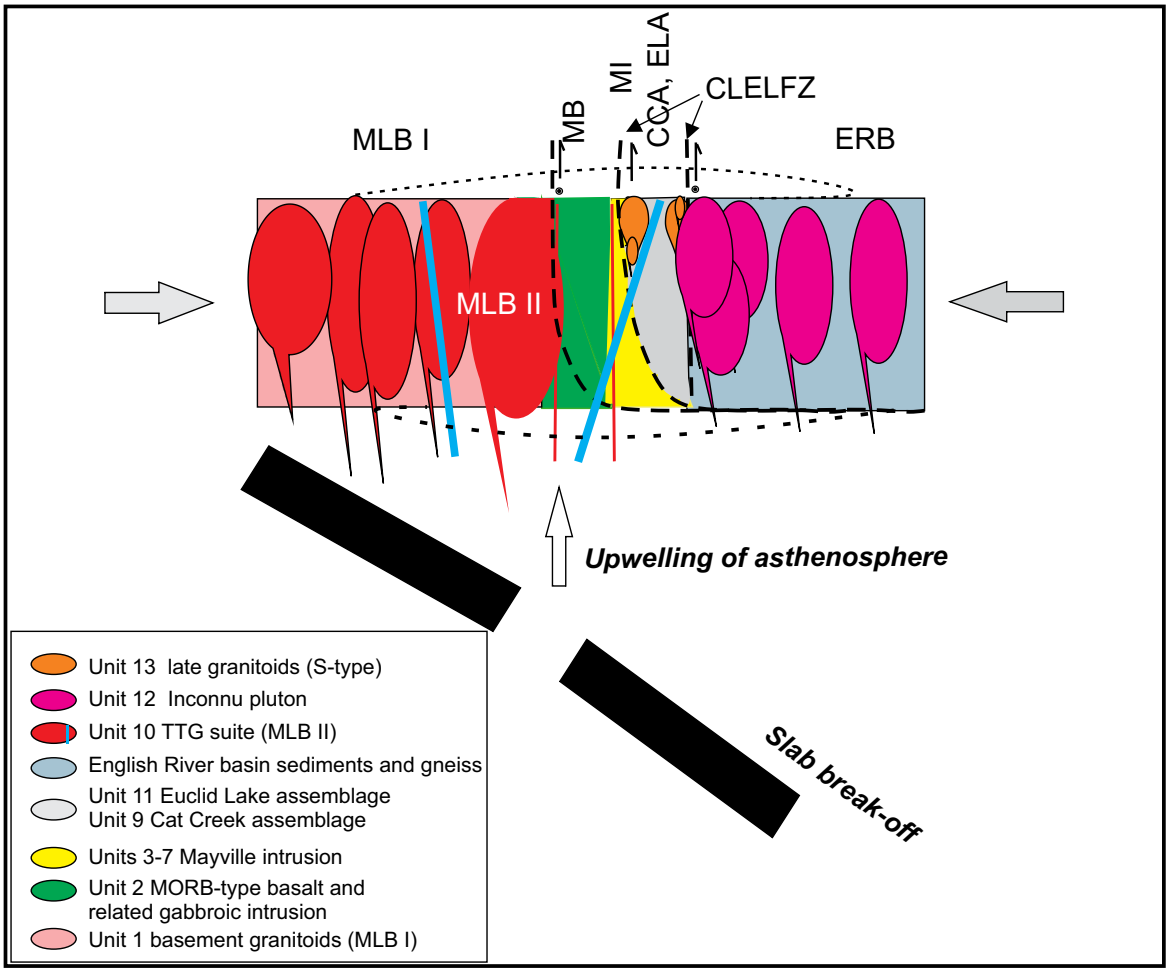

Figure 67: *Schematic diagram of the tectonic configuration recorded by the major map units in the Cat Creek–Euclid Lake area on the northern limb of the Bird River greenstone belt. Black dot in circle indicates upward vertical movement. Dotted curve is indicative of thickened crust (in the terrane boundary zone) that had been eroded. Basal portion of the thickened lithospheric root could have delaminated and sunk into the mantle. Note that the strata dip subvertically to the south due to doming of the Maskwa Lake batholith II into the belt, which may have caused overturning of dip directions from south to north to the current state. Abbreviations: CCA, Cat Creek assemblage; CLELFZ, Cat Lake–Euclid Lake fault zone; ELA, Euclid Lake assemblage; ERB, English River basin; MB, MORB-type basalt and associated gabbroic intrusions; MI, Mayville intrusion; MLB (I and II), Maskwa Lake batholith (I and II); MORB, mid-ocean–ridge basalt.*

granitoid intrusions and associated unit 14 granites and pegmatites; subducting slab roll-back and break-off, triggering the upwelling of asthenospheric mantle and formation of sanukitoids as dikes or small stocks (e.g., Gilbert et al., 2008; Yang and Gilbert, 2014a; Yang et al., 2019); the D_2 and D_3 structures are present

Comparison of the lithostratigraphic units, chromite chemistry, structural characteristics and patterns, lithogeochemistry and U-Pb zircon geochronological data supports a correlation between the northern and southern (main) limbs of the BRGB. Table 9 shows a simplified lithostratigraphic correlation, suggesting that the supracrustal packages in the Cat Creek–Euclid Lake area constitute an overturned northern limb, whereas the Bird River area (Trueman, 1980; Gilbert et al., 2008; Duguet et al., 2009) forms the southern limb, including a secondary synclinorial structure (Černý et al., 1981; Gilbert et al., 2008), as part of a regional anticlinorium.

Economic considerations

Manitoba Geological Survey mapping in the Cat Creek–Euclid Lake area, carried out in collaboration with phases 4 and 5 of the Geological Survey of Canada's Targeted Geoscience Initiative (TGI) program, has reassessed known magmatic base-metal mineralization in several mafic–ultramafic intrusions (e.g., Mayville, New Manitoba Mine and Euclid Lake intrusions) and identified potential for porphyry Cu (Au) and skarn-type mineralization (Yang et al., 2013), hitherto not considered for the BRGB. Notably, the Cat Creek assemblage volcano-sedimentary rocks, which display arc-like geochemical signatures, must be further assessed in terms of their potential for volcanogenic massive sulphide (VMS) mineralization (e.g., Syme, 1998; Syme et al., 1999; Percival et al., 2012).

The Cat Creek–Euclid Lake area contains several Neoarchean layered mafic–ultramafic intrusions (dated at ca. 2743 Ma), geochemically similar to those that host signifi-

Table 9: Lithostratigraphic correlation of the northern and southern arms of the Bird River greenstone belt, southeastern Manitoba.

BIRD RIVER BELT, SOUTHERN ARM	BIRD RIVER BELT, NORTHERN ARM
Late intrusive rocks	**Late intrusive rocks**
Granodiorite, granite, pegmatitic granite, pegmatite/aplite	Pegmatitic granite, pegmatite and minor aplite (unit 14)
TANCO pegmatite (2640 ±7 Ma[1])	Muscovite- and/or garnet-bearing S-type granite (<~2733 Ma ±10 Ma[9]; unit 13)
Marijane Lake pluton (2645.6 ±1.3 Ma[2]); Lac du Bonnet batholith (2660 ±3 Ma[3])	Inconnu pluton II (unit 12b): gneisic to stongly foliated granitoid rocks
Diabase, gabbro and andesitic to dacitic intrusive rocks	Inconnu pluton I (unit 12a): I-type granodiorite, and granite
Sedimentary rocks	**Sedimentary rocks**
?	EUCLID LAKE ASSEMBLAGE (~2657 Ma[9]; unit 11)
	Greywacke, siltstone, polymictic conglomerate intercalated with mafic rocks
FLANDERS LAKE FORMATION (2697 ±18 Ma[4])	
Lithic arenite, polymictic conglomerate	
Fault, inferred	**?**
BOOSTER LAKE FORMATION (2712 ±17 Ma[4])	
Greywacke-siltstone turbidite, conglomerate	
Fault, inferred	***Fault, inferred***
Intrusive rocks	**Intrusive rocks**
SYNVOLCANIC INTRUSIONS	TTG SUITE (unit 10)
Gabbro, diorite, quartz-feldspar porphyry; granodiorite	Tonalite-trondhjemite-granodiorite suite; quartz diorite, quartz-feldspar porphyry, granodiorite
(Birse Lake pluton, 2723.2 ±0.7 Ma[2]; Maskwa Lake batholith II, 2725 ±6 Ma[3]; Pointe du Bois batholith, 2729 ±8.7 Ma[3])	Maskwa Lake batholith II (2725 ±6 Ma[3])
TANCO gabbro (2723.1 ±0.8 Ma[2])	
Metavolcanic and metasedimentary rocks	**Volcaniclastic rocks and sedimentary rocks**
BIRD RIVER BELT NORTH PANEL	
DIVERSE ARC ASSEMBLAGE (2706 ±23 Ma[5])	
Basalt, andesite, rhyolite, heterolithic volcanic fragmental rocks; greywacke-siltstone turbidite, chert, iron formation; polymictic conglomerate (with clasts from the Bird River Sill)	?
PETERSON CREEK FORMATION (2731.1 ±1 Ma[2]; 2734.6 ±3.1 Ma[6])	CAT CREEK ASSEMBLAGE (2735.7 ±3.8 Ma[9]; unit 9)
Dacite, rhyolite; felsic tuff and heterolithic felsic volcanic breccia	Lithic greywacke, siltstone, conglomerate with felsic volcanic and granitoid clasts, and garnet-bearing gneiss; minor volcaniclastic sandstone, lapillistone
BIRD RIVER BELT SOUTH PANEL	
BERNIC LAKE FORMATION (2724.6 ±1.1 Ma[2])	**?**
Basalt, andesite, dacite and rhyolite; heterolithic volcanic breccia	
Unconformity/Fault	***Unconformity/Fault***
Intrusive rocks	**Intrusive rocks**
BIRD RIVER SILL (2744.7 ±5.2 Ma[3]; 2743.0 ±0.5[7])	MAFIC–ULTRAMAFIC INTRUSIVE ROCKS (unit 8): Gabbroic and minor ultramafic rocks
Dunite, peridotite, picrite, anorthosite and gabbro	MAYVILLE MAFIC–ULTRAMAFIC INTRUSION (2742.8 ±0.8 Ma[8]; units 3 to 7)
	Gabbro, leucogabbro, anorthosite, intrusion breccia and pyroxenite
Metavolcanic and metasedimentary rocks	**Metavolcanic and metasedimentary rocks**
MORB-type VOLCANIC ROCKS	MORB-type VOLCANIC ROCKS (Mayville assemblage, Bailes et al., 2003; unit 2)
Basalt, aphyric to plagioclase-phyric, locally megacrystic; oxide-facies iron formation	Basalt, aphyric to plagioclase-phyric, locally megacrystic; synvolcanic gabbroic rocks
Fault, inferred	***Nonconformity/Fault, inferred***
EAGLENEST LAKE FORMATION	**?**
Greywacke-siltstone turbidite	
Older granitoid rocks (basement; unit 1)	
Granodiorite, tonalite, diorite and orthogneiss (Maskwa Lake batholith I, 2782 ±11 Ma[3], 2832.3 ±0.9 Ma[2], 2852.8 ±1.1 Ma[2], 2844 ±12 Ma[3])	

[1] Unit numbers in the northern arm of the Bird River greenstone belt correspond to those in Table 1.

References for geochronological data: [1] Baadsgaard and Černý, 1993; [2] Gilbert et al., 2008; [3] Wang, 1993; [4] Gilbert, 2006; [5] Gilbert, 2008a; [6] H.P. Gilbert, unpublished data, 2007; [7] Scoates and Scoates, 2013; [8] Houlé et al., 2013; [9] This study.

cant Ni-Cu-PGE-Cr mineralization worldwide (e.g., Hoatson, 1998; Naldrett, 2004; Lightfoot, 2016). Recent mapping and lithogeochemical and Nd isotopic studies summarized in this report suggest that the Mayville intrusion formed from multiple injections of alumina-rich, hydrous tholeiitic magma derived from high-degree partial melting of a sub-arc, lithospheric, depleted-mantle source; during the emplacement of each magma batch, assimilation and fractional crystallization may have played important roles in petrogenesis, and may have triggered sulphide saturation in the magma(s) and subsequent liquidation and mineralization. Cooling of the intrusion appears to have occurred from north to south, regardless of replenishment by subsequent batches of mafic–ultramafic magma(s) into the intrusive system, within an arc- to back-arc setting. The continuity of the heterolithic breccia zone (HBX) in the Mayville intrusion suggests a dynamic system favourable for the formation of magmatic Ni-Cu-PGE-Cr–sulphide mineralization. It is noted that arc-related Ni-Cu-PGE–sulphide deposits are commonly high grade but small tonnage (e.g., Yildirim et al., 2020). Thus, it appears that the potential for high-grade mineralization in the northern arm of the BRGB needs be further explored.

The Mayville intrusion, the largest mafic–ultramafic intrusion in the area, hosts a significant amount of Ni-Cu-PGE mineralization in the M2 deposit, recognized as contact-style magmatic-sulphide mineralization (Yang et al., 2012). At the M2 deposit, the sulphide-rich mineralization is typically located near the base of the HBX and basal contact of the intrusion, whereas disseminated sulphide minerals are widespread throughout the HBX and basal mafic–ultramafic rocks (e.g., Copper contact and Hititrite occurrences, M2W zone; Map GR2020-1-1). Furthermore, other styles of mineralization, such as reef, stratiform PGE and stratiform chromitite, also occur in the Mayville intrusion (e.g., PGE zone). The transitional and/or contact zones between major rock units may be particularly enriched in PGEs (e.g., PGE zone). In addition to Ni-Cu-PGE–sulphide mineralization, the Mayville intrusion may host significant chromite mineralization, as suggested by the presence of massive chromitite bands and disrupted chromitite-pyroxenite layers within the HBX. Copper-nickel mineralization also occurs in unit 8 gabbroic intrusions (e.g., New Manitoba mine, Acme occurrence).

This report emphasizes that mineralization and the formation of various mineral deposits and/or occurrences resulted from distinct stages (events) of a protracted geological and geodynamic evolution. First, in the northern arm of the Neoarchean BRGB, magmatic Ni-Cu-PGE-Cr mineralization (e.g., Mayville, Euclid Lake chromite deposits, New Manitoba mine) probably formed in an extensional regime within an arc- to back-arc setting at a continental margin. Second, porphyry Cu (Au) and skarn Cu-Au-Ag mineralization (e.g., Cat Lake Au-Ag mine), associated with some granitoid rocks of the TTG suite, is likely related to arc magmatism due to plate subduction. Granite-hosted Au deposits (e.g., Little Bear Lake Au deposit hosted in the Maskwa Lake batholith; Kretschmar and McBride, 2015) require further evaluation in the BRGB. Ore fluids responsible for such mineralization can be assessed by studies (e.g., Banks et al., 1994; Yang et al., 2004; Yang and Lentz, 2005; Yang, 2019) of REE-partitioning behaviour (between granite magmas and associated hydrothermal fluids), mineral chemistry, fluid inclusions and stable isotopes (O, H). Finally, rare-metal–bearing pegmatites (e.g., Irgon mine at Cat Lake), related to younger, S-type peraluminous granitoid rocks, may have been emplaced in a continental-collision environment. Establishing the spatial and temporal relationships between the host geological units through detailed bedrock mapping and geological analysis is thus a key approach in resolving the fundamental questions of the geology, geodynamic evolution and metallogeny of the associated mineral deposits (and/or occurrences) in the study area.

It is necessary to point out that a large portion of the Maskwa Lake batholith between the northern and southern limbs of the BRGB has not been mapped so far, although this report has generally divided it into two units (unit 1 basement and unit 10 TTG suite) in the northern limb of the belt. More complexity of this batholith was noticed in terms of the field relationships. For example, unit 8 gabbro intrusions (e.g., the ca. 2743 Ga New Manitoba Mine intrusion; Houlé et al., 2013, 2015, 2020; Yang et al., 2013) have been emplaced into the TTG suite, suggesting that this part of the TTG (despite the lack U-Pb age data) must have been older than the unit 8 gabbro. The problem is that unit 8 gabbroic rocks are similar in geochemical composition to those gabbro dikes cutting the younger phases of the Maskwa Lake batholith II, thus requiring further investigation of their trace Nd-isotope compositions to probe the nature of their magma sources.

The occurrence of diopside-garnet (±epidote±scapolite ±vesuvianite±magnetite±quartz±calcite±sulphide minerals ±scheelite) skarn, normally formed by contact metasomatism between carbonate and granitoid rocks at Cat Lake (Yang et al., 2013), indicates the possible presence of carbonate rocks beneath unit 2 basalts that have been intruded by granitoid intrusions of the unit 10 TTG suite. However, surface exposures of carbonate rocks were not encountered during the course of mapping. It was noted that minor interlayers of chert, carbonate and argillite are present in the Rice Lake belt (RLB; Anderson, 2013). A regional comparison between the BRGB and the RLB appears to be needed in the form of a future mapping and/or compilation project covering all of southeastern Manitoba.

Multiple lines of evidence from the mapping and detailed schematic investigations (e.g., Percival et al., 2006a, b, 2012; Percival, 2007; Sotiriou et al., 2019, 2020; Yang et al., 2019; Polat et al., 2020) suggest that a modern style of plate tectonics may have started at least in the Neoarchean in the western Superior province, consistent with the conclusion of Brown and Johnson (2018) based on thermal gradients defined by

temperature/pressure ratios documented at peak metamorphism from metamorphic rocks worldwide. A more detailed discussion on this fundamental question of geoscience is included in a recent review by Palin et al. (2020). Thus, Cu-(Au) mineralization related to magmatic-arc granitoid intrusions in subduction zones could be a potential exploration target in the BRGB, although erosion level of the granitoids (i.e., arc-related granitoid intrusions) and hydrothermal alteration styles must be further evaluated through estimation of their emplacement depth (e.g., Yang, 2017; Yang et al., 2020). The significance of such Au-Cu–type deposits is considerable in the Abitibi greenstone belt of Ontario and Quebec (e.g., Robert, 2001; Mathieu and Racicot, 2019).

Aluminum chemicals are used as industrial coatings, fillers, absorbent materials and cement additives. Archean anorthosite complexes, including the Mayville and Euclid Lake intrusions, and the Bird River sill in the southern limb, have potential for industrial-mineral production of Al chemicals via acid-separation processes (Veldhuyzen, 1995).

Acknowledgments

The authors are indebted to M.T. Corkery and H.P. Gilbert for introducing the field project and for help during the course of this project. C. Galeschuk and R. Dunbar from Mustang Minerals Corp. (now Grid Metals Corp.), D. Reeson and K. Ringland from Gossan Resources Limited, D. Good from Marathon PGM Corp., L. Lafreniere, S. Kushner and D. Drayson from the University of Manitoba, M. Hamilton from Brandon University and C. Boudreau and M.-P. Bédard from Université Laval are thanked for assistance in the field. The completion of this report could not have happened without assistance from MGS staff past and present (N. Brandson, E. Anderson, C.O. Böhm, S.D. Anderson, E.C. Syme, P. Kremer, G. Keller, P. Lenton, L. Chackowsky, H. Adediran, B. Lenton, M. McFarlane, M. Pacey, T. Booth, L. Janower, G. Benger, R. Unruh, V. Varga, and C. Epp); A. Polat and P. Sotiriou from the University of Windsor; and V. Bécu and V. McNicoll from the GSC. Finally, constructive reviews by M.L. Rinne and C.O. Böhm, report layout by C. Steffano and technical editing by R.F. Davie are gratefully acknowledged.

References

Allègre, C.J. and Minster, J.F. 1978: Quantitative models of trace element behavior in magmatic processes; Earth and Planetary Science Letters, v. 38 p. 1–25.

Anderson, S.D. 2008: Geology of the Rice Lake area, Rice Lake greenstone belt, southeastern Manitoba (parts of NTS 52L13, 52M4); Manitoba Science, Technology, Energy and Mines, Manitoba Geological Survey, Geoscientific Report GR2008-1, 96 p.

Anderson, S.D. 2013: Geology of the Garner–Gem lakes area, Rice Lake greenstone belt, southeastern Manitoba (parts of NTS 52L11, 14); Manitoba Mineral Resources, Manitoba Geological Survey, Geoscientific Report GR2013-1, 135 p.

Arif, M. and Jan, M.Q. 2006: Petrotectonic significance of the chemistry of chromite in the ultramafic-mafic complexes of Pakistan; Journal of Asian Earth Sciences, v. 27, p. 628–646.

Ashwal, L.D. 1993: Anorthosites; Springer-Verlag, Berlin, Germany, 422 p.

Baadsgaard, H. and Černý, P. 1993: Geochronological studies in the Winnipeg River pegmatite populations, southeastern Manitoba; Geological Association of Canada–Mineralogical Association of Canada, Joint Annual Meeting, Program with Abstracts, v. 18, p. A5.

Babuŝka, V. and Plomerová, J. 2020: Growth of primordial continents by cycles of oceanic lithosphere subductions: evidence from tilted seismic anisotropy supported by geochemical and petrological findings; Solid Earth Sciences, v. 5, p. 50–68.

Bailes, A.H., Percival, J.A., Corkery, M.T., McNicoll, V.J., Tomlinson, K.Y., Sasseville, C., Rogers, N., Whalen, J.B. and Stone, D. 2003: Geology and tectonostratigraphic assemblages, West Uchi map area, Manitoba and Ontario; Manitoba Geological Survey, Open File OF2003-1, Geological Survey of Canada, Open File 1522, Ontario Geological Survey, Preliminary Map P. 3461, 1:250 000 scale.

Ballhaus, C., Berry, R.F. and Green, D.H. 1991: High pressure experimental calibration of the olivine-orthopyroxene-spinel oxygen geobarometer: implications for the oxidation state of the upper mantle; Contributions to Mineralogy and Petrology, v. 107, p. 27–40.

Ballouard, C., Poujol, M., Boulvais, P., Branquet, Y., Tartese, R. and Vigneresse, J.-L. 2016: Nb-Ta fractionation in peraluminous granites: a marker of the magmatic-hydrothermal transition; Geology, v. 44, p. 231–234.

Banks, D.A., Yardley, B.W.D., Campbell, A.R. and Jarvis, K.E. 1994: REE composition of an aqueous magmatic fluid: a fluid inclusion study from the Capitan Pluton, New Mexico, USA; Chemical Geology, v. 113, p. 259–272.

Bannatyne, B.B. and Trueman, D.L. 1982: Chromite reserves and geology of the Bird River sill, Manitoba; Manitoba Energy and Mines, Mineral Resources Division, Open File Report OF82-1, 73 p.

Barker, F. 1979: Trondhjemite: definition, environment and hypotheses of origin; Chapter 1 *in* Trondhjemites, Dacites, and Related Rocks, F. Barker (ed.), Elsevier Science, Developments in Petrology, v. 6, p. 1–12.

Barnes, S.J. 1998: Chromite in komatiites, I. magmatic controls on crystallization and composition; Journal of Petrology, v. 39, no. 10, p. 1689–1720.

Barnes, S.J. 2000: Chromite in komatiites, II. modification during greenschist to mid-amphibolite facies metamorphism; Journal of Petrology, v. 41, no. 3, p. 387–409.

Barnes, S.J. and Kunilov, V.Y. 2000: Spinels and Mg ilmenites from the Noril'sk 1 and Talnakh intrusions and other mafic rocks of the Siberian flood basalt province; Economic Geology, v. 95, p. 1701–1717.

Barnes, S.J. and Roeder, P.L. 2001: The range of spinel compositions in terrestrial mafic and ultramafic rocks; Journal of Petrology, v. 42, p. 2279–2302.

Barnes, S.J. and Tang, Z.-L. 1999: Chrome spinels from the Jinchuan Ni-Cu sulfide deposit, Gansu Province, People's Republic of China; Economic Geology, v. 94, p. 343–356.

Bateman, J.D. 1943: Bird River chromite deposits, Manitoba; Canadian Institute of Mining and Metallurgy Transactions, v. 46, p. 154–183.

Bateman, J.D. 1945: Composition of the Bird River chromite, Manitoba; American Mineralogist, v. 30, p. 596–600.

Bécu, V. Houlé, M.G., Yang, X.M. and Gilbert, H.P. 2013: The Euclid Lake intrusion: a revisited cross-section through a historical chrome deposit of the Bird River greenstone belt, southeastern Manitoba; *in* Report of Activities 2013, Manitoba Mineral Resources, Manitoba Geological Survey, p. 85–94.

Bécu, V., Houlé, M.G., McNicoll, V.J., Yang, X.M. and Gilbert, H.P. 2015: Mafic intrusive rocks from the Bird River intrusive suite, Bird River greenstone belt, southeast Manitoba; *in* Targeted Geoscience Initiative 4: Canadian nickel–copper–platinum group elements–chromium ore systems — fertility, pathfinders, new and revised models, D.E. Ames and M.G. Houlé, (ed.), Geological Survey of Canada, Open File 7856, p. 49–60.

Bhatia, M.R. and Crook, K.A.W. 1986: Trace element characteristics of graywackes and tectonic discrimination of sedimentary basins; Contributions to Mineralogy and Petrology, v. 92, p. 181–193.

Blevin, P.L. 2004: Redox and compositional parameters for interpreting the granitoid metallogeny of eastern Australia: implications for gold-rich ore systems; Resource Geology v. 54, no. 3, p. 241–252.

Böhm, C.O., Heaman, L.M., Creaser, R.A. and Corkery, M.T. 2000: Discovery of pre–3.5 Ga exotic crust at the northwestern Superior Province margin, Manitoba; Geology, v. 28, p. 75–78.

Böhm, C.O., Zwanzig, H.V. and Creaser, R.A. 2007: Sm-Nd isotope technique as an exploration tool: delineating the northern extension of the Thompson Nickel Belt, Manitoba, Canada; Economic Geology, v. 102, p. 1217–1231.

Bonin, B. 2007: A-type granites and related rocks: evolution of a concept, problems and prospects; Lithos, v. 97, p. 1–29.

Brown, J.A., Martins, T. and Černý, P. 2017: The Tanco pegmatite at Bernic Lake, Manitoba, XVII: mineralogy and geochemistry of alkali feldspar; The Canadian Mineralogist, v. 55, p. 483–500.

Brown, M. and Johnson, T. 2018: Secular change in metamorphism and the onset of global plate tectonics; American Mineralogist, v. 103, p. 181–196.

Bruand, E., Fowler, M., Storey, C., Laurent, O., Antoine, C., Guitreau, M., Heilimo, E. and Nebel, O. 2020: Accessory mineral constraints on crustal evolution: elemental fingerprints for magma discrimination; Geochemical Perspectives Letters, v. 13, p. 7–12.

Burke, K. 2011: Plate tectonics, the Wilson cycle, and mantle plumes: geodynamics from the top; Annual Review of Earth and Planetary Sciences, v. 39, p. 1–29.

Camacho, A., Baadsgaard, H., Davis, D.W. and Černý, P. 2012: Radiogenic isotope systematics of the Tanco and Silverleaf pegmatites, Winnipeg River pegmatite district, Manitoba; The Canadian Mineralogist, v. 50, p. 1775–1792.

Castillo, P.R., Janney, P.E. and Solidum, R.U. 1999: Petrology and geochemistry of Camiguin Island, southern Philippines: insights to the source of adakites and other lavas in a complex arc setting; Contributions to Mineralogy and Petrology, v. 134, p. 33–51.

Černý, P. and Ercit, T.S. 2005: The classification of granitic pegmatites revisited; The Canadian Mineralogist, v. 43, p. 2005–2016.

Černý, P., Trueman, D.L., Ziehlke, D.V., Goad, B.E. and Paul, B.J. 1981: The Cat Lake–Winnipeg River and the Wekusko Lake pegmatite fields, Manitoba; Manitoba Energy and Mines, Mineral Resources Division, Economic Geology Report ER80-1, 216 p.

Chappell, B.W. and White, A.J.R. 1974: Two contrasting granite types; Pacific Geology, v. 8, p. 173–174.

Chappell, B.W. and White, A.J.R. 1992: I- and S-type granites in the Lachlan Fold Belt; Transactions of the Royal Society of Edinburgh: Earth Sciences, v. 83, p. 1–26.

Chappell, B.W. and White, A.J.R. 2001: Two contrasting granite types: 25 years later; Australian Journal of Earth Sciences, v. 48, p. 489–499.

Clarke, D.B. 1992: Granitoid Rocks; Chapman & Hall, London, England, 283 p.

Clarke, D.B. 2019: The origins of strongly peraluminous granitoid rocks; The Canadian Mineralogist, v. 57, p. 529–550.

Clemens, J.D. 2018: Granitic magmas with I-type affinities, from mainly metasedimentary sources: the Harcourt batholith of southeastern Australia; Contributions to Mineralogy and Petrology, v. 173, p. 93.

Clemens, J.D., Stevens, G. and Bryan, S.E. 2020: Conditions during the formation of granitic magmas by crustal melting – hot or cold; drenched, damp or dry? Earth-Science Reviews, v. 2020, 102982, URL <https://doi.org/10.1016/j.earscirev.2019.102982>.

Corfu, F., Stott, G.M. and Breaks, F.W. 1995: U-Pb geochronology and evolution of the English River subprovince, an Archean low P–high T metasedimentary belt in the Superior Province; Tectonics, v. 14, p. 1220–1233.

Corkery, M.T., Murphy, L.A. and Zwanzig, H.V. 2010: Re-evaluation of the geology of the Berens River Domain, east-central Manitoba (parts of NTS 52L, M, 53D, E, 62P, 63A, H); *in* Report of Activities 2010, Manitoba Innovation, Energy and Mines, Manitoba Geological Survey, p. 135–145.

Davies, J.F., Bannatyne, B.B., Barry, G.S. and McCabe, H.R. 1962: Geology and mineral resources of Manitoba; Manitoba Mines and Natural Resources, Mines Branch, 190 p.

Deer, W.A., Howie, R.A. and Zussman, J. 1962: Rock forming minerals: volume 5 – non-silicates; Longmans, London, United Kingdom, 371 p.

Deer, W.A., Howie, R.A. and Zussman, J. 1992: An introduction to the rock-forming minerals, second edition; Longmans, Essex, United Kingdom, 696 p.

Defant, M.J. and Drummond, M.S. 1990: Derivation of some modern arc magmas by melting of young subducted lithosphere; Nature, v. 347, p. 662–665.

DePaolo, D.J. 1981: Neodymium isotopes in the Colorado Front Range and crust-mantle evolution in the Proterozoic; Nature, v. 291, p. 193–196.

DePaolo, D.J. 1988: Neodymium isotope geochemistry: an introduction; Springer, Berlin, Germany, 187 p.

Dostal, J. and Chatterjee, A.K. 2000: Contrasting behaviour of Nb/Ta and Zr/Hf ratios in a peraluminous granitic pluton (Nova Scotia, Canada); Chemical Geology, v. 163, p. 207–218.

Drummond, M.S. and Defant, M.J. 1990: A model for trondhjemite-tonalite-dacite genesis and crustal growth via slab melting: Archaean to modern comparison; Journal of Geophysical Research, v. 95, p. 21503–21521.

Duguet, M., Lin, S., Davis, D.W., Corkery, M.T. and McDonald, J. 2009: Long-lived transpression in the Archean Bird River greenstone belt, western Superior Province, southeastern Manitoba; Precambrian Research, v. 174, p. 381–407.

Duke, J.M. 1983: Magmatic segregation deposits of chromite; Geoscience Canada, v. 10, p. 15–24.

Eby, G.N. 1990: The A-type granitoids: a review of their occurrence and chemical characteristics and speculations on their petrogenesis; Lithos, v. 26, p. 115–134.

Fitton, J.G., Saunders, A.D., Norry, M.J., Hardarson, B.S. and Taylor, R.N. 1997: Thermal and chemical structure of the Iceland plume; Earth and Planetary Science Letters, v. 153, p. 197–208.

Foley, S., Tiepolo, M. and Vannucci, R. 2002: Growth of early continental crust controlled by melting of amphibolite in subduction zones; Nature, v. 417, p. 837–840.

Frost, B.R. and Frost, C.D. 2008: A geochemical classification for feldspathic igneous rocks; Journal of Petrology, v. 49, p. 1955–1969.

Frost, B.R., Barnes, C.G., Collins, W.J., Arculus, R.J., Ellis, D.J. and Frost, C.D. 2001: A geochemical classification for granitic rocks; Journal of Petrology, v. 42, p. 2033–2048.

Frisch, W., Meschede, M. and Blakey, R. 2011: Plate tectonics: continental drift and mountain building; Springer, Heidelberg, 212 p.

Gait, R.I. 1964: The mineralogy of the chrome spinels of the Bird River Sill, Manitoba; M.Sc. thesis, University of Manitoba, Winnipeg, Manitoba, 64 p.

Gilbert, H.P. 2006: Geological investigations in the Bird River area, southeastern Manitoba (parts of NTS 52L5N and 6); *in* Report of Activities 2006, Manitoba Science, Technology, Energy and Mines, Manitoba Geological Survey, p. 184–205.

Gilbert, H.P. 2007: Stratigraphic investigations in the Bird River greenstone belt, Manitoba (part of NTS 52L5, 6); *in* Report of Activities 2007, Manitoba Science, Technology, Energy and Mines, Manitoba Geological Survey, p. 129–143.

Gilbert, H.P. 2008: Geology of the west part of the Bird River area, southeastern Manitoba (NTS 52L5); Manitoba Science, Technology, Energy and Mines, Manitoba Geological Survey, Preliminary Map PMAP2008-6, scale 1:20 000.

Gilbert, H.P. 2011: Stratigraphic investigation of the Neoarchean Bird River Belt, southeast Manitoba, Canada; Institute on Lake Superior Geology, 57th Annual Meeting, Ashland, Wisconsin, May 18–21, 2011, Proceedings Volume 57, Program and Abstracts, p. 42–43.

Gilbert, H.P. 2012: Stratigraphy and tectonic setting of the Neoarchean arc volcanic rocks in the Bird River Belt, Manitoba, Canada; Institute on Lake Superior Geology, 58th Annual Meeting, Proceedings Volume 58, Proceedings and Abstracts, p. 31–32.

Gilbert, H.P. and Kremer, P.D. 2008: Geology of the east part of the Bird River area, southeastern Manitoba (NTS 52L6); Manitoba Science, Technology, Energy and Mines, Manitoba Geological Survey, Preliminary Map PMAP2008-5, scale 1:20 000.

Gilbert, H.P., Davis, D.W., Duguet, M., Kremer, P.D., Mealin, C.A. and MacDonald, J. 2008: Geology of the Bird River Belt, southeastern Manitoba (parts of NTS 52L5, 6); Manitoba Science, Technology, Energy and Mines, Manitoba Geological Survey, Geoscientific Map MAP2008-1, scale 1:50 000.

Gilbert, H.P., Houlé, M.G., Yang, X.M., Scoates, J.S., Scoates, R.F.J., Mealin, C.A., Bécu, V., McNicoll, V. and Galeschuk, C.R. 2013: Mafic and ultramafic intrusive rocks and associated Ni-Cu-(PGE) and Cr-(PGE) mineralization in the Bird River greenstone belt, southeast Manitoba; Geological Association of Canada–Mineralogical Association of Canada, Joint Annual Meeting, Field Trip Guidebook FT-C2; Manitoba Innovation, Energy and Mines, Manitoba Geological Survey, Open File OF2013-7, 51 p.

Goldstein, S.L., O'Nions, R.K. and Hamilton, P.J. 1984: A Sm-Nd study of atmospheric dusts and particulates from major river systems; Earth and Planetary Science Letters, v. 70, p. 221–236.

Good, D., Mealin, C. and Walford, P. 2009: Geology of the Ore Fault Ni-Cu deposit, Bird River Sill complex, Manitoba; Exploration and Mining Geology, v. 18, p. 41–57.

Gorton, M.P. and Schandl, E.S. 2000: From continents to island arcs: a geochemical index of tectonic setting for arc-related and within-plate felsic to intermediate volcanic rocks; The Canadian Mineralogist, v. 38, p. 1065–1073.

Gottini, V. 1968: The TiO_2 frequency in volcanic rocks; Geologische Rundschau, v. 57, p. 930–935.

Hammarstrom, J.M. and Zen, E.-A. 1986: Aluminum in hornblende: an empirical igneous geobarometer; American Mineralogist, v. 71, p. 1297–1313.

Hanson, G.N. 1978: The application of trace elements to the petrogenesis of igneous rocks of granitic composition; Earth and Planetary Science Letters, v. 38, p. 26–43.

Hattie, A.R., Kerr, A.C., Pearce, J.A. and Mitchell, S.F. 2007: Classification of altered volcanic island arc rocks using immobile trace elements: development of the Th-Co discrimination diagram; Journal of Petrology, v. 48, p. 2341–2357.

Hawkesworth C. and Kemp, A.I.S. 2006: Evolution of the continental crust; Nature, v. 443, p. 811–817.

Hiebert, R. 2003: Composition and genesis of chromite in the Mayville intrusion, southeastern Manitoba; B.Sc. thesis, University of Manitoba, Winnipeg, Manitoba, 96 p.

Hildebrand, R.S., Whalen, J.B. and Bowring, S.A. 2018: Resolving the crustal composition paradox by 3.8 billion years of slab failure magmatism and collisional recycling of continental crust; Tectonophysics, v. 734–735, p. 69–88, URL <https://doi.org/10.1016/j.tecto.2018.04.001>.

Hoatson, D.H. 1998: Platinum-group element mineralisation in Australian Precambrian layered mafic-ultramafic intrusions; AGSO Journal of Australian Geology & Geophysics, v. 17, p. 139–151.

Hoffman, P.H. 1988: United plates of America, the birth of a craton: Early Proterozoic assembly and growth of Laurentia; Annual Review of Earth and Planetary Sciences, v. 16, p. 543–603.

Houlé, M.G., McNicoll, V.J., Bécu, V., Yang, X.M. and Gilbert, H.P. 2013: New age for the Mayville Intrusion: implication for a large mafic-ultramafic event in the Bird River Greenstone Belt, southeastern Manitoba; Geological Association of Canada–Mineralogical Association of Canada, Joint Annual Meeting, Winnipeg, Manitoba, May 22–24, 2013, Abstract with Programs.

Houlé, M.G., Lesher, C.M., McNicoll, V.J., Metsaranta, R.T., Sappin, A.-A., Goutier, J., Bécu, V., Gilbert, H.P. and Yang, X.M. 2015: Temporal and spatial distribution of magmatic Cr-(PGE), Ni-Cu-(PGE), and Fe-Ti-(V) deposits in the Bird River–Uchi–Oxford-Stull–La Grande Rivière–Eastmain domains: a new metallogenic province within the Superior Craton; *in* Targeted Geoscience Initiative 4: Canadian Nickel–Copper–Platinum Group Elements–Chromium Ore Systems — Fertility, Pathfinders, New and Revised Models, D.E. Ames and M.G. Houlé, (ed.), Geological Survey of Canada, Open File 7856, p. 35–48.

Houlé, M.G., Lesher, C.M., Sappin, A.-A., Metsaranta, R.T., Goutier, J. and Yang, X.-M. 2020: Overview of Ni-Cu-(PGE), Cr-(PGE), and Fe-Ti-V magmatic mineralization in the Superior Province: insights on metallotects and metal endowment; *in* Targeted Geoscience Initiative 5: Advances in the Understanding of Canadian Ni-Cu-PGE and Cr Ore Systems - Examples from the Midcontinent Rift, the Circum-Superior Belt, the Archean Superior Province, and Cordilleran Alaskan-type Intrusions, W. Bleeker and M.G. Houlé, (ed.), Geological Survey of Canada, Open File 8722, p. 117-139, URL <https://doi.org/10.4095/326890>.

Hulbert, L. and Scoates, J. 2000: Digital map and database of magmatic Ni-Cu±PGE occurrences and mafic-ultramafic bodies in Manitoba; Manitoba Industry, Trade and Mines, Manitoba Geological Survey, Economic Geology Report ER2000-1, CD-ROM.

Irvine, T.N. 1965: Chromian spinel as a petrogenetic indicator, part I: theory; Canadian Journal of Earth Sciences, v. 2, p. 648–672.

Irvine, T.N. 1967: Chromian spinel as a petrogenetic indicator, part II: petrologic application; Canadian Journal of Earth Sciences, v. 4, p. 71–103.

Irvine, T.N. 1975: Crystallization sequences in the Muskox intrusion and other layered intrusions, II: origin of chromitite layers and similar deposits of other magmatic ores; Geochimica et Cosmochimica Acta, v. 39, p. 991–1020.

Irvine, T.N. and Baragar, W.R.A. 1971: A guide to the chemical classification of the common volcanic rocks; Canadian Journal of Earth Sciences, v. 8, p. 523–548.

Ishihara, S. 1977: The magnetite-series and ilmenite-series granitic rocks; Mining Geology, v. 27, p. 293–305.

Ishihara, S. 1981: The granitoid series and mineralization; Economic Geology, 75th Anniversary Volume, p. 458–484.

Ishihara S. 2004: The redox state of granitoids relative to tectonic setting and Earth history: the magnetite-ilmenite series 30 years later; Transactions of the Royal Society of Edinburgh: Earth Sciences, v. 95, p. 23–33.

Janoušek, V. 1999: Interpreting Sr-Nd isotopic data from magmatic and metamorphic rocks: numerical recipes and exercises; Czech Geological Survey, Prague, p. 1–15.

Johnson, M.C. and Rutherford, M.J. 1989: Experimental calibration of the aluminum-in-hornblende geobarometer with application to Long Valley caldera (California) volcanic rocks; Geology, v. 17, p. 837–841.

Kamenetsky, V.S., Crawford, A.J. and Meffre, S. 2001: Factors controlling chemistry of magmatic spinel: an empirical study of associated olivine, Cr-spinel and melt inclusions from primitive rocks; Journal of Petrology, v. 42, p. 655–671.

Keays, R.R. and Lightfoot, P.C. 2010: Crustal sulfur is required to form magmatic Ni-Cu sulfide deposits: evidence from chalcophile element signatures of Siberian and Deccan Trap basalts; Mineralium Deposita, v. 45, p. 241–257.

Kirkland, C.L., Smithies, R.H., Taylor, R.J.M., Evans, N. and McDonald, B. 2015: Zircon Th/U ratios in magmatic environs; Lithos, v. 212–215, p. 397–414.

Krause, J., Brügmann, G.E. and Pushkarev, E.V. 2011: Chemical composition of spinel from Uralian-Alaskan–type mafic-ultramafic complexes and its petrogenetic significance; Contributions to Mineralogy and Petrology, v. 161, p. 255–273.

Kremer, P. 2010: Structural geology and geochronology of the Bernic Lake area in the Bird River greenstone belt, Manitoba: evidence for syn-deformational emplacement of the Bernic Lake pegmatite group; M.Sc. thesis, University of Waterloo, Waterloo, Ontario, 100 p.

Kremer, P.D. and Lin, S. 2006: Structural geology of the Bernic Lake area, Bird River greenstone belt, southeastern Manitoba (NTS 52L6): implications for rare element pegmatite emplacement; *in* Report of Activities 2006, Manitoba Science, Technology, Energy and Mines, Manitoba Geological Survey, p. 206–213.

Kretschmar, U. and McBride, D. 2015: The metallogeny of lode gold deposits: a syngenetic perspective; Elsevier, Amsterdam, Netherlands, 350 p.

Kushner, D.S. 2016: Petrographic and geochemical analysis of a granitic unit within the Inconnu Batholith, southeastern Manitoba; B.Sc. thesis, University of Manitoba, Winnipeg, 32 p.

Leake, B.E., Woolley, A.R., Arps, C.E.S, Birch, W.D., Gilbert, M.C., Grice, J.D., Hawthorne, F.C., Kato, A., Kisch, H.J., Krivovichev, V.G., Linthout, K., Laird, J., Mandarino, J.A., Maresch, W.V., Nickel, E.H., Rock, N.M.S., Schumacher, J.C., Smith, D.C., Stephenson, N.C.N., Ungaretti, L., Whittaker, E.J.W. and Guo, Y. 1997: Nomenclature of amphiboles: report of the Subcommittee on Amphiboles of the International Mineralogical Association, Commission on New Minerals and Mineral Names; American Mineralogist, v. 82, p. 1019–1037.

Leake, B.E., Woolley, A.R., Birch, W.D., Burke, E.J., Ferraris, G., Grice, J.D., Hawthorne, F.C., Kisch, H.J., Krivovichev, V.G., Schumacher, J.C., Stephenson, N.C.N. and Whittaker, E.J.W. 2003: Nomenclature of amphiboles: additions and revisions to the International Mineralogical Association's 1997 recommendations; The Canadian Mineralogist, v. 41, p. 1355–1362.

Le Bas, M.J., Le Maitre, R.W., Streckeisen, A. and Zanettin, B. 1986: A chemical classification of volcanic rocks based on the total alkali silica diagram; Journal of Petrology, v. 27, p. 745–750.

Lee, C.-T.A., Luffi, P. and Chin, E.J. 2011: Building and destroying continental mantle; Annual Review of Earth and Planetary Sciences, v. 39, p. 59–90.

Le Mée, L., Girardeau, J. and Monnier, C. 2004: Mantle segmentation along the Oman ophiolite fossil midocean ridge; Nature, v. 432, p. 167–172.

Lemkow, D.R., Sanborn-Barrie, M., Bailes, A.H., Percival, J.A., Rogers, N., Skulski, T., Anderson, S.D, McNicoll, V., Whalen, J.B., Tomlinson, K.Y., Parker, J.R., Hollings, P. and Young, M. 2006: GIS compilation of geology and tectonostratigraphic assemblages, western Uchi Subprovince, western Superior Province, Ontario and Manitoba; Geological Survey of Canada, Open File 5269, Manitoba Geological Survey, Open File OF2006-30, Ontario Geological Survey, Miscellaneous Release–Data 203, scale 1:250 000, CD-ROM.

Liew, T.C. and Hofmann, A.W. 1988: Precambrian crustal components, plutonic associations, plate environment of the Hercynian Fold Belt of central Europe: indications from Nd and Sr isotopic study; Contributions to Mineralogy and Petrology, v. 98, p. 129–138.

Lightfoot, P.C. 2016: Nickel sulfide ores and impact melts: origin of the Sudbury Igneous Complex; Elsevier, Amsterdam, Netherlands, 680 p.

Lightfoot, P.C., Naldrett, A.J., Gorbachev, N.S., Doherty, W. and Fedorenko, V.A. 1990: Geochemistry of the Siberian Trap of the Noril'sk area, USSR, with implications for the relative contributions of crust and mantle to flood basalt magmatism; Contributions to Mineralogy and Petrology, v. 104, p. 631–644.

Lin, S. 2005: Synchronous vertical and horizontal tectonism in the Neoarchean: kinematic evidence from a synclinal keel in the northwestern Superior craton, Canada; Precambrian Research, v. 139, p. 181–194.

Linnen, R.L. and Keppler, H. 2002: Melt composition control of Zr/Hf fractionation in magmatic processes; Geochimica et Cosmochimica Acta, v. 66, p. 3293–3301.

Loiselle, M.C. and Wones, D.R. 1979: Characteristics and origin of anorogenic granites; Geological Society of America, Abstracts with Programs, v. 11, no. 7, p. 468.

Ludwig, K.R. 2008: User's manual for Isoplot 3.70: a geochronological toolkit for Microsoft Excel; Berkeley Geochronology Center, Special Publication 4, 76 p.

Macek, J.J. 1985a: Cat Creek project (parts of 52L/1, 8); *in* Report of Activities 1985, Manitoba Energy and Mines, Mineral Resources Division, p. 122–129.

Macek, J.J. 1985b: Cat Creek; Manitoba Energy and Mines, Preliminary Map PMAP1985C-1, scale 1:10 000.

Mackie, R.A. 2003: Emplacement history and PGE-enriched sulphide mineralization of the heterolithic breccia zone in the Mayville intrusion; B.Sc. thesis, University of Manitoba, Winnipeg, Manitoba, 135 p.

Maniar, P.D. and Piccoli, P.M. 1989: Tectonic discrimination of granitoids; Geological Society of America Bulletin, v. 101, p. 635–643.

Manitoba Energy and Mines 1987: Pointe du Bois, NTS 52L; Manitoba Energy and Mines, Minerals Division, Bedrock Geology Compilation Map Series, NTS 52L, preliminary edition, scale 1:250 000.

Mantle, G.W. and Collins, W.J. 2008: Quantifying crustal thickness variations in evolving orogens: correlation between arc basalt composition and Moho depth; Geology, v. 36, p. 87–90.

Martin, H., Smithies, R.H., Rapp, R., Moyen, J.-F. and Champion, D. 2005: An overview of adakite, tonalite–trondhjemite–granodiorite (TTG), and sanukitoid: relationships and some implications for crustal evolution; Lithos, v. 79, p. 1–24.

Martins, T., Kremer, P.D., Corrigan, D. and Rayner, N. 2019: Geology of the Southern Indian Lake area, north-central Manitoba (parts of NTS 64G1, 2, 7–10, 64H3–6); Manitoba Growth, Enterprise and Trade, Manitoba Geological Survey, Geoscientific Report GR2019-1, 51 p. plus 4 colour maps at 1:50 000 scale.

Mathieu, L. and Racicot, D. 2019: Petrogenetic study of the multiphase Chibougamau Pluton: Archaean magmas associated with Cu-Au magmato-hydrothermal systems; Minerals, v. 9, p. 174.

McDonough, W.F. and Sun, S.-s. 1995: The composition of the Earth; Chemical Geology, v. 120, p. 223–253.

McGregor, C.R. 1986: Subsurface Precambrian geology of southeastern Manitoba south of 49 degrees 30 minutes; *in* Report of Field Activities 1986, Manitoba Energy and Mines, Minerals Division, p. 139–140.

McRitchie, W.D. 1971: Petrology and environment of the acidic plutonic rocks of the Wanipigow-Winnipeg rivers region, southeastern Manitoba; *in* Geology and Geophysics of the Rice Lake Region, Southeastern Manitoba (Project Pioneer), W.D. McRitchie and W. Weber (ed.), Manitoba Mines and Natural Resources, Mines Branch, Publication 71-1, p. 7–61.

Mealin, C.A. 2008: Geology, geochemistry and Cr-Ni-Cu-PGE mineralization of the Bird River sill: evidence for a multiple intrusion model; M.Sc. thesis, University of Waterloo, Waterloo, Ontario, 155 p.

Miyashiro, A. 1974: Volcanic-rock series in island arcs and active continental margins; American Journal of Science, v. 274, p. 321–355.

Middlemost, E.A.K. 1994: Naming materials in the magma/igneous rock system; Earth-Science Reviews, v. 37, p. 215–224.

Moyen, J.-F. 2011: The composite Archaean grey gneisses: petrological significance, and evidence for a non-unique tectonic setting for Archaean crustal growth; Lithos, v. 123, p. 21–36.

Moyen, J.-F. and Martin, H. 2012: Forty years of TTG research; Lithos, v. 148, p. 312–336.

Mustang Minerals Corp. 2011: Annual report, 2010; Mustang Minerals Corp., 40 p.

Mutch, E.J.F., Blundy, J.D., Tattitch, B.C., Cooper, F.J. and Brooker, R.A. 2016: An experimental study of amphibole stability in low-pressure granitic magmas and a revised Al-in-hornblende geobarometer; Contributions to Mineralogy and Petrology, v. 171, p. 85.

Naldrett, A.J. 2004: Magmatic sulfide deposits; Springer, Berlin, 727 p.

Nickel, E.H. 1992: Solid solutions in mineral nomenclature; Mineralogical Magazine, v. 56, p. 127–130.

O'Nions, R.K., Carter, S.R., Evensen, N.M. and Hamilton, P.J. 1979: Geochemical and cosmochemical applications of Nd isotope analysis; Annual Review of Earth and Planetary Science, v. 7, p. 11–38.

Palin, R.M., Santosh, M., Cao, W., Li, S.-S., Hernández-Uribe, D. and Parsons, A. 2020: Secular change and the onset of plate tectonics on Earth; Earth-Science Reviews, v. 207, p. 103172, URL <https://doi.org/10.1016/j.earscirev.2020.103172>.

Parks, J., Lin, S., Davis, D.W., Yang, X.M., Creaser, R.A. and Corkery, M.T. 2014: Meso- and Neoarchean evolution of the Island Lake greenstone belt and the northwestern Superior Province: evidence from lithogeochemistry, Nd isotope data, and U-Pb zircon geochronology; Precambrian Research, v. 246, p. 160–179.

Pearce, J.A. 1983: Role of the sub-continental lithosphere in magma genesis at active continental margins; *in* Continental Basalts and Mantle Xenoliths, C.J. Hawkesworth and M.J. Norry (ed.), Shiva Publishing Limited, Nantwich, United Kingdom, p. 230–249.

Pearce, J.A. 1996: A user's guide to basalt discrimination diagrams; *in* Trace Element Geochemistry of Volcanic Rocks: Applications for Massive Sulphide Exploration, D.A. Wyman (ed.), Geological Association of Canada, Short Course Notes 12, p. 79–113.

Pearce, J.A. 2008: Geochemical fingerprinting of oceanic basalts with applications to ophiolite classification and the search for Archean oceanic crust; Lithos, v. 100, p. 14–48.

Pearce, J.A., Harris, N.B.W. and Tindle, A.G. 1984: Trace element discrimination diagrams for the tectonic interpretation of granitic rocks; Journal of Petrology, v. 25, p. 956–983.

Pearce, J.A. and Peate, D.W. 1995: Tectonic implications of the composition of volcanic arc magmas; Annual Review of Earth and Planetary Sciences, v. 23, p. 251–285.

Pearce, J.A., Stern, R.J., Bloomer, S.H. and Fryer, P. 2005: Geochemical mapping of the Mariana arc-basin system: implications for the nature and distribution of subduction components; Geochemistry, Geophysics, Geosystems, v. 6, p. 1–27.

Peccerillo, A. and Taylor, S.R. 1976: Geochemistry of Eocene calc-alkaline volcanic rocks from the Kastamonu area, northern Turkey; Contributions to Mineralogy and Petrology, v. 58, p. 63–81.

Peck, D.C. and Keays, R.R. 1990: Geology, geochemistry, and origin of platinum-group element-chromitite occurrences in the Heazlewood River Complex, Tasmania; Economic Geology, v. 85, p. 765–793.

Peck, D.C., Theyer, P., Bailes, A.H. and Chornoby, J. 1999: Field and lithogeochemical investigations of mafic and ultramafic rocks and associated Cu-Ni-PGE mineralization in the Bird River greenstone belt (parts of NTS 52L); *in* Report of Activities 1999, Manitoba Industry, Trade and Mines, Geological Services, p. 106–110.

Peck, D.C., Theyer, P., Hulbert, L., Xiong, J., Fedikow, M.A.F. and Cameron, H.D.M. 2000: Preliminary exploration database for platinum-group elements in Manitoba; Manitoba Industry, Trade and Mines, Manitoba Geological Survey, Open File OF2000-5, CD-ROM.

Peck, D.C., Keays, R.R., James, R.S., Chubb, P.T. and Reeves, S.J. 2001: Controls on the formation of contact-type platinum-group element mineralization in the East Bull Lake intrusion; Economic Geology, v. 96, p. 559–581.

Peck, D.C., Scoates, R.F.J., Theyer, P., Desharnais, G., Hulbert, L.J. and Huminicki, M.A.E. 2002: Stratiform and contact-type PGE-Cu-Ni mineralization in the Fox River Sill and the Bird River Belt, Manitoba; *in* The Geology, Geochemistry, Mineralogy and Mineral Beneficiation of Platinum-Group Elements, L.J. Cabri (ed.), Canadian Institute of Mining and Metallurgy, Special Volume 54, p. 367–387.

Percival, J.A. 2007: Geology and metallogeny of the Superior Province, Canada; *in* Mineral Deposits of Canada: A Synthesis of Major Deposit-Types, District Metallogeny, the Evolution of Geological Provinces, and Exploration Methods, W.D. Goodfellow (ed.), Geological Association of Canada, Mineral Deposits Division, Special Publication 5, p. 903–928.

Percival, J.A., McNicoll, V. and Bailes, A.H. 2006a: Strike-slip juxtaposition of ca. 2.72 Ga juvenile arc and >2.98 Ga continent margin sequences, and its implications for Archean terrane accretion, western Superior Province, Canada; Canadian Journal of Earth Sciences, v. 43, p. 895–927.

Percival, J.A., Sanborn-Barrie, M., Skulski, T., Stott, G.M., Helmstaedt, H. and White, D.J. 2006b: Tectonic evolution of the western Superior Province from NATMAP and LITHOPROBE studies; Canadian Journal of Earth Sciences, v. 43, p. 1085–1117.

Percival, J.A., Skulski, T., Sanborn-Barrie, M., Stott, G.M., Leclair, A.D., Corkery, M.T. and Boily, M. 2012: Geology and tectonic evolution of the Superior Province, Canada; *in* Tectonic Styles in Canada: The LITHOPROBE perspective, J.A. Percival, F.A. Cook and R.M. Clowes (ed.), Geological Association of Canada, Special Paper 49, p. 321–378.

Phinney, W.C., Morrison, D.E. and Maczuga, D.E. 1985: Widespread tholeiitic melts in Archean crustal genesis; EOS, v. 66, p. 405.

Polat, A. and Kerrich, R. 2001: Geodynamic processes, continental growth, and mantle evolution recorded in late Archean greenstone belts of the southern Superior Province, Canada; Precambrian Research, v. 112, p. 5–25.

Polat, A. and Kerrich, R. 2002: Nd-isotope systematics of ~2.7 Ga adakites, magnesian andesites, and arc basalts, Superior Craton: evidence for shallow crustal recycling at Archean subduction zones; Earth and Planetary Science Letters, v. 202, p. 345–360.

Polat, A., Kokfelt, T., Burke, K.C., Kusky, T.M., Bradley, D.C., Dziggel, A. and Kolb, J. 2016: Lithological, structural, and geochemical characteristics of the Mesoarchean Târtoq greenstone belt, southern West Greenland, and the Chugach–Prince William accretionary complex, southern Alaska: evidence for uniformitarian plate-tectonic processes; Canadian Journal of Earth Sciences, v. 53, p. 1336–1371.

Polat, A., Sotiriou, P. and Yang, X.M. 2020: Convergent margin origin of Neoarchean anorthosite-bearing layered intrusions in the Superior Province, Canada [abstract]; Geoconvention 2020 - Geological Association of Canada–Mineralogical Association of Canada, Joint Annual Meeting, Calgary, Alberta, September 21–23, 2020, Program with Abstracts, URL <https://geoconvention.com/wp-content/uploads/abstracts/2020/56669-convergent-margin-origin-of-neoarchean-anorthosite.pdf> [September 2020].

Prouteau, G., Scaillet, B., Pichavant, M. and Maury, R.C. 1999: Fluid-present melting of ocean crust in subduction zones; Geology, v. 27, p. 1111–1114.

Prouteau, G., Scaillet, B., Pichavant, M. and Maury, R. 2001: Evidence for mantle metasomatism by hydrous silicic melts derived from subducted oceanic crust; Nature, v. 410, p. 197–200.

Rinne, M.L. 2017: Preliminary results of bedrock mapping at Bigstone Lake and Knight Lake, northwestern Superior province, Manitoba (parts of NTS 53E11, 12, 13, 14); *in* Report of Activities 2017, Manitoba Growth, Enterprise and Trade, Manitoba Geological Survey, p. 19–29.

Rittmann, A. 1973: Stable mineral assemblages of igneous rocks; Springer-Verlag, Berlin, Germany, 262 p.

Robert, F. 2001: Syenite-associated disseminated gold deposits in the Abitibi greenstone belt, Canada; Mineralium Deposita, v. 36, p. 503–516.

Roeder, P.L. 1994: Chromite: from the fiery rain of chondrules to the Kilauea Iki lava lake; The Canadian Mineralogist, v. 32, p. 155–196.

Rollinson, H.R. 1993: Using geochemical data: evaluation, presentation, interpretation; Longman Scientific & Technical, London, United Kingdom, 352 p.

Rollinson, H.R., Appel, P.W.U. and Frei, R. 2002: A metamorphosed, Early Archean chromitite from West Greenland: implications for the genesis of Archaean anorthositic chromitites; Journal of Petrology, v. 43, p. 2143–2170.

Rollinson, H.R., Reid, C. and Windley, B. 2010: Chromitites from the Fiskenæsset anorthositic complex, West Greenland: clues to late Archaean mantle processes; *in* The Evolving Continents: Understanding Processes of Continental Growth, T.M. Kusky, M.-G. Zhai and W. Xiao (ed.), Geological Society of London, Special Publication 338, p. 197–212.

Ross, P.-S. and Bédard, J.H. 2009: Magmatic affinity of modern and ancient subalkaline volcanic rocks determined from trace-element discriminant diagrams; Canadian Journal of Earth Sciences, v. 46, p. 823–839.

Rudnick, R.L. and Gao, S. 2010: Composition of the continental crust; Chapter 5 *in* Treatise On Geochemistry, H.D. Holland and K.K. Turetian (ed.), Elsevier, Amsterdam, The Netherlands, p. 197–234.

Scaillet, B., Holtz, F. and Pichavant, M. 2016: Experimental constraints on the formation of silicic magmas; Elements, v. 12, p. 109–114.

Scoates, R.F.J. 1983: A preliminary stratigraphic examination of the ultramafic zone of the Bird River Sill, southeastern Manitoba; *in* Report of Field Activities, Manitoba Department of Energy and Mines, Mineral Resources Division, p. 70–83.

Scoates, R.F.J., Williamson, B.L. and Duke, J.M. 1986: Igneous layering in the Ultramafic Series, Bird River Sill; *in* Layered intrusions of southeastern Manitoba and northwestern Ontario, R.F.J. Scoates, B.L. Williamson, J.M. Duke, W. Mandziuk, W.C. Brisbin and R.H. Sutcliffe (ed.), Geological Association of Canada, Field Trip 13 Guidebook, May 12–14, 1986, p. 1–19.

Scoates, R.F.J., Williamson, B.L., Eckstrand, O.R. and Duke, J.M. 1989: Stratigraphy of the Bird River Sill and its chromitiferous zone, and preliminary geochemistry of the chromitite layers and PGE-bearing units, Chrome property, Manitoba; *in* Investigations by the Geological Survey of Canada in Manitoba and Saskatchewan during the 1984–1989 Mineral Development Agreements, A.G. Galley (ed.), Geological Survey of Canada, Open File 2133, p. 69–82.

Scoates, J.S. and Scoates, R.F.J. 2013: Age of the Bird River Sill, southeastern Manitoba, Canada, with implications for the secular variation of layered intrusion–hosted stratiform chromite mineralization; Economic Geology, v. 108, p. 895–907.

Shirey, S.B. and Hanson, G.N. 1984: Mantle-derived Archaean monzodiorites and trachyandesites; Nature, v. 310, p. 222–224.

Siivola, J. and Schmid, R. 2007: Systematic nomenclature for metamorphic rocks: list of mineral abbreviations, recommendations by the IUGS Subcommission on the Systematics of Metamorphic Rocks, URL <http://www.bgs.ac.uk/scmr/docs/papers/paper_12.pdf> [June 2012].

Sobolev, N.V. and Logvinova, A.M. 2005: Significance of accessory chrome spinel in identifying serpentinite paragenesis; International Geology Review, v. 47, p. 58–64.

Sotiriou, P., Polat, A., Frei, R., Yang, X.M. and van Vessem, J. 2019: A back-arc origin for the Neoarchaean megacrystic anorthosite-bearing Bird River Sill and the associated greenstone belt, Bird River subprovince, western Superior Province, Manitoba, Canada; International Journal of Earth Sciences, v. 108, p. 2177–2207.

Sotiriou, P., Polat, A., Frei, R., Yang, X.M. and van Vessem, J. 2020: Evidence for Neoarchean hydrous arc magmatism, the anorthosite-bearing Mayville Intrusion, western Superior Province, Canada; Lithos, v. 362–363, p. 105482.

Springer, G.D. 1949: Geology of the Cat Lake–Winnipeg River area; Manitoba Mines Branch, Preliminary Report 48-7, 15 p.

Springer, G.D. 1950: Mineral deposits of the Cat Lake–Winnipeg River area; Manitoba Mines and Natural Resources, Mines Branch, Publication 49-7, 14 p.

Stepanov, A., Mavrogenes, J.A., Meffre, S. and Davison, P. 2014: The key role of mica during igneous concentration of tantalum; Contributions to Mineralogy and Petrology, v. 167, p. 1009.

Stevens, R.E. 1944: Compositions of some chromites of the western hemisphere; American Mineralogist, v. 29, p. 1–34.

Stevenson, R.K., Bernier, F., Courteau, G. and Achado, N. 2000: Nd isotopic studies of the buried Precambrian crust in southern Manitoba; *in* Western Superior Transect, 6th Annual Workshop, R.M. Harrap and H.H. Helmstaedt (ed.), LITHOPROBE Secretariat, University of British Colombia, Vancouver, British Columbia, LITHOPROBE Report 77, p. 116–118.

Stevenson, R., Machado, N., Bernier, F. and Courteau, G. 2001: Nd isotopic studies of the buried Precambrian crust in southern Manitoba; *in* 2001 Western Superior Transect Seventh Annual Workshop, R.M. Harrap and H.H. Helmstaedt (ed.), LITHOPROBE Secretariat, University of British Columbia, Vancouver, British Columbia, Report 80, p. 17–25.

Stott, G.M., Corkery, M.T., Percival, J.A., Simard, M. and Goutier, J. 2010: A revised terrane subdivision of the Superior Province; *in* Summary of Field Work and Other Activities 2010, Ontario Geological Survey, Open File Report 6260, p. 20-1–20-10.

Stowe, C.W. 1994: Compositions and tectonic settings of chromite deposits through time; Economic Geology, v. 89, p. 528–546.

Streckeisen, A. 1976: To each plutonic rock its proper name; Earth-Science Reviews, v. 12, p. 1–33.

Streckeisen, A.L. and LeMaitre, R.W. 1979: A chemical approximation to modal QAPF classification of the igneous rocks; Neues Jahrbuch für Mineralogie, v. 136, p. 169–206.

Sun, S.-s. and McDonough, W.F. 1989: Chemical and isotopic systematics of oceanic basalts: implications for mantle composition and processes; *in* Magmatism in the Ocean Basins, A.D. Saunders and M.J. Norry (ed.), Geological Society, Special Publication 42, p. 313–345.

Syme, E.C. 1998: Ore-associated and barren rhyolites in the central Flin Flon belt: case study of the Flin Flon mine sequence; Manitoba Energy and Mines, Geological Services, Open File OF98-9, 26 p.

Syme, E.C., Lucas, S.B., Bailes, A.H. and Stern, R.A. 1999: Contrasting arc and MORB-like assemblages in the Paleoproterozoic Flin Flon Belt, Manitoba, and the role of intra-arc extension in localizing volcanic-hosted massive sulphide deposits; Canadian Journal of Earth Sciences, v. 36, p. 1767–1788.

Tatsumi, Y. and Eggins, S. 1995: Subduction zone magmatism; Blackwell Science, Cambridge, Massachusetts, 211 p.

Taylor, S.R. and Mclennan S.M. 1985: The continental crust: its composition and evolution; Blackwell, Oxford, United Kingdom, 312 p.

Theyer, P. 1986: Platinum group elements in southeastern Manitoba; *in* Report of Field Activities 1986, Manitoba Energy and Mines, Minerals Division, p. 125–130.

Theyer, P. 1991: Petrography, chemistry and distribution of platinum and palladium in ultramafic rocks of the Bird River Sill, SE Manitoba, Canada; Mineralium Deposita, v. 26, no. 3, p. 165–174.

Theyer, P. 1994: Mineral deposits and occurrences in the Flintstone Lake area, NTS 52L/11; Manitoba Energy and Mines, Geological Services, Mineral Deposit Series Report 22, 60 p.

Theyer, P. 2003: Platinum group element investigations in the Mayville igneous complex, southeastern Manitoba (NTS 52L12); *in* Report of Activities 2003, Manitoba Industry, Trade and Mines, Manitoba Geological Survey, p. 196–199.

Trueman, D.L. 1980: Stratigraphy, structure and metamorphic petrology of the Archean greenstone belt at Bird River, Manitoba; Ph.D. thesis, University of Manitoba, Winnipeg, Manitoba, 150 p.

Trueman, D.L. and Macek, J.J. 1971: Ultramafic project: geology of the Bird River Sill; Manitoba Department of Mines, Resources and Environmental Management, Mines Branch, Preliminary Map 1971-A1, scale 1:31 680.

Veldhuyzen, H. 1995: Aluminum extraction from an Ontario calcic anorthosite by acid processes and resultant products—aluminum chemicals, coatings, fillers, absorbent and cement additive; Ontario Geological Survey, Open File Report 5919, 281 p.

Voigt, M. and von der Handt, A. 2011: Influence of subsolidus processes on the chromium number in the spinel in ultramafic rocks; Contributions to Mineralogy and Petrology, v. 162, p. 675–689.

Wang, X. 1993: U-Pb zircon geochronology study of the Bird River greenstone belt, southeastern Manitoba; M.Sc. thesis, University of Windsor, Windsor, Ontario, 96 p.

Watson, D.M. 1985: Chromite reserves of the Bird River Sill; Manitoba Energy and Mines, Geological Services, Open File Report 85-8, 22 p.

Whalen, J.B. and Frost, C.D. 2013: The Q-ANOR diagram: a tool for the petro-genetic and tectonomagmatic characterization of granitic suites; URL <https://www.researchgate.net/publication/290161821> [September 2018].

Whalen, J.B. and Hildebrand, R.S. 2019: Trace element discrimination of arc, slab failure, and A-type granitic rocks; Lithos, v. 348–349, p. 105–179.

Whalen, J.B., Currie, K.L. and Chappell, B.W. 1987: A-type granites: geochemical characteristics, discrimination and petrogenesis; Contributions to Mineralogy and Petrology, v. 95, p. 407–419.

Williamson, B.L. 1990: Geology of the Bird River Sill at the Chrome property, southeast Manitoba; Geological Survey of Canada, Open File 2067, 44 p.

Windley, B.F. and Garde, A.A. 2009: Arc-generated blocks with crustal sections in the North Atlantic craton of West Greenland: crustal growth in the Archean with modern analogues; Earth-Science Reviews, v. 93, p. 1–30.

Winter, J.D. 2010: Principles of igneous and metamorphic petrology (second edition); Pearson, New York, U.S.A., 737 p.

Whyman, D. and Kerrich, R. 2010: Mantle plume – volcanic arc interaction: consequences for magmatism, metallogeny, and cratonization in the Abitibi and Wawa subprovinces, Canada; Canadian Journal of Earth Sciences, v. 47, p. 565–589.

Yang, X.M. 2007: Using the Rittmann Serial Index to define the alkalinity of igneous rocks; Neues Jahrbuch für Mineralogie, v. 184, p. 95–103.

Yang, X.M. 2012: Bedrock geology of the Cat Creek area, Bird River greenstone belt, southeastern Manitoba (part of NTS 52L12); Manitoba Innovation, Energy and Mines, Manitoba Geological Survey, Preliminary Map PMAP2012-3, scale 1:12 500.

Yang, X.M. 2013: Bedrock geology of the Cat Lake–Euclid Lake area, Bird River greenstone belt, southeastern Manitoba (parts of NTS 52L11, 12); Manitoba Mineral Resources, Manitoba Geological Survey, Preliminary Map PMAP2013-7, scale 1:10 000.

Yang, X.M. 2014a: Bedrock geology of the Cat Creek area, Bird River greenstone belt, southeastern Manitoba (part of NTS 52L12); Manitoba Mineral Resources, Manitoba Geological Survey, Preliminary Map PMAP2014-3, scale 1:10 000.

Yang, X.M. 2014b: Granitoid rocks in southeastern Manitoba: preliminary results of reconnaissance mapping and sampling; *in* Report of Activities 2014, Manitoba Mineral Resources, Manitoba Geological Survey, p. 49–63.

Yang, X.M. 2017: Estimation of crystallization pressure of granite intrusions; Lithos, v. 286–287, p. 324–329, URL <https://doi.org/10.1016/j.lithos.2017.06.018>.

Yang, X.M. 2019: Using rare earth elements (REE) to decipher the origin of ore fluids associated with granite intrusions; Minerals, v. 9, p. 426, URL <https://doi.org/10.3390/min9070426>.

Yang, X.M., Drayson, D. and Polat, A. 2019: S-type granites in the western Superior Province: a marker of Archean collision zones; Canadian Journal of Earth Sciences, v. 56, p. 1409–1436, URL <https://doi.org/10.1139/cjes-2018-0056>.

Yang, X.M. and Gilbert, H.P. 2014a: Archean tonalite-trondhjemite-granodiorite (TTG) suite in the Bird River greenstone belt, southeastern Manitoba: lithogeochemical characteristics, geodynamic evolution, and potential for porphyry Cu-(Au) mineralization (abstract); Geological Association of Canada–Mineralogical Association of Canada, Joint Annual Meeting, Fredericton, New Brunswick, May 21–23, 2014, Program with Abstracts, p. 294.

Yang, X.M. and Gilbert, H.P. 2014b: Mineral chemistry of chromite in the Mayville intrusion: evidence for petrogenesis and linkage to the Bird River sill in the Neoarchean Bird River greenstone belt, southeastern Manitoba (NTS 52L5, 6, 12); *in* Report of Activities 2014, Manitoba Mineral Resources, Manitoba Geological Survey, p. 32–48.

Yang, X.M. and Lentz, D.R. 2005: Chemical composition of rock-forming minerals in gold-related granitoid intrusions, southwestern New Brunswick, Canada: implications for crystallization conditions, volatile exsolution and fluorine-chlorine activity; Contributions to Mineralogy and Petrology, v. 150, p. 287–305.

Yang, X.M., Gilbert, H.P., Corkery, M.T. and Houlé, M.G. 2011: The Mayville mafic–ultramafic intrusion in the Neoarchean Bird River greenstone belt, southeastern Manitoba (part of NTS 52L12): preliminary geochemical investigation and implication for PGE-Ni-Cu-(Cr) mineralization; *in* Report of Activities 2011, Manitoba Innovation, Energy and Mines, Manitoba Geological Survey, p. 127–142.

Yang, X.M., Gilbert, H.P. and Houlé, M.G. 2012: Geological investigations of the Cat Creek area in the Neoarchean Bird River greenstone belt, southeastern Manitoba (part of NTS 52L12): new insights into PGE-Ni-Cu-Cr mineralization; *in* Report of Activities 2012, Manitoba Innovation, Energy and Mines, Manitoba Geological Survey, p. 32–53.

Yang, X.M., Gilbert, H.P. and Houlé, M.G. 2013: Cat Lake–Euclid Lake area in the Neoarchean Bird River greenstone belt, southeastern Manitoba (parts of NTS 52L11, 12): preliminary results of bedrock geological mapping and their implications for geodynamic evolution and metallogeny; *in* Report of Activities 2013, Manitoba Mineral Resources, Manitoba Geological Survey, p. 70–84.

Yang, X.M., Lentz, D.R. and Chi, G. 2020: Redox effect on estimating crystallization pressure of granites [extended abstract]; Geoconvention 2020: Geological Association of Canada–Mineralogical Association of Canada, Joint Annual Meeting, Calgary, Alberta, September 21–23, 2020, Program with Abstracts, p. 1–2, URL <https://geoconvention.com/wp-content/uploads/abstracts/2020/56244-redox-effect-on-estimating-crystallization-pressur.pdf> [September 2020].

Yang, X.M., Lentz, D.R., Chi, G. and Kyser, T.K. 2004: Fluid-mineral reaction in the Lake George granodiorite, New Brunswick: implications for Au-W-Mo-Sb mineralization; The Canadian Mineralogist, v. 42, p. 1443–1464.

Yang, X.M., Lentz, D.R., Chi, G. and Thorne, K.G. 2008: Geochemical characteristics of gold-related granitoids in southwestern New Brunswick, Canada; Lithos, v. 104, p. 355–377.

Yang, X.Z., Matsueda, H. and Ishihara, S. 1994: Mode of occurrence, chemical composition, and origin of Cr-Fe-Ti oxides of the Jinchuan Ni-Cu-PGE deposits, China; International Geology Review, v. 36, p. 311–327.

Yildirim, E., Yildirim, N., Dönmez, C., Günay, K., Korkmaz, T., Akyildiz, M. and Gören, B. 2020: Composition of Pancarli magmatic Ni-Cu±(PGE) sulfide deposit in the Cadomian-Avalonian Belt, eastern Turkey; Journal of Earth Science, v. 31, p. 536–550.

Yuan, F., Zhou, T., Zhang, D., Jowitt, S.M., Keays, R.R., Liu, S. and Fan, Y. 2012: Siderophile and chalcophile metal variations in basalts: implications for the sulphide saturation history and Ni-Cu-PGE mineralization potential of the Tarim continental flood basalt province, Xinjiang Province, China; Ore Review Geology, v. 45, p. 5–15.

Zhang, Q., Wang, Y., Li, C.-D., Jin, W.-J. and Jia, X.-Q. 2006: A granite classification based on pressures; Geological Bulletin of China, v. 25, p. 1274–1278.